



PROGRAMA DE DESARROLLO  
DE LAS CIENCIAS BÁSICAS  
MEC - UDELAR



UNIVERSIDAD  
DE LA REPÚBLICA  
URUGUAY

# Plasticity of the electrical synaptic transmission between neurons from the mesencephalic trigeminal nucleus

Mechanisms and functional operations

Federico Davoine

Programa de Posgrado en Ciencias Biológicas, opción Neurociencias  
PEDECIBA

Universidad de la República - Universidad de la República

Montevideo – Uruguay

Noviembre de 2021



PROGRAMA DE DESARROLLO  
DE LAS CIENCIAS BÁSICAS  
MEC - UDELAR



UNIVERSIDAD  
DE LA REPÚBLICA  
URUGUAY

# Plasticity of the electrical synaptic transmission between neurons from the mesencephalic trigeminal nucleus

Mechanisms and functional operations

Federico Davoine

Tesis de Doctorado presentada al Programa de  
Desarrollo de las Ciencias Básicas , como parte de los  
requisitos necesarios para la obtención del título de  
Doctor en Ciencias Biológicas, opción Neurociencias

Directors:

Dr. Sebastián Curti

Dr. Alberto Pereda

Montevideo – Uruguay

Noviembre de 2021

Davoine, Federico

Plasticity of the electrical synaptic transmission between neurons from the mesencephalic trigeminal nucleus / Federico Davoine. - Montevideo: Universidad de la República, Universidad de la República, PEDECIBA, 2021.

xv, 177 p.: il.; 29, 7cm.

Directors:

Sebastián Curti

Alberto Pereda

Tesis de Doctorado – Universidad de la República, Programa en Ciencias Biológicas, opción Neurociencias, 2021.

References: p. 141 – 177.


1. Uniones gap, 2. Plasticidad sináptica, 3. Corriente activada por hiperpolarización  $I_H$ . I. Curti, Sebastián, Pereda, Alberto, . II. Universidad de la República, Programa de Posgrado en Ciencias Biológicas, opción Neurociencias. III. Título.

Fundamentación de la nota de aprobación de la tesis de Doctorado del Mag. Federico Davoine

La tesis del Mag. Federico Davoine, titulada "Plasticity of the electrical synaptic transmission between neurons from the mesencephalic trigeminal nucleus" tiene como tema central la comunicación a través uniones de tipo "gap junction" entre neuronas del núcleo del trigémino. Davoine utiliza técnicas de registro de "patch-clamp" tanto en modalidad de fijación de voltaje como de corriente en rodajas de tronco mantenidas in vitro, combinando los registros electrofisiológicos con modelos computacionales. El trabajo de tesis reporta la heterogeneidad entre los coeficientes de acople de las neuronas del núcleo trigémino y cómo la sinapsis eléctrica contribuye a la detección de coincidencia. Buena parte de la tesis está dedicada a estudiar la plasticidad inducida por una estimulación que remeda la actividad fisiológica en estas neuronas sensoriales. Davoine muestra que la actividad repetida genera una disminución de larga duración del acople y aporta datos sobre los posibles mecanismos a nivel molecular. Los registros son de excelente calidad y los resultados están ilustrados en forma clara y la discusión de los mismos es presentada en forma rigurosa, planteando interpretaciones alternativas cuando corresponde. Finalmente, la presentación oral del trabajo de tesis fue muy clara, respondiendo a las preguntas formuladas por el tribunal con solvencia. El trabajo del Mag. Davoine es un valioso aporte al campo de la comunicación eléctrica en las redes neurales de los mamíferos.

Por los motivos antes expuestos y de acuerdo al reglamento PEDECIBA vigente, el tribunal por unanimidad llega al siguiente fallo: Aceptación.

  
Raúl E. Russo

  
FEDERICO F. TIZABI

  
Gonzalo Pizarro



# I would like to thank...

Sebastián Curti and Alberto Pereda, for taking up the role of guiding me through my doctorate studies. Alberto was key to expand tremendously my culture on electrical synapses, as I hope this thesis' introductory chapter reflects. Sebastián has deeply shape my formation as a researcher, not only teaching me technical stuff (even things that are trivial for a undergraduate student on Biology/Medicine), but also on how to be scientifically rigorous. From our discussions, I have learnt that asking good questions is the basis of performing relevant research.

Pablo Monzón, for backing my interdisciplinary career, from my master studies to my consolidation as a full-time teaching assistant at the Instituto de Ingeniería Eléctrica.

Julieta López, Ana Asuaga, Daniel Ariosa and María Simon for their unwavering and vital support, that provided me stability during this process.

All the friends that I have made during my undergraduate and graduate studies at the Facultad de Ingeniería. In particular, even though I do not work in the Instituto de Física anymore, I keep cherished memories from dear coworkers and friends, especially from the rooms 10, 18 and  $\beta$ .

My parents Graciela and Roberto, and my brother Valentín, for their affection and unconditional support. It is not a coincidence that my brother and I have followed academic paths: it is a product of our parents' efforts to foster our intellectual inquisitiveness and critical thinking.

Last, but not least, I would like to thank Antonella. She has not only collaborated on performing experiments for this thesis, but also she has became my life partner.

# Abbreviations

- I<sub>H</sub>* Hyperpolarization-activated current 3, 134
- g<sub>J</sub>* Gap junction conductance 3, 8, 9, 10, 14, 31, 32, 121, 134
- A-MN** A-motor neurons 21, 22
- AC** Adenylyl cyclase 99, 102, 108, 109, 111
- ACSF** Artificial cerebrospinal fluid 87, 88, 138
- AF6** Afadin 11
- AHP** After-hyperpolarization potential 18, 26
- AM251** Antagonist of CB<sub>1</sub> receptors. Chemical name: 1- (2,4- dichlorophenyl) -5- (4-iodophenyl)- 4-methyl-N- 1-piperidinyl- 1H-pyrazole-3- carboxamide 62, 96, 97, 123, 124
- ATP** Adenosine triphosphate 99, 106, 109, 120
- AVA** Command interneurons in the *Caenorhabditis elegans* escape circuit 20, 21, 22
- BAPTA** Fast calcium chelator. Chemical name: 1,2- Bis(o-aminophenoxy)ethane-N,N,N',N'- tetraacetic acid 87, 88, 108, 114, 123, 124, 127, 130, 138
- Botox** Botulinum Toxin 103, 104, 106, 113, 120, 124
- CAM** Cell adhesion molecules 11
- CB<sub>1</sub>** Cannabinoid receptor type 1 vi, 96, 97, 110, 111, 113, 123, 131, 139
- CC** Coupling coefficient 67, 69, 70, 72, 76, 78, 85, 107, 115, 116, 120, 121, 132
- CPG** Central pattern generator 135, 136
- CT** Carboxyl terminus 10, 11, 12
- CaM** Calmodulin 11, 12
- CaMKII** Ca<sup>2+</sup>/calmodulin-dependent protein kinase II x, xiv, 12, 30, 31, 33, 64, 98, 108, 113, 123, 131, 135, 138, 139
- CaV** Voltage-gated calcium channels 108, 109, 111, 138, 139
- Cx** Connexin xv, 4, 6, 7, 8, 9, 10, 11, 12, 13, 14, 21, 23, 24, 26, 30, 31, 32, 33, 61, 64, 72, 83, 99, 103, 108, 109, 111, 112, 113, 133, 138, 139
- DC** Direct current 16
- DCN** Deep cerebellar nuclei 26

**DRG** Dorsal root ganglion 109

**DSGC** Directionally selective ganglion cell 24, 25

**FFT** Fast Fourier Transform 70

**FS** Fast spiking neocortical interneurons 16, 17, 19

**GABA**  $\gamma$ -aminobutyric acid 7, 26, 110

**GC** Ganglion cell 23

**GJ** Gap junctions ix, x, xv, 1, 2, 3, 4, 5, 6, 7, 8, 9, 10, 11, 12, 13, 14, 15, 16, 17, 20, 21, 23, 24, 25, 26, 27, 28, 30, 31, 32, 33, 34, 60, 61, 63, 64, 67, 71, 72, 73, 74, 75, 83, 84, 85, 99, 103, 107, 108, 111, 112, 113, 114, 115, 117, 131, 132, 133, 134, 135, 137, 138, 139

**HCN** Hyperpolarization-activated cyclic nucleotide-gated channels xv, 3, 92, 109, 111, 113, 114, 116, 123, 127, 130, 131, 132, 133, 134, 135, 138

**IO** Inferior olive 8, 25, 26, 27, 31, 33, 87, 90, 108

**IP3** Inositol 1,4,5-trisphosphate 137, 138

**Inx** Innexin 8, 9, 21

**K(Ca)**  $\text{Ca}^{2+}$ -activated  $\text{K}^+$  channels 115, 116, 123, 130, 131

**KIR**  $\text{K}^+$  inward rectifier channels 123, 130, 131

**KN93**  $\text{Ca}^{2+}$ /calmodulin-dependent protein kinase II inhibitor. Chemical name: N-[2- [ [ 3- (4- Chlorophenyl)- 2- propenyl] methylamino] methyl] phenyl] - N- (2-hydroxyethyl)- 4-methoxybenzenesulphonamide 62, 123, 124

**KO** Knockout 23, 110

**LTD** Long-term depression 31, 32, 80, 85, 108, 111, 120

**LTP** Long-term potentiation 31, 32, 115

**LTS** Low-threshold spiking neocortical interneurons 16, 17

**M-cell** Mauthner cell 21, 22, 23, 31, 32, 33, 90, 96, 108, 111

**MAPK** Mitogen-activated protein kinase 12, 131

**MUPP** Multi-PDZ domain protein 11

**MesV** Mesencephalic trigeminal nucleus ix, x, xi, xiii, xiv, xv, 2, 3, 4, 7, 8, 16, 17, 19, 27, 28, 29, 33, 34, 60, 61, 62, 63, 64, 66, 67, 69, 70, 71, 72, 73, 74, 80, 83, 87, 90, 92, 96, 98, 99, 102, 103, 104, 106, 107, 108, 109, 110, 111, 113, 114, 115, 116, 118, 119, 120, 125, 126, 127, 128, 130, 131, 132, 133, 134, 135, 136, 137, 138, 140

**NMDA** N-Methyl-D-aspartate x, xiv, 3, 7, 8, 31, 60, 90, 91, 108, 109, 111, 113, 115, 116

**PJS** Postjunctional spikelet 18, 19

**PKA** Protein kinase A xiv, 11, 30, 32, 33, 64, 98, 99, 100, 102, 108, 111, 113, 131, 135, 138

**PKC** Protein kinase C 12, 131, 139

**PKG** Protein kinase G 12

**Panx** Pannexin 109, 110

**RMP** Resting membrane potential 19, 31, 34, 63, 72, 76, 85, 92

**SEM** Standard error of the mean 78

**SQ22536** Adenylyl cyclase inhibitor. Chemical name: 9-(Tetrahydro-2- furanyl)-9H-purin-6-amine 62, 102, 123, 124

**STD** Short-term depression 80, 85

**STO** Subthreshold oscillations 26, 27, 31

**TEA** Tetraethylammonium 130, 132

**TRN** Thalamic reticular nucleus 16, 17, 19, 31, 32, 83, 87, 107, 108, 111, 138

**UdelaR** Universidad de la República 4

**WT** Wild type 26, 110

**ZAP** Variable-frequency sinusoid 70

**ZO** Zonula occludens 10, 11, 12

**cAMP** Cyclic adenosine monophosphate 99, 100, 111, 135, 137

**cGMP** Cyclic guanosine monophosphate 2, 3, 34, 61, 125, 133, 134, 135, 136

**eCB** Endocannabinoids 96, 110, 111, 113

**mGluR** Metabotropic glutamate receptors 32

# List of Figures

2.1	Schematic representation of a gap junction (GJ) and its components. . . .	6
2.2	Rectification of heterotypic GJ . . . . .	10
2.3	Trafficking of GJ in a pair of electrically coupled HeLa cells . . . . .	13
2.4	Electrical transmission between coupled cells . . . . .	15
2.5	Frequency-dependence of the coupling coefficient . . . . .	17
2.6	Role of non-synaptic conductances in electrical synaptic transmission. . . .	19
2.7	Escape circuits of <i>C. elegans</i> and the fish . . . . .	22
2.8	Schematic representation of the retinal circuitry and its electrical synaptic connectivity . . . . .	23
2.9	Lag normalization in ON-OFF directionally selective ganglion cells . . . . .	25
2.10	Coincidence detection between AII amacrine cells from the retina . . . . .	27
2.11	Temporal window of coincidence detection . . . . .	29
3.1	Electrical coupling between MesV neurons supports coincidence detection . .	40
3.2	Coincidence detection between pairs of electrically coupled MesV neurons is heterogeneous . . . . .	41
3.3	Characterization of hyperpolarization-activated cationic current ( $I_H$ ) of MesV neurons . . . . .	43
3.4	$I_H$ of MesV neurons is strongly modulated by cGMP . . . . .	45
3.5	cGMP modulates the firing properties and resting potential of MesV neurons	46
3.6	cGMP effects on input resistance and subthreshold potential of MesV neurons	47
3.7	cGMP does not target other membrane conductances of MesV neurons . .	48
3.8	The $I_H$ is necessary for the cGMP-induced effects on neuronal excitability	50
3.9	Upregulation of the $I_H$ is sufficient to increase firing . . . . .	51
3.10	cGMP enhances coincidence detection gain . . . . .	52
3.11	cGMP-induced enhancement of coincidence detection gain does not involve changes in gap junction conductance . . . . .	53
3.12	Upregulation of the $I_H$ is sufficient to enhance coincidence detection gain .	54
4.1	Temperature dependence of $g_J$ in MesV neurons . . . . .	66

4.2	Coupling coefficient is heterogeneous in the population of MesV neurons. .	68
4.3	Characteristics of spike transmission . . . . .	70
4.4	The impact of electrical coupling on the effective input resistance is extremely varied . . . . .	71
4.5	Gap junction conductance $g_J$ is heterogeneous . . . . .	73
4.6	Simultaneous repetitive firing elicits GJ short-term depression . . . . .	75
4.7	Coupling coefficient decreases after repeated stimulation . . . . .	77
4.8	$g_J$ decreases after repeated stimulation . . . . .	79
4.9	Time courses of the $g_J$ depression and recovery . . . . .	81
4.10	Repeated stimulation induces stronger plasticity . . . . .	82
4.11	Unilateral stimulation induces half of the plasticity . . . . .	84
4.12	Long-term depression induced by activity-like stimulation at physiological temperature . . . . .	86
4.13	Lack of free $\text{Ca}^{2+}$ weakens the activity-induced $g_J$ plasticity, but does not prevent it . . . . .	89
4.14	Current through NMDA receptors decreases $g_J$ without firing activity . . .	91
4.15	$I_H$ constitutes a major inward current during the plasticity-inducing stimulation and its blockade diminished $g_J$ depression . . . . .	93
4.16	Blocking basal $I_H$ current enhances $g_J$ . . . . .	95
4.17	Inhibition of the $\text{CB}_1$ receptor augments the $g_J$ depression after the activity-like stimulation . . . . .	97
4.18	CaMKII is not involved in the activity-induced $g_J$ plasticity . . . . .	98
4.19	Stimulation of adenylyl cyclase elicits $g_J$ decrease without electrical activity	101
4.20	Inhibition of adenylyl cyclase does not impair the activity-induced $g_J$ plasticity . . . . .	102
4.21	Fast turnover rate of MesV gap junctions . . . . .	105
4.22	Inhibition of exocytosis does not impair the activity-induced $g_J$ plasticity .	106
4.23	Knock-out of Pannexin 1 does not alter the activity-induced $g_J$ plasticity .	110
4.24	Summary of the possible pathways involved in the plasticity of GJ between MesV neurons . . . . .	113
5.1	Role of $g_J$ and $R_{in}$ in setting the coupling coefficient . . . . .	116
5.2	Measurement of the input resistance $R_{in}$ in voltage clamp . . . . .	118
5.3	The $I_H$ can be accurately described without subtraction of CsCl traces . .	119
5.4	Time courses of the coupling coefficient and its components, after the activity-like stimulation . . . . .	121
5.5	Several non-synaptic membrane currents get affected by the activity-like stimulation . . . . .	122

5.6	Blockade of $I_H$ and $K^+$ currents abolishes activity-induced $R_{in}$ modifications	124
5.7	Characterization of $I_H$ in mice MesV neurons . . . . .	126
5.8	$I_H$ properties in coupled and uncoupled MesV neurons . . . . .	128
5.9	Activity-like stimulation diminishes $I_H$ maximum conductance, without modifying its biophysical properties . . . . .	129
5.10	Summary of some possible pathways involved in the regulation of intrinsic properties . . . . .	133

# Contents

<b>Abbreviations</b>	<b>viii</b>
<b>List of Figures</b>	<b>ix</b>
<b>1 Introduction</b>	<b>1</b>
1.1 Organization . . . . .	1
1.2 Main contributions . . . . .	3
1.3 Acknowledgments . . . . .	4
<b>2 Electrical synapses: from structure to function</b>	<b>5</b>
2.1 Introduction . . . . .	5
2.2 Structural basis . . . . .	5
2.2.1 Gap junctions . . . . .	5
2.2.2 Structural interactions with other proteins . . . . .	9
2.2.3 Trafficking . . . . .	12
2.3 Electrical synaptic transmission . . . . .	14
2.3.1 Main properties . . . . .	14
2.3.2 Coupling coefficient . . . . .	14
2.3.3 Frequency dependence of the coupling coefficient . . . . .	16
2.3.4 Spike transmission . . . . .	17
2.3.5 Interaction with intrinsic properties . . . . .	18
2.4 Functional role in neuronal circuits . . . . .	20
2.4.1 Introduction . . . . .	20
2.4.2 Synergy between chemical and electrical synapses in escape circuits	20
2.4.3 Lateral excitation in the retina . . . . .	23
2.4.4 Synchronization and inhibitory shunting in the inferior olive . . . .	25
2.4.5 Coincidence detection in the mammalian brain . . . . .	27
2.5 Plasticity . . . . .	30
2.5.1 Introduction . . . . .	30
2.5.2 Induction . . . . .	30



2.5.3	Expression . . . . .	33
<b>3</b>	<b>Role of the intrinsic properties on coincidence detection</b>	<b>34</b>
3.1	Introduction . . . . .	35
3.2	Materials and methods . . . . .	36
3.2.1	Experimental design . . . . .	36
3.2.2	Calculation of coupling coefficient . . . . .	36
3.2.3	Estimation of gap junction conductance . . . . .	36
3.2.4	Calculation of coincidence detection index . . . . .	37
3.2.5	Assessment of MesV neurons excitability . . . . .	37
3.2.6	Recording of the persistent $Na^+$ current . . . . .	37
3.2.7	Recording of the $I_H$ . . . . .	37
3.2.8	Statistical analysis . . . . .	38
3.2.9	MesV cells model and computational simulations . . . . .	38
3.3	Results . . . . .	39
3.3.1	Coincidence detection between pairs of electrically coupled mesencephalic trigeminal (MesV) neurons is heterogeneous . . . . .	39
3.3.2	Coincidence detection gain critically depends on the intrinsic excitability of coupled neurons . . . . .	39
3.3.3	Regulation of the $I_H$ as a way to modulate MesV neuron excitability	42
3.3.4	Upregulation of the $I_H$ increases MesV neuron excitability . . . . .	44
3.3.5	cGMP selectively targets the $I_H$ of MesV neurons . . . . .	47
3.3.6	The $I_H$ is necessary for the cGMP-induced effects on neuronal excitability . . . . .	49
3.3.7	Computer simulations show that the upregulation of the $I_H$ is sufficient to induce the cGMP effects on MesV neuron excitability . . . . .	49
3.3.8	cGMP-induced enhancement of coincidence detection gain cannot be explained by changes of the strength of electrical coupling . . . . .	51
3.3.9	Computer simulations show that upregulation of the $I_H$ enhances the gain of coincidence detection in networks of electrically coupled MesV neurons . . . . .	53
3.4	Discussion . . . . .	54
3.4.1	Coincidence detection in the MesV nucleus is heterogeneous and is critically determined by the intrinsic excitability of neurons . . . . .	54
3.4.2	cGMP-induced upregulation of the $I_H$ increases MesV neuron's excitability and coincidence detection gain . . . . .	54
3.4.3	Functional relevance . . . . .	55
3.5	References . . . . .	56

<b>4</b>	<b>Activity-induced gap junctions plasticity</b>	<b>60</b>
4.1	Introduction . . . . .	61
4.2	Materials and methods . . . . .	62
4.2.1	Experimental design . . . . .	62
4.2.2	Data processing . . . . .	63
4.2.3	Calculation of the gap junction conductance . . . . .	63
4.2.4	Temperature dependence of $g_J$ in MesV neurons . . . . .	64
4.2.5	Statistical analysis . . . . .	65
4.3	Results . . . . .	67
4.3.1	Characteristics and impact of electrical coupling between MesV neurons . . . . .	67
4.3.2	Gap junction conductance $g_J$ is heterogeneous in the MesV neurons population . . . . .	72
4.3.3	<i>In vivo</i> -like firing diminishes $g_J$ . . . . .	74
4.3.4	Activity-like voltage clamp stimulation decreases the coupling coefficient and $g_J$ . . . . .	74
4.3.5	The depression of $g_J$ has transient and long-term components . . .	80
4.3.6	Activity-induced $g_J$ plasticity is primed by previous stimulation . .	82
4.3.7	$g_J$ plasticity results from side-additive contribution of each coupled partner . . . . .	83
4.3.8	Activity-like stimulation at physiological temperature elicits long-term depression of $g_J$ . . . . .	85
4.3.9	Calcium weakens, but does not prevent, the activity-induced $g_J$ depression . . . . .	87
4.3.10	Bath application of NMDA produced $g_J$ depression . . . . .	90
4.3.11	$I_H$ participates in setting basal $g_J$ and in the activity-induced plasticity . . . . .	92
4.3.12	Blockade of cannabinoid type 1 receptors enhances activity-induced plasticity . . . . .	96
4.3.13	Neither CaMKII nor PKA are involved in the activity-induced plasticity in MesV neurons . . . . .	98
4.3.14	Fast gap junction turnover rate in control conditions . . . . .	103
4.3.15	Somatic exocytosis is not involved in the activity-induced plasticity	106
4.4	Discussion . . . . .	107
4.4.1	Heterogeneity of electrical synapses 'can be explained by activity-dependent plasticity . . . . .	107
4.4.2	Unilateral stimulation produced half of the plasticity . . . . .	107

4.4.3	Ca <sup>2+</sup> participates in the basal regulation and activity-dependent plasticity . . . . .	108
4.4.4	HCN channels participate in the regulation of $g_J$ . . . . .	109
4.4.5	Endocannabinoids are involved in the $g_J$ plasticity induced by activity	110
4.4.6	Trafficking of Cx36 might participate in electrical synaptic plasticity	111
<b>5</b>	<b>Activity-induced plasticity of intrinsic properties</b>	<b>114</b>
5.1	Introduction . . . . .	115
5.2	Materials and methods . . . . .	117
5.2.1	Measurement of $R_{in}$ from current traces in voltage clamp . . . . .	117
5.2.2	Measurement of $I_H$ . . . . .	119
5.3	Results . . . . .	120
5.3.1	Activity-like stimulation reduces the input resistance . . . . .	120
5.3.2	Characterization of $I_H$ in mice MesV neurons . . . . .	125
5.3.3	The maximum conductances of $I_H$ and the gap junctions may be correlated dynamically . . . . .	125
5.4	Discussion . . . . .	130
5.4.1	Activation of K <sup>+</sup> channels is most likely behind the activity-induced decrease of $R_{in}$ . . . . .	130
5.4.2	Co-regulation of the abundance of HCN and GJ channels . . . . .	131
<b>6</b>	<b>General discussion</b>	<b>134</b>
6.1	Main findings . . . . .	134
6.2	Diversity of regulation through signaling pathways . . . . .	135
6.3	Future directions . . . . .	137
	<b>Bibliography</b>	<b>141</b>
	<b>Glossary</b>	<b>177</b>

# Chapter 1

## Introduction

Synapses are specialized contacts that support the signal transmission between neurons. By far, chemical synapses have received most of the researchers' attention, due to their ubiquity in the nervous system and their relevance in superior functions. Nevertheless, electrical synapses have been considerably less studied, due to their apparent simplicity and understated role within important neural networks. However, in the past decades, their functional relevance has been asserted in several regions of the mammalian central nervous system. This thesis aims to contribute to the understanding of electrical synapses and their plasticity, using the mesencephalic trigeminal nucleus (MesV) of rodents as experimental model. Our hypothesis is that the electrical synaptic transmission can be regulated by plastic changes in both synaptic and non-synaptic mechanisms, due to neuromodulators and firing activity. We will see in the introductory chapter 2 that the electrical synapses are complex systems, driven by the interaction between synaptic and non-synaptic channels, among other things. We will focus on the role of only two of these multiple components: the hyperpolarization-activated current  $I_H$  and the gap junction (GJ), whose plastic modifications by different stimuli drastically alter the operation of the electrical synapses.

### 1.1 Organization

The content of this thesis is organized in the following five chapters:

The chapter 2 is a general review on electrical synapses, from their structure to their function, whose aim is to present their diversity and complexity. It starts with the GJ, which are the main structural component of the electrical synapses, but are also present in non-neuronal cell types. As a consequence, we analyze some of the abundant information about the molecular properties of GJ, some of which are not even expressed in neurons, but

whose properties are similar. Afterwards, we provide a review on the electrical synaptic transmission, emphasizing the relevance of synaptic and non-synaptic membrane mechanisms. To discuss the functional role of electrical synapses, we briefly present three types of networks: escape circuits (in *C. elegans* and the fish), the retina and the inferior olive, each one representing key aspects of their operation. We also introduce the coincidence detection in electrically-coupled mammalian neural networks. Finally, we describe the plasticity of the electrical synapses dividing it on two phases: induction and expression. This last section brings together the regulation of GJ presented in the section 2.2.1, with the modification of the properties presented in section 2.3 and the circuits discussed in section 2.4.

The chapter 3 examines the mechanisms of the coincidence detection, an emergent property of the electrical synaptic transmission, which enables coupled neurons to discern between simultaneous and non-simultaneous inputs. After a brief summary of our key findings, the paper presenting our results is reproduced in integrity, as it was published in the Journal of Neurophysiology. We start by studying the diversity of the coincidence detection in the MesV neurons' population and its correlation with the coupling and intrinsic properties. A conspicuous determinant of the later is the hyperpolarization-activated current  $I_H$ , which is modulated by cyclic nucleotides, such as the cyclic GMP (cGMP). In the paper, we characterize the biophysical properties of the  $I_H$  current and its modulation by cGMP. Interestingly, cGMP modulates the excitability of individual MesV neurons and augments the coincidence detection of coupled pairs. Using pharmacological and computational tools, we show that the modulation of  $I_H$  by cGMP is necessary and sufficient to produce the enhancement of the coincidence detection.

The chapter 4 deals with the GJ and their plasticity. First, we characterize the diversity of electrical coupling and its impact on the effective input resistance of the neurons. Then, we focus on the GJ conductance  $g_J$ , which is a key parameter affecting both. Given that MesV neurons fire during masticatory behaviors in rodents, we test the effect of activity-like electrical stimulation, finding a diminution in the coupling strength, explained by reduction of both input resistance  $R_{in}$  and  $g_J$ . We focus on the decrease of  $g_J$ , which partially recovers after few minutes. After a thorough description of the plasticity phenomenon in control conditions, we study the mechanisms responsible for its induction with surprising results: calcium ( $\text{Ca}^{2+}$ ) seems to be sufficient but not necessary, the  $I_H$  current contributes to it, and the cannabinoid receptor 1 modulates it. We explore some intracellular second messengers, confirming that the protein kinase A (through the activation of the adenylyl cyclase) depresses it, but it is not involved in the induction. In order

to understand how GJ may modify their strength, we interfere with their trafficking in basal conditions, uncovering a fast rate of turnover that might be regulated.

The chapter 5 goes back to the activity-induced diminution of  $R_{in}$ , that accounts for half the reduction in coupling strength. Using the data from voltage clamp experiments performed in the chapter 4, we show that the decreases of  $R_{in}$  and  $g_J$  seem to be caused by different mechanisms, due to their distinct time courses during the induction and the partial recovery. Holding current augments during the phenomenon, suggesting the upregulation of  $K^+$  currents, with possible participation of a  $Ca^{2+}$ -activated one. In addition, other membrane currents could also be affected by the electrical stimulation. Among them, we center our analysis on the  $I_H$ , characterizing it in control conditions and finding a correlation between maximum  $I_H$  conductance  $g_{Hmax}$  and  $g_J$ . Interestingly, the maximum  $I_H$  is reduced after the stimulation, with a strong correlation with  $g_J$ -depression during its induction, suggesting possible shared mechanisms that remain to be explored.

The final chapter 6 quickly summarizes our main findings, going later to ask more questions that arose from the thesis, sketching some experiments to answer them.

## 1.2 Main contributions

- The susceptibility to coincident inputs of electrically coupled MesV neurons is very heterogeneous, and can be increased by the upregulation of the  $I_H$  by cGMP. This property heavily relies on the combination of coupling strength and neuronal excitability.
- Both the  $I_H$  and the  $g_J$  are highly variable in the MesV nucleus, with diversity even within the same animal.
- There is a correlation between the maximum conductance of  $I_H$  ( $g_{Hmax}$ ) and  $g_J$  in control conditions.
- *In vivo*-like electrical activity of coupled MesV neurons induces a drop in  $g_J$  and  $g_{Hmax}$ .
- The activity-dependent plasticity of  $g_J$  has short- and long-term components, and is strongly  $Ca^{2+}$ -depending.
- The plasticity of  $g_J$  induced by the activation of one coupled neuron seems to be independent on the state of its coupled partner.
- The activation of NMDA receptors and HCN channels modifies  $g_J$ .
- Endocannabinoids acting on  $CB_1$  receptors appear to be involved in the metaplasticity of the electrical synapses.

- The basal turnover of GJ between MesV neurons is extremely fast.
- The temperature dependence of  $g_J$  seems to indicate gating of the Cx36 in the MesV nucleus.

## 1.3 Acknowledgments

The work associated with chapter 3 received financial support by Agencia Nacional de Investigación e Innovación (ANII, FCE\_1\_2014\_1\_104725). I received two doctoral grants from the Comisión Académica de Posgrados from Universidad de la República (UdelaR), that were key to allow me almost complete dedication to this thesis. In addition, the Comisión Sectorial de Investigación from UdelaR awarded us the project “Plasticidad de la transmisión sináptica eléctrica inducida por actividad en mamíferos” to support the research related to chapter 4.

# Chapter 2

## Electrical synapses: from structure to function

### 2.1 Introduction

According to a textbook definition, “*Complex systems are co-evolving multilayer networks*” (Stefan Thurner, 2018). In this chapter, we present the electrical synapses as complex systems, layer by layer. Indeed, their structure is determined by their interaction with scaffolding and regulatory proteins involved in intricate signaling cascades, acting in response to electrical and chemical stimuli in the cellular membrane, within the context of neural networks. The aim of this introductory chapter is to understand how these complex interactions provide electrical synapses with such an outstanding flexibility, which will be further explored in the following chapters 3 and 4.

### 2.2 Structural basis

#### 2.2.1 Gap junctions

Gap junctions (GJ) are the main structural basis of the electrical synaptic transmission between neurons, also supporting the communication in other cell types. They are composed by clusters of intercellular channels (termed “plaques”), resulting from the assembly of hemichannels from two adjacent cells (Fig. 2.1). These hemichannels are composed by two genetically different protein families: connexins (Cx) in vertebrates and innexins (Inx) in invertebrates, being called connexons and innexons, respectively. In vertebrates, innexin-like (Abascal and Zardoya, 2013) genes express pannexins (Panx), which usually form hemichannels, even though it has been shown that they can form GJ when over-expressed in oocytes (Bruzzone et al., 2003). Connexins and innexins are an example of



convergent evolution, due to their strikingly resembling structure: four transmembrane subunits, two extracellular loops and the intracellular amino and carboxyl termini (Söhl and Willecke, 2004; Oshima et al., 2016). They also display general similar characteristics in terms of permeability, regulation by pH and calcium, and sensitivity to the difference between the membrane potentials of the coupled cells (tranjunctional voltage  $V_J$ ; Skerrett and Williams (2017)).

While the naming of innexins is not standardized (Güiza et al., 2018), connexins are designated according to their predicted molecular weight in kilodaltons (Skerrett and Williams, 2017), with a prefix for species if necessary. For example, hCx36 stands for the human connexin 36.

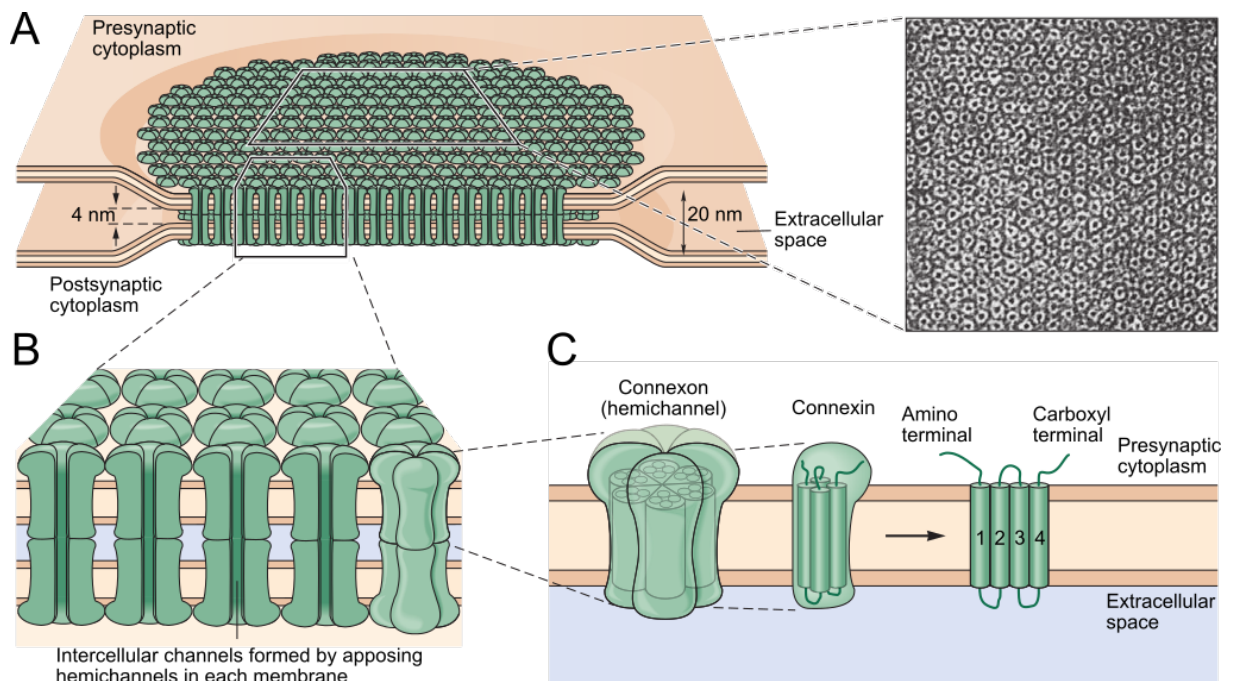


**Figure 2.1: Schematic representation of a gap junction (GJ) and its components.** *A*: GJ plaque, made by an array of several intercellular channels that communicate the cytoplasm of two apposing cells. The electron micrograph on the right shows one side of a GJ, where each channel is displayed in white (Magnification x307,800). Note its almost crystal-like hexagonal structure. *B*: detailed lateral view of the GJ, with the two connexons (hemichannels) forming the intercellular channel. *C*: each connexon is composed by six connexins, that have four transmembrane units, two extracellular loops, one intracellular and the carboxyl and amino termini. Modified from (Kandel et al., 2012).

GJ can assemble involving identical (homotypic configuration) or different (heterotypic) hemichannels. Furthermore, each hemichannel can be constituted by identical or different subunits too, being called heteromeric or homomeric respectively. Given that there are 20 connexins in mice, 21 in humans (Willecke et al., 2002) and more than 40

orthologues across species (Connors and Long, 2004), hypothetically there could be a large number of possible GJ. However, most of the possible combinations are not functional (Palacios-Prado and Bukauskas, 2012). In particular, Cx36 appears to be unable to form heterotypic GJ (Al-Ubaidi et al., 2000).

## Distribution

The distribution of connexins is widespread and cell-dependent. Just to name some examples, Cx43 -the most abundantly expressed Cx (Thévenin et al., 2013)- is found in blood vessels (Bruzzone et al., 1993), cardiomyocytes (Vozzi et al., 1999) and astrocytes (Nagy and Rash, 2000), Cx32 in oligodendrocytes (Rash et al., 2001) and liver cells (Serre-Beinier et al., 2008), Cx36 in neurons (Condorelli et al., 1998) and pancreatic  $\beta$ -cells (Serre-Beinier et al., 2008). See (Buniello et al., 2004) for an exhaustive review of the expression of the different Cx genes in the mouse.

Cx36 is the mammalian neuronal connexin *par excellence* (Rash et al., 2000; Bennett and Zukin, 2004), even though Cx43 has been reported in olfactory receptor neurons (Zhang et al., 2000), Cx57 in the olfactory bulb (Zhang, 2011) and the retina (Hombach et al., 2004), whereas Cx45 is expressed in several regions (Hormuzdi et al., 2004), such as the neocortex (Condorelli et al., 2003) and the retina (Söhl et al., 2000). Cx36 has been found in the neocortex (Deans et al., 2001), retina (Deans et al., 2002), thalamic reticular nucleus (TRN) (Landisman et al., 2002), inferior olive nucleus (IO) (Long et al., 2002), mesencephalic trigeminal nucleus (MesV) (Curti et al., 2012) and hippocampus (Hormuzdi et al., 2001), among other structures (Connors and Long, 2004). In the fish, Cx35 is an orthologue of Cx36 (O'Brien et al., 1996), and plays a similar role in neuronal circuits (Pereda et al., 2003).

GJ coupling is prevalent during the embryonic and early postnatal developmental stages of the rat brain (Söhl et al., 1998; Meier and Dermietzel, 2006), reaching a peak of expression in the first two weeks of life, decreasing afterwards (Belluardo et al., 2000; Meyer et al., 2002). Indeed, GJ might aid the maturation of the chemical synaptic circuitry (Maher et al., 2009; Jabeen and Thirumalai, 2018), which in turn fetches the electrical uncoupling (Mentis et al., 2002). In hypothalamic neurons, calcium entry through NMDA receptors activates the calcium-cyclic AMP response element binding protein (CREB), inducing Cx36 downregulation (Arumugam et al., 2005). The developmental expression of Cx36-mediated coupling is finely regulated by chemical synapses: remaining in a low level while GABA<sub>A</sub> receptors are excitatory, increasing when they become

inhibitory and metabotropic glutamate II receptors activate, finally decreasing due to NMDA receptors' activation (Park et al., 2011). Nevertheless, there is evidence of persistent electrical coupling in the adult brain in several nuclei, such as the neocortex (Galarreta and Hestrin, 2002), hippocampus (Hamzei-Sichani et al., 2012), MesV (Curti et al., 2012), IO and retina (Rash et al., 2000).

## Permeability

GJ form aqueous channels that are permeable to ions (Beblo and Veenstra, 1997; Wang and Veenstra, 1997) and small molecules below 1 kDa, approximately (Bennett and Zukin, 2004). Thus, not only these intercellular channels allow the electrical communication between coupled cells, but also biochemical signaling through second messengers, like cyclic AMP (cAMP) (Bedner et al., 2006; Kanaporis et al., 2008) and inositol 1,4,5-trisphosphate (IP3) (Kandler and Katz, 1998; Niessen et al., 2000). It has been also shown that GJ may participate in neuronal differentiation (Hartfield et al., 2011) and cell death (de Rivero Vaccari et al., 2007) in embryonic stages. In fact, their role in apoptosis seems to be dual, given that they may aid but also impede the spread of cell death signals (Decrock et al., 2011; Akopian et al., 2014). See (Harris and Locke, 2009) for a complete review on the permeability of Cx GJ.

Tracer molecules can diffuse through GJ too. Taking advantage of that, Lucifer Yellow and Neurobiotin (among others) are routinely used to map cellular connectivity mediated by GJ (Harris, 2001), though their spread is connexin-dependent (Weber et al., 2004). Unluckily, it is difficult to extract more coupling properties from dye transfer experiments, because there is no linear relationship between the dye permeability and the absolute permeability of the GJ (Nitsche et al., 2004), or its electrical conductance  $g_J$  (Ek-Vitorin and Burt, 2013).

## Gating

The synaptic current  $I_J$  between two cells is proportional to  $V_J$  and the GJ conductance  $g_J$ , whose value is sensitive to  $V_J$  for all Cx-based GJ, but less so to the membrane potential  $V_m$  (Palacios-Prado and Bukauskas, 2012).  $g_J$  diminishes in a sigmoidal way when  $V_J$  increases, with large variability depending on the Cx or Inx units composing the channel. For Cx36 homotypic junctions, macroscopic  $g_J$  is almost independent of  $V_J$  in the region  $\pm 40$  mV, and then falls to 30-40 % of its maximum value, with very slow kinetics (Teubner et al., 2000; Al-Ubaidi et al., 2000). Single channel recordings show that the unitary

conductance  $\gamma_j$  goes from its maximum (7-15 pS for Cx36 to 310 pS for Cx37 (Harris, 2001)) to a residual value as  $V_J$  augments. Therefore, GJ transition between substates that are not completely closed or open, due to two gating mechanisms: one “fast” and the other “slow” (also called “loop”) (Bukauskas and Verselis, 2004). Their time constants are submillisecond and seconds, respectively, so they are not usually visible in patch-clamp recordings (Bargiello et al., 2012). The fast gating has been associated to the movement of the Cx amino terminus into the cytoplasmatic vestibule of the hemichannel, narrowing the pore (Oh et al., 1999; Bukauskas et al., 2002; Xin et al., 2010; Santos-Miranda et al., 2020). The length of the amino terminus of different isoforms of the Inx UNC-7 have been correlated with their  $V_J$ -dependence (Shui et al., 2020). This “ball-and-chain” mechanism has also been found in human Cx26 gating by pH (Khan et al., 2020). Indeed, GJ are very sensitive to the intracellular pH, in a connexin-specific manner: alkalization increases  $g_J$  for Cx30.2 and Cx45 (Skeberdis et al., 2011), but diminishes it for Cx36 (González-Nieto et al., 2008). Recently, it has been shown that the cytosolic magnesium concentration plays a major role in the pH-regulation of GJ (Rimkute et al., 2018).

For homotypic GJ,  $g_J$  is bidirectional in control conditions, with a symmetrical dependence on the transjunctional potential  $V_J$ , centered at  $V_J = 0$  mV, as expected (Fig. 2.2A,B). However, an asymmetrical relationship has been reported in several Cx and Inx-mediated electrical synapses (Furshpan and Potter, 1959; Auerbach and Bennett, 1969; Miller and Pereda, 2017), resulting in diode-like electrical transmission. Further research has demonstrated that this rectification property arises when the gap junction is heterotypical (Barrio et al., 1991; Phelan et al., 2008) (Fig. 2.2C), due to the disparate electrical properties of the hemichannels (Suchyna et al. (1999); see review Palacios-Prado et al. (2014b)). In particular, different fast gating of apposed hemichannels has been shown to underlie electrical rectification in both Cx (Verselis et al., 1994) and Inx (Shui et al., 2020). Asymmetric cytosolic magnesium concentration can also generate rectification in Cx-based GJ (Palacios-Prado et al., 2013, 2014a).

## 2.2.2 Structural interactions with other proteins

Electron microscopy images of electrical synapses show that GJ are surrounded by electron dense structures, similar to the postsynaptic densities of chemical synapses (Miller and Pereda, 2017). In fact, the intercellular channels interact with several proteins involved in their maintenance and regulation (Hervé et al., 2012).

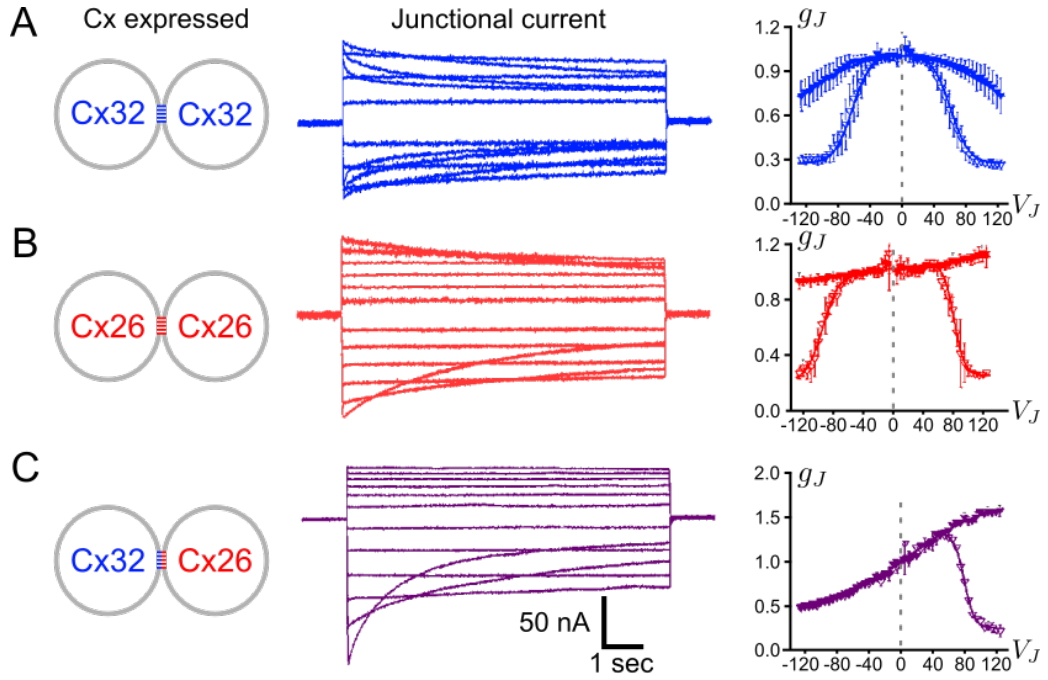


**Figure 2.2: Rectification of heterotypic GJ.** *A, B:* junctional current responses to long voltage steps *Xenopus* oocytes with homotypic Cx32/Cx32 and Cx26/Cx26. The instantaneous current response is larger than the steady-state one, as a result of the slow gating. On the right, normalized gap junction conductance  $g_J$  against the transjunctional potential  $V_J$  (in mV). Filled (empty) symbols represent the instantaneous (steady-state) values. Note the contrast between the marked voltage-dependence of the steady-state  $g_J$ , compared with the instantaneous conductance. *C:* in heterotypic Cx32/Cx26 GJ, both instantaneous and steady-state  $g_J$  display rectification. Scale bars for all current traces are the same. Adapted from Oh et al. (1999).

### Scaffolding proteins

Zonula occludens-1 (ZO-1) is a scaffolding protein, originally found in tight junctions, that is also associated with Cx GJ (Hervé et al., 2014). It interacts with the carboxyl terminus (CT) of Cx43, through its PDZ2 domain (Giepmans and Moolenaar, 1998), in a region surrounding the GJ, named “perinexus” (Rhett and Gourdie, 2012). The binding of ZO-1 to Cx43 has been proposed as a regulatory mechanism for GJ channel accrual, participating in the transition from undocked connexons to GJ (Chen et al., 2008; Chakraborty et al., 2010; Rhett et al., 2011; Dunn and Lampe, 2014; Thévenin et al., 2017). In the case of Cx35 and Cx36, ZO-1 binds to a conserved region of their CT, but through its PDZ1 domain (Li et al., 2004; Flores et al., 2008). This domain has lower affinity and faster dissociation kinetics than PDZ2, suggesting more dynamic interactions between these two proteins (Flores et al., 2008). Cx36 also interacts with two other members of the zonula occludens family of proteins, ZO-2 and ZO-3, via the same domains (Li et al., 2009).

It is not a coincidence that gap, adherens and tight junctions need zonula occludens



proteins in their scaffolds. From the structural point of view, all these types of junctions require two membranes to be closely apposed, hinting that they may interact with similar scaffolding and/or regulatory proteins. Based on this insight, several more proteins have been identified colocalizing with Cx GJ. For example, proteins MUPP1 and AF6, known to be associated with ZO-1 at tight junctions, have also been found to colocalize with Cx36 and to bind directly to its CT (Li et al., 2012b; Lynn et al., 2012; Nagy and Lynn, 2018; Tetenborg et al., 2020). Cingulin has also been localized in GJ, probably mediating the interaction between GJ scaffolding proteins and the cytoskeleton (Lynn et al., 2012). Even though Cx may act as cell adhesion molecules (CAM) (Martin et al., 2020), there are still putative electrical synaptic sites in Cx36 knockout mice (De Zeeuw et al., 2003; Nagy and Lynn, 2018). Adherens junctions CAM, like nectin-1 (Nagy and Lynn, 2018), E- (Govindarajan et al., 2010) and N-cadherins (Nagy and Lynn, 2018), have been found to be expressed in the regions surrounding Cx in GJ.

## Regulatory proteins

GJ strength is regulated by several molecules, being the  $\text{Ca}^{2+}$  signaling the first described to close them, as a way to avoid the spread of cell-death signals after tissue damage (Belousov et al., 2017; Peracchia, 2020b). Since intracellular  $\text{Ca}^{2+}$  plays a role in several signaling cascades, several studies have been focused in isolating the GJ regulatory mechanisms triggered by its increase inside the cells. Given that Cx do not have high-affinity  $\text{Ca}^{2+}$  sites (Peracchia, 2020b), the research focus has been on  $\text{Ca}^{2+}$ -regulated proteins. Indeed,  $\text{Ca}^{2+}$ -induced uncoupling can be prevented by inhibiting calmodulin (CaM) or its expression (Peracchia, 2020b). Molecular studies have shown that CaM binds to the CT of Cx35 and Cx36 (Burr et al., 2005), even outside the GJ (Siu et al., 2016), possibly blocking the pore with its N-lobe at basal concentration of internal  $\text{Ca}^{2+}$  (Peracchia, 2020a). Moreover,  $\text{Ca}^{2+}$ /calmodulin-dependent protein kinase II (CaMKII) potentiates Cx35 and Cx36 GJ (Pereda et al., 1998; del Corosso et al., 2012), by phosphorylating (Alev et al., 2008) at the same CT region where CaM binds (Siu et al., 2016; Aseervatham et al., 2020). Finally,  $\text{Ca}^{2+}$ /calmodulin-activated protein phosphatase 2B calcineurin also may modify the strength of Cx36 synapses (Sevetson et al., 2017), though if there is direct interaction with Cx is yet unknown.

Furthermore, protein kinase A (PKA) phosphorylates sites at the cytoplasmatic loop (Mitropoulou and Bruzzone, 2003) and CT (Ouyang et al., 2005; Kothmann et al., 2007) of Cx35 and Cx36 GJ, regulating their strength (Urschel et al., 2006; Bazzigaluppi et al., 2017). Remarkably, PKA can inhibit or enhance coupling, depending on the state of a minor phosphorylation site in the CT, that acts as a “switch” (Ouyang et al., 2005). Other

protein kinases also interact with Cx GJ, such as PKG (Patel et al., 2006), PKC (Lampe et al., 2000), MAPK (Warn-Cramer et al., 1996) and membrane-associated guanylate kinases (Hervé et al., 2012). Some of these phosphorylations may alter the binding to Cx of scaffolding proteins like ZO-1, modifying the size of the GJ plaques (Chen et al., 2008; Dunn and Lampe, 2014; Thévenin et al., 2017).

### 2.2.3 Trafficking

The Cx proteins are synthesized in the endoplasmic reticulum and assembled as hemichannels in the Golgi apparatus (Musil and Goodenough, 1993; Falk et al., 2016). They travel in vesicles to the cellular membrane, through microtubules, in the case of Cx26 (Martin et al., 2001), Cx43 (Lauf et al., 2002; Gaietta et al., 2002) and Cx36 (Brown et al., 2019). Interestingly, the interaction between tubulin and Cx36 happens at a binding site in the CT, where also CaM and CaMKII interact with Cx36 (Brown et al., 2019), suggesting that these proteins may interfere with the transport of the Cx.

Fluorescence tags have been attached to the CT of several Cx to study their turnover, using pulse-chase analysis. A surprisingly short half-life, of 1 to 5 hours, is a common feature for all Cx studied, both *in vivo* and *in vitro* (Segretain and Falk, 2004). Interfering with Cx insertion (or removal) results in a large decrease (or increase) of GJ conductance (Flores et al., 2012). It is important to note that there are qualitative variations in the trafficking processes for different Cx. Newly synthesized Cx43 hemichannels insert in the periphery of existing GJ, while older channels are removed from the GJ plaque center (Lauf et al., 2002; Gaietta et al., 2002). In contrast, Cx36 insertion and removal may happen at any place in the plaque (Wang et al., 2015), with immunofluorescence data from postnatal rats suggesting that they may even insert elsewhere in the plasma membrane (Curti et al., 2012). This key difference may explain why Cx43 GJ are arranged in large plaques, while Cx35 and Cx36 GJ are organized in smaller ones (called “puncta”).

Whereas single membrane vesicles are responsible for the insertion of Cx hemichannels, the entire GJ channels are endocytosed to either coupled cells, in double-membrane annular vesicles (also known as connexosomes), both in native (Fukuda, 2009) and expression systems (Piehl et al., 2007; Falk et al., 2009; Nickel et al., 2013; Wang et al., 2015). Therefore, even in homotypic (symmetrical) GJ, their endocytosis is asymmetrical, as shown in Fig. 2.3. Another stunning consequence of this is that cytosolic content of one cell can be internalized by its coupled partner, as the cargo of the endocytosed vesicle (see Fig. 2.3). The endocytosis of GJ depends on dynamin and clathrin (Piehl et al., 2007; Gumpert et al., 2008; Nickel et al., 2013) and triggered by Cx ubiquitination (Totland

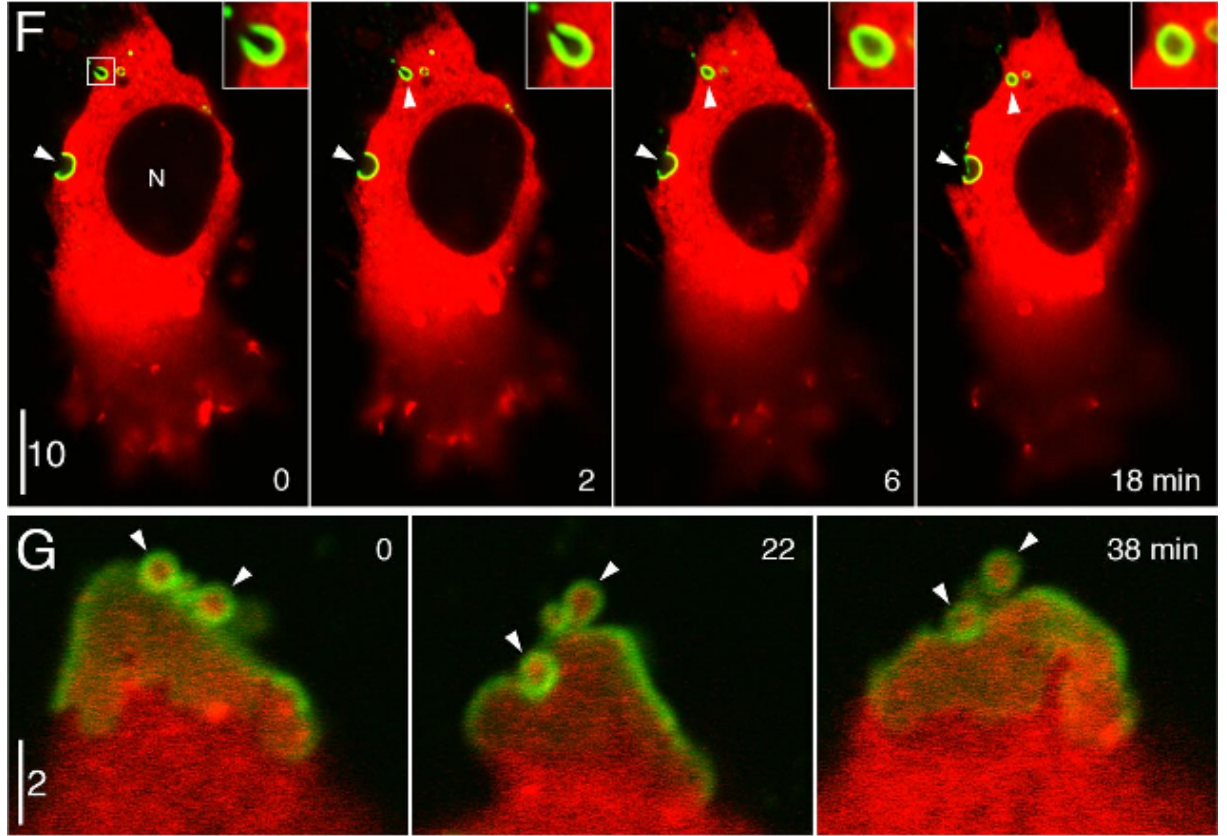


**Figure 2.3: Trafficking of GJ in a pair of electrically coupled HeLa cells, expressing Cx43-CFP (green).** One cell was injected with red fluorescent quantum dots (GJ impermeable). The series of images at the top shows the internalization process of GJ by the red-labeled cell, from 0 to 18 minutes. The lumen of the internalized vesicles is dark, as it contains the cytoplasm of the non fluorescent cell. At the bottom, a non fluorescent cell is internalizing Cx43-CFP GJ from a red fluorescent one. Scale bars are in  $\mu\text{m}$ . From Piehl et al. (2007).

et al., 2020), which may be regulated by protein kinase C (Leithe and Rivedal, 2004). A recent study has also suggested that Cx36 internalization is mediated by interaction with caveolin-1 and dependent on the intracellular calcium concentration (Kotova et al., 2020). Finally, connexosomes are mostly degraded via autophagy (Lichtenstein et al., 2011; Fong et al., 2012; Bejarano et al., 2012) or via the cellular endo-/lysosomal degradation pathway (Piehl et al., 2007; Falk et al., 2012; Bell et al., 2019). Some researchers have also found Cx43 connexosomes interacting with mitochondria (Bell et al., 2019) or being recycled back to the plasma membrane (Boassa et al., 2010; Vanderpuye et al., 2016).



## 2.3 Electrical synaptic transmission

### 2.3.1 Main properties

In the context of the nervous system, GJ provide low resistance pathways between coupled neurons, allowing the continuous flow of junctional current  $I_J$  from one neuron to its coupled partner (Alcamí and Pereda, 2019). This uninterrupted communication sets them aside from most of the chemical synapses, whose transmission is not usually sustained in time, but reflect the arrival of action potentials to the presynaptic neuron (there are a few exceptions though (Matthews and Fuchs, 2010; Trigo, 2019)). Furthermore, action potentials may also fail to trigger chemical synaptic transmission, for example in the case of sites with low probability of release or if the neurotransmitter vesicles are depleted. On the contrary, given the simpler structure of GJ, electrical synaptic transmission is very reliable over extended periods of time (Alcamí and Pereda, 2019).

As Furshpan and Potter recognized in their first preliminary report of electrical synapses in the crayfish (Furshpan and Potter, 1957), they are able to transmit both depolarized and hyperpolarized signals. The synaptic current  $I_J$  is proportional to the voltage difference between the coupled cells  $V_J$  and the GJ conductance  $g_J$ , and could be unidirectional or bidirectional, depending on the hetero- or homotypic conformation of the GJ (see section 2.2.1). Therefore, any change on the membrane potential -of any of the coupled neurons- induces instantaneous change in  $I_J$ , contrasting with the delays in chemical synaptic transmission, due to their more complex chain of events.

### 2.3.2 Coupling coefficient

The easiest way to understand the factors that determine the efficacy of electrical synaptic transmission is by analyzing the circuit conformed by two neurons coupled by a GJ (Curti and O'Brien, 2016), schematically represented in Fig. 2.4. Each neuron  $k = 1, 2$  is represented by its membrane capacitance  $C_k$  and input resistance  $R_{in k}$ , which usually depends on the membrane voltage  $V_k$ . Given that most GJ between mammalian neurons are homotypic Cx36/Cx36, the GJ can be modeled as a simple ohmic resistor  $R_J = \frac{1}{g_J}$ <sup>1</sup>. A change  $\Delta V_1$  in the membrane potential of neuron 1 (presynaptic) induces a change on the synaptic current  $I_J$  which, in turn, produces a voltage deflection  $\Delta V_2$  in neuron 2. After the charge of the postsynaptic membrane capacitance  $C_2$ , the ratio between these

---

<sup>1</sup>In the case of heterotypic GJ,  $g_J$  is modeled as a diode, whose current-voltage relationship is nonlinear (Furshpan and Potter, 1959)

two voltage deflections is defined as the coupling coefficient in steady state  $CC_{SS} = \frac{\Delta V_2}{\Delta V_1}$ .  $CC_{SS}$  measures the steady state efficacy of electrical synaptic transmission: the attenuation of the synapse for DC signals. For example, in neocortical somatostatin-containing interneurons the median  $CC_{SS} = 0.06$  (Hu and Agmon, 2015), meaning that a sustained presynaptic voltage deflection of 100 mV generates a postsynaptic response of 6 mV.

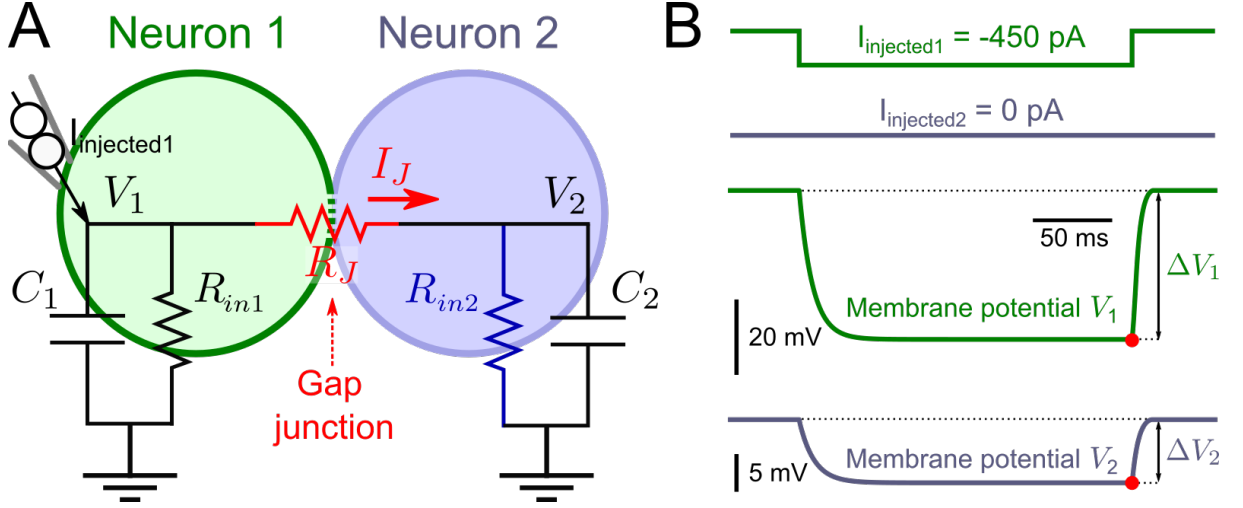


**Figure 2.4: Electrical transmission between coupled cells.** *A*: equivalent circuit of two single-compartment neurons electrically coupled. Their input resistances are  $R_{in1}$  and  $R_{in2}$ , whereas  $C_1$  and  $C_2$  represent their membrane capacitances. The GJ resistance is  $R_J = \frac{1}{g_J}$ . An external current  $I_{injected1}$  is injected to neuron 1, in the whole-cell configuration. The synaptic current from neuron 1 to 2 is  $I_J = g_J (V_1 - V_2)$ , where  $V_1$  and  $V_2$  are their respective membrane potentials. *B*: signal transmission between passive neurons when one of them (neuron 1) is hyperpolarized by a negative current step of -450 pA. The coupling coefficient for DC signals  $CC_{SS}$  is defined as the ratio between the post and presynaptic voltages at the red points. Time scale is the same for all traces.

In terms of the electrical circuit of Fig. 2.4,  $CC_{SS}$  can be calculated as:

$$CC_{SS} = \frac{\Delta V_2}{\Delta V_1} = \frac{R_{in2}}{R_{in2} + R_J} = \frac{1}{1 + \frac{R_J}{R_{in2}}} \quad (2.1)$$

A straightforward consequence of equation 2.1 is that  $CC_{SS}$  is determined only by the ratio between the junctional and postsynaptic resistances,  $R_J$  and  $R_{in2}$  respectively (red and blue in Fig. 2.4). So, when  $R_J \gg R_{in2}$  the neurons are weakly coupled:  $CC_{SS} \ll 1$ . Conversely, if  $R_J \ll R_{in2}$ ,  $CC_{SS} \rightarrow 1$  and the two cells behave as being in the same compartment.

Experimentally, the  $CC_{SS}$  is measured by injecting long (200-600 ms) current pulses to one neuron and, simultaneously, recording the potential of the coupled neurons, both

in whole-cell patch clamp configuration. Reported mean  $CC_{SS}$  in mammalian electrical synapses are quite low: 0.03 to 0.04 in the TRN (Landisman et al., 2002), inferior olive (Long et al., 2002) and hippocampus (Zsiros and Maccaferri, 2005), 0.09 and 0.13 in fast-spiking (FS) and low-threshold spiking (LTS) neocortical neurons (Gibson et al., 2005). Nonetheless, it has to be noted that the GJ in these neurons are located at the dendrites, but the signals are recorded at the somas, so the low  $CC_{SS}$  might be underestimated. The  $CC_{SS}$  might be higher if directly measured at the coupled dendritic compartments, due to their larger input resistances (probably  $R_{\text{dendrite}} \gg R_J$ ). Consistently, the recorded  $CC_{SS}$  of coupled MesV neurons (which are coupled at their somas) almost double those of FS and LTS neurons (Curti et al., 2012). Hopefully, future imaging experiments will be able to estimate directly the coupling coefficient between dendritic compartments, maybe by using voltage fluorescent probes together with advanced microscopy (Antic et al., 2019).

### 2.3.3 Frequency dependence of the coupling coefficient

The  $CC_{SS}$  is a widespread metric used to determine the strength of electrical synapses. However, it is not suited for describing the transmission of most physiologically relevant signals, like action potentials and chemical postsynaptic potentials, because they are faster than the time constant of the postsynaptic neuron. To thoroughly characterize the electrical synaptic transmission, it would be useful to study the dependence on the frequency  $f$  of the coupling coefficient  $CC(f)$ . According to the circuit of Fig. 2.4, the presynaptic signal is filtered by  $R_J$  connected in series to the parallel of the  $C_2$  and  $R_{in2}$ . On one hand, for DC signals  $C_2$  behaves as an open circuit, and  $CC(f = 0 \text{ Hz}) = CC_{SS}$ , as expected. On the other hand, for signals with high frequency content,  $C_2$  will act as a short-circuit that produces  $V_2 = 0$ , regardless of the amplitude of  $V_1$ . As a result,  $CC(f) \xrightarrow{f \rightarrow \infty} 0$ : i.e. the postsynaptic neuron cannot follow the fluctuations of the presynaptic one if they are infinitely fast. These asymptotic results are valid for any electrical synapse, but they do not provide information on the filtering behavior for intermediate frequencies.

The complete frequency-dependence of  $CC(f)$  can be experimentally obtained by injecting, in the presynaptic neuron, either single- or variable-frequency (also called “zaps”) current sinusoids (Puil et al., 1986), and computing the  $CC(f)$  as the ratio between the Fast Fourier Transforms of post and presynaptic voltage signals, as displayed in Fig. 2.5. Theoretically, the  $CC(f)$  can be expressed with a generalized version of equation 2.1, where the input resistance of the postsynaptic neuron is substituted by its complex impedance.

If all the intrinsic components were passive, the expected  $CC(f)$  should behave as

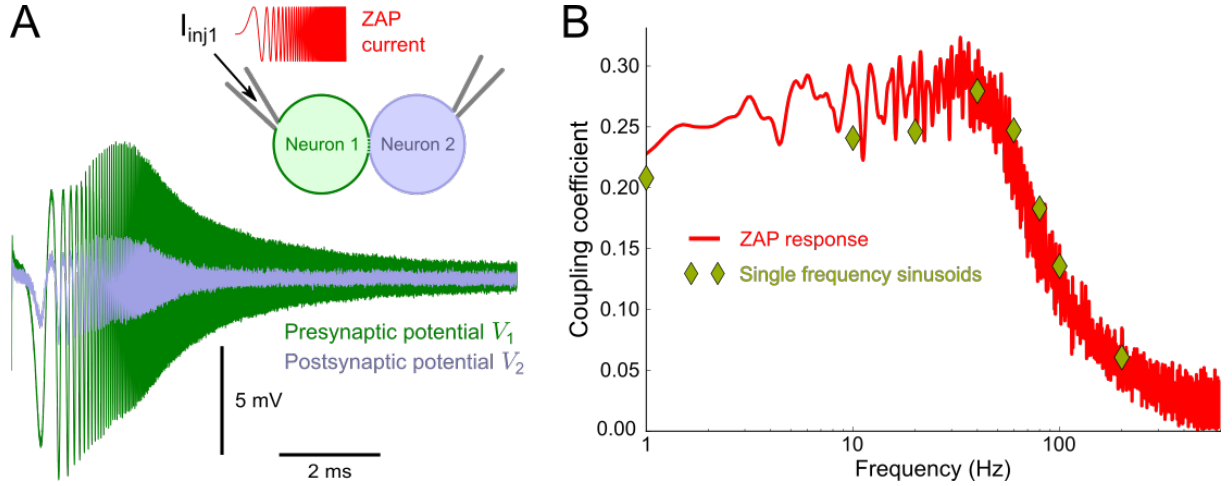


**Figure 2.5: Frequency-dependence of the coupling coefficient ( $CC(f)$ ).** *A*: the  $CC(f)$  can be experimentally obtained by injecting a variable-frequency sinusoidal current in Neuron 1 and computing the ratio of the Fast Fourier Transforms of the post and presynaptic voltage responses. *B*: in this case, the magnitude of the  $CC(f)$  for these MesV neurons displays a maximum around 40 Hz. Observe that the  $CC(f)$  can also be computed using single-frequency sinusoids. Adapted from (Davoine et al., 2020).

a low-pass filter. Indeed, that is the case for most reported  $CC(f)$  in the mammalian brain, in regions such as the neocortex (Gibson et al., 2005), cerebellum (Dugué et al., 2009), TRN (Landisman et al., 2002) and the retina (Veruki and Hartveit, 2002; Trenholm et al., 2013a). However, it should not be discarded a more complex behavior in the dendritic compartments where most GJ are located, given that they cannot be recorded by the standard patch clamp technique. Strikingly, a band-pass behavior was reported in the MesV, due to active ionic conductances operating at the resting membrane potential (Curti et al., 2012) (see Fig. 2.5 and section 2.3.5) <sup>1</sup>.

### 2.3.4 Spike transmission

A clear consequence of the filtering properties is that faster signals get more attenuated than slower ones. In particular, presynaptic action potentials usually induce small-amplitude broad spikelets in the postsynaptic neuron, as was already attested in the first detailed characterizations of electrical synaptic coupling (Watanabe, 1958; Furshpan and Potter, 1959). The coupling coefficient for spikes  $CC_{\text{spike}}$ , defined as the ratio between the amplitudes of the postsynaptic spikelet and the presynaptic spike, is about 10 times smaller than  $CC_{SS}$  for LTS and FS neurons (Gibson et al., 2005). For MesV neurons,  $CC_{SS}$  is only 5 times  $CC_{\text{spike}}$ , as a result of the band-pass filter properties (Curti et al.,

<sup>1</sup>The  $CC(f)$  between bipolar cells in the adult goldfish retina also displays a resonance, even though the researchers who characterized it were not aware of that (Arai et al., 2010).

2012; Davoine et al., 2020).

The postsynaptic spikelets (PJS) are not only shaped by the filter properties, but also by the presynaptic signals' waveforms. On one hand, when the later display shallow after-hyperpolarization potentials (AHP), the elicited PJS are monophasic (Veruki and Hartveit, 2002; Landisman et al., 2002; Gibson et al., 2005; Curti et al., 2012), with a net depolarizing effect on the coupled cell. On the other hand, spikes with deep and long-lasting AHP produce biphasic PJS (Gibson et al., 2005; Dugué et al., 2009), whose net impact could be more complex. For example, Dugué and coworkers studied cerebellar Golgi neurons, which produce very fast action potentials (0.35 ms in half width), followed by a profound and long-lasting AHP (Dugué et al., 2009). The presynaptic spike gets severely attenuated ( $CC_{\text{spike}} = 0.007$ ) by the low-pass filter, whereas the AHP is less affected due to its lower-frequency content (its associated  $CC_{\text{AHP}} = 0.1$ ). Hence, the resulting PJS have a very small and short depolarizing phase and a stronger hyperpolarizing one, with a net inhibitory effect on the postsynaptic neuron excitability.

Finally, even though the synaptic current reacts instantaneously to presynaptic voltage changes, the postsynaptic membrane response is delayed by the phase lag introduced by the filter (Curti and O'Brien, 2016). The latency for spike transmission is usually below 1 ms, both *in vitro* (Galarreta and Hestrin, 2001; Vandecasteele et al., 2005; Dugué et al., 2009; Alcami and Marty, 2013) and *in vivo* (van Welie et al., 2016). Nevertheless, submillisecond latency alone cannot be used as a criterion to identify electrical synapses in the mammalian brain (Bennett and Zukin, 2004), given that chemical synaptic communication may also be very fast (Hu et al., 2011).

### 2.3.5 Interaction with intrinsic properties

As explained in the section 2.3.3, the frequency dependence of the coupling coefficient is determined by the junctional and postsynaptic electrical properties. Therefore, modifications of the later may dramatically alter the  $CC(f)$  and, consequently, the spike transmission. For example, postsynaptic depolarizations enhance the antidromic electrical transmission from goldfish Mauthner cells to auditory afferents (Pereda et al., 1995), due to increased activation of the persistent sodium current  $I_{NaP}$ . In fact,  $I_{NaP}$  is a strong amplifying mechanism (Izhikevich, 2006) which augments the postsynaptic input resistance  $R_{in2}$ , in a voltage-dependent manner, boosting the coupling coefficient (Curti and Pereda, 2004), according to the equation 2.1.

In mammals, pharmacological blockade of  $I_{NaP}$  abolishes the depolarization-induced

amplification of PJS (Mann-Metzer and Yarom, 1999; Dugué et al., 2009; Curti et al., 2012). PJS also get wider, due to the increase of the time constant of the postsynaptic cell, further accentuating their excitatory effect. In coupled TRN neurons, this mechanism acts in a state-dependent way, only when they are in the tonic spiking regime but not when they are bursting (Haas and Landisman, 2012). This results from the difference in the resting membrane potential (RMP) at which each behavior is expressed: tonic spiking occurs when the RMP is within the activation range of  $I_{NaP}$  (around  $-53$  mV, close to the  $I_{NaP}$  half-activation voltage), while bursting happens with more hyperpolarized RMP ( $-76$  mV, approximately). PJS in FS neurons are state-dependent as well: biphasic when the cells are depolarized, monophasic if hyperpolarized (Otsuka and Kawaguchi, 2013).

Subthreshold potassium currents have an impact on the  $CC(f)$  and spike transmission too. Their blockade modifies the voltage-dependent enhancement of antidromic PJS at goldfish club endings (Curti and Pereda, 2004). The A-type potassium current  $I_A$  is responsible for shaping the band-pass filter behavior of the  $CC(f)$  in MesV neurons, by introducing a resonant bump around 80 Hz (Curti et al., 2012), due to its time constant. In these neurons,  $I_A$  diminishes the gain of  $CC(f)$  for signals slower than its activation time constant, being counterbalanced by  $I_{NaP}$ -induced boosting, as computational models show in Fig. 2.6. In addition, blocking these two active mechanisms increases the phase lag of the transmission (Curti et al., 2012).

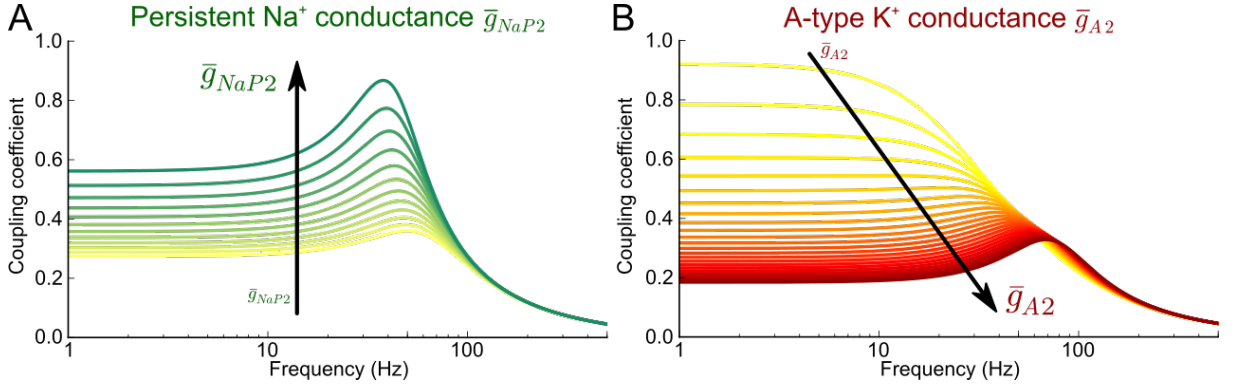


**Figure 2.6: Computational simulations explain the role of non-synaptic conductances in electrical synaptic transmission.** A: increasing the persistent sodium maximum conductance in the postsynaptic neuron  $\bar{g}_{NaP2}$  boosts the gain of the  $CC(f)$  over all the frequency range, without modifying its shape. B: on the contrary, augmenting the maximum conductance of the  $I_A$  turns the filter from a low-pass to a band-pass. Adapted from (Davoine et al., 2020).

## 2.4 Functional role in neuronal circuits

### 2.4.1 Introduction

In the previous sections, we described how GJ are the structural basis of electrical synapses and how they endow coupled neurons with a simple, yet sophisticated, tool for information processing. Yet, the functional contribution of electrical synapses to neuronal circuits has been underestimated historically, in comparison to the chemical synaptic communication (Alcamí and Pereda, 2019). As a matter of fact, electrical and chemical synaptic transmission coexist in several neuronal circuits, acting together to perform complex operations. Here, we will succinctly review four outstanding examples of these, some of which will be further discussed in the context of synaptic plasticity (see section 2.5). First, the escape circuits in *Caenorhabditis elegans* and the fish, where mixed electrical-chemical synapses ensure a fast and reliable response in life-threatening situations. Then, two examples from the mammalian central nervous system, which are involved in sensory and motor operations: the retina and the inferior olive, respectively. Finally, we introduce the coincidence detection in mammalian circuits, which will be explored in detail later, in chapter 3. Jing (2017) provides an up-to-date compilation of neuronal circuits where electrical synapses play a major role.

### 2.4.2 Synergy between chemical and electrical synapses in escape circuits

Fast and reliable escape circuits are essential for the survival of individual animals. One basic network architecture found in many species consists on a sensory element connected, to an interneuron whose large-diameter axon projects directly to motor neurons, which execute the escape action. Whereas axon properties maximize the speed of transmission, its reliability is ensured by electrical synapses, that also minimize its delay. Interestingly, in these circuits, electrical synapses are commonly associated with chemical ones, forming mixed synapses that boost the signal transmission.

The basic structure of the *Caenorhabditis elegans* escape circuit is composed by a pair of command interneurons (AVA), which project onto A-motor neurons (A-MN) (Chalfie et al., 1985; Piggott et al., 2011) (Fig. 2.7A-B). Located in the head of the animal, the AVA integrate sensory information (for example, from mechanical touch) in order to trigger an avoidance response, executed via a backwards movement of the worm (Pirri and Alkema, 2012). Taking advantage of the genetic tools available in the *C. elegans* and with exceptional technical skill, Liu and coworkers were able to characterize this small



network, using paired whole-cell electrophysiological recordings (Liu et al., 2017). The synapses between the AVA neurons and the A-MN are mixed: the chemical components is cholinergic, while the electrical one is made by heterotypical GJ, composed by the Inx UNC-7 and UNC-9. Amazingly, the almost total rectification of this electrical synapse (Shui et al., 2020) (see 2.2.1) promotes antidromic transmission that amplifies the chemical transmission. Consistently, knockdown of one of the Inx reduces the frequency of the postsynaptic currents in the A-MN and hinders the backward locomotion behavior (Liu et al., 2017).

In the teleost fish, pressure waves (sound) coming from one side of the animal may signal the approach of a predator, which is transduced to electrical signals by hair cells in the inner ear, and conveyed to the CNS by auditory afferents. These afferents terminate as large myelinated “club endings” in the lateral dendrite of the Mauthner (M) cell (Fig. 2.7C-D), providing a strong excitatory input. M-cells are a pair of gigantic reticulo-spinal neuron whose axon crosses the midline and commands motor neurons, generating a rapid contraction of the contralateral side muscles, in a maneuver known as “C-start” for the shape the fish adopts (Faber and Pereda, 2011). There are only two M-cells in the animal, one on each side. Therefore, during this movement, the contralateral M-cell must be inhibited, in order to avoid a simultaneous ipsilateral contraction that impedes the fast side-turning<sup>1</sup> This constitutes the startle response of the animal, and is followed by a counter-bending, from which the fish often starts a escape response by fast swimming (Berg et al., 2018).

The M-cell is essential for the success of the startle response (Hecker et al., 2020). Being the largest known neuron in the vertebrate brain, its properties are especially tuned for the transmission of this reflex. Its low time constant and large-diameter axon are particularly well suited for maximizing the speed of transmission, while its low input resistance sets a high threshold for the response, avoiding spontaneous activation of the circuit that may interfere with the normal swimming behavior (Faber and Pereda, 2011). Noteworthy, club endings form mixed -electrical and chemical- contacts onto the M-cell. Thus, upon activation of these auditory afferents, postsynaptic responses display a short latency electrical component followed by a glutamatergic component (Furshpan, 1964). The structural substrate of these electrical synapses are heterotypic GJ, made by Cx35 and Cx34.7 in the pre and postsynaptic sides, respectively (Rash et al., 2013). Even though the unitary conductance of Cx35 is 10 times that of Cx34.7 (O’Brien et al., 1998),

---

<sup>1</sup>Both M-cells are simultaneously activated in another stereotypical response: the “S-start” elicited by tail stimulation, whose performance depends on the hyperpolarized state of motor neurons at the time when M-cell spikes arrive (Liu and Hale, 2017).



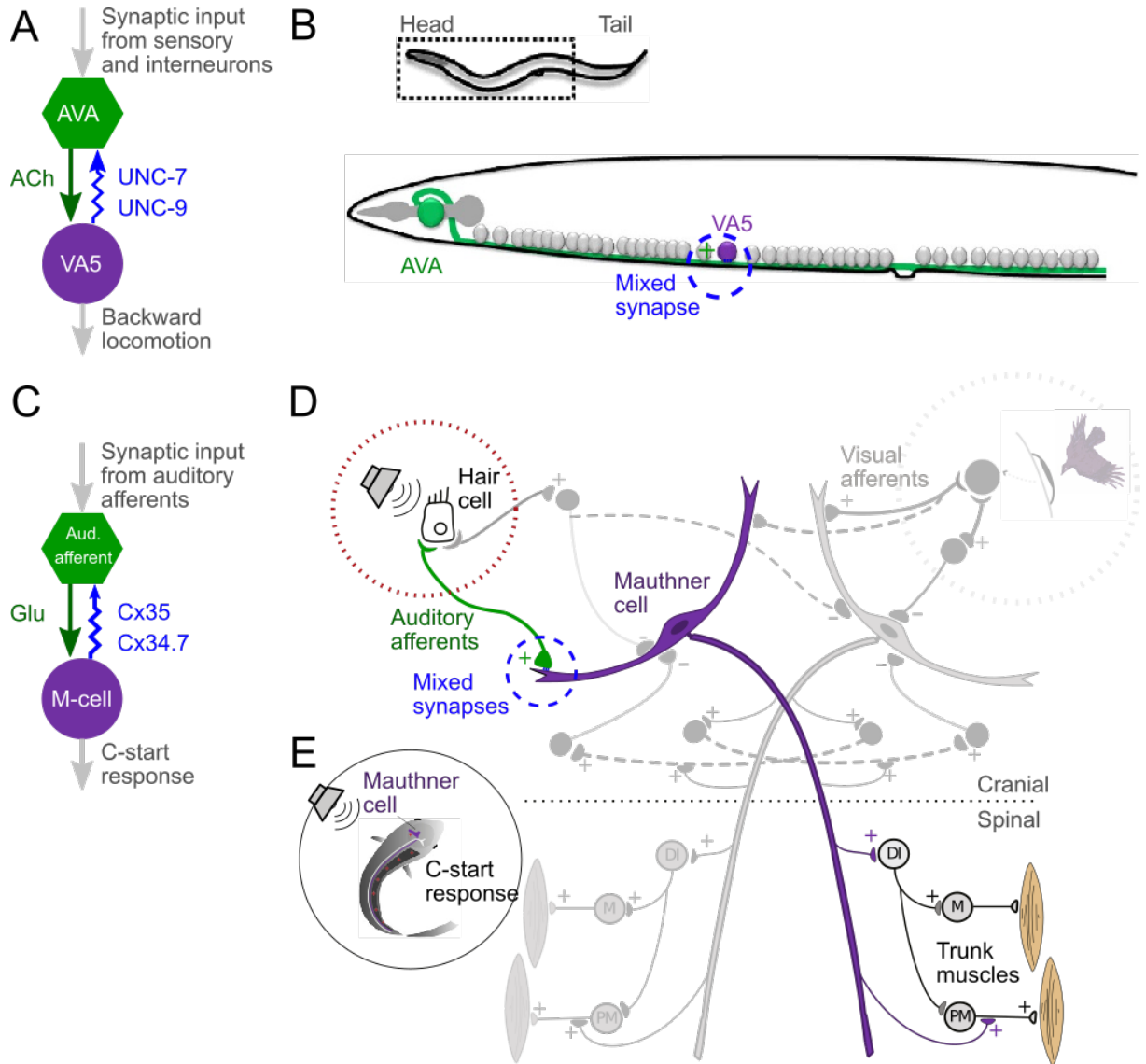


**Figure 2.7: Escape circuits of *C. elegans* and the fish.** *A*: AVA interneurons, which receive information from sensory and interneurons, project onto A-MN (like the VA5) via mixed synapses, triggering a escape response. *B*: schematic representation of the worm and the AVA and VA5 neurons. *C*: C-start circuit of the fish, consisting on auditory afferents that project to the Mauthner cell via mixed synapses. *D*: In the fish, the axon of the M-cell crosses the midline, in order to activate the contralateral motoneurons, generating the C-start response (*E*). *A* and *B* adapted from Liu et al. (2017), *D* and *E* from Medan and Preuss (2014).

the rectification of the electrical synapses is only 4 times larger in the antidromic direction, compared to the orthodromic one (Rash et al., 2013). The rectification, together with the disparity between the input resistances of the club-endings and the M-cell (Faber and Pereda, 2011), provide a mechanism that favors antidromic transmission, which is further boosted by the persistent sodium current in the presynaptic side (Curti and Pereda, 2004). Given that the electrical synapse operates faster than the chemical one, this backpropagation enhances the presynaptic depolarization, contributing to improve the later chemical transmission. In addition, the backpropagated potential also invades other club endings, acting as a cooperativity mechanism between them (Rash et al., 2013).

### 2.4.3 Lateral excitation in the retina

The vision relies on the information processed by the retina, which converts light stimuli into electrical signals, for further processing in the brain. In order to accomplish that, the retinal circuitry is composed by a complex network of different cells, schematically represented in figure 2.8. Cones and rods constitute its input layer, where the phototransduction takes place, while the ganglion cells (GC) generate its output, which is conveyed through their axons (the optic nerve) to the brain. These two layers are connected through a convoluted network of bipolar, horizontal and amacrine cells, giving structural support for many different signaling pathways between the photoreceptors and the GC.

Remarkably, several Cx are expressed in all layers of the retina, forming GJ between cells (Fig. 2.8). Using rod and cone-specific Cx36 KO mice, it was shown that photoreceptors' coupling

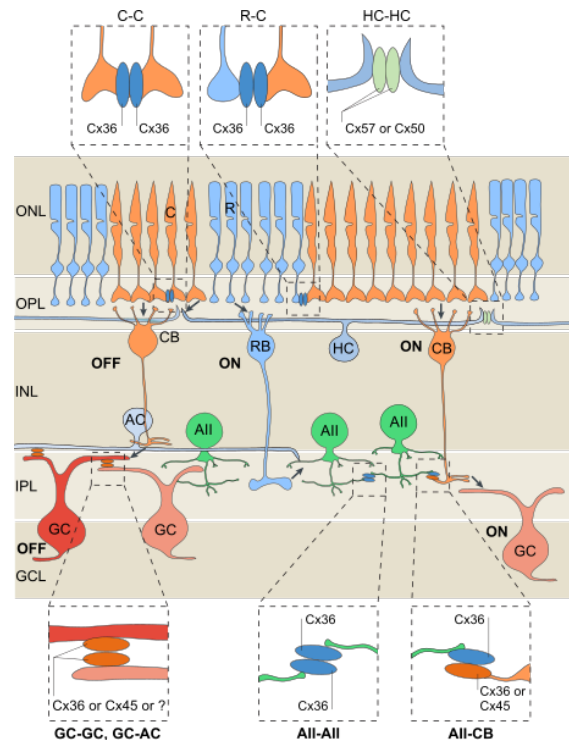


**Figure 2.8: Schematic representation of the retinal circuitry and its electrical synaptic connectivity.** The input layer is the ONL (outer nuclear layer), where cones (C) and rods (R) are. The output are the ganglion cells' (GC) axons in the GC layer (GCL). The figure from (Bloomfield and Volgyi, 2009) was modified to include the recent findings on coupling in the ONL (Jin et al., 2020). Abbreviations: HC, horizontal cell; RB and CB, rod and cone bipolar cells, respectively; AC, amacrine cell; AII, AII amacrine cell.

mainly depends on Cx36 GJ between cones and rods, while direct cone/cone coupling is rare and rod/rod nonexistent (Jin et al., 2020). Previous reports of direct rod/rod coupling (Hornstein et al., 2005; Li et al., 2012a) can be explained in terms of rod/cone/rod coupling. Cx36 is expressed in bipolar (Deans et al., 2002; Feigenspan et al., 2004), amacrine (Deans et al., 2002) and ganglion (Schubert et al., 2005a; Pan et al., 2010) cells, all of which also express Cx45 (Schubert et al., 2005b; Dedek et al., 2006). Within the context of the diversity of Cx expression in the retina, provocative immunofluorescence data suggested heterotypic Cx45/Cx36 between AII amacrine and ON bipolar cells (Dedek et al., 2006). However, in a technical *tour de force*, Li and coworkers demonstrated that Cx45 and Cx36 in the retina can be coexpressed in the same GJ plaques, but each of them forms homotypic GJ (Li et al., 2008). Uniquely, horizontal cells, which provide surround inhibition on the first retina layer, do not express neither Cx36 nor Cx45, but Cx50 (Dorgau et al., 2015) and Cx57 (Hombach et al., 2004; Janssen-Bienhold et al., 2009). Due to their ubiquity in the retinal circuitry, GJ are critical in the processing of visual information (Bloomfield and Volgyi, 2009; Trenholm and Awatramani, 2019).

Lag normalization in ON-OFF directionally selective ganglion cells (DSGC) is an amazing example of the role of electrical synapses in the retina. There are four subtypes of DSGC, each of which responds preferentially to edges moving in a specific cardinal direction. The spatial location of the edge is signalled by the initiation of spiking activity in DSGC, whereas their peak firing rates encode the stimulus velocity information (Gollisch and Meister, 2008). In a series of papers, Trenholm et al. studied these cells, using a transgenic mice line that expressed GFP in this neuronal population (Trenholm et al., 2011). Interestingly, only a subpopulation of DSGC are electrically coupled through their dendrites (Weng et al., 2005), via homotypic Cx45 GJ (Schubert et al., 2005a; Pan et al., 2010; Trenholm et al., 2013a) between themselves, with no evidence of heterologous coupling (Trenholm et al., 2013a). Whereas the dendritic arbors of uncoupled DSGC are symmetrical, in coupled cells they align with their preferred direction (Trenholm et al., 2011) (Fig. 2.9a). The spiking of uncoupled cells only starts when the leading edge of a bar is inside their dendritic tree, and the timing depends on its velocity. Coupled DSGC firing begins when the incoming edge is 100  $\mu\text{m}$  of their somas and dendrites, irrespective of the input velocity (Trenholm et al., 2013b), in a phenomenon designated “lag normalization”. This is due to the early activation of coupled DSGC, which recruit their neighbors even before the leading edge arrives (Trenholm et al., 2013b). Thus, electrical synapses between DSGC provide a lateral excitation mechanism, that enables a precise detection of the spatial location of the stimulus, disregarding its velocity.

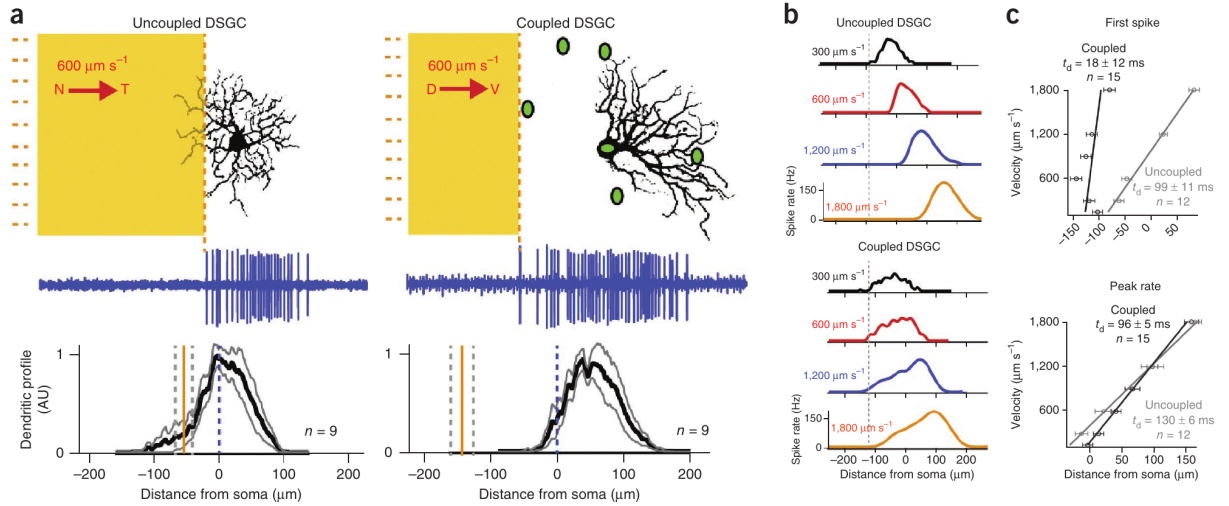


**Figure 2.9: Lag normalization in ON-OFF directionally selective ganglion cells.** *a*: an incoming edge elicits spiking in uncoupled DSGC when it enters the dendritic arbor, while asymmetric coupled DSGC start firing before, due to the activation of other coupled cells (somas in green). *b*, *c*: the lag of the response of uncoupled DSGC is proportional to the edge velocity, while in coupled cells it is almost not affected. Coupling does not seem to play a major role in the coding of the velocity by the peak firing rate. From (Trenholm et al., 2013b).

#### 2.4.4 Synchronization and inhibitory shunting in the inferior olive

The inferior olive (IO) is a nucleus located in the medulla oblongata that forms one of the most extensive GJ coupled neuronal networks in the adult mammalian brain (Condorelli et al., 1998; Belluardo et al., 2000). Each IO neuron is electrically coupled to  $\sim 19$  other neurons (Hoge et al., 2011; Lefler et al., 2020), via dendritic GJ, located in special functional units called glomeruli, where 4-10 dendrites converge, forming a syncytium (Sotelo et al., 1974). IO neurons provide inputs to the Purkinje neurons of the cerebellar cortex (Llinas et al., 1974), through the climbing fibers, which are the terminal portions of their axons (Schweighofer et al., 2013). Each Purkinje cell receives inputs from only one climbing fiber, through hundreds of synapses that generate strong bursts called “complex spikes”, which are completely different from the “simple spikes” induced by parallel fibers’ activation (Llinás, 2014). However, while parallel fibers can induce firing rates up to 200 Hz, the climbing fibers’ input is far more sporadic, generating 1 or 2 complex spikes per second (Welsh and Turecek, 2017). Therefore, these two pathways convey different information: the climbing fibers are “event detectors” that modify the weight of parallel fibers synapses, in a supervised learning paradigm of motor control (Schweighofer et al., 2013). Consistently, lesions in the IO provoke severe movement coordination deficits (ataxia) (Murphy and O’Leary, 1971; Horn et al., 2013).

IO neurons also send collaterals to cells of the deep cerebellar nuclei (DCN), which in turn project back to the IO, making GABAergic synapses at the glomeruli (Best and Regehr, 2009). In 1974, Llinás et al. already postulated that the activation of these inhibitory synapses, located adjacent to the GJ, may decrease the electrotonic coupling by shunting (Llinas et al., 1974). In this hypothesis, DCN neurons provide a negative feedback to the IO, by activating GABA<sub>A</sub> receptors that decrease the membrane resistance in close proximity to the electrical synapses. Consistently, pharmacological blockade of these receptors increases the complex spike firing rates and widens spatial synchronization in the cerebellar cortex (Lang et al., 1996). The final demonstration of the shunting hypothesis was provided 40 years later by Lefler and coworkers, who transfected channelrhodopsin-2 to photoactivate the DCN GABAergic terminals, evoking inhibitory postsynaptic potentials in IO neurons and decreasing the coupling coefficient by 43% (Lefler et al., 2014). Thus, DCN input modifies the functional architecture of the IO network by diminishing the coupling strength.

Synchronization is a common emergent behavior in large networks of electrically coupled neurons (Bennett and Zukin, 2004)<sup>1</sup>, even in the presence of noise and heterogeneities (Ostojic et al., 2009). IO neurons display synchronous spontaneous subthreshold oscillations (STO), both *in vitro* (Llinás and Yarom, 1986; Turecek et al., 2016) and *in vivo* (Khosrovani et al., 2007), that could be the basis of a temporal pattern generator (Yarom and Cohen, 2002; Jacobson et al., 2008). For several years, it was not completely clear if the STO derived from the intrinsic resonant characteristics of single IO neurons, or from an emergent network property, as the dissection of these two components is not straightforward. Pharmacological blockade of GJ does not abolish STO, but that does not answer the question, as it also increases the IO neurons' input resistance (Leznik and Llinás, 2005). GABA application decreases the amplitude of the IO oscillations (Devor and Yarom, 2000), but its effect on the input resistance also affects the coupling coefficient. A different approach employed knock-out (KO) Cx36 mice as a model, whose IO neurons generate spontaneous (although not synchronized) STO (Long et al., 2002), supporting the idea of them as single-cell oscillators synced by electrical coupling. However, their STO are qualitatively different from those in wild type (WT) animals, due to compensatory changes on their intrinsic properties (De Zeeuw et al., 2003). Finally, Placantonakis and coworkers developed a Cx36 knock-down model, whose IO neurons have the same morphological and electrophysiological properties as the WT (Placantonakis et al., 2004), but do not display sustained STO, strongly suggesting that electrical

---

<sup>1</sup>A notable counterexample are the Golgi neurons, whose profound AHP (see section 2.3.4) inhibit their coupled neighbors, transiently *desynchronizing* the network (Dugué et al., 2009; Vervaeke et al., 2010).

synapses are needed to generate robust synchronous STO in the IO.

### 2.4.5 Coincidence detection in the mammalian brain

The temporal distribution of input signals shapes the response of a network of electrically coupled neurons. On one hand, when they all receive simultaneous inputs, their membrane potentials depolarize (or hyperpolarize) more or less at the same time, canceling the tranjunctional potential across the GJ, effectively augmenting their respective input resistances  $R_{in}$ . On the other hand, if only one receives an input, its response is diminished due to the leak of junctional current to its coupled partners, which act as a “load”. Thus, the electrical synapses endow neural networks with the ability to respond selectively to coincident inputs. An experimental method to test coincidence detection relies on individual and simultaneous current injections to coupled cells, comparing their responses in both cases, as Fig. 2.10 shows for AII amacrine cells from the retina (Veruki and Hartveit, 2002). In this case, current stimuli that elicited subthreshold responses when applied to only one cell, produced firing if both cells were stimulated at the same time. Similarly, coincidence stimulation increases the number of spikes fired in basket cells in the cerebellum (Alcami, 2018) and in the MesV neurons (Curti et al., 2012).

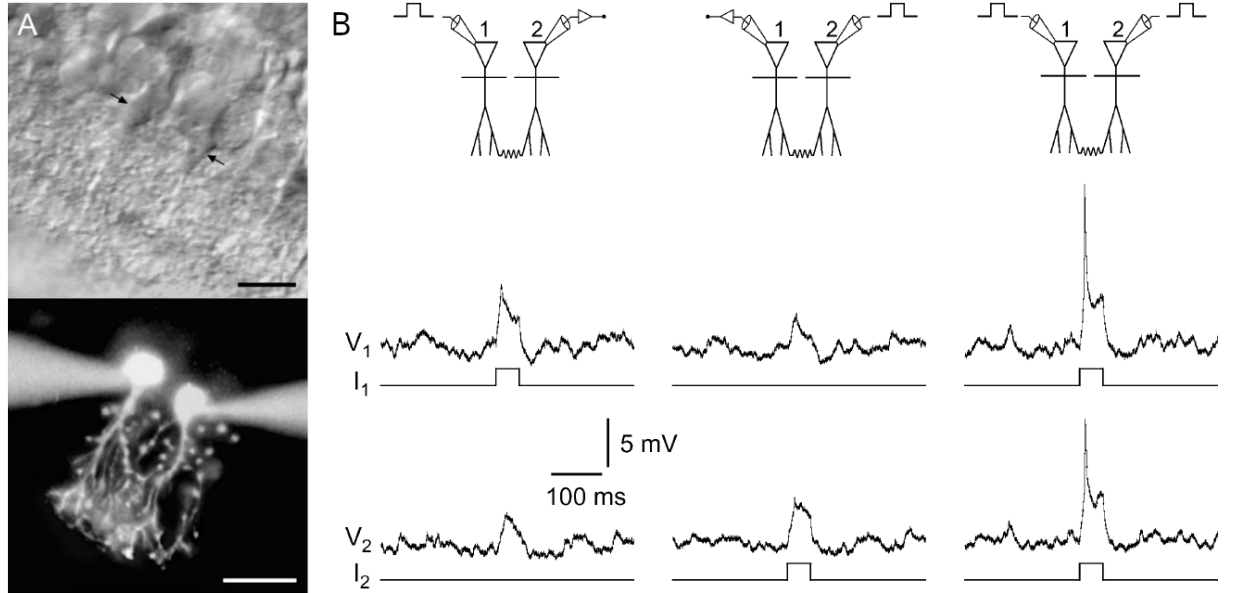


**Figure 2.10: Coincidence detection between AII amacrine cells from the retina.** *A*: differential interference contrast (above) and fluorescence (below) images of two electrically coupled AII amacrine cells from the rat retina. Scale bars indicate 20  $\mu\text{m}$ . *B*: when each coupled cell was stimulated individually by a current pulse (left and center panels), both it and its coupled partner generated a subthreshold voltage responses. However, they fired when both were simultaneously stimulated (right), indicating coincidence detection. Modified from (Veruki and Hartveit, 2002).



The effective canceling of the GJ contribution to  $R_{in}$  relies on how simultaneous are the voltage deflections of the coupled neurons, defining a time window for coincidence detection. We performed an illustrative experiment, injecting short current pulses to two electrically coupled MesV neurons, with varying stimulation delay  $\Delta t = t_2 - t_1$  (Fig. 2.11A). When the delay was long enough (Fig. 2.11B), each cell produced always a subthreshold response (spike probability = 0). However, when  $\Delta t$  shortened to -3.0 ms, the subthreshold depolarization of cell 2 facilitated the response of cell 1, which was able to fire an action potential (Fig. 2.11C). Finally, when  $\Delta t \leq 1.0$  ms, both cells fired, signaling the coincident input (Fig. 2.11D, E). For larger  $\Delta t$ , cell 1 ceased to spike first while still facilitating cell 2 (Fig. 2.11F), and then both cells came back to subthreshold responses (Fig. 2.11G). Thus, coincidence detection only occurs within a very narrow time window of  $\pm 1.0$  ms (Fig. 2.11H). Alcami carried out a similar experiment in electrically coupled basket cells, but with a spike probability of  $\sim 0.4$  for independent stimuli, finding a temporal window of  $\pm 5.0$  ms (Alcami, 2018). The interaction between the electrical coupling and reciprocal inhibitory chemical synapses can reduce this time window even further (Galarreta and Hestrin, 2001).

Electrical coupling in the mammalian brain occurs mostly within the context of networks of more than two cells. Computational simulations of fast spiking neurons showed that electrical coupling reduced the average frequency, of a network of 10 cells, by  $\sim 40\%$  when they receive uncorrelated inputs (Hjorth et al., 2009). However, if their inputs became correlated during a 20-ms time window, the average frequency jumped  $\sim 40\%$ , due to the cancelation of the junctional currents during the coincident stimulation (Hjorth et al., 2009). In the retina, electrical coupling between photoreceptors allows them to distinguish between signal and noise. Indeed, while the noise of a photoreceptor is independent of the others, its signal is not, as it has to be partially shared with its coupled neighbors (DeVries et al., 2002). Therefore, the impact of noisy activations in individual photoreceptors is reduced, as they leak current to their non-activated neighbors through the GJ. Nevertheless, if there is a light signal, junctional current will be minimal, as coupled neighbors activate at the same time. Thus, electrical coupling improves the signal-to-noise ratio in phototransduction, with the cost of some spatial blurring though (DeVries et al., 2002).

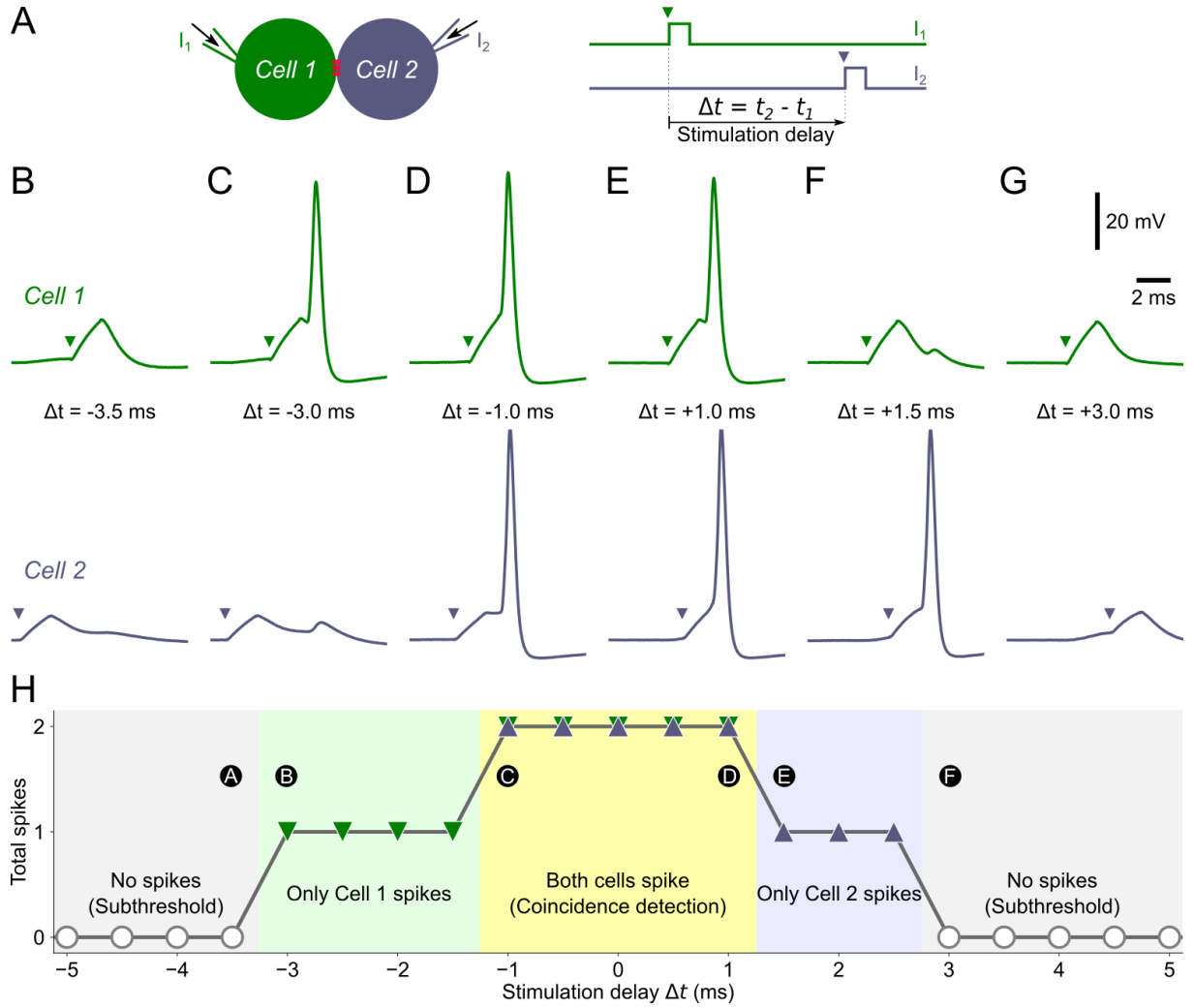


**Figure 2.11: Temporal window of coincidence detection for MesV neurons.** *A:* we stimulated two coupled MesV neurons with short (2-ms) current pulses of constant amplitude, with varying time delay  $\Delta t$  between them. Arrowheads indicate the respective stimulation times. *B:* subthreshold voltage responses of both neurons, for  $\Delta t = -3.5$  ms (Cell 2 was stimulated 3.5 ms before Cell 1). *C:* for  $\Delta t = -3.0$  ms, the response in Cell 1 gets facilitated by the depolarization of Cell 2, eliciting an action potential. *D-E:* there is coincidence detection within the time window  $|\Delta t| \leq 1.0$  ms, as both cells spike. *F* and *G* are analog to *B* and *A*, respectively.



## 2.5 Plasticity

### 2.5.1 Introduction

The strength of the electrical synapses depends on the interplay between the GJ and the intrinsic properties of coupled neurons (see section 2.3.5). Within the context of functional neuronal circuits, both can be modified by changes of the neurons' activity pattern, neurotransmitters, interactions with surrounding glia, trophic factors, metabolites, etc. The impact in electrical coupling of the modulation of a non-synaptic membrane conductance will be studied in chapters 3 and 5, while regulations and activity-driven modifications of GJ will be explored in chapter 4. In this section, we will review the dynamic modifications of the conductance of the GJ by the interactions of their constituent Cx with enzymes and scaffolding proteins, triggered by neuronal electrical activity or neurotransmitters. Indeed, the experimental evidence indicates that GJ are subject to plastic modifications in native neural systems. Note that the plasticity of electrical synaptic transmission would not only result from changes in the efficacy of preexisting contacts, but also might involve the formation of new contacts, as well as the elimination of old ones. In fact, the whole electrical connectome of *C. elegans* undergoes profound modifications when the worm enters a stress-resistant stage in response to an adverse environment (Bhattacharya et al., 2019).

Inspired by the descriptions of chemical synaptic plasticity (Lüscher and Malenka, 2012), we will divide electrical synaptic plasticity into two stages: induction and expression, where the first describes the mechanisms that trigger the phenomenon, while the second explains how the GJ is modified.

### 2.5.2 Induction

Despite the diversity of neurotransmitters and activity patterns that have been studied as triggers of electrical synaptic plasticity (Curti and O'Brien, 2016; O'Brien, 2019), its induction mostly involves intracellular pathways where CaMKII or PKA plays a major role (see section 2.2.2). In order to simplify, we will classify the induction mechanisms into two categories:  $\text{Ca}^{2+}$ -dependent or  $\text{Ca}^{2+}$ -independent. The next examples of plasticity will be centered around Cx36 and its orthologue Cx35, within the context of the neural circuits presented in section 2.4 and others.

## Calcium-dependent plasticity

The first evidence of GJ plasticity was obtained from the mixed synapses between the club endings and the M-cell, where tetanic stimulation elicits a long-term potentiation (LTP) of both electrical and chemical synaptic components, mediated by NMDA receptors, which allow  $\text{Ca}^{2+}$  to enter the postsynaptic cell (Yang et al., 1990). The increase in the intracellular  $\text{Ca}^{2+}$  concentration promotes the activation of CaMKII, leading to the potentiation of the neighbouring GJ (Pereda et al., 1998).

The activation of NMDA receptors in mammalian IO neurons also triggers a CaMKII-mediated long-term modification of the electrical synaptic strength. In 2014, the journal *Neuron* published two papers that, at first glance, seemed to be contradicting each other: one reporting LTP (Turecek et al., 2014) and the other long-term depression (LTD) (Mathy et al., 2014) in the IO, upon activation of NMDA receptors. The apparent discrepancy between these results might reside on their different stimulation protocols: whereas LTD was achieved with a weak activation (50 synaptic stimuli at 1 Hz), LTP was induced by stimulating at higher frequencies or directly applying NMDA to the bath. Thus, possibly low increases of intracellular  $\text{Ca}^{2+}$  trigger LTD, while larger ones induce LTP. From the functional point of view, NMDA application increases the extent and synchronization of STO of electrically coupled IO neurons (Turecek et al., 2014). Furthermore, during LTP, the increase in  $\text{Ca}^{2+}$  concentration occurs locally within microdomains at the dendrites, where NMDA receptors are structurally close to GJ (Turecek et al., 2014). Cx36 GJ at retinal AII amacrine cells also colocalize with nonsynaptic NMDA receptors, whose activation leads to a CaMKII-mediated strengthening of electrical coupling (Kothmann et al., 2012). This phenomenon can be triggered by spillover of glutamate from ON-bipolar cells, activated by an increment in background light (Kothmann et al., 2012).

Electrically coupled neurons in the Thalamic Reticular Nucleus (TRN) operate in two modes, depending on their RMP: bursting from  $-70$  mV or tonic spiking from  $-55$  mV. When bursting activity is induced by current injection, the coupling coefficient and GJ conductance  $g_J$  decrease (Haas et al., 2011), due to calcineurin activation by  $\text{Ca}^{2+}$  going into the cells through low-threshold voltage-activated  $I_T$  channels, and boosted by  $\text{Ca}^{2+}$ -induced  $\text{Ca}^{2+}$  release from ryanodine receptors in the endoplasmic reticulum (Sevetson et al., 2017). Notably, the magnitude of the LTD is the same whether both or only one neuron is in the bursting mode (Haas et al., 2011). In addition,  $\text{Ca}^{2+}$ -dependent LTP can be elicited when one TRN neuron is firing tonically, in the presence of an  $I_T$ -channel blocker (Fricker et al., 2021). Therefore, it is suggested that LTP is elicited by a small increase in intracellular  $\text{Ca}^{2+}$  concentration, while larger ones provoke LTD (Fricker et al.,

2021). Nevertheless, it should be noted that the reported  $g_J$  and its modifications are estimated from current clamp measurements, using an electrical equivalent suitable for single-compartment coupled cells (Bennett, 1966). Limitations of this approach applied to multicompartment TRN neurons with dendritic GJ may account for the reported 20% asymmetry of  $g_J$  in control conditions (Haas et al., 2011), given that homotypic GJ are not rectifying (see section 2.2.1).

## Calcium-independent plasticity

Rode-cone coupling strength is regulated by retinal circadian clocks and light intensity: it increases during nighttime/darkness and returns to a lower level in the daytime/light conditions (Ribelayga et al., 2008). Coupling between AII-amacrine cells displays a more complex pattern: it is low in both complete darkness and bright light conditions, but high at intermediate light intensities (Bloomfield and Xin, 1997; Bloomfield and Völgyi, 2004). Dopamine and adenosine act as light-sensitive signals in the retina that drive these changes, by either promoting or repressing the adenylylate cyclase activity, which in turn activate or inhibit the PKA-mediated phosphorylation of the Cx (Urschel et al., 2006; Kothmann et al., 2009; Li et al., 2013). The interplay between the diversity of dopamine and adenosine receptors present in the retina and the bidirectional regulation of GJ by PKA (see section 2.2.2) produces complex light/circadian regulated modifications in the signal processing (O'Brien, 2019).

Activation of metabotropic glutamatergic receptors (mGluR) also modulates the electrical coupling strength between rat TRN neurons (Landisman and Connors, 2005), through the PKA pathway. In fact, mGluR I and II have opposite effects on it, because of their respective promotion or inhibition of the adenylylate cyclase activity (Wang et al., 2015). In this case, the increased intracellular PKA reduces  $g_J$  (Wang et al., 2015), similarly to what happens between inhibitory interneurons in the hippocampus due to the activation of  $\beta$ -adrenergic receptors (Zsiros and Maccaferri, 2008). Interestingly, the effect of mGluR-activation is occluded by the  $\text{Ca}^{2+}$ -dependent LTD induced by activity reviewed before, suggesting that both pathways converge at some point (Sevetson et al., 2017).

Dopamine acting on D1 receptor at the M-cell was shown to elicit LTP in the electrical synapses between the M-cell and the club endings, also via the PKA-pathway (Pereda et al., 1994). Remarkably, this dopamine may come from neighboring varicosities, which are stimulated by activity-induced endocannabinoid release from the M-cell (Cachope et al., 2007).

### 2.5.3 Expression

The expression of synaptic plasticity is far less studied than its induction, due to the difficulty of discerning if there is a change in the number of channels, their single conductance and/or their open probability. In fact, in the case of Cx36, its single conductance is among the smallest for Cx channels, below the resolution of typical electrophysiological recordings. Fluctuation (nonstationary noise) analysis is an electrophysiological tool that could potentially dissect these three components (Sigworth, 1980), but its application on the GJ channels is not straightforward, as it requires experimentally-induced changes in the open probability of the channels (Alvarez et al., 2002).

Using an indirect histological approach, Bazzigalupi et al. compared the number of coupled neurons in the IO, in different conditions, finding that both stimulation of PKA or inhibition of CaMKII diminishes the coupling (Bazzigalupi et al., 2017). Interestingly, whereas PKA activation does not modify the number of Cx36 puncta between cells, inhibition of CaMKII significantly reduces it, suggesting that the PKA pathway may modify the permeability and/or the open probability of the channels, while CaMKII activation increases their number (Bazzigalupi et al., 2017). However, this indirect approach is not able to tell if the additional available channels in the presence of CaMKII are functional or not. In vertebrates, there is evidence that most of GJ channels are not functional and might operate as a reserve pool to support plasticity. Combining electrophysiological recordings and GJ plaque area measurements, with estimations for single-channel conductance and Cx density, Curti and coworkers estimated that only  $\sim 0.1\%$  of functional GJ channels in MesV neurons (Curti et al., 2012). This result is consistent with the small percentage ( $\sim 1\%$ ) of open channels found in the M-cell (Lin and Faber, 1988).

## Chapter 3

# Role of the intrinsic properties on coincidence detection

Coincidence detection is an important functional property of electrically coupled neurons, that enables them to respond selectively to simultaneous inputs. During coincident stimulation, neurons are approximately at the same membrane potential, with almost no leakage of current through the GJ, effectively enlarging their input resistance  $R_{in}$  by “unloading” them of their coupled partners. This property may manifest as an increase of the number of action potentials elicited during simultaneous current injection, compared with the obtained when only one neuron is stimulated. In the following paper ([Davoine and Curti, 2019](#)), we show that this property is heterogeneous within the population of rat MesV neurons, and depends on both the excitability and the loading of the coupled cell through the GJ. We use the hyperpolarization-activated current  $I_H$  as a tool to showcase the significant role of the intrinsic properties on coincidence detection. Although, in control conditions, the complete activation of  $I_H$  occurs well below the usual RMP of MesV cells, it is a prominent current, due to its large maximum amplitude. Interestingly, its biophysical characteristics are quite diverse, even across neurons from the same animal, suggesting that it is subject to regulation. As  $I_H$  is modulated by cyclic nucleotides, we studied the effect of cGMP on the intrinsic properties of single neurons, finding that it decreases the  $R_{in}$  and increases the excitability.  $I_H$  is necessary for these modifications to happen, given that its blockade abolishes the cGMP-induced modifications. Even though cGMP reduces the coupling strength, due mostly to a reduction on the  $R_{in}$ , the coincidence detection is boosted, driven by the excitability enlargement. Indeed, using a computational model we show that the modifications of the biophysical features of  $I_H$  by cGMP are sufficient to explain the enhancement in coincidence detection. Thus, the modulation of the intrinsic properties acts as a source of plasticity of the functional properties of electrical transmission, allowing neural networks to dynamically modify their behavior.

RESEARCH ARTICLE | *Cellular and Molecular Properties of Neurons*

## Response to coincident inputs in electrically coupled primary afferents is heterogeneous and is enhanced by H-current ( $I_H$ ) modulation

Federico Davoine<sup>1</sup> and Sebastian Curti<sup>2</sup>

<sup>1</sup>*Instituto de Física e Instituto de Ingeniería Eléctrica, Facultad de Ingeniería, Universidad de la República, Montevideo, Uruguay; and* <sup>2</sup>*Laboratorio de Neurofisiología Celular, Departamento de Fisiología, Facultad de Medicina, Universidad de la República, Montevideo, Uruguay*

Submitted 15 January 2019; accepted in final form 22 April 2019

**Davoine F, Curti S.** Response to coincident inputs in electrically coupled primary afferents is heterogeneous and is enhanced by H-current ( $I_H$ ) modulation. *J Neurophysiol* 122: 151–175, 2019. First published May 1, 2019; doi:10.1152/jn.00029.2019.—Electrical synapses represent a widespread modality of interneuronal communication in the mammalian brain. These contacts, by lowering the effectiveness of random or temporally uncorrelated inputs, endow circuits of coupled neurons with the ability to selectively respond to simultaneous depolarizations. This mechanism may support coincidence detection, a property involved in sensory perception, organization of motor outputs, and improvement signal-to-noise ratio. While the role of electrical coupling is well established, little is known about the contribution of the cellular excitability and its modulations to the susceptibility of groups of neurons to coincident inputs. Here, we obtained dual whole cell patch-clamp recordings of pairs of mesencephalic trigeminal (MesV) neurons in brainstem slices from rats to evaluate coincidence detection and its determinants. MesV neurons are primary afferents involved in the organization of orofacial behaviors whose cell bodies are electrically coupled mainly in pairs through soma-somatic gap junctions. We found that coincidence detection is highly heterogeneous across the population of coupled neurons. Furthermore, combined electrophysiological and modeling approaches reveal that this heterogeneity arises from the diversity of MesV neuron intrinsic excitability. Consistently, increasing these cells' excitability by upregulating the hyperpolarization-activated cationic current ( $I_H$ ) triggered by cGMP results in a dramatic enhancement of the susceptibility of coupled neurons to coincident inputs. In conclusion, the ability of coupled neurons to detect coincident inputs is critically shaped by their intrinsic electrophysiological properties, emphasizing the relevance of neuronal excitability for the many functional operations supported by electrical transmission in mammals.

**NEW & NOTEWORTHY** We show that the susceptibility of pairs of coupled mesencephalic trigeminal (MesV) neurons to coincident inputs is highly heterogeneous and depends on the interaction between electrical coupling and neuronal excitability. Additionally, upregulating the hyperpolarization-activated cationic current ( $I_H$ ) by cGMP results in a dramatic increase of this susceptibility. The  $I_H$  and electrical synapses have been shown to coexist in many neuronal populations, suggesting that modulation of this conductance could represent a common strategy to regulate circuit operation supported by electrical coupling.

electrical synapses; HCN channels; mesencephalic trigeminal neurons

### INTRODUCTION

Electrical transmission through gap junctions is typically fast and bidirectional, supporting the synchronized activation of networks of coupled neurons (Bennett and Zukin 2004; Connors and Long 2004; Perez Velazquez and Carlen 2000). Also, these contacts may endow neural circuits with the ability to selectively respond to excitatory synchronic inputs (Curti et al. 2012; Galarreta and Hestrin 2001; Veruki and Hartveit 2002a). In fact, if a cell of a network of coupled neurons receives a synaptic input, part of the underlying current flows through gap junctions toward nonstimulated cells. Thereby, by acting as current sinks, electrical synapses reduce the input resistance of all cells of the network. This effect, termed loading, greatly reduces the excitability of electrically coupled neurons (Getting 1974). In contrast, synchronic inputs to all coupled cells promote parallel variations of the membrane potential of each neuron, reducing the voltage drop across junctions and minimizing the flow of current to neighbor cells. Thus, by canceling the loading effect, simultaneous inputs induce larger changes in membrane potential of all neurons of the network, facilitating their activation. This property allows electrical coupling to maximize the impact of coincident inputs while dampening that of temporally dispersed ones, supporting coincidence detection (Chillemi et al. 2007; Edwards et al. 1998; Hjorth et al. 2009; Rabinowitch et al. 2013; Rela and Szczupak 2004). In this way circuits of coupled neurons can discriminate inputs based on their arrival times. Critical for this network operation is the difference of neuronal responses evoked by coincident excitatory inputs compared with randomly distributed ones. The greater the contrast between maximal (due to coincident inputs) and minimal responses (due to temporally dispersed inputs), the higher the gain of coincidence detection. Thus any mechanism that increases this contrast, whether increasing the response to coincident inputs or by reducing it to uncorrelated ones, will enhance coincidence detection (Agmon-Snir et al. 1998). While the mechanisms determining the precision of coincidence detection in networks of coupled neurons have been studied (Edwards et al. 1998), much less is known about the mechanisms that support its gain.

The mesencephalic trigeminal (MesV) nucleus of the rat is a particularly good model to study electrical transmission and its contributions to the computational capabilities of neural networks. These neurons are primary afferents, therefore exhibit

Address for reprint requests and other correspondence: S. Curti, Gral. Flores 2125, Montevideo 11800, Uruguay (e-mail: scurti@fmed.edu.uy).



ing a simple morphology characterized by a large cell body from which only one process emerges. Also, they are electrically coupled in pairs or small clusters through distinct somasomatic connexin36 (Cx36)-containing gap junctions (Curti et al. 2012). Interestingly, MesV neurons receive profuse synaptic inputs from several brain structures (Lazarov 2002) by way of neurotransmitters and neuromodulators that have been shown to modulate either neuronal excitability or electrical coupling in other systems, raising the possibility of regulatory control.

In a previous study, we showed that electrically coupled MesV neurons act as coincidence detectors (Curti et al. 2012). Beyond the well-established role of electrical coupling in coincidence detection, the present study shows that the intrinsic electrophysiological properties of coupled neurons are also critical determinants of this network operation. Moreover, the susceptibility to coincident inputs, corresponding to the gain of coincidence detection, is highly heterogeneous across the population of coupled cells. Furthermore, by combining electrophysiological and modeling approaches, we provide evidence supporting the notion that this heterogeneity arises to a great extent from the diverse regulatory states of MesV neuron's intrinsic excitability. Consistently, the upregulation of the hyperpolarization-activated cationic current ( $I_H$ ) triggered by cGMP results in a dramatic enhancement of the susceptibility of coupled MesV neurons to coincident excitatory inputs. Modulatory actions induced by cGMP consist of a shift of the  $I_H$  activation curve toward more positive values and an acceleration of its kinetics, resulting in a depolarization of the resting membrane potential, a reduction of the input resistance, and an enhancement in neuronal firing. In coupled neurons, these modulatory changes in combination with the loading effect result in a dramatic increase in firing mainly in response to coincident depolarizations. Thus, by preferentially increasing neuronal excitability to simultaneous inputs, upregulation of  $I_H$  causes an enhancement of coincidence detection gain.

These results indicate that modulation of the  $I_H$  might impart highly dynamic and relevant characteristics to electrical synaptic transmission. According to that, network operations supported by this modality of intercellular communication are critically shaped by the intrinsic excitability of neurons, emphasizing the relevance of the neuronal electrophysiological properties and its modulations in the many functional operations supported by electrical transmission in the mammalian brain.

## MATERIALS AND METHODS

The experimental protocol was approved by the local animal ethics committee of Facultad de Medicina, according to the guidelines of Comisión Honoraria de Experimentación Animal of Universidad de la República (Uruguay), with minimization of the numbers of animals used.

**Experimental design.** Transverse brain stem slices (250- $\mu$ m thick) were prepared from Wistar or Sprague-Dawley rats of either sex (age: postnatal days 8–18). Rats were decapitated without anesthesia, and brains were quickly removed. Slices obtained using a vibratome (Leica VT 1000s or DSK DTK-1000) were placed in cold sucrose solution containing the following (in mM): 248 sucrose, 2.69 KCl, 1.25  $\text{KH}_2\text{PO}_4$ , 26  $\text{NaHCO}_3$ , 10 glucose, 2  $\text{CaCl}_2$ , and 2  $\text{MgSO}_4$  bubbled with 95%  $\text{O}_2$ -5%  $\text{CO}_2$  (pH ~7.4). The slices were then transferred to an incubation chamber filled with sucrose solution at

room temperature and kept there for 60 min. The sucrose solution was slowly replaced by physiological solution containing the following (in mM): 124 NaCl, 2.69 KCl, 1.25  $\text{KH}_2\text{PO}_4$ , 26  $\text{NaHCO}_3$ , 10 glucose, 2  $\text{CaCl}_2$ , and 2  $\text{MgSO}_4$  bubbled with 95%  $\text{O}_2$ -5%  $\text{CO}_2$  (pH ~7.4). Sections were kept at room temperature in the physiological solution until they were transferred into the recording chamber. The recording chamber, mounted on an upright microscope stage (Nikon Eclipse E600), was continuously perfused with physiological solution (1–1.5 ml/min) at room temperature. Whole cell patch recordings were performed under visual control using infrared differential interference contrast optics. MesV neurons were identified on the basis of their location, large spherical somata, and characteristic electrophysiological properties in response to both depolarizing and hyperpolarizing current pulses (Del Negro and Chandler 1997; Liem et al. 1991; Pedroarena et al. 1999). Recording pipettes pulled from borosilicate glass (4–8 M $\Omega$ ) were filled with intracellular solution containing the following (in mM): 144 K-gluconate, 3  $\text{MgCl}_2$ , 0.2 EGTA, 4 Mg-ATP, 0.3 Na-ATP, and 10 HEPES (pH ~7.2). The seal resistance between the electrode tip and the cell membrane was >1 G $\Omega$ , and pipette capacitance was compensated before breaking the seal. Simultaneous recordings from pairs of MesV neurons whose cell bodies lie in close apposition were made using one Axopatch 200B and one Axoclamp 2A amplifiers or a Multiclamp 700B amplifier (Molecular Devices, Sunnyvale, CA). Only cells displaying resting membrane potential more negative than –50 mV and spike amplitude above 70 mV were included in this report. Recordings were low-pass-filtered at 5 kHz and acquired by means of an analog to digital converter connected to a computer, sampled at 20 or 10 KHz depending on the experiment. Data were analyzed using Axograph X, pClamp 9 (Molecular Devices) and Igor (Wave Metrics, Portland OR) software.

**Calculation of coupling coefficient.** During simultaneous intracellular recordings of pairs of MesV neurons in current clamp, hyperpolarizing current pulses of 200–400 ms in duration were alternatively injected to each cell and the resulting membrane voltage deflections were measured in both cells. The coupling coefficient (CC) from a presynaptic to a postsynaptic cell, being the presynaptic cell defined as the one receiving the current injection, was calculated as  $V_{\text{post}}/V_{\text{pre}}$ , where  $V_{\text{pre}}$  is the voltage deflection in the presynaptic neuron and  $V_{\text{post}}$  the concomitant voltage deflection in the postsynaptic neuron. A total of 10 to 100 single responses were averaged to improve the signal-to-noise ratio. Because the strength of an electrical synapse measured as the CC is influenced by both the gap junction conductance and the input resistance of the postsynaptic cell (Bennett 1966; Curti and O'Brien 2016), any voltage-dependent change of the input resistance of the postsynaptic cell might modify the CC. Hence, to improve the accuracy of CC estimation, instead of same amplitude current pulses a series of hyperpolarizing current pulses of different amplitudes (–50 to –450 pA) were applied. This method was employed in some cases in which inconsistencies in the CC estimation were observed due to the above-mentioned pitfalls. From these recordings, plots of the voltage change in the postsynaptic neuron as a function of the voltage change in the presynaptic neuron were constructed and CC was estimated from the slope of linear regressions (see Fig. 11, C and D). For each pair of coupled neurons, the CC was calculated in opposite directions and both values were reported (two directions per coupled pair).

**Estimation of gap junction conductance.** With the use of the same experimental protocol described in *Calculation of coupling coefficient*, the conductance of electrical contacts was estimated as the reciprocal of the resistance ( $R_c$ ) calculated following (Bennett 1966):

$$R_c = \frac{R_{\text{in}_{\text{pre}}} \times R_{\text{in}_{\text{post}}} - R_t^2}{R_t}$$

where  $R_{\text{in}_{\text{pre}}}$  and  $R_{\text{in}_{\text{post}}}$  are the input resistance of the pre- and postsynaptic cells, respectively, and  $R_t$  is the transfer resistance defined as the voltage response amplitude in the postsynaptic cell

divided by the current intensity injected in the presynaptic cell. Conductance values estimated by this method are reported as directions (2 directions per coupled pair). To assess the accuracy of this method in estimating the gap junction conductance between MesV neurons, in an independent experimental series we compared the results obtained by using this indirect method with those obtained from direct measurements of junctional current under voltage clamping. For that purpose dual voltage-clamp experiments were performed following the same procedure we employed previously for the characterization of electrical transmission in the MesV nucleus (Curti et al. 2012). The results obtained by these two approaches were indistinguishable, averaging  $4.0 \pm 0.59$  and  $4.2 \pm 0.72$  nS (SE) for current- and voltage-clamp experiments, respectively ( $P = 0.582$ ,  $n = 8$ ; paired, two-tailed  $t$ -test).

**Calculation of coincidence detection index.** To assess coincidence detection, suprathreshold depolarizing current pulses were applied to pairs of MesV neurons. Pulses, whose intensity were adjusted to evoke only one or two spikes when applied individually, were repeated 10–20 times independently to each cell and then to both cells at the same time. From these recordings, the average number of spikes evoked in each cell during these stimulation protocols was determined. To quantify coincidence detection, two alternative methods were considered. The first one consisted of calculating the ratio of the number of spikes when cells were simultaneously activated over the number of spikes when cells were independently activated. This index will indicate how much stronger is the response to coincident stimulation relative to individual responses. The second method consisted of calculating an index defined as the subtraction of the mean number of spikes when cells were independently activated from the mean number of spikes when cells were simultaneously activated (coincident activation). This index reflects how many spikes are added to the neuronal response when this cell and its coupled neighbor were activated at the same time (when the loading effect is canceled, see text) in comparison to when the cell was activated in isolation. For the whole population of recorded coupled cells ( $n = 76$ ), the two methods yield comparable results as indicated by paired, two-tailed  $t$ -test ( $P = 0.19$ ) and the fact that they present a clear positive correlation [slope =  $0.63 \pm 0.036$  [95% confidence interval (CI)],  $R^2 = 0.8$ ]. Because difference in firing evoked by simultaneous and uncorrelated inputs is considered a direct indicator of coincidence detection function (Agmon-Snir et al. 1998), the subtraction index (coincidence detection index) was adopted. Thus this index represents a measurement of the susceptibility of coupled neurons to coincident inputs and has units of spikes. Despite coincidence detection in coupled neurons represents an emergent property of groups of cells, we calculated the coincidence detection index based on the activity of single neurons (considering the activity in the stimulated neuron) to be able to correlate this property with their intrinsic excitability.

**Assessment of MesV neurons excitability.** During current-clamp recordings, series of depolarizing current pulses of 200 ms in duration were applied, whose intensities ranged most typically from 50 to 650 pA, in steps of 50 pA. From these recordings, curves of the number of spikes versus current intensity were constructed and threshold intensity and the number of spikes evoked by current pulses three to six times this intensity were determined. This analysis showed that even at comparable ages healthy neurons display a wide diversity of firing properties in terms of the number of spikes and the threshold intensity. To assess excitability, straight line functions were fitted to spikes versus current curves. Even though in some cases the goodness of fit to these functions was relatively poor (particularly for step like curves), by forcing the fitting through the origin, the slope of this curve represents a valuable indicator of neuronal excitability. In fact, by pivoting around the origin, the slope of this function is a highly sensitive indicator that combines both the ability of the neuron to produce repetitive discharges and the threshold level.

**Recording of the persistent  $\text{Na}^+$  current.** To isolate the persistent  $\text{Na}^+$  current ( $I_{\text{NaP}}$ ),  $\text{K}^+$  currents were blocked either by using a Cs<sup>+</sup>

based intracellular solution (in mM: 123 Cs-glutamate, 9 HEPES, 4.5 EGTA, 0.27 Na-GTP, 3.6 Na<sub>2</sub>-ATP, and 9.5 MgCl<sub>2</sub>, pH ~7.2 and osmolality adjusted to 295–305 mosM), or by using a normal K<sup>+</sup>-based intracellular solution (see above) and adding a combination of blockers to the extracellular solution (5 mM TEA-Cl, 1 mM 4-aminopyridine, and 1 mM CsCl). In both cases, 0.2 mM CdCl<sub>2</sub> were added to the extracellular solution to block Ca<sup>2+</sup> currents. Both methods yield comparable results. MesV neurons were voltage clamped and ramp protocols were applied from a holding potential of  $-70$  to  $0$  mV in 4 s (Fleiderovich and Gutnick 1996). These protocols evoked a slow inward current that peaked at about  $-40$  mV and that was totally abolished by adding  $0.5 \mu\text{M}$  tetrodotoxin to the extracellular solution.

**Recording of  $I_{\text{H}}$ .** In the whole cell configuration, compensation of the cell capacitance and series resistance (80%) was performed and monitored during the course of experiments. Recordings were low-pass filtered at 5 KHz and sampled at 20 KHz. Voltage steps of 0.5 to 2 s in duration and from  $-40$  to  $-140$  mV were applied starting from a holding potential of  $-50$  mV and returning to a postpulse potential of  $-70$  or  $-80$  mV. This protocol was applied in control conditions and in the presence of 2 mM CsCl in the bath, which almost completely blocks the  $I_{\text{H}}$  (Pape 1996). To isolate this current from other voltage activated membrane currents, total currents obtained in presence of CsCl were subtracted from those obtained in control conditions. In selected control experiments ( $n = 4$ ),  $I_{\text{H}}$  isolation was achieved by using a combination of  $0.5 \mu\text{M}$  tetrodotoxin and 1 mM 4-aminopyridine to block the main voltage-activated currents of MesV neurons at the explored voltage range, that is, the persistent sodium current and the A-type K<sup>+</sup> current, respectively (Del Negro and Chandler 1997; Wu et al. 2001). Membrane currents obtained by these two procedures were undistinguishable; therefore, the CsCl procedure was adopted for simplicity.

Steady-state activation curves were determined from the amplitude of tail currents after voltage steps return to  $-70$  or  $-80$  mV. Tail current amplitudes were measured after the decay of the capacitive transients (typically ~4 ms of terminated the pulse) and transformed to conductance values dividing by the driving force ( $-41.3$  and  $-51.3$  mV, respectively). For this purpose, the reversal potential of the  $I_{\text{H}}$  was determined following standard protocols consisting in voltage steps to  $-110$  mV from a holding potential of  $-50$  mV. Voltage steps lasted for 700 ms to 1 s to produce near maximal activation of the  $I_{\text{H}}$  and were followed by a series of voltage postpulses that ranged from  $-10$  to  $-80$  mV. Membrane currents were recorded during the postpulses after the decay of the capacitive transient. Measured membrane current values were plotted against the postpulse voltage, and the reversal potential was determined as the point where  $I_{\text{H}} = 0$  (intersection with the voltage axis). Following this procedure, the reversal potential was determined in five neurons and averaged  $-28.7 \pm 1.52$  mV (SE).

For each cell, the conductance values ( $G$ ) obtained following this procedure were normalized by its maximum value ( $G_{\text{max}}$ ) and plotted as a function of the step voltages and fitted to a Boltzmann equation of the form:

$$\frac{G}{G_{\text{max}}}(V) = \frac{1}{1 + \exp[(V_{1/2} - V)/K]}$$

where  $V$  is the voltage during the command pulse in millivolts,  $V_{1/2}$  is the half activation voltage, and  $K$  is the slope of the fitting curve at  $V_{1/2}$ .

For the population of recorded MesV neurons, the series resistance ( $R_s$ ) averaged  $12.4 \pm 0.59$  M $\Omega$  (SE) and was compensated by 80%. The maximum error in voltage-clamp commands introduced by the uncompensated  $R_s$  was estimated for each experiment by multiplying the uncompensated series resistance (20% of  $R_s$ ) times the maximum membrane current at steady state elicited by the most hyperpolarizing command potential. This error averaged  $6.2 \pm 2.72\%$  (SD, range



2–13%,  $n = 34$ ) of command potentials and did not show any correlation with the estimated  $V_{1/2}$ . Indeed, the relationship between  $V_{1/2}$  and the  $R_s$  presents a slope not statistically different from 0 [slope =  $0.05 \pm 0.72$  (95% CI),  $R^2 = 6 \times 10^{-4}$ ,  $n = 34$ ], indicating that the uncompensated  $R_s$  did not introduced any significant bias in the determination of this parameter. When recordings were obtained from electrically coupled neurons, identical voltage-clamp protocols were applied simultaneously to both cells to improve space clamp. The membrane capacitance of MesV neurons was obtained from the readout provided by the Multiclamp 700B amplifier during the procedure of cell capacitance compensation.

Activation time constants were determined by fitting the current traces evoked during voltage steps to single or double exponential functions using SciPy library from Python (<https://www.scipy.org/>). The uncompensated capacitive transients and activation delays occurring at the beginning of voltage commands were excluded from the fitting windows. In three representative cells, we compared the results of single versus double exponential fits. Simultaneous fitting with two exponential components yielded a fast and a slow component that presented activation time constants that averaged  $0.56 \pm 0.05$  and  $2.64 \pm 0.14$  s (SE), respectively, at  $-88.9$  mV (close to the population  $V_{1/2}$  of  $-88.5$  mV, see RESULTS). However, the amplitude of the slow exponential component at this voltage step represented only 7.4% of the fast component. Accordingly, the inclusion of the second exponential term resulted in a negligible improvement of fitting in comparison to single exponential fitting as indicated by the reduction of  $R^2$ . In fact,  $R^2$  from double exponential fittings was reduced on average by only 0.24% in comparison to  $R^2$  from single exponential fittings at  $-88.9$  mV and at  $-118$  mV this reduction averaged 1.5%. On the other hand, fast time constants obtained from double exponential fits to current traces obtained in response to voltage steps ranging from  $-70$  to  $-120$  mV were almost indistinguishable from time constants from single exponential fits. For instance, at  $-88.9$  mV the activation time constant averaged  $0.56 \pm 0.05$  and  $0.61 \pm 0.05$  s (SE), respectively ( $P = 0.48$ ; paired, two-tailed  $t$ -test). Therefore, based on these observations and for the sake of simplicity of both fitting procedures and computational modeling, the activation time constant of the  $I_H$  was determined from single exponential fits.

Because recordings were obtained at room temperature ( $20$ – $25^\circ\text{C}$ ) and activation kinetics is a highly temperature-dependent process (Sterratt 2014), time constants were normalized to  $20^\circ\text{C}$  assuming a  $Q_{10}$  of 4 (Robinson and Siegelbaum 2003).

**Statistical analysis.** Results were expressed as average value  $\pm$  SD or means  $\pm$  SE. Significance of quantitative data was determined by using  $\chi^2$ -test and Student's  $t$ -test (GraphPad Software). Correlation between data sets was assessed by linear regression analysis using Igor 7 (WaveMetrics). Slope values of best-fit lines were reported as value  $\pm$  95% CIs. Two data sets were considered to be correlated if zero is not included in this confidence interval (Canavos 1988).  $P$  values for linear regression analysis was obtained using the P Value from Pearson (R) Calculator retrieved from <https://www.socscistatistics.com/pvalues/pearsondistribution.aspx> (Social Science Statistics, March 3, 2019).

**MesV cells model and computational simulations.** A reduced computational model of MesV neurons was implemented in NEURON + Python (Hines et al. 2009). This model consisted in two compartments, one representing the soma and the other the axon. The geometry of each compartment was initially set based on previous work using intracellular injections of neurobiotin (Curti et al. 2012), and final values were tuned following standard procedures by fitting exponential functions to the decay of passive voltage membrane responses to long current steps. According to that, the soma of these cells was modeled as a compartment of  $25\ \mu\text{m}$  in diameter and  $25\ \mu\text{m}$  in length connected to a cylindrical axon compartment of  $3\ \mu\text{m}$  in diameter and  $450\ \mu\text{m}$  in length [axon length was obtained after further optimization through evolutionary multiobjective optimization algo-

rithm (EMOO; see below) due to uncertainty of axonal length after the slicing procedure].

The following six Hodgkin-Huxley type active conductances were inserted into the soma compartment: persistent sodium current ( $I_{\text{NaP}}$ ) (Enomoto et al. 2007), transient sodium current ( $I_{\text{NaT}}$ ) (Enomoto et al. 2007), delayed rectifier ( $I_{\text{DRK}}$ ) (Del Negro and Chandler 1997), A-type potassium current [ $I_A$  (this conductance presents low activation threshold, sensitivity to 4-aminopyridine in the  $\mu\text{M}$  range, almost no inactivation, and most probably is mediated by Kv1.1 and Kv1.6 channels)] (Saito et al. 2006; Yang et al. 2009), high-threshold fast potassium current ( $I_{\text{HT}}$ ) slightly modified from a previous report (Wang et al. 1998) and most probably mediated by Kv3.1 channels, and hyperpolarization-activated current ( $I_H$ ). All these active conductances were previously described in MesV neurons except for the  $I_{\text{HT}}$ , which was included instead of the fast transient outward current ( $I_{\text{TOC-F}}$ ) (Del Negro and Chandler 1997) to obtain spikes whose durations are consistent with experimental observations. In fact, including  $I_{\text{TOC-F}}$  as the only spike repolarizing mechanism yielded action potentials with durations of  $\sim 3$ – $4$  ms at its base, which is significantly longer than the recorded spikes ( $\sim 1$  ms at the base and half-widths of  $\sim 450\ \mu\text{s}$ ; see Fig. 9A, bottom). In contrast, currents mediated by Kv3.1 channels, analog to our  $I_{\text{HT}}$  current, present rapid kinetics and a high threshold of activation consistent with the brief duration of MesV neuron's spikes, similar to neurons of the MNTB (Johnston et al. 2010; Wang et al. 1998). In addition, Kv3 subunits have been detected in MesV neurons (Saito et al. 2006). For the sake of modeling spike-based electrical transmission (essential for the study of synchronization and coincidence detection), spike duration is a critical parameter as longer than real spikes will correspond to an overrepresentation of low-frequency components of the spike power spectrum. Thus long-lasting spikes in combination with the filter frequency characteristics of electrical transmission between MesV neurons (Curti et al. 2012) would result in coupling potentials larger than normal for a given gap junction conductance.

On the other hand, the axon compartment contained the same active mechanisms as the soma except for the  $I_A$  that was not included because Kv1.1 and Kv1.6 were localized only in the somata and not in axons of MesV neurons (Saito et al. 2006).

To generate a biophysically realistic model of MesV neurons, it is necessary to know what kind of active conductances are present in each cellular compartment as well as the relative densities of these mechanisms. Despite the fact that the presence of several voltage-dependent conductances in the soma is well documented by the work of several groups, the densities of these conductances might vary according to age, sex, modulatory state, recording conditions and species among other factors. Moreover, the presence of voltage-dependent conductances in the axon is inferred mainly from morphological studies and most of them have not been directly measured experimentally. Therefore, these model parameters have been tuned to match the experimentally observed electrophysiological properties and input-output relation of MesV neurons using an EMOO (Bahl et al. 2012) (Python library available in <https://projects.g-node.org/emoo>). This algorithm was applied in a step-wise manner: first, its passive properties (axon length, membrane and axial resistances), then the maximum values of subthreshold active conductances ( $I_{\text{NaP}}$ ,  $I_A$ , and  $I_H$ ), and finally those that operate mainly in the suprathreshold range of membrane potentials ( $I_{\text{NaT}}$ ,  $I_{\text{HT}}$ , and  $I_{\text{DRK}}$ ). This procedure defines a set of objective parameters [resting membrane potential, input resistance, spike characteristics (height and duration), and time constant and firing characteristics (frequency and number of spikes)], which describe the basic properties and input-output relation of neurons. On the other hand, a set of variable or free parameters like the membrane and axial resistances, axon length, time constant of  $I_{\text{HT}}$ , and maximum densities of leak- and voltage-dependent conductances are allowed to fluctuate within predetermined lower and upper search bounds during the fitting procedure to minimize the least square

difference between the real parameters obtained from recordings and the model's objective parameters (Bahl et al. 2012).

After optimization of the objective parameters, a family of 35 reduced models of MesV neurons was obtained. Electrophysiological properties of these models reasonably matched those of a sample ( $n = 15$ ) of experimentally recorded neurons in terms of resting membrane potential [ $-54.7 \pm 0.5$  mV (SE) experimental vs.  $-55.2 \pm 0.2$  mV (SE) model,  $P = 0.38$ ], input resistance [ $118.3 \pm 8.1$  M $\Omega$  (SE) experimental vs.  $114.9 \pm 1.1$  M $\Omega$  (SE) model,  $P = 0.54$ ], spike amplitude [ $93.3 \pm 2.0$  mV (SE) experimental vs.  $98.6 \pm 1.9$  mV (SE) model,  $P = 0.13$ ], spike duration at  $-20$  mV [ $0.7 \pm 0.1$  ms (SE) experimental vs.  $0.7 \pm 0.0$  ms (SE) model,  $P = 0.77$ ], spike afterhyperpolarization level [ $-62.01 \pm 0.7$  mV (SE) experimental vs.  $-64.2 \pm 1.1$  mV (SE) model,  $P = 0.23$ ], and frequency of the first interspike interval in response to a current step of  $+400$  pA [ $119.0 \pm 7.9$  Hz (SE) experimental vs.  $111.4 \pm 3.3$  Hz (SE) model,  $P = 0.32$ ] (unpaired, two-tailed  $t$ -test). Fitting parameters obtained from these simulations were averaged and fine-tuned to obtain a representative model of the MesV cells population that mimics the main characteristics of repetitive discharges in control conditions (see Fig. 9, A–D). The equations describing the model's membrane conductances are the following:

Leak current:  $I_L = \bar{g}_L(V - E_L)$ , where  $\bar{g}_L = 3 \times 10^{-5}$  S/cm $^2$  in the soma and  $\bar{g}_L = 15 \times 10^{-5}$  S/cm $^2$  in the axon.

Hyperpolarization-activated current:  $I_h = \bar{g}_h n_h(V - E_h)$ , where  $n_{h\infty}(V) = \left(1 + e^{\frac{V+89}{8}}\right)^{-1}$  and  $\tau_h(V) = 417 \left(1 + \left(\frac{V+70}{4}\right)^2\right)^{-1} + 366$  ms,  $\bar{g}_L = 6 \times 10^{-4}$  S/cm $^2$

A-type potassium current:  $I_A = \bar{g}_A n_A(V - E_K)$ , where  $n_{A\infty}(V) = \left(1 + e^{\frac{V+48}{4}}\right)^{-1}$ ,  $\tau_A = 3.4$  ms,  $\bar{g}_L = 1 \times 10^{-3}$  S/cm $^2$

Delayed rectifier potassium current:  $I_{DRK} = \bar{g}_{DRK} n_{DRK}(V - E_K)$ , where  $n_{DRK}(V) = \left(1 + e^{\frac{V+4.2}{12.9}}\right)^{-1}$ ,  $\tau_{DRK}(V) = 25 \left[ \left(1 + e^{\frac{V+40}{15}}\right)^{-1} + \left(1 + e^{\frac{V-25}{2}}\right)^{-1} \right] - 23$  ms,  $\bar{g}_{DRK} = 1.3 \times 10^{-4}$  S/cm $^2$

High-threshold fast potassium current:  $I_{HT} = \bar{g}_{HT} m_{HT}^3(V - E_K)$ , where  $m_{HT\infty}(V) = \left(1 + e^{\frac{V-5}{15}}\right)^{-1}$ ,  $\tau_{HT}(V) = 0.5 + 0.6 \left(1 + e^{\frac{V+57}{31}}\right)^{-1}$  ms,  $\bar{g}_{HT} = 1.2 \times 10^{-1}$  S/cm $^2$

Persistent sodium current:  $I_{NaP} = \bar{g}_{NaP} n_{NaP\infty}(V - E_{Na})$ , where  $n_{NaP\infty}(V) = \left(1 + e^{\frac{V+50}{5.3}}\right)^{-1}$ ,  $\bar{g}_{NaP} = 1.8 \times 10^{-5}$  S/cm $^2$

Transient sodium current:  $I_{NaT} = \bar{g}_{NaT} m_{NaT}^3 h_{NaT}(V - E_{Na})$ , where  $m_{NaT\infty}(V) = \left(1 + e^{\frac{V+24}{5.5}}\right)^{-1}$ ,  $\tau_{mNaT}(V) = 0.2$  ms,  $h_{NaT\infty}(V) = \left(1 + e^{\frac{V+77}{8.6}}\right)^{-1}$ ,  $\tau_{hNaT}(V) = 0.3 + 5e^{-\frac{V+50}{10}}$  ms,  $\bar{g}_{NaT} = 8 \times 10^{-2}$  S/cm $^2$

The corresponding reversal potentials are  $E_h = -28.7$  mV,  $E_K = -93.0$  mV,  $E_{Na} = 78.0$  mV, and  $E_L = -58$  mV.

The effects of cGMP on  $I_h$  current were simulated by modifying the parameters describing the activation at steady state ( $V_{1/2}$ ,  $K$ , and  $\bar{g}_h$ ), as well as its kinetics consistently with experimental results. Accordingly, the equation describing the modulated  $I_h$  current is the following:

$I_h = \alpha \bar{g}_h n_h(V - E_h)$ , where  $n_{h\infty}(V) = \left(1 + e^{\frac{V+83.1}{9.7}}\right)^{-1}$ ,  $\tau_h(V) = 296e^{-\left(\frac{V+75.4}{17.4}\right)^2} + 42$  ms and  $\alpha = 1.26$ .

Small networks consisting of pairs of coupled MesV neurons were simulated as two identical representative model neurons connected by a voltage independent conductance in agreement with previous results obtained in this neuronal population (Curti et al. 2012). The value of this conductance representing gap junctions was 4 nS also in agreement with our previous work and the equation describing these electrical contacts is the following:

$$I_{jpre \rightarrow post} = g_j(V_{post} - V_{pre})$$

where  $g_j$  is the gap junction conductance and  $V_{post}$  and  $V_{pre}$  are the membrane potentials of the post- and presynaptic cells, respectively.

## RESULTS

*Coincidence detection between pairs of electrically coupled MesV neurons is heterogeneous.* We previously reported that pairs of electrically coupled MesV neurons may be highly susceptible to synchronic or coincident depolarizing inputs. In fact, simultaneous depolarizations tend to be much more efficient in evoking repetitive discharges in comparison to temporally distributed inputs (Curti et al. 2012). This phenomenon, herein referred to as coincidence detection, is illustrated in Fig. 1 for a pair of electrically coupled neurons (Fig. 1A), where depolarizing current pulses evoked only one or two spikes when applied alternatively to each cell (Fig. 1B, *left* and *middle*), whereas simultaneously applied current pulses of the same intensity evoke repetitive discharges in both cells (Fig. 1B, *right*). The number of spikes when cells were coactivated is significantly higher than when cells were activated in isolation averaging  $5.56 \pm 0.78$  and  $1.51 \pm 0.13$  (SE), respectively ( $P = 1 \times 10^{-4}$ ;  $n = 76$  from 38 pairs, paired, two-tailed  $t$ -test; Fig. 1C, black circles), confirming that pairs of coupled MesV neurons behave as coincidence detectors. To quantify this property, a coincidence detection index (coincidence detection index) was calculated (see MATERIALS AND METHODS). This index, calculated as the difference in spike number when stimuli were delivered simultaneously to both cells or individually to each one, represents the gain of coincidence detection or susceptibility to coincident inputs and has units of spikes. The coincidence detection index for the population of coupled neurons ( $n = 76$  from 38 pairs) averaged  $4.05 \pm 0.74$  spikes (SE) (Fig. 1D). In contrast, when the same stimulation protocol was applied to pairs of MesV neurons whose cell bodies were juxtaposed but electrically uncoupled (Fig. 1E), neuronal firing evoked by individual and coincident stimulation showed no differences, averaging  $1.70 \pm 0.37$  and  $1.85 \pm 0.49$  (SE), respectively ( $P = 0.76$ ;  $n = 20$  from 10 pairs, paired, two-tailed  $t$ -test; Fig. 1, F and G). Consistently, the coincidence detection index of uncoupled cells averaged  $0.15 \pm 0.48$  spikes (SE). These results support the idea that electrical coupling is indispensable for coincidence detection between MesV neurons.

Electrical coupling represents an attribute that divides the population of MesV neurons in seemingly homogeneous categories in terms of their computational capabilities; that is, those that are able to detect coincident inputs from those that are not. However, coincidence detection among coupled neurons is diverse. Indeed, the plots of the number of spikes according to the stimulation protocol, independent versus simultaneous depolarizations, display a great diversity of slopes (Fig. 1C, gray circles). The slope of these plots is indicative of how cells perform as coincidence detectors, being directly proportional to the coincidence detection index. Consistently, the coincidence detection index in control conditions ranges between  $\sim 0$  and 31 spikes confirming that coincidence detection in terms of its gain is highly heterogeneous across the population of MesV neurons (Fig. 1D).

*Coincidence detection gain critically depends on the intrinsic excitability of coupled neurons.* As shown, coincidence detection between MesV neurons depends on electrical cou-

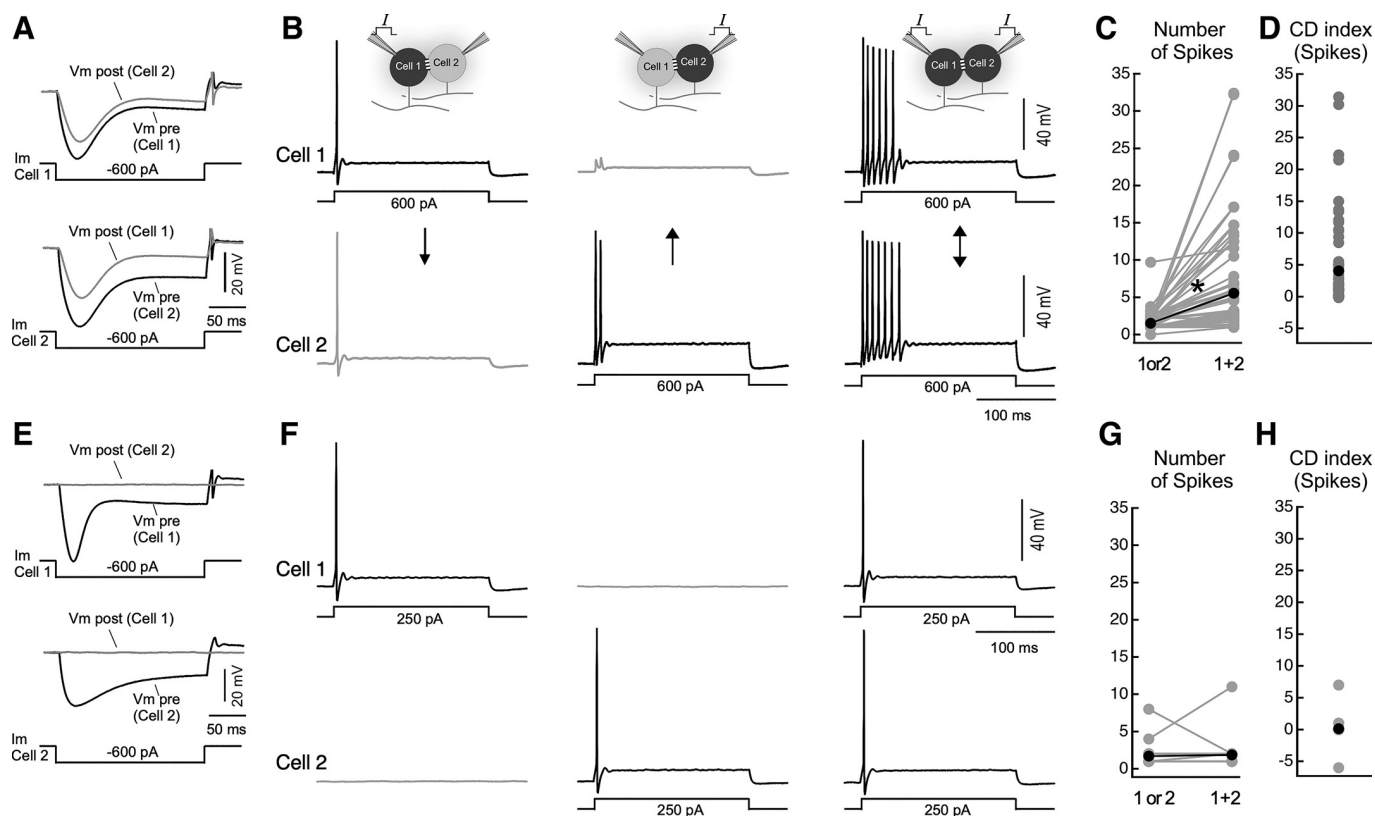


Fig. 1. Electrical coupling between mesencephalic trigeminal (MesV) neurons supports coincidence detection. **A**: simultaneous membrane voltage ( $V_m$ ) responses to hyperpolarizing current ( $I_m$ ) pulses injected either in *cell 1* (top) or in *cell 2* (bottom) of a pair of adjacent coupled neurons. **B**: in the same pair of neurons, injection of a depolarizing current pulse in *cell 1* (left) or *cell 2* (middle) induced a brief response consisting of 1 or 2 spikes at the beginning of the current step, with their corresponding coupling potentials (spikelet) in the coupled cell. Simultaneous activation of these 2 neurons with the current pulses of the same magnitude (right) evoked instead a repetitive discharge at each cell, consisting of 6–7 spikes. Schemes above each set of traces indicate the stimulation protocol. **C**: plot of the number of spikes when cells were independently activated (1 or 2) and when simultaneously activated (1 + 2) for the sample of recorded coupled neurons. Values represented by gray circles correspond to the average number of spikes evoked by 20 consecutive identical current pulses to each recorded cell belonging to a coupled pair. Superimposed are illustrated the average values (black circles) for the population of recorded neurons ( $P = 1 \times 10^{-4}$ ;  $n = 76$  from 38 pairs recorded in 32 animals, paired, two-tailed  $t$ -test). \*Significant difference,  $P < 0.05$ . **D**: plot of the coincidence detection (CD) index calculated as the mean difference of the number of spikes when cells are simultaneously activated (1 + 2) minus when independently activated (1 or 2) for the same sample illustrated in **C**. Individual values (gray circles) and the average value for the whole sample (black circle) are superimposed. **E**: simultaneous membrane voltage responses to hyperpolarizing current pulses injected either in *cell 1* (top) or in *cell 2* (bottom) of a pair of adjacent uncoupled neurons. **F**: in the pair of neurons depicted in **E**, membrane voltage responses of both cells when depolarizing current pulses were injected in *cell 1* or in *cell 2* (left and middle, respectively) and when current pulses were simultaneously injected to both cells (right). **G**: plot of the number of spikes when cells were independently activated (1 or 2) and when simultaneously activated (1 + 2) for the sample of recorded uncoupled neurons. Values from individual cells (gray circles) and average values (black circles) for the population of recorded neurons ( $P = 0.76$ ;  $n = 20$ , from 10 pairs, 8 animals, paired, two-tailed  $t$ -test) are illustrated superimposed. **H**: plot of the CD index for the same sample illustrated in **G**.

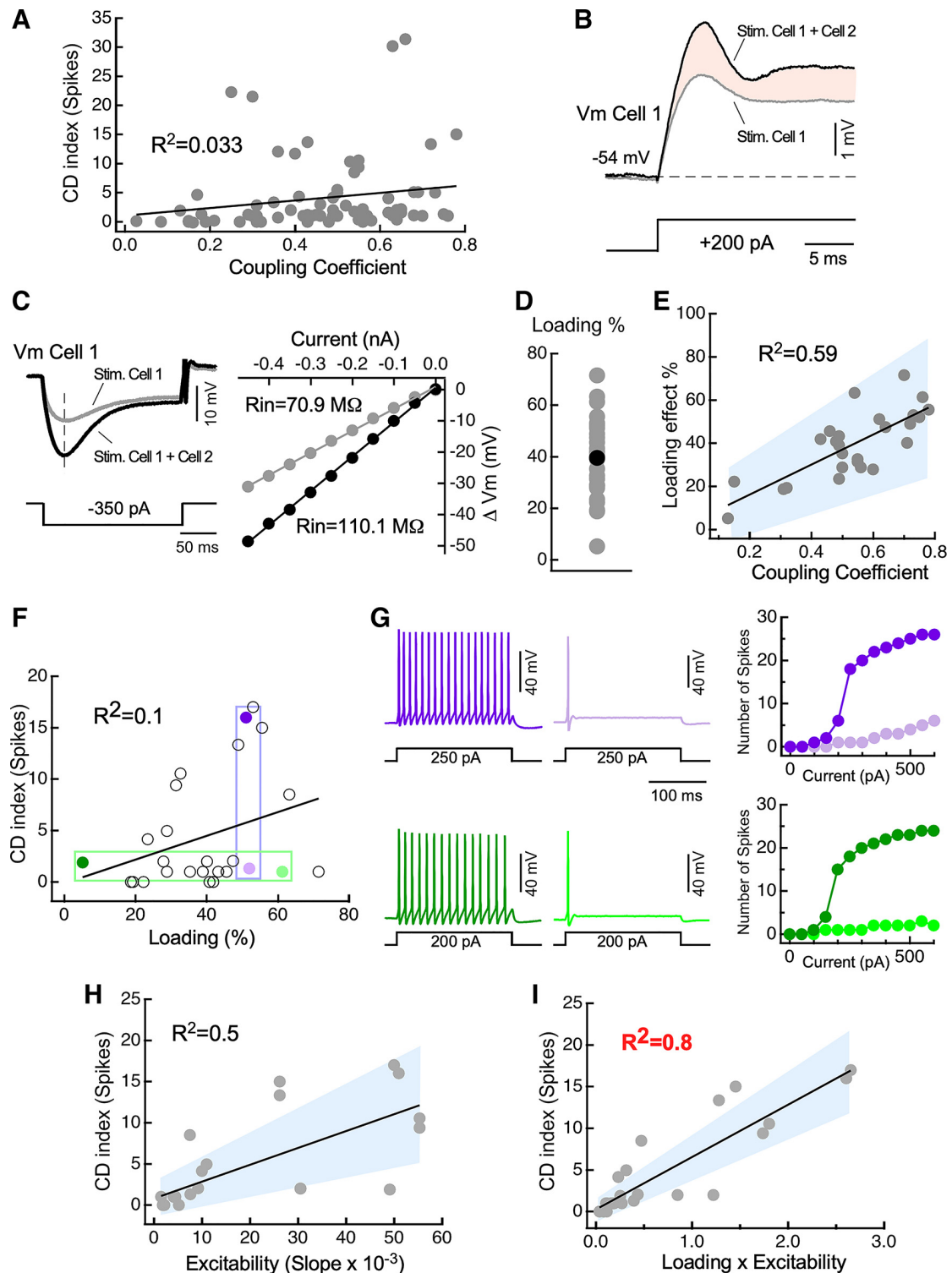
pling, raising the possibility that the heterogeneity of this network operation results from the diversity of coupling strengths in our sample of recorded pairs. However, surprisingly, the coincidence detection index and the CC in the forward direction (from the cell under consideration to its coupled partner) did not show any correlation as indicated by linear regression analysis [slope =  $6.50 \pm 8.13$  (95% CI),  $R^2 = 0.033$ ,  $P = 0.12$ ; Fig. 2A]. This analysis using CC in the opposite direction would yield similar results as electrical transmission between MesV neurons is highly bidirectional (Curti et al. 2012). To gain direct insights into the determinants of such heterogeneity, we focused on the study of the loading effect. In fact, the contrast in firing between individual and simultaneous depolarizations, corresponding to the gain of coincidence detection, is caused by larger depolarizations of the membrane potential, due to the cancelation of the loading effect during simultaneous inputs in comparison to when inputs arrive independently (Fig. 2B). We estimated the loading effect

(the impact on input resistance due to coupled cells) in a subset of neurons as we did previously (Curti et al. 2012). The input resistance ( $R_{in}$ ) of cells belonging to coupled pairs was measured by applying hyperpolarizing current pulses, either individually to each cell or simultaneously to both cells (Fig. 2C, left). From these recordings, current-voltage curves were constructed and  $R_{in}$  values were estimated from the slope of linear regressions (Fig. 2C, right). Simultaneous pulse protocols yielded significantly higher  $R_{in}$  values than those obtained with individual stimulation, averaging  $118.3 \pm 6.84$  and  $86.6 \pm 5.88$  M $\Omega$  (SE), respectively ( $P = 9 \times 10^{-5}$ ;  $n = 26$ , paired, two-tailed  $t$ -test). From these values, the loading effect in each cell was quantified as the difference of  $R_{in}$  obtained with these two protocols, expressed as percentage of the  $R_{in}$  obtained with individual pulses (loaded condition). This value averaged  $39.6 \pm 3.06\%$  (SE) for the population of studied neurons ( $n = 26$  from 13 pairs; Fig. 2D), and individual values present a positive correlation with the



CC in the forward direction [slope of linear regression =  $69.3 \pm 24.2$  (95% CI),  $R^2 = 0.59$ ,  $P < 1 \times 10^{-5}$ ; Fig. 2E] consistent with our previous work (Curti et al. 2012). We reasoned that if the loading effect would be the only or main mechanism involved in coincidence detection, the susceptibility of coupled neurons to simultaneous inputs (measured as the coincidence detection index) should be proportional to the magnitude of the loading effect. Surprisingly, these two data

sets did not show any correlation [slope of linear regression =  $0.12 \pm 0.14$  (95% CI),  $R^2 = 0.1$ ,  $P = 0.107$ ; Fig. 2F]. In fact, neurons with comparable loading effect magnitude can perform quite different as coincidence detectors (Fig. 2F, purple circles) and conversely, neurons with dissimilar loading effect can perform similar in terms of coincidence detection gain (Fig. 2F, green circles). These results indicate that the gain of coincidence detection cannot be explained solely in



terms of the magnitude of the loading effect and suggest the involvement of other mechanisms. On the other hand, the loading effect not only depends on the coupling strength but also on the number of cells each neuron is connected to (Getting 1974). However, the MesV nucleus is organized almost exclusively in pairs of cells (pairs ~90%, triplets ~10%) (Curti et al. 2012), ruling out the possibility that the heterogeneity in coincidence detection resulted from differences in the size of networks of coupled neurons.

Because neuronal spiking represents the functional expression of coincidence detection, the intrinsic excitability of neurons may also play, along with the loading effect, a relevant role in determining the susceptibility of coupled neurons to coincident inputs. Coincidentally, MesV neuron excitability displays great variety even at comparable ages. Indeed, neuronal responses range from single spikes at the beginning of current pulses, regardless of the stimulation intensity, to strong repetitive discharges (see below), possibly contributing to the heterogeneity of coincidence detection gain. In fact, comparison of the cells indicated by purple circles in Fig. 2*F* (loading effect of similar magnitude, ~50%) reveals that the one presenting higher susceptibility to coincident inputs (coincidence detection index = 16 spikes, dark purple circle) is also the more excitable one as indicated by its firing properties (Fig. 2*G*, compare dark and light purple traces and curves in the *top*). On the other hand, the cells, indicated by green circles in Fig. 2*F*, are comparable in terms of their susceptibility to coincident inputs (coincidence detection index between 1 and 2 spikes), in spite of presenting quite dissimilar loading effect (5 vs. 61%). Strikingly, the neuron with the lower loading effect magnitude presents stronger spiking in comparison to the neuron with the higher loading (Fig. 2*G*, compare dark and light green traces and curves in the *bottom*). In this case, neuronal excitability seems able to compensate for differences in loading effect, suggesting a relevant role of firing properties. Consistently, neuronal excitability, quantified as the slope of curves of the number of spikes versus current (see MATERIALS AND METHODS), is positively correlated with the coincidence detection index [slope of linear regression =  $204.9 \pm 85.8$  (95% CI),  $R^2 = 0.5$ ,  $P = 5 \times 10^{-5}$ ; Fig. 2*H*]. Moreover, when the excitability

is weighted by the loading effect (calculated as the product of these 2 variables), the fit to a straight line improves considerably [slope of linear regression =  $6.29 \pm 1.34$  (95% CI),  $R^2 = 0.8$ ,  $P < 1 \times 10^{-5}$ ; Fig. 2*I*]. These results indicate that while electrical coupling is absolutely necessary for coincidence detection to occur, the intrinsic excitability of neurons critically contributes to set the gain of this relevant functional operation in networks of coupled neurons. Therefore, the heterogeneity of coincidence detection gain does not result solely from differences in coupling strengths but also from the diversity of the intrinsic excitability of coupled neurons.

**Regulation of the  $I_H$  as a way to modulate MesV neuron excitability.** Our results suggest that the firing properties of coupled neurons play a critical role in determining the gain of coincidence detection, raising the possibility that its heterogeneity resulted in part from the diverse regulatory states of intrinsic electrophysiological properties across the population of MesV neurons. Hence, modulations of firing properties are good candidates to mediate forms of plasticity that alter the way coupled neurons respond to coincident inputs. To test this, we sought to modulate the excitability of MesV neurons by way of upregulating the  $I_H$  through applications of cyclic nucleotides (Biel et al. 2009). The  $I_H$  is a widespread current in the mammalian brain, which operates in the subthreshold range of membrane potential and has been shown to be critically involved in repetitive discharges, rhythmic oscillatory activity, and integration of synaptic inputs (Pape 1996). On the other hand, the  $I_H$  is a common feature of many populations of electrically coupled neurons, like inferior olive neurons (Devor and Yarom 2002; Schweighofer et al. 1999), GABAergic neurons of thalamic reticular nucleus (Landisman et al. 2002; Rateau and Ropert 2006), pyramidal neurons from the hippocampus (Maccafferri et al. 1993; Mercer et al. 2006) and neocortex (Trenholm et al. 2013; Wang et al. 2010), Golgi cells of the cerebellar cortex (Dugué et al. 2009; Forti et al. 2006), bipolar cells of the retina (Müller et al. 2003; Veruki and Hartveit 2002b), and mitral cells of the olfactory bulb (Angelo and Margrie 2011; Schoppa and Westbrook 2002) among others. The coexistence of this conductance and electrical synapses raises the possibility of functional interaction between them as suggested by a theoretical study (Publio et al. 2009).

Fig. 2. Coincidence detection (CD) between pairs of electrically coupled mesencephalic trigeminal (MesV) neurons is heterogeneous. *A*: plot of CD index against the coupling coefficient for the whole sample of recorded coupled MesV neurons ( $n = 76$  from 38 pairs recorded in 32 animals). Slope of linear regression =  $6.5 \pm 8.13$  [95% confidence interval (CI)] represented by the continuous line;  $R^2 = 0.033$ ,  $P = 0.12$ . *B*: superimposed are representative traces showing membrane voltage ( $V_m$ ) responses when subthreshold current pulses were injected only into the recorded neuron (*stim. cell 1*, gray trace) or simultaneously to both coupled neurons (*stim. cells 1 + 2*, black trace). Solid pink area represents the difference between these 2 stimulation protocols, corresponding to the increase in membrane responses due to the cancellation of the loading effect during coincident depolarizations. *C*, *left*: estimation of the loading effect in coupled cells by injecting hyperpolarizing current pulses, either individually to each cell (*stim. cell 1*, gray trace) or simultaneously to both cells (*stim. cell 1 + cell 2*, black trace). *C*, *right*: from these recordings, change in membrane voltage versus current relationships were constructed for both individual (gray circles) and simultaneous (black circles) stimulation protocols. Membrane voltage changes were measured at the time indicated by the vertical dashed line at *left*. Continuous lines represent best fit to straight-line functions and slopes, corresponding to input resistance ( $R_{in}$ ) values, are indicated. *D*: plot of the loading effect values (see text) measured in 26 coupled neurons. Superimposed to values from individual cells (gray circles) is the average value (black circle). *E*: plot of the loading effect against the coupling coefficient in the same neuronal population depicted in *D*. Slope of linear regression =  $69.3 \pm 24.2$  (95% CI), represented by the continuous line;  $R^2 = 0.59$ ,  $P < 1 \times 10^{-5}$ ,  $n = 26$ . *F*: plot of the CD index as a function of the loading effect. Slope of linear regression =  $0.12 \pm 0.14$  (95% CI), represented by the continuous line;  $R^2 = 0.1$ ,  $P = 0.107$ ,  $n = 26$ . Representative cells displaying nearly the same loading effect magnitude (purple tones) and coincidence detection index (green tones) are boxed. *G*, *left*: traces of voltage membrane responses to depolarizing current pulses (250 pA) of the neurons indicated in *F* with purple tones (similar loading effect, above) and with green tones (similar CD index, below). *G*, *right*: plots of the number of spikes evoked by current pulses of 200 ms in duration as a function of the current intensity for the cells shown at *left*. The same color code (purple/green, dark/light) applies in *F* and *G* for the identification of corresponding neurons. *H*: plot of the CD index against neuronal excitability (quantified as the slope of spikes vs. current curves). Slope of linear regression =  $204.93 \pm 85.8$  (95% CI), represented by the continuous line;  $R^2 = 0.5$ ,  $P = 5 \times 10^{-5}$ ,  $n = 26$ . *I*: plot of the CD index (ordinates) against the product of the loading effect magnitude times the slope of spikes versus current curves (loading  $\times$  excitability, abscissa). Slope of linear regression =  $6.2863 \pm 1.34$  (95% CI), represented by the continuous line;  $R^2 = 0.8$ ,  $P < 1 \times 10^{-5}$ ,  $n = 26$ . In *E*, *H*, and *I*, the solid blue area represents the 95% confidence interval. Plots in *D*, *E*, *F*, *H*, and *I* show results obtained in the same neuronal population ( $n = 26$ , from 13 pairs recorded in 10 animals).

MesV neurons also express a prominent  $I_H$  (Khakh and Henderson 1998) that contributes to stabilize the resting membrane potential and control cell excitability (Tanaka et al. 2003). Moreover, the channel-forming subunits HCN1 and HCN2 have been detected and present a somatic distribution in this neuronal population (Kang et al. 2004; Notomi and Shigemoto 2004). Consistent with that, voltage responses more negative than  $-70$  mV are dominated by a prominent sag (Fig. 3A), which are almost

completely abolished after the addition of CsCl (2 mM) to the extracellular solution (Fig. 3B). On the other hand, an important characteristic of  $I_H$  is its ability to be regulated by cyclic nucleotides like cAMP and cGMP with relevant consequences on the electrophysiological properties of neurons (Biel et al. 2009; Lüthi and McCormick 1998; Pape 1996), thus representing a potentially valuable tool to manipulate the intrinsic excitability of MesV neurons.

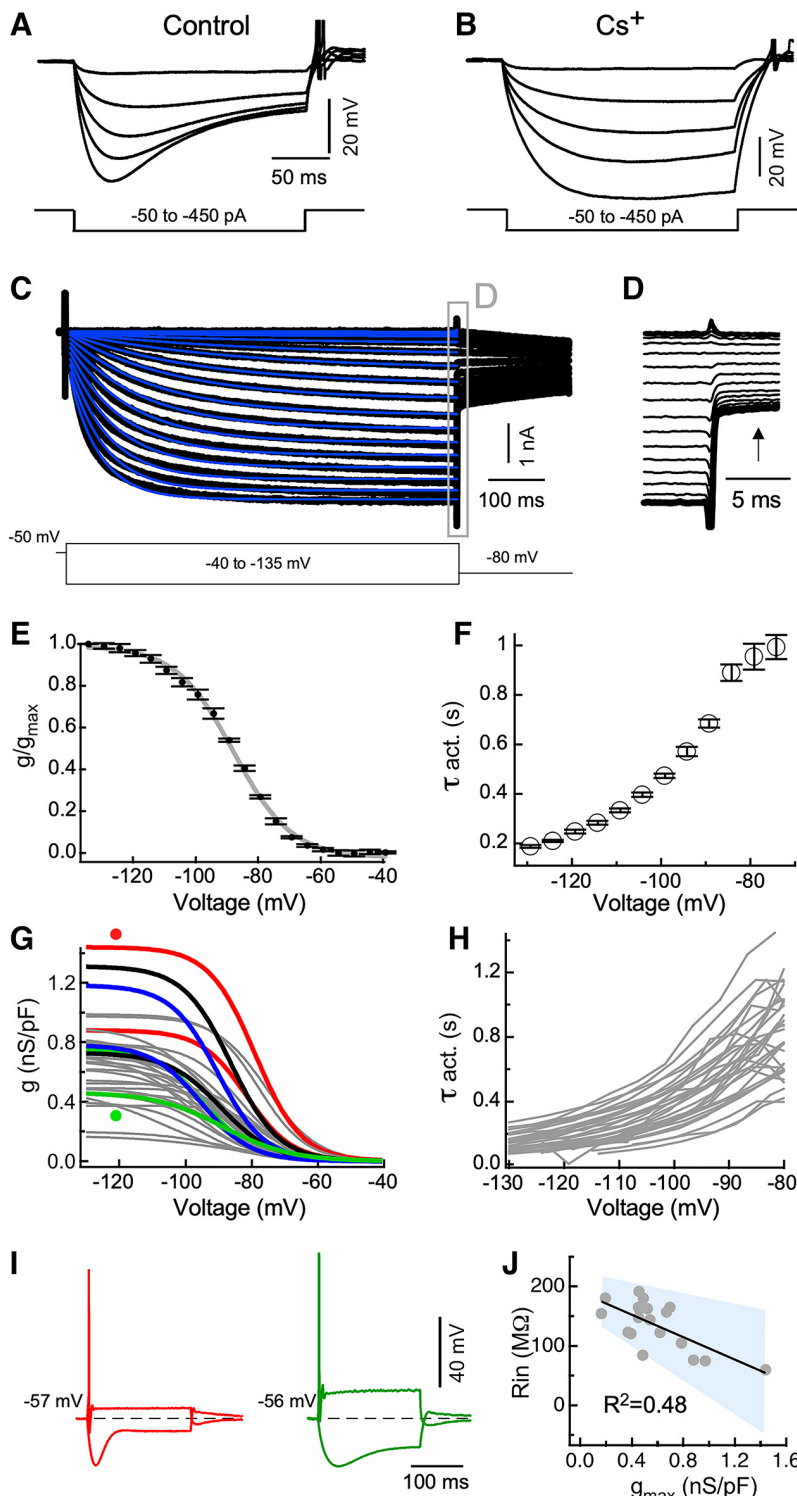


Fig. 3. Characterization of hyperpolarization-activated cationic current ( $I_H$ ) of mesencephalic trigeminal (MesV) neurons. **A:** representative traces of membrane voltage responses of a MesV neuron in control conditions to a series of hyperpolarizing current pulses of different intensities from  $-50$  to  $-450$  pA in steps of  $100$  pA; **B:** same cell and current injecting protocol as in **A** after the addition of  $2$  mM CsCl to the bath. **C:** sample traces of the  $I_H$  evoked with a series of voltage steps from  $-135$  to  $-40$  mV, in  $5$ -mV increments, from a holding potential of  $-50$  mV, and followed by a test pulse to  $-80$  mV. Each trace represents the subtraction of total membrane currents obtained in the presence of Cs<sup>+</sup> from those obtained in control conditions. A scheme of the voltage-clamp protocol is at *bottom*. **D:** the boxed area in **C** is illustrated at an expanded temporal scale. **E:**  $I_H$  steady-state activation curve of the cell depicted in **C** and **D**, obtained by plotting the normalized conductance against the voltage pulse commands. Conductance values ( $g$ ) were determined from tail currents measured at the time indicated by the upward arrow in **D**. Each value represents the average of 4 single values obtained in the same cell and error bars represent SD. Experimental data were fit to a Boltzmann function (gray trace). **F:** plot of the  $I_H$  activation time constant ( $\tau_{act}$ ) of the cell shown in **C** against the voltage pulse commands. The activation kinetics was determined by fitting exponential functions to the activation phase of current traces evoked by different voltage commands (superimposed blue traces in **C**). Each value represents the average of 4 single values obtained in the same cell, and error bars represent SD. **G:** plot of Boltzmann function fits to  $I_H$  steady-state activation curves of the whole sample of recorded neurons ( $n = 33$  recorded in 17 animals). Note that conductance values were normalized to the cell's capacitance for comparing neurons of different sizes. Curves from 4 animals are colored (red, green, blue, and black) to illustrate that variety of  $I_H$  expression results from both inter- and intraindividual diversity. **H:** plot of activation time constant against voltage pulse commands of the same neurons depicted in **G**. **I:** membrane voltage responses to depolarizing and hyperpolarizing current pulses of cells identified by filled circles of the same color in **G**. **J:** plot of the input resistance ( $R_{in}$ ) against the  $I_H$  maximum density in a sample of 19 uncoupled MesV neurons recorded in 10 animals. Slope of linear regression =  $-94.5 \pm 50.4$  (95% CI), represented by the continuous line;  $R^2 = 0.48$ ,  $P = 0.001$ . The solid blue area represents the 95% confidence interval.



We started by characterizing the  $I_H$  of MesV neurons in control conditions by applying standard protocols in voltage clamp (see MATERIALS AND METHODS). Figure 3C shows representative results from one neuron, in which  $I_H$  was recorded in voltage clamp, during protocols consisting in a series of voltage steps from  $-40$  to  $-135$  mV starting from a holding potential of  $-50$  mV and returning to a potential of  $-80$  mV. Stepping negative to  $-70$  mV elicited an inward current with slow activation kinetics and no signs of inactivation within this time window that also deactivates with a slow time course. Figure 3E depicts the activation curve obtained from these recordings. This curve was constructed by measuring tail currents at the time indicated by the upward arrow in Fig. 3D at a constant membrane voltage of  $-80$  mV. Superimposed are the conductance values normalized to its maximum (black circles) and the fit to a Boltzmann function (gray trace) (Fig. 3E). For the whole population of recorded neurons ( $n = 34$ ), fits of the Boltzmann relation to activation curves showed that the  $V_{1/2}$  averaged  $-88.5 \pm 1.17$  mV (SE), with a slope factor of  $8.4 \pm 0.29$  mV (SE). Maximal conductance averaged  $30.9 \pm 2.8$  nS (SE) and when normalized to the cell's capacitance averaged  $0.68 \pm 0.05$  nS/pF (SE). Activation kinetics of the  $I_H$  was determined from the fits of single exponential functions to current traces (superimposed blue traces on Fig. 3C). Plots of the activation time constant as a function of the voltage step showed the typical behavior characterized by a progressive lowering of the time constant (faster activation) with increasing hyperpolarized voltage steps (Fig. 3F). Maximal time constant averaged  $938.7 \pm 52.8$  ms (SE) and occurred at voltage steps ranging from  $-68$  to  $-88.4$  mV (average  $-78.8$  mV). Interestingly, steady-state activation characteristics and activation kinetics showed considerable variety across the population of recorded neurons. Figure 3G shows superimposed results of fits to activation curves for the whole sample of recorded neurons ( $n = 34$ ), where maximal conductance ranged almost over an order of magnitude (from  $0.17$  to  $1.44$  nS/pF) whereas the  $V_{1/2}$  did so over more than  $30$  mV (from  $-74.9$  to  $-106.5$  mV). Note that as conductance is normalized by the cell's capacitance, the diversity in maximal conductance values does not result from differences in the cell sizes of our sample. Interestingly, this diversity is the outcome of both interindividual and intraindividual differences, as can be appreciated in Fig. 3G where curves from four animals are indicated in colors (red, green, blue, and black). To support this conclusion, we computed the difference in maximal conductance between 15 pairs of cells recorded from 15 animals and compared it to the difference between pairs obtained by combining cells from different animals ( $n = 210$ ). These values, indicative of  $I_H$  diversity, were similar and showed no statistical difference. In fact, intraindividual difference averaged  $0.22 \pm 0.045$  nS/pF (SE) ( $n = 15$ ), whereas interindividual difference averaged  $0.31 \pm 0.018$  nS/pF (SE) ( $n = 210$ ) ( $P = 0.058$ , unpaired, two-tailed  $t$ -test).

On the other hand, as expected, neurons presenting high  $I_H$  density display large amplitude sag potentials (activation curves from cells depicted in Fig. 3I are identified in Fig. 3G with circles of the same color). Also,  $I_H$  density presents a negative correlation with the  $R_{in}$  value [slope of linear regression =  $-94.5 \pm 50.4$  (95% CI,  $P = 0.001$ ),  $R^2 = 0.48$ ; Fig. 3J], suggesting the involvement of this conductance in the determination of MesV neuron passive properties.

Additionally, activation kinetics also showed considerable variety, as can be appreciated in Fig. 3H where curves of the time constant as a function of the voltage step for all recorded cells are shown superimposed. In fact, the maximal time constant ranged from  $401$  to  $1,657$  ms. These results indicate that  $I_H$  presents a great diversity of functional states across the population of MesV neurons, suggesting that this conductance is under regulatory control, which in turn could contribute to the diversity of intrinsic excitability displayed by this population.

We next explored if the  $I_H$  of MesV neurons is susceptible of modulation by cGMP applying its membrane permeable analogue 8-bromoguanosine cyclic 3',5'-monophosphate sodium salt ( $0.5$ – $1$  mM, herein referred simply as cGMP; Fig. 4). Of the two most common cyclic nucleotides, cAMP and cGMP, the latter was chosen in an attempt to selectively modulate  $I_H$  (see later), as in MesV neuron activation of the cAMP/protein kinase A signaling pathway participates in the regulation of the persistent sodium current (Tanaka and Chandler 2006). As expected, cGMP applications resulted in a shift of the  $V_{1/2}$  toward positive values, as well as an increase of the  $I_H$  magnitude (Fig. 4, A and B) and acceleration of activation kinetics (Fig. 4C). For the sample of recorded cells ( $n = 13$ ), the  $V_{1/2}$  changed from  $-89.8 \pm 1.4$  mV (SE) in control conditions to  $-82.9 \pm 20.8$  mV (SE) after cGMP ( $P = 0.0015$ ; paired, two-tailed  $t$ -test; Fig. 4D), whereas the slope factor increased from  $8.2 \pm 0.2$  mV (SE) in control to  $10.4 \pm 0.74$  mV (SE) after cGMP ( $P = 0.0061$ ; paired, two-tailed  $t$ -test; Fig. 4E) and the maximal conductance showed an increase from  $0.68 \pm 0.05$  nS/pF (SE) in control to  $0.81 \pm 0.06$  nS/pF (SE) after cGMP ( $P = 0.0049$ ; paired, two-tailed; Fig. 4F). Remarkably, the combined effect of cGMP on  $V_{1/2}$ , slope and maximal conductance resulted in an almost threefold increase in the  $I_H$  conductance at  $-70$  mV, a membrane voltage level close to the postspike afterhyperpolarization. In fact,  $I_H$  conductance at  $-70$  mV increased from  $0.07 \pm 0.017$  nS/pF (SE) in control to  $0.2 \pm 0.043$  nS/pF (SE) after cGMP ( $P = 0.0066$ ; paired, two-tailed  $t$ -test). On the other hand,  $I_H$  activation kinetics becomes faster after cGMP for almost the whole range of voltage steps (Fig. 4C) as indicated by the significant reduction of the maximal time constant, which varied from  $814.1 \pm 86.6$  ms (SE) in control to  $623.7 \pm 59.9$  ms (SE) after cGMP ( $P = 0.0015$ ; paired, two-tailed  $t$ -test; Fig. 4G). Interestingly, this change in activation kinetics favors the involvement of the  $I_H$  during the time course of the interspike interval. These results show that the  $I_H$  of MesV neurons is strongly modulated by cGMP.

*Upregulation of the  $I_H$  increases MesV neuron excitability.* Next, we studied the impact of  $I_H$  upregulation on MesV neuron excitability. For this, the effects of cGMP applications on the electrophysiological properties of these neurons were characterized by applying protocols of depolarizing current pulses whose intensity were adjusted to evoke one to three spikes (Fig. 5A, left). As illustrated in Fig. 5A, right, after inclusion of cGMP in the bath, there was an increase in the number of spikes evoked by current pulses in comparison to control conditions, and this effect was accompanied by a depolarizing shift of the resting membrane potential. These effects can be better appreciated in Fig. 5B, in which the number of spikes during current pulses repeated every  $10$  s and the resting membrane potential were plotted as a function of

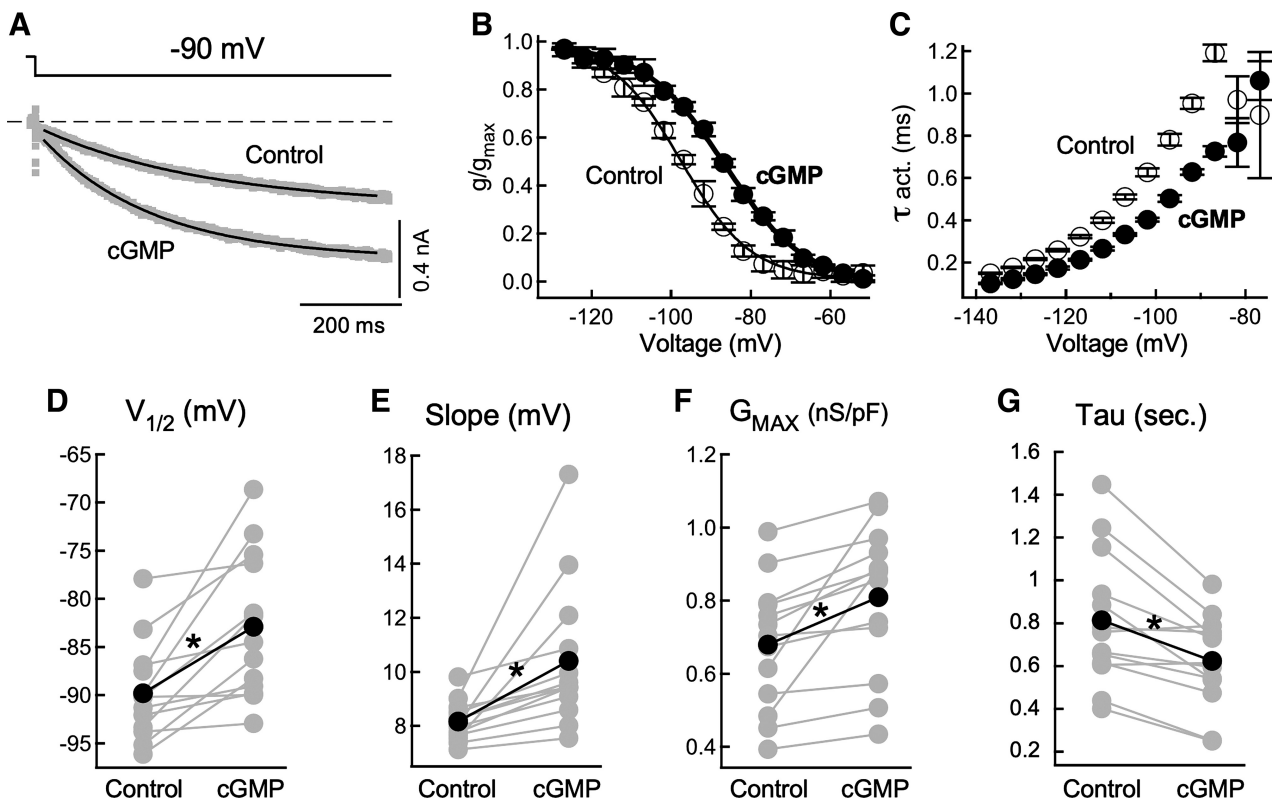


Fig. 4. Hyperpolarization-activated cationic current ( $I_H$ ) of mesencephalic trigeminal (MesV) neurons is strongly modulated by cGMP. **A**: sample current traces evoked with voltage steps from  $-50$  mV to  $-90$  mV in control conditions (gray trace, control) and after cGMP (gray trace, cGMP). Superimposed are fits to exponential functions (black traces). **B**:  $I_H$  steady-state activation curve of the cell shown in **A** before (white circles, control) and after cGMP (black circles, cGMP). Each curve was fitted with Boltzmann functions, and results are shown superimposed (continuous traces). Each value represents the average of 4 (control) or 3 (cGMP) single values obtained in the same cell and error bars represent SD;  $g$ , conductance. **C**: plot of the  $I_H$  activation time constant of the cell shown in **A** against the voltage pulse commands before (white circles, control) and after cGMP (black circles, cGMP). **D**: plot of the half activation voltage ( $V_{1/2}$ ) values of the Boltzmann function before (gray circles) and after cGMP (gray circles) for the whole population of recorded MesV neurons, ( $P = 0.0015$ ; paired, two-tailed  $t$ -test,  $n = 13$ ). **E**: plot of the slope values of the Boltzmann function at  $V_{1/2}$  before (gray circles) and after cGMP (gray circles) for the whole population of recorded MesV neurons, ( $P = 0.0061$ ; paired, two-tailed  $t$ -test,  $n = 13$ ). **F**: plot of the maximal conductance values normalized to the cell's capacitance before (gray circles) and after cGMP (gray circles) for the whole population of recorded MesV neurons, ( $P = 0.0049$ ; paired, two-tailed,  $n = 13$ ). **G**: plot of the maximum activation time constant (determined from current traces evoked by voltage steps of  $-70$  to  $-90$  mV) before (gray circles) and after cGMP (gray circles) for the whole population of recorded MesV neurons, ( $P = 0.0015$ ; paired, two-tailed  $t$ -test,  $n = 13$ ). Plots in **D**, **E**, **F**, and **G** show results obtained in the same neuronal population ( $n = 13$ , recorded in 7 animals). Superimposed to the individual values are the corresponding average values in control (black circle) and after cGMP (black circle). \*Significant difference,  $P < 0.05$ .

time before, during, and after bath application of cGMP (1 mM). Most typically, the maximum effects on firing and resting potential were attained between 15 and 20 min after initiation of perfusion and were long lasting as reversion was rarely observed, consistently with findings by others (Ingram and Williams 1996). A detailed characterization of cGMP effects on firing was performed by using experimental protocols consisting on a series of depolarizing current pulses of increasing intensity (50 to 600 pA; Fig. 5C). From these experiments, plots of the number of spikes as a function of injected current were constructed (Fig. 5D). These plots show a dramatic increase of firing particularly for current pulses of twice the threshold intensity and above. The average behavior of our sample can be seen in Fig. 5E, in which the mean number of spikes was plotted as a function of current pulse intensity before (control) and after cGMP application. This graph shows that cGMP induces a statistically significant increase ( $P < 0.01$ ) in the number of spikes for most of the current pulses tested, indicating a dramatic increase in MesV neurons excitability and hence in the way this neuronal population encode depolarizing inputs. Consistently, the threshold

current for spike activation was reduced from  $171.1 \pm 19.6$  pA (SE) in control conditions to  $147.4 \pm 15.2$  pA (SE) after cGMP ( $P = 0.016$ ,  $n = 19$ , paired, two-tailed  $t$ -test).

The number of spikes per current pulses of three- to sixfold its threshold intensity (determined in control conditions) showed an increase from  $2.9 \pm 0.68$  (SE) in control to  $8.7 \pm 1.55$  (SE) after cGMP, and this difference was statistically significant ( $P = 5.9 \times 10^{-5}$ ;  $n = 30$ , paired, two-tailed  $t$ -test). Additionally, the resting membrane potential varied from  $-59.3 \pm 0.88$  mV (SE) in control to  $-54.5 \pm 0.73$  mV (SE) after cGMP ( $P = 2.3 \times 10^{-9}$ ;  $n = 30$ , paired, two-tailed  $t$ -test; Fig. 5F). These effects did not show any significant difference in coupled versus uncoupled cells. The average number of spikes evoked by current pulses after cGMP increased  $4.8 \pm 1.55$  (SE) in coupled cells ( $n = 19$ ) and  $7.7 \pm 2.09$  (SE) in uncoupled cells ( $n = 11$ ) ( $P = 0.27$ ; unpaired, two-tailed  $t$ -test), whereas the resting membrane potential depolarized in average  $4.8 \pm 0.75$  mV (SE) and  $4.7 \pm 0.87$  mV (SE) in coupled ( $n = 19$ ) and in uncoupled cells ( $n = 11$ ), respectively ( $P = 0.95$ ; unpaired, two-tailed  $t$ -test).



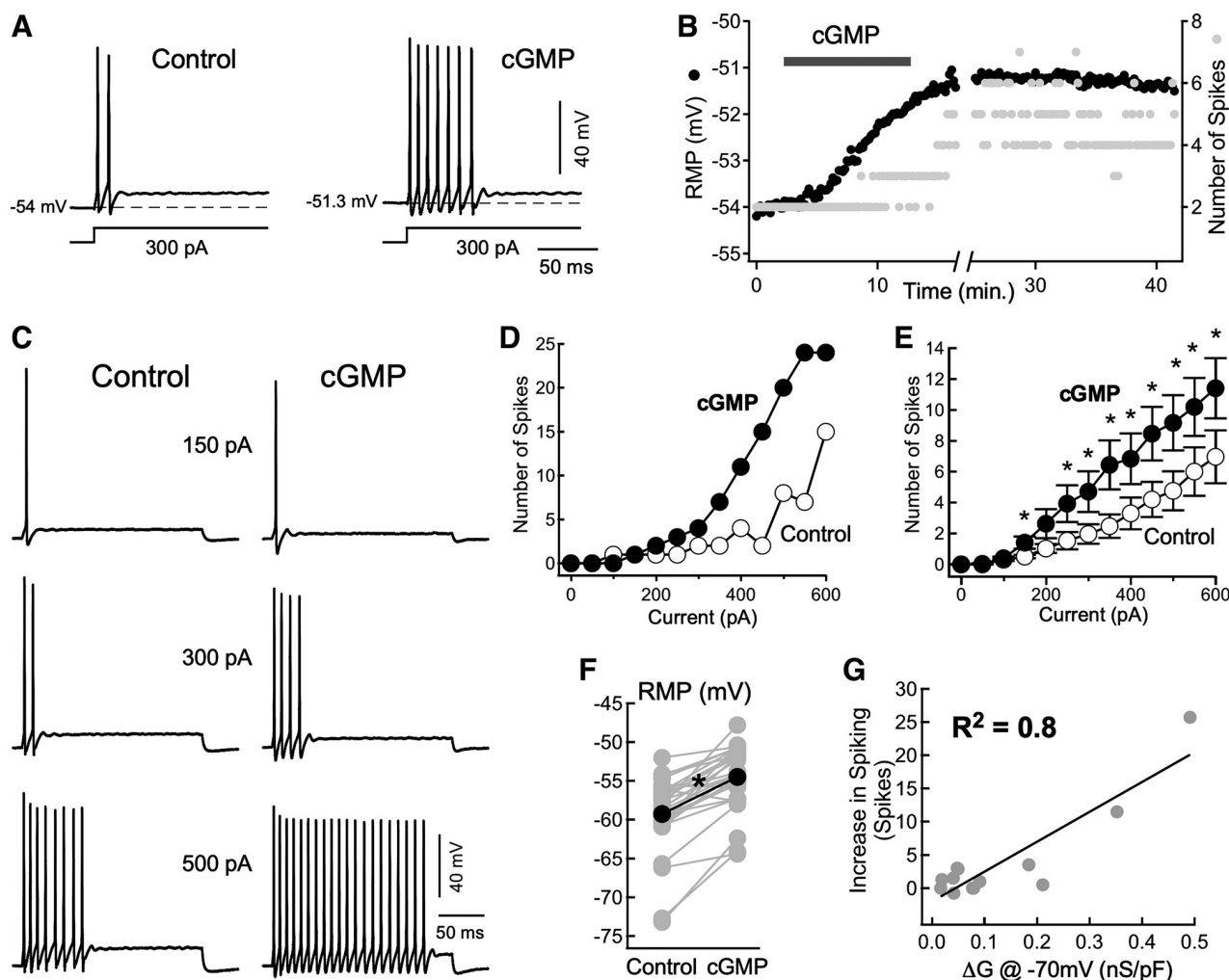


Fig. 5. cGMP modulates the firing properties and resting potential of mesencephalic trigeminal (MesV) neurons. **A**: repetitive discharge of a MesV neuron induced by a depolarizing current pulse (300 pA) in control (left) and after cGMP (1 mM) (right). **B**: plot of the resting membrane potential (RMP; left ordinates, black circles) and number of spikes (right ordinates, gray circles) of a MesV neuron evoked by depolarizing current pulses of 300 pA as a function of time before, during and after cGMP (1 mM) application to the bath. Application of cGMP is indicated by the black horizontal bar. **C**: responses of a MesV neuron to intracellular depolarizing current pulses of increasing magnitude in control (left) and after cGMP (right); 150 pA was the threshold intensity in control conditions. **D**: plot of the number of spikes evoked by current pulses of 200 ms in duration as a function of the current intensity in control (white circles) and after cGMP (black circles) for the same neuron as in **C**. **E**: plot of the mean number of spikes evoked by 200 ms current pulses as a function of the current intensity for the population of recorded cells before (white circles) and after cGMP (black circles). Error bars represent SE. \*Statistically significant difference between the 2 data sets,  $P < 0.05$  [ $P = 0.3256$  (50 pA),  $P = 0.0831$  (100 pA),  $P = 0.0264$  (150 pA),  $P = 0.0567$  (200 pA),  $P = 0.0227$  (250 pA),  $P = 0.0186$  (300 pA),  $P = 0.0032$  (350 pA),  $P = 0.0024$  (400 pA),  $P = 0.0008$  (450 pA),  $P = 0.0007$  (500 pA),  $P = 0.0059$  (550 pA),  $P = 0.0012$  (600 pA); paired, two-tailed  $t$ -test,  $n = 30$  from 15 animals]. **F**: plot of the resting membrane potential values before (gray circles, control) and after cGMP (gray circles, cGMP), superimposed to the individual values are the corresponding average values in control (black circle) and after cGMP (black circle), ( $P = 2.35 \times 10^{-9}$ ; paired, two-tailed  $t$ -test,  $n = 30$  from 15 animals). \*Significant difference,  $P < 0.05$ . **G**: plot of the increase in the number of spikes evoked by current pulses against the increase in the hyperpolarization-activated cationic current ( $I_H$ ) conductance at  $-70$  mV after cGMP in comparison to control conditions. Data were fitted with a straight-line function and the  $R$ -squared value is indicated. Slope of linear regression =  $45.1 \pm 14.9$  (95% confidence interval) represented by the continuous line;  $R^2 = 0.8$ ,  $P = 3.5 \times 10^{-5}$  ( $n = 13$  from 7 animals).

Furthermore, the cGMP effects on firing were accompanied by a reduction of  $R_{in}$  of  $\sim 15\%$ , from  $108.6 \pm 6.51$  M $\Omega$  (SE) in control to  $91.8 \pm 5.83$  M $\Omega$  (SE) after cGMP ( $P = 1.03 \times 10^{-10}$ ;  $n = 30$ , paired, two-tailed  $t$ -test; Fig. 6, A–C), most probably as an outcome of the greater open probability of HCN channels at resting potential. Also consistent with the upregulation of the  $I_H$ , the rate of rise of pacemaker potentials during repetitive discharges showed a moderate but significant increase after cGMP (Fig. 6D). The slope of this potential, determined from fits to linear regressions, averaged  $2.28 \pm 0.18$  mV/ms (SE) in control and  $2.92 \pm 0.27$  mV/ms (SE) after cGMP ( $P = 3.5 \times 10^{-5}$ ;  $n = 18$ , paired, two-tailed  $t$ -test; Fig. 6E, left).

The acceleration of the pacemaker potential is translated in corresponding increase of the instantaneous frequency of the first interspike interval, which averaged  $105.1 \pm 5.84$  Hz (SE) in control and  $122.5 \pm 7.63$  Hz (SE) after cGMP ( $P = 2.45 \times 10^{-6}$ ;  $n = 18$ , paired, two-tailed  $t$ -test; Fig. 6E, right). The increase of instantaneous frequency and of the pacemaker potential slope showed a positive correlation [slope of linear regression =  $19.2 \pm 6.67$  (95% CI),  $R^2 = 0.7$ ,  $P = 1.5 \times 10^{-5}$ ; Fig. 6F]. Results depicted in Figs. 5 and 6 show that cGMP induces modulatory changes of MesV neuron electrophysiological properties in a highly consistent fashion, most probably through upregulation of the  $I_H$ . Supporting this no-

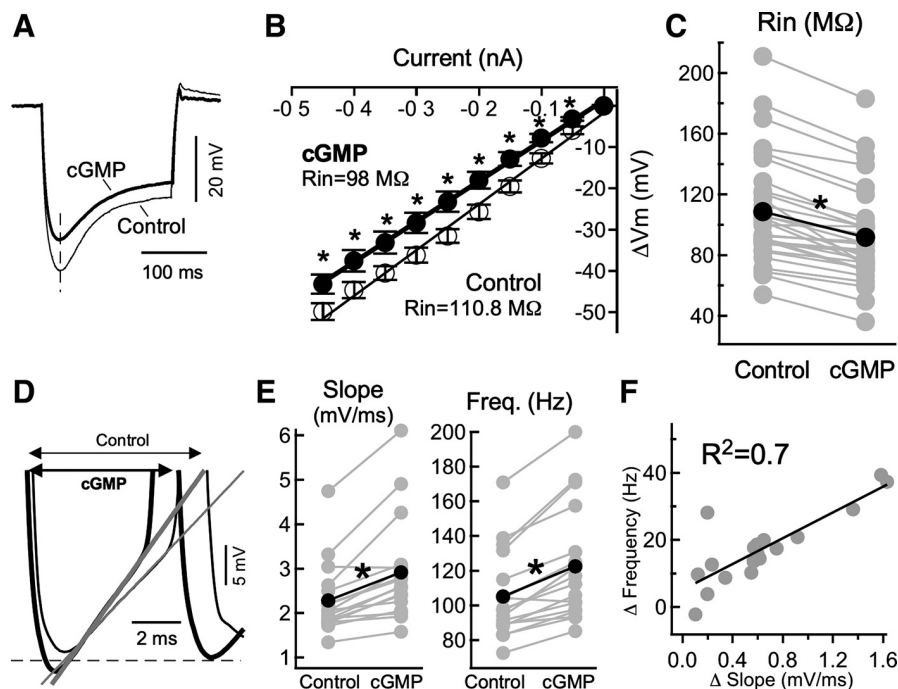


Fig. 6. cGMP effects on input resistance and subthreshold potential of mesencephalic trigeminal (MesV) neurons. **A**: voltage membrane responses of a MesV neuron to hyperpolarizing current pulses of  $-450$  pA (control, thin trace) and after application of cGMP (thick trace). **B**: membrane voltage change versus injected current relationships obtained in the same MesV neuron as in **A** before (white circles) and after cGMP (black circles). Membrane voltage changes were measured at the time indicated by the vertical dashed line in **A**. Each value corresponds to the mean of 4 to 6 individual values, error bars indicate SD. \*Statistically significant difference,  $P < 0.05$  [ $P = 0.3122$  (0 pA),  $P = 2 \times 10^{-4}$  ( $-50$  pA),  $P = 1 \times 10^{-4}$  ( $-100$  pA),  $P = 2 \times 10^{-4}$  ( $-150$  pA),  $P = 2 \times 10^{-4}$  ( $-200$  pA),  $P = 4 \times 10^{-4}$  ( $-250$  pA),  $P = 7 \times 10^{-4}$  ( $-300$  pA),  $P = 0.0013$  ( $-350$  pA),  $P = 0.0018$  ( $-400$  pA),  $P = 0.0017$  ( $-450$  pA); unpaired, two-tailed  $t$ -test] between the 2 data sets. Each curve was fitted with a straight-line function and the slope values representing the corresponding input resistance are indicated. **C**: plot of the input resistance ( $R_{in}$ ) values before (gray circles, Control) and after cGMP (gray circles, cGMP) ( $P = 1 \times 10^{-4}$ ; paired, two-tailed  $t$ -test). Superimposed to the values from individual cells ( $n = 30$  from 15 animals) are the corresponding average values in control (black circle) and after cGMP (black circle). \*Significant difference,  $P < 0.05$ . **D**: superimposed traces showing the membrane potential trajectory between the first 2 successive spikes of repetitive discharges evoked by depolarizing current pulses before (thin trace) and after cGMP (thick trace). Oblique straight lines indicate the slope of the pacemaker potentials for each trace. Spikes are truncated. **E**: plots showing the values of the pacemaker potential slope preceding the second spike of repetitive discharges (left) and instantaneous frequency (right) of the first interspike interval before (gray circles, Control) and after cGMP (gray circles, cGMP) (slope:  $P = 3.5 \times 10^{-5}$ , frequency:  $P = 2.45 \times 10^{-6}$ ;  $n = 18$  from 11 animals, paired, two-tailed  $t$ -test). Superimposed to the values from individual cells are the corresponding average values in control (black circle) and after cGMP (black circle). \*Significant difference,  $P < 0.05$ . **F**: plot of the frequency increase of the first interspike interval versus the increase of the slope for the data shown in **E**. Data were fitted to a straight line. Slope of linear regression =  $19.2 \pm 6.67$  (95% confidence interval);  $R^2 = 0.7$ ,  $P = 1.5 \times 10^{-5}$ .

tion, the increase in  $I_H$  conductance at  $-70$  mV after cGMP shows a positive correlation with the concomitant increase in firing [slope of linear regression =  $45.1 \pm 14.9$  (95% CI),  $R^2 = 0.8$ ,  $P = 3.5 \times 10^{-5}$ ; Fig. 5G].

**cGMP selectively targets the  $I_H$  of MesV neurons.** While modulation of MesV neuron's firing properties by cGMP can be consistent with the upregulation of the  $I_H$  (see DISCUSSION), this does not rule out the involvement of other mechanisms as this second messenger participates in multiple signaling pathways. In fact, firing properties of neurons critically depend on the dynamic interaction between multiple voltage and ligand-gated membrane conductances that operate at both the subthreshold and the suprathreshold ranges of membrane potential. In MesV neurons, the pacemaker potential trajectory between successive spikes, critical for repetitive firing, results from the interplay between several currents (Enomoto et al. 2006; Tanaka et al. 2003; Wu et al. 2001, 2005). Among them, the  $I_{NaP}$  activates during the pacemaker potential and significantly contributes to the bursting behavior of these neurons (Enomoto et al. 2006; Wu et al. 2005). To test if cGMP actions involve the modulation of the  $I_{NaP}$ , we recorded this membrane current following standard proce-

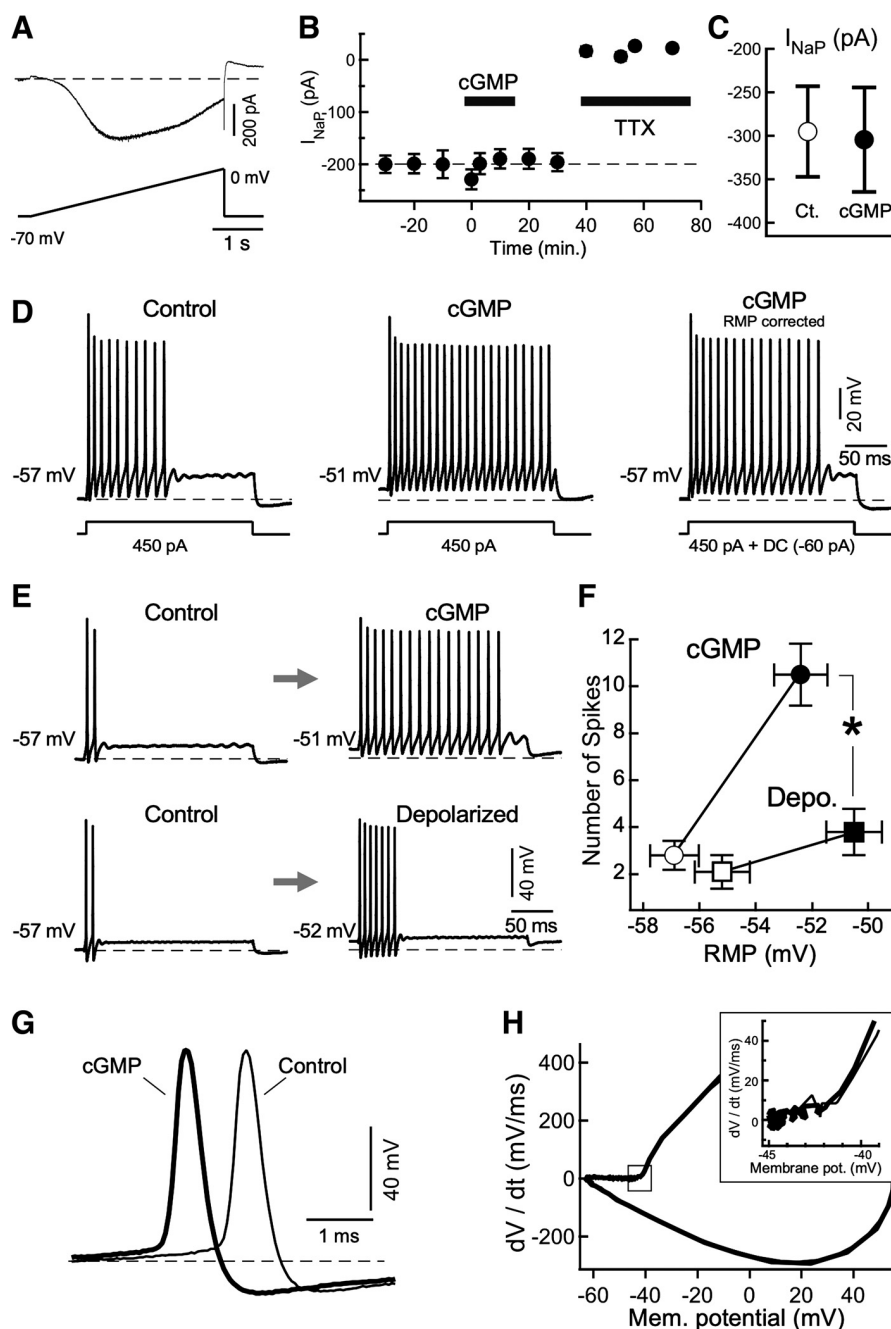
dures in voltage clamp by using ramp protocols (see MATERIALS AND METHODS). Noteworthy,  $I_{NaP}$  did not show any change after cGMP (1 mM), as peak current measured around  $-40$  mV averaged  $-295 \pm 52$  pA (SE) in control and  $-305 \pm 60$  pA (SE) after cGMP ( $P = 0.46$ ,  $n = 3$ ; paired, two-tailed  $t$ -test; Fig. 7, A–C). This result excludes the possibility that the modulation of the  $I_{NaP}$  is involved in the increase of MesV neuron's excitability.

Ligand-gated channels operated by cyclic nucleotides might also significantly contribute to regulate the excitability of neurons. For instance, CNG channels are activated by cGMP and by inducing tonic depolarizations (Kaupp and Seifert 2002) can increase neuronal firing (Kawa and Sterling 2002). Noteworthy, cGMP-induced modulatory actions on excitability are accompanied by a small but highly consistent depolarization of the resting membrane potential (Fig. 5, A, B, and F), raising the possibility that the depolarization may be responsible for the increase in firing. To test if such a mechanism is involved in MesV neurons, we asked whether the depolarization of the membrane potential by itself is enough to explain the observed changes in firing properties induced by cGMP. First, we tried to revert the effects of cGMP on repetitive firing

by repolarizing the membrane potential to previous control levels by injecting hyperpolarizing DC current. As depicted in Fig. 7D, although the repolarization of the membrane potential somewhat reduces the number of spikes after cGMP, spiking is still well above control (Fig. 7D, compare *left* and *right*). Conversely, depolarizing the membrane potential by 4–5 mV with DC current injection in control conditions did not produce an increment in firing comparable to that induced by cGMP (Fig. 7E, compare *top* and *bottom*). These results are summarized in Fig. 7F, where the number of spikes evoked by current pulses is plotted against the membrane potential value for cells that were depolarized by DC current (squares) and for cells that were exposed to cGMP (circles). Remarkably, responses from cells exposed to cGMP present significantly more spikes than

responses from cells unexposed to cGMP that were depolarized to the same level with DC current, averaging  $10.5 \pm 1.32$  spikes (SE) and  $3.8 \pm 0.98$  spikes (SE), respectively ( $P = 6 \times 10^{-4}$ ,  $n = 10$ ; unpaired, one-tailed  $t$ -test). Prepulse membrane potential averaged  $-52.4 \pm 0.952$  mV (SE) and  $-50.5 \pm 1.0$  (SE) in neurons exposed to cGMP and depolarized with DC current, respectively ( $P = 0.179$ ;  $n = 10$ , unpaired, two-tailed  $t$ -test). These results show that the depolarization of the membrane potential by itself is not enough to explain the observed increase in excitability of MesV neurons, suggesting the involvement of a mechanism different than the modulation of a voltage insensitive leak-type membrane conductance.

The observed increase in neuronal firing can result not only from the acceleration of the membrane potential trajectory



between successive spikes (pacemaker potential, Fig. 6, *D* and *E*) but also from the hyperpolarization of the voltage threshold for spike generation (lower firing level). Indeed, spike threshold was shown to be dynamically modulated with relevant consequences on neuronal excitability (Fontaine et al. 2014). To evaluate the possible contribution of such a mechanism, we examined the properties of MesV neuron's action potentials (Fig. 7*G*), particularly the spike threshold by constructing plots of the time derivative of membrane voltage versus membrane voltage (phase plots in Fig. 7*H*). The firing level determined from these plots and defined as the value of membrane voltage at which the rate of change reaches 10 mV/ms in a monotonically increasing interval did not differ significantly after cGMP (Fig. 7*H*, *inset*). This value averaged  $-44.0 \pm 1.02$  mV (SE) in control conditions and  $-42.4 \pm 0.76$  mV (SE) after cGMP ( $P = 0.06$ ;  $n = 10$ , paired, two-tailed *t*-test), suggesting that cGMP did not induce changes in the spike-generating mechanisms and that the increase in excitability does not result from the lowering of the threshold for spike initiation.

The  $I_H$  is necessary for the cGMP-induced effects on neuronal excitability. The  $I_H$  can significantly contribute to the resting membrane potential, input resistance, and subthreshold behavior of neurons (Benarroch 2013; Biel et al. 2009; Robinson and Siegelbaum 2003). However, the unique biophysical properties of this conductance make difficult to unambiguously predict the functional impact of modulatory actions. Indeed, depolarization of the resting potential and acceleration of the pacemaker potential tend to increase firing, whereas the reduction of input resistance might have the opposite effect. Therefore, to obtain direct evidence indicating that the cGMP-induced changes of  $I_H$  is the mechanism responsible for the increase of MesV neuron excitability, we next asked whether this membrane conductance is necessary for the induction of such modulatory changes in excitability. For this, we studied the effects of cGMP (0.5–1 mM) in the presence of nearly saturating concentrations of the bradycardic agent ZD7288 (100  $\mu$ M), which is a potent blocker of the  $I_H$ . This blocker was included in the electrode filling solution as the blocking effect of this compound is from the intracellular side of the channels (Shin et al. 2001) and at these concentrations it does not simply block the ionic current but also significantly reduces the binding of cyclic nucleotides to the channel intracellular domain (Wu et al. 2012). As expected,

under these conditions MesV neuron voltage responses to hyperpolarizing current pulses lack the characteristic sag due to the activation of the  $I_H$  (Fig. 8*A*).

ZD7288 largely prevented the cGMP-induced effects on MesV neuron excitability, thus confirming our hypothesis. In fact, addition of cGMP to the bath has no effect on spiking or resting membrane potential (Fig. 8*B*). These results can be better appreciated in Fig. 8*C*, where the average resting membrane potential and number of spikes for a population of 12 cells were plotted as function of time. Confirming these results, the plot in Fig. 8*D* shows the mean number of spikes as a function of current pulse intensity before (ZD7288) and after cGMP application (cGMP + ZD7288). Spiking do not show a statistically significant increase after cGMP ( $P > 0.05$ ,  $n = 9$ ; paired, one-tailed *t*-test) for the whole range of tested currents. Note that although the range of current pulses explored in the presence of ZD7288 is not as extended as in control conditions, the concomitant increase in  $R_{in}$  (108.6 M $\Omega$  in control vs. 445.2 M $\Omega$  in ZD7288) suggests that the lack of effect of cGMP applications do not result from differences in stimulation protocols. Moreover, for the sample of recorded neurons ( $n = 12$ ), the resting membrane potential do not show a statistically significant depolarization after cGMP, averaging  $-55.6 \pm 1.38$  mV (SE) before and  $-54.6 \pm 1.13$  mV (SE) after cGMP ( $P = 0.135$ ; paired, one-tailed *t*-test; Fig. 8*E*). However, in the presence of ZD7288, cGMP applications still induce a significant reduction of the input resistance, averaging  $445.2 \pm 61.9$  M $\Omega$  (SE) before and  $381.7 \pm 46.5$  M $\Omega$  (SE) after cGMP ( $P = 0.047$ ; paired, one-tailed *t*-test; Fig. 8*F*) possibly due to the modulation of a membrane mechanism different from HCN channels. These results clearly show that the  $I_H$  is necessary for the modulation of the intrinsic excitability of MesV neurons induced by cGMP, supporting the notion that the regulation of this membrane current is the underlying mechanism.

Computer simulations show that upregulation of the  $I_H$  is sufficient to induce the cGMP effects on MesV neuron excitability. The experimental results so far presented provide compelling evidence that regulation of the  $I_H$  represents the main mechanism involved in cGMP-induced increase in excitability. However, to obtain further evidence about the functional impact of such mechanism, we next asked whether the

Fig. 7. cGMP does not target other membrane conductances of mesencephalic trigeminal (MesV) neurons. *A*: representative recording of the persistent  $\text{Na}^+$  current ( $I_{\text{NaP}}$ ) in control conditions (*top trace*) in response to a voltage command consisting in a slowly rising ramp (rate  $\sim 20$  mV/s) from a holding potential of  $-70$  mV to a final potential of 0 mV (*bottom trace*). *B*: plot of the  $I_{\text{NaP}}$  magnitude (measured at the most negative value) as a function of time in another neuron in control conditions (black circles), during application of cGMP (horizontal black bar), and during application of  $0.5 \mu\text{M}$  tetrodotoxin (TTX; horizontal black bar). Each value represents the average of 10 single values, and error bars represent SE. *C*: summary plot of the average  $I_{\text{NaP}}$  amplitude from 3 different MesV neurons in control (white circle) and after exposure to cGMP (0.5–1 mM; black circle). Error bars represent SE ( $P = 0.46$ ;  $n = 3$  from 3 animals, paired, two-tailed *t*-test). *D*: traces showing repetitive discharges of a MesV neuron during the injection of depolarizing current pulses in control (*left*), after cGMP (*middle*), and after cGMP while the resting membrane potential was corrected to previous control levels by injecting hyperpolarizing DC current ( $-60$  pA) (*right*). *E*, *top*: illustration of the response of a MesV neuron during injection of a depolarizing current pulse before (*left*) and after application of cGMP (*right*) showing the increase in repetitive firing and the accompanying depolarization of the resting membrane potential. *E*, *bottom*: illustration of the response to a depolarizing current pulse of another neuron that was not exposed to cGMP from resting (*left*) and from a depolarized membrane potential (*right*). During this later condition, the resting membrane potential was depolarized to a level comparable to that obtained after cGMP by injection of depolarizing DC current. In *D* and *E*, values at the *left* of each trace indicate the prepulse membrane potential and dashed horizontal lines represent the resting membrane potential level in control conditions. *F*: plot summarizing results from experiments as those shown in *E*. Average number of spikes evoked during depolarizing current pulses against the prepulse membrane potential is shown. Circles represent firing of cells before (white) and after exposure to cGMP (black). Squares represent firing of cells unexposed to cGMP at their normal resting membrane potential (white) and during depolarization with DC current injection (Depo.; black), error bars represent SE. The number of spikes evoked by current pulses is significantly larger in cells exposed to cGMP compared with cells whose resting potential was depolarized with DC current [ $P = 6 \times 10^{-4}$ ;  $n = 10$  (cells exposed to cGMP:  $n = 10$  from 5 animals; depolarized cells:  $n = 10$  from 3 animals), unpaired, one-tailed *t*-test]. \*Significant difference,  $P < 0.05$ . *G*: traces showing representative action potentials before (thin trace) and after cGMP (thick trace), horizontally displaced for clarity. *H*: phase plots of the first time derivative of the membrane potential ( $dV/dt$ ) against the instantaneous membrane potential, showing the rate of change of membrane potential of the traces depicted in *G*. *Inset*: larger scale of the boxed area in the phase plot.



upregulation of the  $I_H$  is enough to explain the observed changes in MesV neuron excitability after cGMP. For this, a model of a typical MesV neuron was constructed consisting in two compartments, one representing the soma and the other the axon. Six Hodgkin-Huxley type active conductances previously described in MesV neurons were inserted in our deterministic two-compartment model, whose parameters were tuned using an evolutionary multiobjective algorithm (see MATERIALS AND METHODS). Maximum densities of passive and active conductances were tuned to precisely reproduce the main electrophysiological features of MesV neurons (in control conditions) in terms of resting membrane potential, input resistance, spike amplitude and duration, and postspike afterhyperpolarization potential, as well as the main firing characteristics (see MATERIALS AND METHODS). In fact, voltage membrane responses of MesV neurons to current pulses of both polarities (Fig. 9A), as well as the spike waveform (Fig. 9A, inset) were faithfully reproduced by our model, indicating that the results obtained from simulations can be translated to experiments and vice versa. Thus our model represents a valuable tool to understand how the different voltage dependent membrane conductances interact to give rise to the elec-

trophysiological phenotype of MesV neurons and the impact of  $I_H$  modulation.

Then, we investigated whether our model could reproduce the increase in excitability after upregulation of the  $I_H$ . We compared the electrophysiological properties and input-output relation of the model cell in control conditions and after modifying the  $I_H$  parameters according to our characterization of this current in voltage-clamp experiments during the effects of cGMP ( $I_H$  modulated, see MATERIALS AND METHODS). Figure 9B illustrates results from these simulations showing the response of the model cell in control (*top*) and after modulation of the  $I_H$  (*bottom*). Consistent with our experimental results, modulation of the  $I_H$  leads to a depolarization of the resting membrane potential, an increase in spiking and a reduction of the input resistance. The extent of these changes is also in agreement with experimental observations. The resting membrane potential of model cell changed from  $-58.4$  mV in control to  $-56.0$  mV after  $I_H$  modulation, whereas the number of spikes in response to current pulses of  $+350$  pA increased from 2 spikes in control to 18 after  $I_H$  modulation (Fig. 9B). Additionally, upregulation of the  $I_H$  in these simulations resulted in a reduction of the input resistance of  $\sim 12\%$  (from  $113.0$  to  $99.6$  M $\Omega$ ), which is comparable to the reduction observed during experiments after addition of cGMP ( $\sim 15\%$ ). Moreover, plots of the number of spikes and the frequency of the first interspike interval as a function of the intensity of current pulses show qualitatively similar results to those experimentally obtained (Fig. 5). In fact, upregulation of  $I_H$  resulted in a leftward displacement of these relations corresponding to an increase in firing, as well as a reduction of the threshold current for eliciting both single spikes and repetitive firing (Fig. 9, C and D).

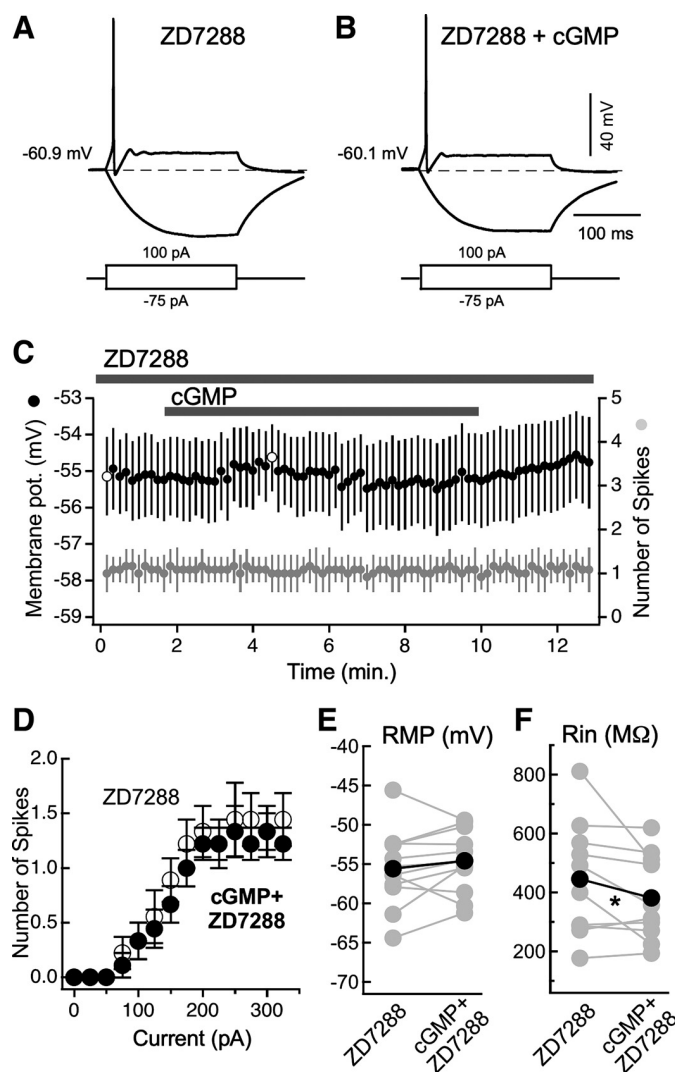


Fig. 8. The hyperpolarization-activated cationic current ( $I_H$ ) is necessary for the cGMP-induced effects on neuronal excitability. *A*: sample traces of membrane voltage responses of a mesencephalic trigeminal (MesV) neuron to current pulses of 100 and  $-75$  pA in the presence of the  $I_H$  blocker ZD7288. *B*: sample traces of membrane voltage responses of the cell shown in *A* during the same stimulation protocol after cGMP in the presence of ZD7288. *C*: plot depicts averaged values from 12 cells recorded in 5 animals of the resting membrane potential (left ordinates, black circles) and number of spikes evoked by depolarizing current pulses (right ordinates, gray circles) as a function of time before, during and after cGMP application to the bath in the presence of ZD7288. Error bars represent SE. Application of cGMP is indicated by the black horizontal bar. Peak average value of the resting membrane potential during cGMP [white circle,  $-54.6 \pm 0.92$  mV (SE)] is not statistically more depolarized in comparison to value before application [white circle,  $-55.1 \pm 1.08$  mV (SE)] ( $P = 0.069$ ;  $n = 12$ , paired, one-tailed  $t$ -test). *D*: plot of the mean number of spikes evoked by current pulses of 200 ms in duration as a function of the current intensity for a population of recorded cells ( $n = 9$  from 4 animals) in the presence of ZD7288 before (white circles) and after cGMP (black circles). Error bars represent SE. Spiking does not show a statistically significant increase after cGMP for the whole range of tested currents [ $P$  undefined (0 to 50 pA, identical data sets),  $P = 0.83$  (75 pA),  $P = 0.5$  (100 pA),  $P = 0.7$  (125 pA),  $P = 0.92$  (150 pA),  $P = 0.78$  (175 pA),  $P = 0.66$  (200 pA),  $P = 0.5$  (225 pA),  $P = 0.61$  (250 pA),  $P = 0.83$  (275 pA),  $P = 0.5$  (300 pA),  $P = 0.83$  (325 pA)  $n = 9$ ; paired, one-tailed  $t$ -test]. *E*: plot of the resting membrane potential values in the presence of ZD7288 before (gray circles, ZD7288) and after cGMP (gray, cGMP + ZD7288) ( $P = 0.135$ ;  $n = 12$  from 5 animals, paired, one-tailed  $t$ -test). *F*: plot of the input resistance values in the presence of ZD7288 before (gray circles, ZD7288) and after cGMP (gray circles, cGMP + ZD7288) ( $P = 0.047$ ;  $n = 10$  from 4 animals, paired, one-tailed  $t$ -test). In *E* and *F*, superimposed to the individual values are the corresponding average values in the presence of ZD7288 before (black circle) and after cGMP (black circle). \*Significant difference,  $P < 0.05$ .

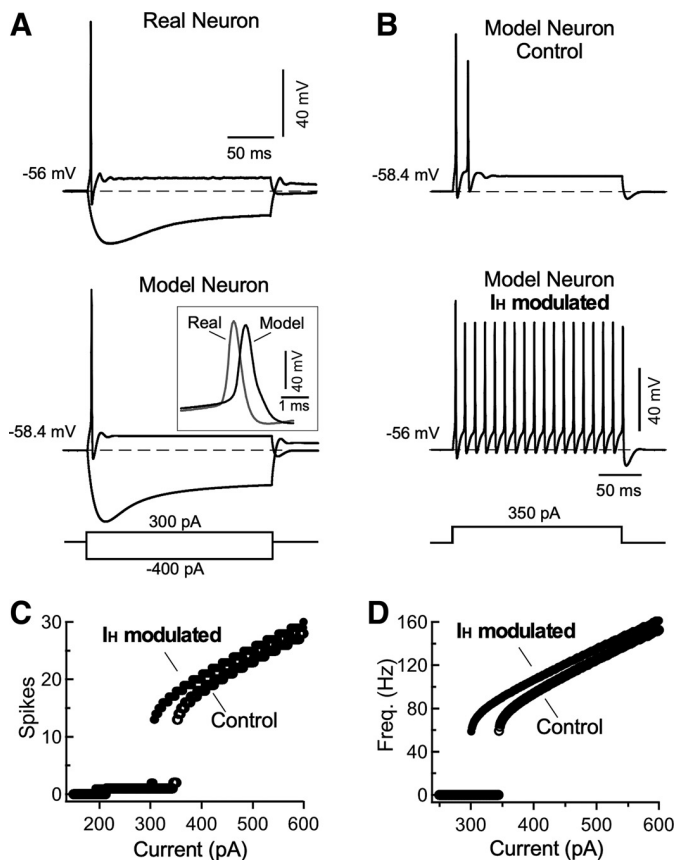


Fig. 9. Computer simulations show that upregulation of the hyperpolarization-activated cationic current ( $I_H$ ) is sufficient to increase firing. **A**, *top*: a typical membrane voltage response of a mesencephalic trigeminal (MesV) neuron to depolarizing (300 pA) and hyperpolarizing (−400 pA) current pulses are illustrated. **A**, *bottom*: voltage responses of the model neuron to the same current pulses are depicted to show the similarity between real and model neuron responses. *Inset*: the spikes of the real and model neurons are displayed at an expanded temporal scale. **B**: voltage responses of the model MesV neuron to depolarizing current pulses (350 pA) in control (*top*) and after modification of the parameters defining the  $I_H$  according to the modulatory effects of the cGMP on this membrane current experimentally determined (*bottom*). Note the dramatic increase in firing and the concomitant depolarization of the resting membrane potential after changes of  $I_H$  parameters. **C**: plot of the number of spikes of the model cell evoked by current pulses of 200 ms in duration as a function of the current intensity in control (black circles, control) and after  $I_H$  modulation (black circles,  $I_H$  modulated). **D**: plot of the instantaneous frequency of the model cell of the first interspike interval during repetitive discharges evoked by depolarizing current pulses as a function of the current intensity in control (black circles, control) and after  $I_H$  modulation (black circles,  $I_H$  modulated).

These simulations show that our biophysically detailed model can reproduce the main aspects of electrophysiological properties and firing characteristics of real MesV neurons. Moreover, upregulating the  $I_H$  of model neurons has qualitatively and quantitatively similar effects on the electrophysiological properties as those experimentally observed in MesV neurons after exposure to cGMP. These findings show that upregulation of the  $I_H$  is sufficient to explain the experimentally observed increase in neuronal excitability induced by cGMP. Therefore, the upregulation of this membrane conductance by cGMP represents a valuable tool to manipulate the intrinsic excitability of MesV neurons and to study its role in coincidence detection.

*cGMP enhances the gain of coincidence detection between electrically coupled MesV neurons.* To test the contribution of the intrinsic excitability of neurons to coincidence detection, depolarizing current pulses of the same intensity were applied alternatively and simultaneously to coupled MesV neurons, in control conditions and after the upregulation of the  $I_H$  induced by cGMP applications (0.5–1 mM). Figure 10 shows representative results of these experiments. While bursts evoked by independent current pulses show a moderate increase after cGMP in terms of spike number (Fig. 10, *A* and *B*, compare *left* and *middle*) responses during coactivation present a dramatic increase (Fig. 10, *A* and *B*, *right*). Moreover, coincident bursts during both control and after cGMP are highly synchronic, as indicated by the cross-correlation analysis exhibiting a single peak of large magnitude and brief delay (Fig. 10, *A* and *B*, *insets*). The effect on coincidence detection gain can be better appreciated in the graph of Fig. 10C where the number of spikes during individual and coincident stimulation were plotted before and after the application of cGMP. In most coupled cells, the slope of this relation displays a striking increase after cGMP, indicating an increase in the gain of coincidence detection. For this population of recorded neurons ( $n = 12$ , from 6 pairs), the average number of spikes during independent activation showed only a modest increase from  $1.81 \pm 0.722$  (SE) in control conditions to  $3.81 \pm 2.096$  (SE) after cGMP ( $P = 0.176$ ; paired,  $t$ -test). In contrast, the number of spikes during coactivation exhibited a much more dramatic increase from  $2.9 \pm 0.815$  (SE) in control to  $13.68 \pm 3.91$  (SE) after cGMP ( $P = 0.0102$ ; paired, two-tailed  $t$ -test; Fig. 10C). Consistently, the coincidence detection index displayed a significant increase from  $1.09 \pm 0.19$  spikes (SE) in control conditions to  $9.83 \pm 3.32$  spikes (SE) after cGMP ( $P = 0.0193$ ; paired, two-tailed  $t$ -test; Fig. 10D), indicating that cGMP preferentially increases firing during coactivation, thus greatly enhancing the gain of coincidence detection.

*cGMP-induced enhancement of coincidence detection gain cannot be explained by changes of the strength of electrical coupling.* After cGMP, presynaptic neurons are significantly more efficient in activating postsynaptic coupled neurons, consistent with its effects on coincidence detection. In fact, the spike-to-spike transfer through electrical contacts between MesV neurons is enhanced after cGMP as indicated by the ability of presynaptic trains of spikes to more faithfully recruit postsynaptic coupled cells (Fig. 11A). This effect was quantified by calculating the recruitment rate as the ratio of the number of postsynaptic spikes over the number of presynaptic evoked spikes. This ratio increased from  $0.31 \pm 0.15$  (SE) in control conditions to  $0.58 \pm 0.16$  (SE) after cGMP applications ( $P = 0.0437$ ;  $n = 10$  from 5 coupled pairs, paired, two-tailed  $t$ -test; Fig. 11B), confirming that presynaptic repetitive discharges are much more efficient in recruiting postsynaptic coupled neurons after cGMP. While this phenomenon is consistent with the modulation of the intrinsic excitability already shown, it could also result from an increase in the CC between MesV neurons. In fact, cGMP was reported to regulate the degree of coupling by targeting gap junction conductance (Hatton and Yang 1996; Rörig and Sutor 1996; Yang and Hatton 1999). To assess the possible contribution of such a mechanism, we measured the CC in control conditions and after cGMP. For this purpose, a series of hyperpolarizing current steps of different intensities were injected in one cell of

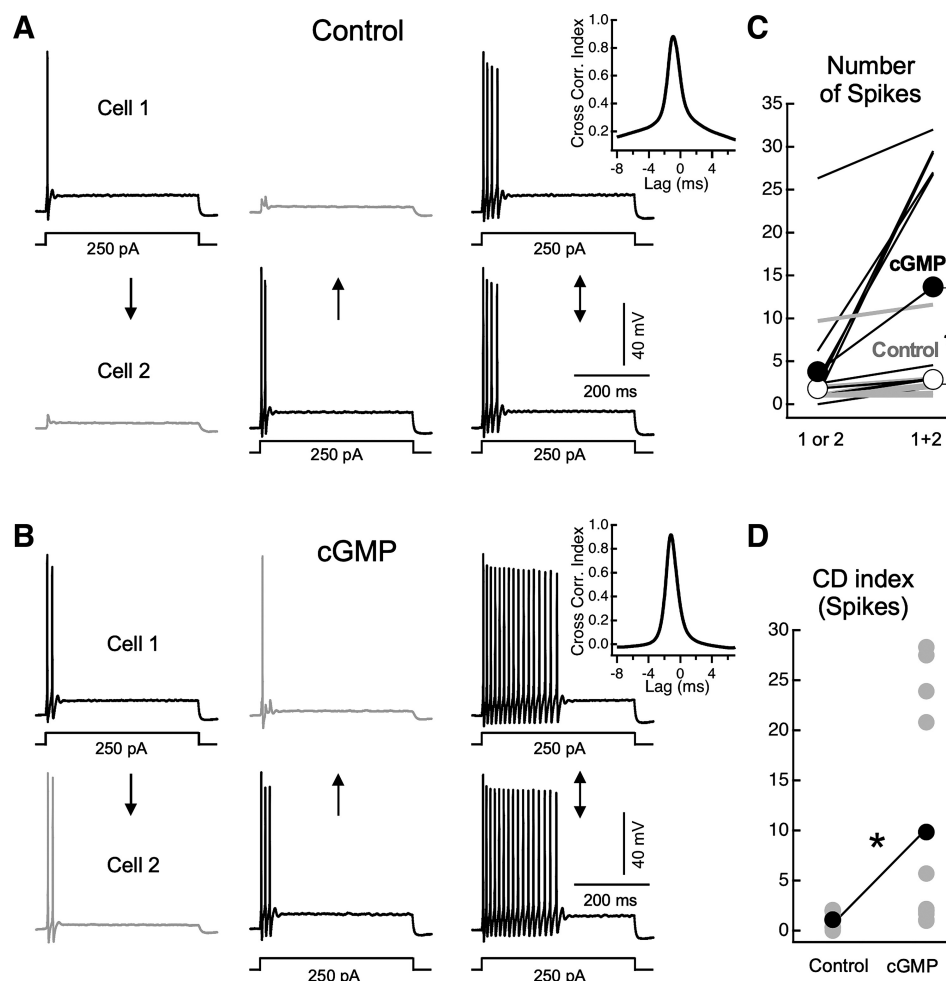


Fig. 10. cGMP enhances coincidence detection gain. *A*: membrane responses of a pair of coupled mesencephalic trigeminal (MesV) neurons during a stimulation protocol consisting in the injection of depolarizing current pulses of the same intensity (250 pA) alternatively to each cell (*left* and *middle*) and simultaneously to both cells (*right*) to show coincidence detection in control conditions. *B*: membrane responses of the same pair depicted in *A* to the same stimulation protocol after application of cGMP (1 mM) showing a dramatic increase in firing when cells were simultaneously activated indicating an increase in coincidence detection gain. *A* and *B*, *insets*: depict the cross correlograms between firing of cells 1 and 2 during coincident activation. *C*: plot of the number of spikes when cells were independently activated (1 or 2) and when simultaneously activated (1 + 2) in control conditions (gray lines) and after cGMP (black lines). Superimposed to the values from individual neurons are the average values for the population of tested neurons in control (white circles) and after cGMP (black circles). Average values during coincident activation in each condition were statistically different ( $P = 0.0096$ ;  $n = 10$  from 6 animals, paired, two-tailed  $t$ -test). *D*: plot of the coincidence detection (CD) index in control conditions (gray circles) and after cGMP (gray circles) of the sample of recorded coupled cells depicted in *C*: superimposed to the values from individual neurons are the corresponding average values in control (black circle) and after cGMP (black circle) ( $P = 0.019$ ;  $n = 10$ , paired, two-tailed  $t$ -test). \*Significant difference,  $P < 0.05$ .

an electrically coupled pair while the induced membrane voltage changes in both cells were monitored before and after cGMP application (Fig. 11C). From these recordings, plots of the voltage change in the postsynaptic coupled cell as a function of the voltage change in the presynaptic injected cell were constructed and the CC was estimated from the slope of the fit to a straight line (see MATERIALS AND METHODS) (Fig. 11D). Instead of increasing, the CC showed a significant reduction after cGMP applications, calculated either at the beginning of voltage responses (at the peak of hyperpolarizing voltage responses) (Fig. 11E) or at the end (steady state, Fig. 11F). In fact, the CC estimated at the peak of hyperpolarizing voltage responses averaged  $0.41 \pm 0.05$  (SE) in control conditions and  $0.33 \pm 0.04$  (SE) after cGMP ( $P = 4.46 \times 10^{-6}$ ;  $n = 20$ , paired, two-tailed  $t$ -test), whereas the CC estimated at steady state averaged  $0.28 \pm 0.03$  (SE) in control and  $0.23 \pm 0.03$  (SE) after cGMP ( $P = 0.0015$ ;  $n = 20$ , paired,

two-tailed). Moreover, the gap junction conductance estimated from the input and transfer resistances determined in current clamp (see MATERIALS AND METHODS) (Bennett 1966) also presented significant reduction, averaging  $6.68 \pm 1.08$  nS (SE) in control and  $6.03 \pm 1.05$  nS (SE) after cGMP ( $P = 0.0365$ ;  $n = 20$ , paired, two-tailed; Fig. 11H). This suggests that the reduction of the CC, estimated from hyperpolarizing pulses, resulted from the combined reduction in  $R_{in}$  and gap junction conductance observed after cGMP application (Fig. 6, A–C and Fig. 11, C–F), as the CC depends on these two parameters (Bennett 1966; Curti and O'Brien 2016). On the other hand, coincidence detection and recruitment of postsynaptic cells depend on depolarizing rather hyperpolarizing coupling potentials. Therefore, coupling potentials evoked by presynaptic spikes (spikelets) were measured before and after cGMP application (Fig. 11A, *inset*). The CCs calculated from these spikelets and the presynaptic spike amplitudes (Fig. 11G) showed no statistical

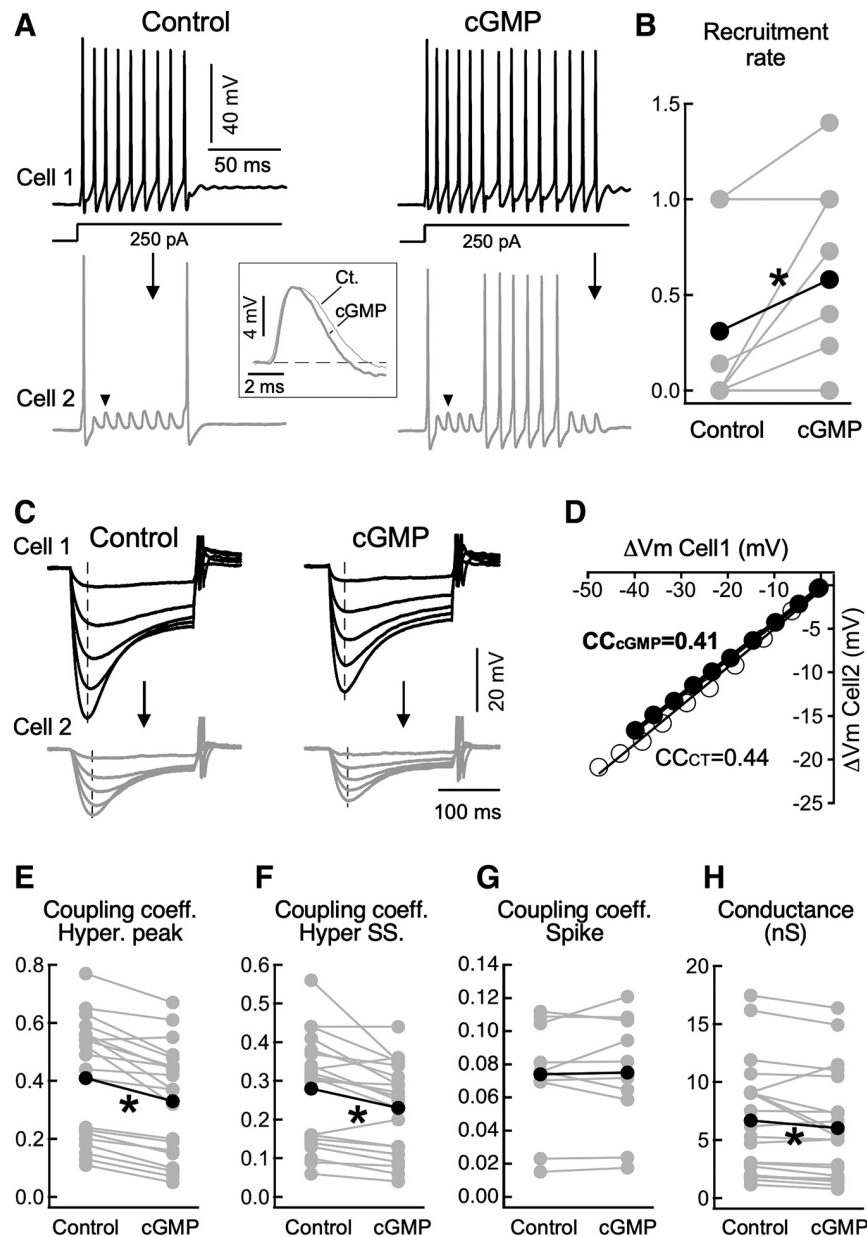
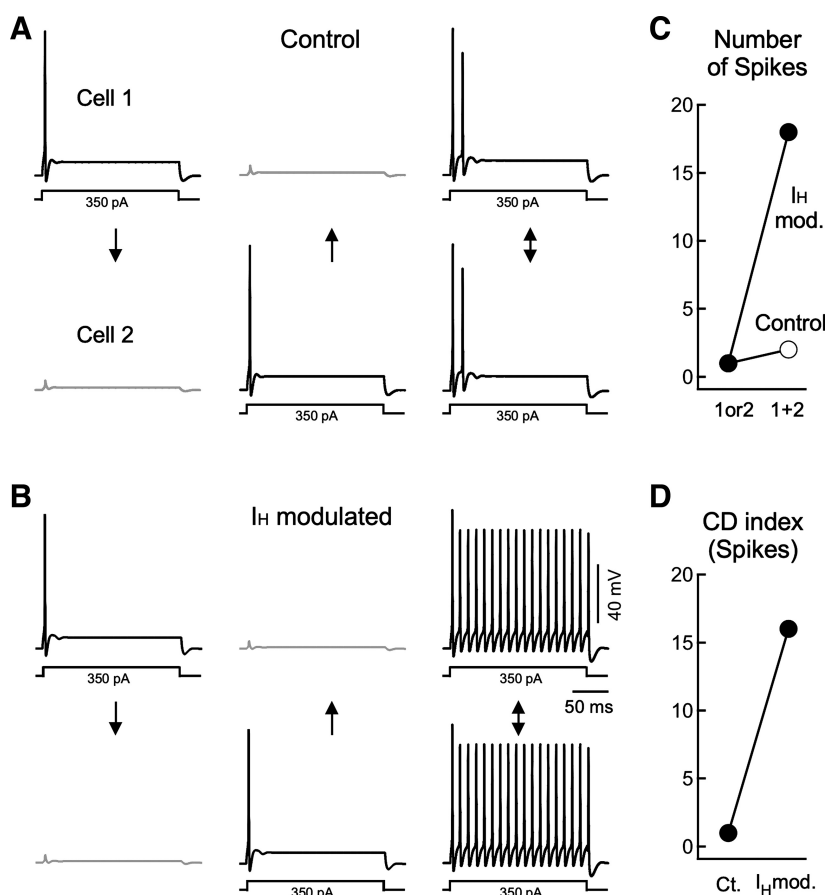


Fig. 11. cGMP-induced enhancement of coincidence detection gain does not involve changes in gap junction conductance. *A, left*: injection of a depolarizing current pulse (250 pA) in a cell belonging to a coupled pair evokes a repetitive discharge in this cell (*cell 1*) and corresponding coupling potentials in the postsynaptic coupled cell (*cell 2*) that eventually produce the activation of this postsynaptic neuron in control conditions. *A, right*: after addition of cGMP to the bath, the same stimulation protocol in the same pair of coupled mesencephalic trigeminal (MesV) neurons evokes now a more vigorous repetitive discharge in the injected cell and a marked increase in the recruitment of the postsynaptic cell. *A, inset*: coupling potentials (spikelets) in the postsynaptic cell indicated by downward arrowheads in corresponding traces before (control, thin trace) and after cGMP (thick trace) are displayed aligned, showing no change in amplitude. *B*: plot of recruitment rate calculated as the ratio of the number of postsynaptic spikes over the number of presynaptic evoked spikes. Individual values (gray circles) and average values for the whole sample (black circles) are illustrated superimposed ( $P = 0.0437$ ;  $n = 10$  from 5 animals, paired, two-tailed  $t$ -test). *C*: characterization of cGMP effects on electrical coupling in a pair of neurons. Injecting a series of hyperpolarizing current pulses of increasing intensity into one cell (*cell 1*) produces corresponding voltage responses in the injected presynaptic cell and in the postsynaptic coupled cell (*cell 2*), in control conditions (*left*), and after cGMP (*right*). *D*: from records depicted in *C* the coupling coefficient was estimated by plotting the amplitude of membrane voltage ( $V_m$ ) changes (measured at the peak of hyperpolarizing responses, vertical dashed lines in *C*) in the postsynaptic cell (*cell 2*, ordinates) as a function of membrane voltage changes in the presynaptic cell (*cell 1*, abscissas) in control conditions (white circles) and after cGMP (black circles). Each data set was fitted with a straight-line function, and the slope value representing the coupling coefficients (CC) are indicated. *E*: plot of the CCs determined at the negative peak of hyperpolarizing responses before (Control) and after cGMP (cGMP) ( $P = 4.46 \times 10^{-6}$ ;  $n = 20$ , paired, two-tailed  $t$ -test). *F*: plot of the CCs determined at steady state (SS) before (Control) and after cGMP (cGMP) ( $P = 0.0015$ ;  $n = 20$ , paired, two-tailed  $t$ -test). *G*: plot of the coupling coefficients determined from presynaptic spikes and corresponding postsynaptic spikelets before (Control) and after cGMP (cGMP) ( $P = 0.697$ ;  $n = 10$  from 8 animals, paired, two-tailed  $t$ -test). *H*: plot of the gap junction conductance value before (Control) and after cGMP (cGMP) ( $P = 0.0365$ ;  $n = 20$ , paired, two-tailed  $t$ -test). *E*, *F*, *G*, and *H* present data from the same set of neurons recorded in 9 animals. In *E*, *F*, *G*, and *H*, gray circles represent individual values in control and after cGMP exposure, respectively, and superimposed are the corresponding average values in control (black circle) and after cGMP (black circle). \*Significant difference,  $P < 0.05$ .



Fig. 12. Computer simulations show that upregulation of the hyperpolarization-activated cationic current ( $I_H$ ) is sufficient to enhance coincidence detection gain. **A**: study of coincidence detection in a network of two coupled model mesencephalic trigeminal (MesV) neurons. Injection of depolarizing current pulses alternatively into *cells 1* or *2* induced a single action potential in the injected cell and the corresponding coupling potentials (spikelets) in the postsynaptic cell (*left* and *middle*). Simultaneous activation of these two neurons with current pulses of the same magnitude (*right*), now evoked a discharge consisting of two spikes at each cell, showing that model coupled cells support coincidence detection. **B**: after modification of the  $I_H$  parameters of both model cells according to modulatory actions of cGMP ( $I_H$  modulated), independent activation of each coupled cell with current pulses of the same intensity still evoke a single spike (*left* and *middle*). However, simultaneous activation of both neurons now induces a robust repetitive discharge (*right*). **C**: plot of the number of spikes of model cells during independent activation (*1* or *2*) and during simultaneous activation (*1 + 2*) in control conditions (white circles, control) and after modification of the  $I_H$  parameters (black circles,  $I_H$  mod.). **D**: plot of the coincidence detection (CD) index in control conditions (Ct.) and after modification of  $I_H$  parameters ( $I_H$  mod.) for the pair of model MesV neurons.



difference in control versus after cGMP as they averaged  $0.074 \pm 0.01$  (SE) and  $0.075 \pm 0.011$  (SE), respectively ( $P = 0.697$ ;  $n = 10$ , paired, two-tailed  $t$ -test). Also, cGMP applications did not induce any significant change in the spikelet's waveform, as indicated by the values of half-amplitude duration and rise time (10–90%), which averaged  $3.32 \pm 0.32$  ms (SE) and  $0.712 \pm 0.024$  ms (SE), respectively, in control conditions, and  $2.91 \pm 0.248$  ms (SE) and  $0.714 \pm 0.031$  ms (SE), respectively, after cGMP ( $P = 0.076$  and  $0.934$ ;  $n = 10$ , paired, two-tailed  $t$ -test). Together, this evidence shows that the enhancement in coincident detection gain do not result from changes in the strength of electrical coupling between MesV neurons. Instead, this effect most probably results from the modulation of the excitability of these neurons, highlighting the relevance of the intrinsic electrophysiological properties in determining the characteristics of coincidence detection among electrically coupled neurons.

Computer simulations show that upregulation of the  $I_H$  enhances the gain of coincidence detection in networks of electrically coupled MesV neurons. To independently evaluate if the upregulation of the  $I_H$  is enough to enhance coincidence detection gain, we extended our single cell model to a network composed of two identical coupled neurons. Because electrical coupling in the MesV nucleus is organized mostly in pairs and is supported by voltage-independent somatic gap junctions (Curti et al. 2012), electrical coupling between model cells was implemented by a simple ohmic conductance connecting the soma compartments of the two cells (see MATERIALS AND METHODS). According to experimental data, the conduc-

tance of this mechanism was set to 4 nS, which corresponded to a CC of 0.29 when measured at the peak of voltage responses to current pulses of  $-400$  pA and of 0.22 at steady state, whereas the CC for spikes was 0.07 (not shown).

To validate these simulations, we began by investigating if this model network can support coincidence detection and then if its gain is enhanced by the upregulation of the  $I_H$  of connected cells. Coincidence detection was studied with the same stimulation protocol as during experiments; that is, suprathreshold depolarizing current pulses were injected alternatively in each cell or in both cells at the same time. As illustrated in Fig. 12A, injection of a  $+350$  pA current pulse in one or the other cell induces one spike (*left* and *middle*), whereas the injection of the same current pulse in both cells at the same time induces a response consisting in two spikes in both cells (*right*), showing that this model network of coupled cells in control conditions supports coincidence detection. Remarkably, when the parameters defining the  $I_H$  were modified according to the characterization of this current after cGMP in voltage-clamp experiments ( $I_H$  modulated), the responses of model cells did not show significant changes to independent activation (Fig. 12B, *left* and *middle*). However, simultaneous activation of both cells induced a dramatic increase in firing compared with control condition (Fig. 12B, *right*). Results from these simulations are summarized in the plot of the number of spikes evoked by these stimulation protocols in control and after modulation of the  $I_H$  shown in Fig. 12C. These simulations show that modulation of the  $I_H$  selectively increases the susceptibility of pairs of coupled

MesV neurons to synchronic inputs, thus representing an increase in coincidence detection gain (Fig. 12D). These results are qualitative similar to those obtained during experiments and indicate that the excitability of coupled neurons critically determines the gain of coincidence detection.

## DISCUSSION

Besides the well-known role of electrical coupling, we show here that the electrophysiological properties of coupled neurons are critical determinants of their ability to detect coincident inputs. The susceptibility or gain of this operation is highly heterogeneous across the population of MesV neurons, and experimental and theoretical evidence suggests that this heterogeneity results in part from the diverse regulatory states of the intrinsic excitability of this neuronal population. Consistently, cGMP-induced upregulation of the  $I_H$  resulted in dramatic changes in coincidence detection gain.

Coincidence detection has been extensively characterized in the auditory brainstem of birds and mammals, where fast-activating  $K^+$  currents and morphologic dendritic specializations endow neurons with the ability to maximally respond to simultaneous inputs (Agmon-Snir et al. 1998; Joris et al. 1998; Reyes et al. 1996). Electrical synapses can also support coincidence detection (Alcami and Pereda 2019; Connors 2017; Marder 1998). This property is based on the reduction of current leak through gap junctions during simultaneous inputs to coupled neurons (cancellation of the loading effect), resulting in larger membrane voltage changes that facilitate neuronal activation (Di Garbo et al. 2006; Hjorth et al. 2009; Relat and Szczupak 2004). Thus a defining characteristic of coincidence detection is that simultaneous depolarizing inputs evoke stronger neuronal firing in comparison to independent inputs, as shown in Fig. 1, A–D. However, there is no clear limit to establish, based solely on its time dependency or precision, if a given neuron or neural circuit operates as a coincidence detector or not. Precision, whether in the microsecond or in the millisecond range is most probably related to the specific function of the neural network (Alonso et al. 1996; Carr and Konishi 1990; König et al. 1996; Roy and Alloway 2001; Usrey et al. 2000). Regardless of the underlying mechanism, coincidence detection is an emergent property involved in brain functions like sound source localization (Carr 1993; Joris et al. 1998), information processing (König et al. 1996), organization of motor outputs (Edwards et al. 1998), sensorimotor integration (Rabinowitch et al. 2013), improvement of signal-to-noise ratio (DeVries et al. 2002; Smith and Vardi 1995), and Hebbian learning (Tsien 2000).

*Coincidence detection in the MesV nucleus is heterogeneous and is critically determined by the intrinsic excitability of neurons.* While both precision (time window over which inputs are summated) and gain (contrast between maximal and minimal responses) are critical aspects of coincidence detection, precision and its determinants have been previously characterized in different structures, including the auditory system (Agmon-Snir et al. 1998; Reyes et al. 1996) and populations of electrically coupled neurons (Alcami 2018; Edwards et al. 1998; Vervaeke et al. 2010). In contrast, much less is known about the determinants of the gain of coincidence detection. Therefore, we focused our efforts in characterizing this particular aspect and its underlying mechanisms by using stimulation

protocols expected to cause maximal contrast between responses, that is, coincident versus independent depolarizing inputs. The spatial segregation of synaptic inputs to electrotonically coupled cellular compartments is among the mechanisms that maximize this contrast, like in neurons of the auditory brainstem that present bipolar dendrites and synaptic inputs that are segregated to each dendrite. In these neurons, coincidence detection is based on the nonlinear summation of excitatory inputs and the function of each dendrite as a current sink for inputs to the other dendrite (Agmon-Snir et al. 1998). Pairs of coupled MesV neurons seem to operate in a similar fashion, wherein each neuron of a coupled pair acts as a current sink for the other, pointing toward the coupling strength as the primary determinant of the gain of coincidence detection.

Nevertheless, heterogeneity in coincidence detection gain across the population of MesV neurons cannot be explained solely in terms of the diversity of coupling strengths. Indeed, while high susceptibility to coincident inputs was displayed almost exclusively by strongly coupled pairs, the reciprocal is not true. This indicates that strong coupling is a necessary condition, although not sufficient, for high gain coincidence detection. On the other hand, highly excitable neurons tend to be more susceptible to coincident inputs unlike low excitable ones. This strongly suggests that neuronal excitability plays, along with electrical coupling, a key role determining the susceptibility of coupled neurons to coincident inputs. Consistent with a prominent role of the neuronal intrinsic properties, cGMP-induced increase in neuronal excitability resulted in a dramatic enhancement of coincidence detection gain. Such changes in coincidence detection were not accompanied by a concomitant increase of spike-triggered coupling potentials, emphasizing the role of the intrinsic excitability. Thus electrical coupling, in conjunction with the active electrophysiological properties, endows circuits of coupled neurons with an efficient mechanism to selectively respond to simultaneous or coincident inputs, as opposed to asynchronous or randomly distributed ones, that is, to act as coincidence detectors.

*cGMP-induced upregulation of the  $I_H$  increases MesV neuron's excitability and coincidence detection gain.* We show that the  $I_H$  is sharply modulated by cGMP as reported previously (Datunashvili et al. 2018; Ingram and Williams 1996; Wilson and Garthwaite 2010; Yang and Hatton 1999). This modulation results in an enhancement of MesV neuron excitability, as was shown in cardiac (Brown et al. 1979) and other neural cells (Bobker and Williams 1989; Cardenas et al. 1999; Maccaferri and McBain 1996; McCormick and Pape 1990a; Tang and Trussell 2015). This is most probably due to an increase of the net inward current at membrane voltage values close to the resting potential. Two lines of evidence support this conclusion. First, in the presence of the  $I_H$  blocker ZD7288, cGMP is unable to modulate MesV neuron spiking and resting potential. Second, computer simulations show that changes in  $I_H$  parameters, consistent with experimental observations, faithfully reproduce the actions of cGMP. Together, these findings indicate that  $I_H$  modulation is necessary and sufficient to mediate the cGMP-induced increase in excitability. However,  $I_H$  has also been reported to reduce excitability rather than to boost it (Berger et al. 2003; Magee 1998; Stuart and Spruston 1998; Tsay et al. 2007; Williams and Stuart 2000), and upregulation of this conductance results in a de-

crease of neuronal output (Fan et al. 2005; Poolos et al. 2002; Rosenkranz and Johnston 2006). This contradictory role of  $I_H$  on neuronal excitability is most likely due to the unique biophysical properties of this conductance. In fact,  $I_H$  is activated by hyperpolarization and presents a reversal potential around  $-30$  mV, resulting in an inward current that promotes firing by bringing membrane voltage closer to its firing level. On the other hand, activation of this conductance results in a reduction of the neuron's input resistance dampening the impact of excitatory inputs (Dyhrfeld-Johnsen et al. 2009; Lippert and Booth 2009; Migliore and Migliore 2012). Which of these outcomes on excitability prevail seems to be related to the spatial distribution of HCN channels in relation to the spiking compartment, most typically the cell body (Harnett et al. 2015). In fact, when located at, or close to the soma compartment, upregulation of the  $I_H$  results in an increase of neuronal excitability (Cardenas et al. 1999; Kanyshkova et al. 2009; McCormick and Pape 1990b; Pál et al. 2003; Tang and Trussell 2015; Tu et al. 2004), whereas at distal locations of the dendritic compartment its activation tends to reduce excitability (Fan et al. 2005; Lörincz et al. 2002; Notomi and Shigemoto 2004; Poolos et al. 2002; Rosenkranz and Johnston 2006; Wang et al. 2007). Moreover, this conductance seems to be tonically active, supporting an inward current at membrane potentials between the spike afterhyperpolarization potential and its reversion, even in the time course of the interspike interval, whose duration is several orders of magnitude shorter than the  $I_H$  activation time constant.

The upregulation of the  $I_H$  preferentially increases firing of coupled MesV neurons during simultaneous depolarizations. In fact, spiking during coincident depolarizing inputs showed a dramatic increase after cGMP, whereas spiking during independent depolarizations displayed little change. This most probably results from the contrasting actions of  $I_H$  on cellular excitability in combination with the loading effect displayed by pairs of coupled neurons. In control conditions, the loading effect reduces on average the  $R_{in}$  of coupled cells by  $\sim 26\%$ , supporting the reduced neuronal spiking during asynchronous inputs in comparison to coincident inputs, thus allowing coupled neurons to act as coincidence detectors. After  $I_H$  upregulation, coupled neurons show an additional reduction of their  $R_{in}$  of between 10% and 15%. This results from the same cell's  $R_{in}$  reduction plus the reduction of the  $R_{in}$  of the coupled cell. This additional reduction in  $R_{in}$  is not translated into a corresponding reduction in firing, most probably thanks to the concomitant increase in net inward current. Thus during uncorrelated inputs to coupled neurons, the reduction of the  $R_{in}$  and the increase in inward current seem to compensate each other. However, under the  $I_H$  modulated condition, by canceling the loading effect, coincident inputs mitigate part of the  $R_{in}$  reduction, potentiating the action of the increased inward current on membrane excitability, and supporting strong repetitive discharges. Therefore, the upregulation of the  $I_H$  increases the contrast between minimal and maximal neuronal responses evoked during uncorrelated and coincident inputs, respectively, thus enhancing the susceptibility of pairs of coupled MesV neurons to coincident inputs. This conclusion is supported by our computer simulations that show a marked increase in firing of model cells during simultaneous depolarizations under  $I_H$  modulated conditions.

**Functional relevance.** MesV neurons are primary afferents that innervate muscle spindles of jaw-closing muscles or mechanoreceptors of periodontal ligaments and establish direct excitatory contacts with trigeminal motoneurons (Morquette et al. 2012). These afferents are strongly activated during jaw movements associated to food intake, thus providing positive proprioceptive feedback for the adjustment of bite force (Lavigne et al. 1987; Yamamoto et al. 1989). Based on our results, it is possible that coincident activation promotes stronger firing of coupled MesV neurons, operating as an amplification mechanism for this sensory input, facilitating jaw-closing muscle activation. Also, the somas of MesV neurons receive synaptic inputs from several brain areas, suggesting that they participate in the organization of orofacial behaviors by integrating sensory information from the periphery with inputs from hierarchically superior structures (Kolta et al. 1990; Nagy et al. 1986). Inputs from the supratrigeminal area evoke short latency excitatory postsynaptic potentials strong enough to induce or enhance oscillatory activity that eventually leads to firing (Verdier et al. 2004). Our findings show that coincident depolarizing inputs to coupled cells promote strong repetitive firing, suggesting that pairs of coupled MesV neurons that share same excitatory inputs will tend to produce synchronic bursts. These synchronic bursts most likely represent strong excitatory inputs onto trigeminal motoneurons. In fact, beyond supporting temporal summation of excitatory postsynaptic potentials, bursts are considered to be robust codes of communication at chemical junctions since they facilitate transmitter release from low probability contacts (Lisman 1997). Moreover, individual  $I_a$  afferents typically evoke weak synaptic actions (Mendell and Henneman 1971), implying that summation of coincident inputs from multiple afferents is required to activate motoneurons. Remarkably, we found that the cGMP-induced modulation of the  $I_H$  greatly enhances the gain of coincidence detection, increasing the duration of repetitive discharges, most probably reinforcing excitatory inputs onto trigeminal motoneurons. Because MesV neurons massively project to trigeminal motoneurons (Stanek et al. 2014), this suggests that such modulatory actions significantly impact on the organization of orofacial behaviors. In addition, MesV neurons receive nitrenergic projections and nitric oxide increases the excitability of these neurons most probably through elevations of intracellular cGMP levels (Pose et al. 2003). Histaminergic projections to the MesV nucleus were also described (Inagaki et al. 1987), and histamine actions have also been shown to involve cGMP in other systems (Hatton and Yang 1996; Hough 1999). This suggests that modulation of coincidence detection between coupled MesV neurons may occur under physiological conditions.

Recent evidence shows that pairs of electrically interconnected GABAergic interneurons from the cortex and the cerebellum are coinnervated, supporting synchronous depolarizing inputs to these interneurons (Otsuka and Kawaguchi 2013; van Welie et al. 2016). This suggests that coincidence detection represents a common feature of networks of coupled neurons of the mammalian brain. In the retina of mammals, electrical coupling between cones and between AII amacrine cells underlies a noise reduction operation through a mechanism analogous to coincidence detection (DeVries et al. 2002; Smith and Vardi 1995), where simultaneous (signal specific) inputs have a larger impact on



membrane potential in comparison to randomly distributed (noisy) ones (Sterling and Demb 2004). It is tempting to speculate that by modulating coincidence detection gain as shown here, the output of these circuits can be readily altered with relevant functional consequences. In fact, HCN channels and electrical synapses have been shown to coexist in many neuronal populations, raising the possibility that circuit operations supported by electrical coupling like coincidence detection are under precise and dynamic regulatory control through modulation of the highly modifiable  $I_H$  current.

#### ACKNOWLEDGMENTS

We thank Alberto Pereda and Inés Pose for critical discussions and comments on an early version of this manuscript.

#### GRANTS

This work was supported by Agencia Nacional de Investigación e Innovación, Uruguay (FCE\_I\_2014\_1\_104725) and Comisión Académica de Posgrado of Universidad de la República.

#### DISCLOSURES

No conflicts of interest, financial or otherwise, are declared by the authors.

#### AUTHOR CONTRIBUTIONS

F.D. and S.C. conceived and designed research; F.D. and S.C. performed experiments; F.D. and S.C. analyzed data; F.D. and S.C. interpreted results of experiments; F.D. and S.C. edited and revised manuscript; F.D. and S.C. approved final version of manuscript; S.C. prepared figures; S.C. drafted manuscript.

#### REFERENCES

- Agmon-Snir H, Carr CE, Rinzel J. The role of dendrites in auditory coincidence detection. *Nature* 393: 268–272, 1998. doi:10.1038/30505.
- Alcami P. Electrical synapses enhance and accelerate interneuron recruitment in response to coincident and sequential excitation. *Front Cell Neurosci* 12: 156, 2018. doi:10.3389/fncel.2018.00156.
- Alcami P, Pereda AE. Beyond plasticity: the dynamic impact of electrical synapses on neural circuits. *Nat Rev Neurosci* 20: 253–271, 2019. doi:10.1038/s41583-019-0133-5.
- Alonso J-M, Usrey WM, Reid RC. Precisely correlated firing in cells of the lateral geniculate nucleus. *Nature* 383: 815–819, 1996. doi:10.1038/383815a0.
- Angelo K, Margrie TW. Population diversity and function of hyperpolarization-activated current in olfactory bulb mitral cells. *Sci Rep* 1: 50, 2011. doi:10.1038/srep00050.
- Bahl A, Stemmler MB, Herz AV, Roth A. Automated optimization of a reduced layer 5 pyramidal cell model based on experimental data. *J Neurosci Methods* 210: 22–34, 2012. doi:10.1016/j.jneumeth.2012.04.006.
- Benarroch EE. HCN channels: function and clinical implications. *Neurology* 80: 304–310, 2013. doi:10.1212/WNL.0b013e31827dec42.
- Bennett MV. Physiology of electrotonic junctions. *Ann N Y Acad Sci* 137: 509–539, 1966. doi:10.1111/j.1749-6632.1966.tb50178.x.
- Bennett MV, Zukin RS. Electrical coupling and neuronal synchronization in the Mammalian brain. *Neuron* 41: 495–511, 2004. doi:10.1016/S0896-6273(04)00043-1.
- Berger T, Senn W, Lüscher HR. Hyperpolarization-activated current  $I_h$  disconnects somatic and dendritic spike initiation zones in layer V pyramidal neurons. *J Neurophysiol* 90: 2428–2437, 2003. doi:10.1152/jn.00377.2003.
- Biel M, Wahl-Schott C, Michalakakis S, Zong X. Hyperpolarization-activated cation channels: from genes to function. *Physiol Rev* 89: 847–885, 2009. doi:10.1152/physrev.00029.2008.
- Bobker DH, Williams JT. Serotonin augments the cationic current  $I_h$  in central neurons. *Neuron* 2: 1535–1540, 1989. doi:10.1016/0896-6273(89)90041-X.
- Brown H, DiFrancesco D, Noble S. Cardiac pacemaker oscillation and its modulation by autonomic transmitters. *J Exp Biol* 81: 175–204, 1979..
- Canavos G. *Applied Probability and Statistical Methods*. New York: Little, Brown, 1988.
- Cardenas CG, Mar LP, Vysokanov AV, Arnold PB, Cardenas LM, Surmeier DJ, Scroggs RS. Serotonergic modulation of hyperpolarization-activated current in acutely isolated rat dorsal root ganglion neurons. *J Physiol* 518: 507–523, 1999. doi:10.1111/j.1469-7793.1999.0507p.x.
- Carr CE. Processing of temporal information in the brain. *Annu Rev Neurosci* 16: 223–243, 1993. doi:10.1146/annurev.ne.16.030193.001255.
- Carr CE, Konishi M. A circuit for detection of interaural time differences in the brain stem of the barn owl. *J Neurosci* 10: 3227–3246, 1990. doi:10.1523/JNEUROSCI.10-10-03227.1990.
- Chillemi B, Barbi M, Di Garbo A. A network of interneurons coupled by electrical synapses behaves as a coincidence detector. In: *International Work-Conference on the Interplay Between Natural and Artificial Computation*, edited by Mira J, Álvarez JR, editors. Berlin, Germany: Springer, 2007, p. 81–89.
- Connors BW. Synchrony and so much more: Diverse roles for electrical synapses in neural circuits. *Dev Neurobiol* 77: 610–624, 2017. doi:10.1002/dneu.22493.
- Connors BW, Long MA. Electrical synapses in the mammalian brain. *Annu Rev Neurosci* 27: 393–418, 2004. doi:10.1146/annurev.neuro.26.041002.131128.
- Curti S, Hoge G, Nagy JI, Pereda AE. Synergy between electrical coupling and membrane properties promotes strong synchronization of neurons of the mesencephalic trigeminal nucleus. *J Neurosci* 32: 4341–4359, 2012. doi:10.1523/JNEUROSCI.6216-11.2012.
- Curti S, O'Brien J. Characteristics and plasticity of electrical synaptic transmission. *BMC Cell Biol* 17, Suppl 1: 13, 2016. doi:10.1186/s12860-016-0091-y.
- Datunashvili M, Chaudhary R, Zobeiri M, Lüttjohann A, Mergia E, Baumann A, Balfanz S, Budde B, van Luijcklaar G, Pape HC, Koelsing D, Budde T. Modulation of hyperpolarization-activated inward current and thalamic activity modes by different cyclic nucleotides. *Front Cell Neurosci* 12: 369, 2018. doi:10.3389/fncel.2018.00369.
- Del Negro CA, Chandler SH. Physiological and theoretical analysis of  $K^+$  currents controlling discharge in neonatal rat mesencephalic trigeminal neurons. *J Neurophysiol* 77: 537–553, 1997. doi:10.1152/jn.1997.77.2.537.
- Devor A, Yarom Y. Electrotonic coupling in the inferior olivary nucleus revealed by simultaneous double patch recordings. *J Neurophysiol* 87: 3048–3058, 2002. doi:10.1152/jn.2002.87.6.3048.
- DeVries SH, Qi X, Smith R, Makous W, Sterling P. Electrical coupling between mammalian cones. *Curr Biol* 12: 1900–1907, 2002. doi:10.1016/S0960-9822(02)01261-7.
- Di Garbo A, Barbi M, Chillemi S. Signal processing properties of fast spiking interneurons. *Biosystems* 86: 27–37, 2006. doi:10.1016/j.biosystems.2006.03.009.
- Dugué GP, Brunel N, Hakim V, Schwartz E, Chat M, Lévesque M, Courtemanche R, Léna C, Dieudonné S. Electrical coupling mediates tunable low-frequency oscillations and resonance in the cerebellar Golgi cell network. *Neuron* 61: 126–139, 2009. doi:10.1016/j.neuron.2008.11.028.
- Dyhrfeld-Johnsen J, Morgan RJ, Soltesz I. Double trouble? Potential for hyperexcitability following both channelopathic up- and downregulation of  $I(h)$  in epilepsy. *Front Neurosci* 3: 25–33, 2009. doi:10.3389/neuro.01.005.2009.
- Edwards DH, Yeh SR, Krasne FB. Neuronal coincidence detection by voltage-sensitive electrical synapses. *Proc Natl Acad Sci USA* 95: 7145–7150, 1998. doi:10.1073/pnas.95.12.7145.
- Enomoto A, Han JM, Hsiao CF, Chandler SH. Sodium currents in mesencephalic trigeminal neurons from  $Na_v1.6$  null mice. *J Neurophysiol* 98: 710–719, 2007. doi:10.1152/jn.00292.2007.
- Enomoto A, Han JM, Hsiao CF, Wu N, Chandler SH. Participation of sodium currents in burst generation and control of membrane excitability in mesencephalic trigeminal neurons. *J Neurosci* 26: 3412–3422, 2006. doi:10.1523/JNEUROSCI.5274-05.2006.
- Fan Y, Fricker D, Brager DH, Chen X, Lu HC, Chitwood RA, Johnston D. Activity-dependent decrease of excitability in rat hippocampal neurons through increases in  $I(h)$ . *Nat Neurosci* 8: 1542–1551, 2005. doi:10.1038/nn1568.
- Fleiderovich IA, Gutnick MJ. Kinetics of slow inactivation of persistent sodium current in layer V neurons of mouse neocortical slices. *J Neurophysiol* 76: 2125–2130, 1996. doi:10.1152/jn.1996.76.3.2125.

- Fontaine B, MacLeod KM, Lubejko ST, Steinberg LJ, Köppl C, Peña JL. Emergence of band-pass filtering through adaptive spiking in the owl's cochlear nucleus. *J Neurophysiol* 112: 430–445, 2014. doi:10.1152/jn.00132.2014.
- Forti L, Cesana E, Mapelli J, D'Angelo E. Ionic mechanisms of autorhythmic firing in rat cerebellar Golgi cells. *J Physiol* 574: 711–729, 2006. doi:10.1113/jphysiol.2006.110858.
- Galarreta M, Hestrin S. Spike transmission and synchrony detection in networks of GABAergic interneurons. *Science* 292: 2295–2299, 2001. doi:10.1126/science.1061395.
- Gettings PA. Modification of neuron properties by electrotonic synapses. I. Input resistance, time constant, and integration. *J Neurophysiol* 37: 846–857, 1974. doi:10.1152/jn.1974.37.5.846.
- Harnett MT, Magee JC, Williams SR. Distribution and function of HCN channels in the apical dendritic tuft of neocortical pyramidal neurons. *J Neurosci* 35: 1024–1037, 2015. doi:10.1523/JNEUROSCI.2813-14.2015.
- Hatton GI, Yang QZ. Synaptically released histamine increases dye coupling among vasopressinergic neurons of the supraoptic nucleus: mediation by H1 receptors and cyclic nucleotides. *J Neurosci* 16: 123–129, 1996. doi:10.1523/JNEUROSCI.16-01-00123.1996.
- Hines ML, Davison AP, Muller E. NEURON and Python. *Front Neuroinform* 3: 1, 2009. doi:10.3389/neuro.11.001.2009.
- Hjorth J, Blackwell KT, Kotaleski JH. Gap junctions between striatal fast-spiking interneurons regulate spiking activity and synchronization as a function of cortical activity. *J Neurosci* 29: 5276–5286, 2009. doi:10.1523/JNEUROSCI.6031-08.2009.
- Hough LB. Histamine. In: *Basic Neurochemistry*, edited by Siegel GJ. Philadelphia, PA: Lippincott-Raven, 1999, p. 293–313.
- Inagaki N, Yamatodani A, Shinoda K, Shiotani Y, Tohyama M, Watanabe T, Wada H. The histaminergic innervation of the mesencephalic nucleus of the trigeminal nerve in rat brain: a light and electron microscopical study. *Brain Res* 418: 388–391, 1987. doi:10.1016/0006-8993(87)90109-0.
- Ingram SL, Williams JT. Modulation of the hyperpolarization-activated current (I<sub>h</sub>) by cyclic nucleotides in guinea-pig primary afferent neurons. *J Physiol* 492: 97–106, 1996. doi:10.1113/jphysiol.1996.sp021292.
- Johnston J, Forsythe ID, Kopp-Scheinpluf G. Going native: voltage-gated potassium channels controlling neuronal excitability. *J Physiol* 588: 3187–3200, 2010. doi:10.1113/jphysiol.2010.191973.
- Joris PX, Smith PH, Yin TC. Coincidence detection in the auditory system: 50 years after Jeffress. *Neuron* 21: 1235–1238, 1998. doi:10.1016/S0896-6273(00)80643-1.
- Kang Y, Notomi T, Saito M, Zhang W, Shigemoto R. Bidirectional interactions between h-channels and Na<sup>+</sup>-K<sup>+</sup> pumps in mesencephalic trigeminal neurons. *J Neurosci* 24: 3694–3702, 2004. doi:10.1523/JNEUROSCI.5641-03.2004.
- Kanyshkova T, Pawlowski M, Meuth P, Dubé C, Bender RA, Brewster AL, Baumann A, Baram TZ, Pape HC, Budde T. Postnatal expression pattern of HCN channel isoforms in thalamic neurons: relationship to maturation of thalamocortical oscillations. *J Neurosci* 29: 8847–8857, 2009. doi:10.1523/JNEUROSCI.0689-09.2009.
- Kaupp UB, Seifert R. Cyclic nucleotide-gated ion channels. *Physiol Rev* 82: 769–824, 2002. doi:10.1152/physrev.00008.2002.
- Kawa F, Sterling P. cGMP modulates spike responses of retinal ganglion cells via a cGMP-gated current. *Vis Neurosci* 19: 373–380, 2002. doi:10.1017/S0952523802193138.
- Khakh BS, Henderson G. Hyperpolarization-activated cationic currents (I<sub>h</sub>) in neurones of the trigeminal mesencephalic nucleus of the rat. *J Physiol* 510: 695–704, 1998. doi:10.1111/j.1469-7793.1998.00695.x.
- Kolta A, Lund JP, Rossignol S. Modulation of activity of spindle afferents recorded in trigeminal mesencephalic nucleus of rabbit during fictive mastication. *J Neurophysiol* 64: 1067–1076, 1990. doi:10.1152/jn.1990.64.4.1067.
- König P, Engel AK, Singer W. Integrator or coincidence detector? The role of the cortical neuron revisited. *Trends Neurosci* 19: 130–137, 1996. doi:10.1016/S0166-2236(96)80019-1.
- Landisman CE, Long MA, Beierlein M, Deans MR, Paul DL, Connors BW. Electrical synapses in the thalamic reticular nucleus. *J Neurosci* 22: 1002–1009, 2002. doi:10.1523/JNEUROSCI.22-03-01002.2002.
- Lavigne G, Kim JS, Valiquette C, Lund JP. Evidence that periodontal pressoreceptors provide positive feedback to jaw closing muscles during mastication. *J Neurophysiol* 58: 342–358, 1987. doi:10.1152/jn.1987.58.2.342.
- Lazarov NE. Comparative analysis of the chemical neuroanatomy of the mammalian trigeminal ganglion and mesencephalic trigeminal nucleus. *Prog Neurobiol* 66: 19–59, 2002. doi:10.1016/S0301-0082(01)00021-1.
- Liem RS, Copray JC, van Willigen JD. Ultrastructure of the rat mesencephalic trigeminal nucleus. *Acta Anat (Basel)* 140: 112–119, 1991. doi:10.1159/000147045.
- Lippert A, Booth V. Understanding effects on excitability of simulated I (h) modulation in simple neuronal models. *Biol Cybern* 101: 297–306, 2009. doi:10.1007/s00422-009-0337-2.
- Lisman JE. Bursts as a unit of neural information: making unreliable synapses reliable. *Trends Neurosci* 20: 38–43, 1997. doi:10.1016/S0166-2236(96)10070-9.
- Lörincz A, Notomi T, Tamás G, Shigemoto R, Nusser Z. Polarized and compartment-dependent distribution of HCN1 in pyramidal cell dendrites. *Nat Neurosci* 5: 1185–1193, 2002. doi:10.1038/nn962.
- Lüthi A, McCormick DA. H-current: properties of a neuronal and network pacemaker. *Neuron* 21: 9–12, 1998. doi:10.1016/S0896-6273(00)80509-7.
- Maccaferri G, Mangoni M, Lazzari A, DiFrancesco D. Properties of the hyperpolarization-activated current in rat hippocampal CA1 pyramidal cells. *J Neurophysiol* 69: 2129–2136, 1993. doi:10.1152/jn.1993.69.6.2129.
- Maccaferri G, McBain CJ. The hyperpolarization-activated current (I<sub>h</sub>) and its contribution to pacemaker activity in rat CA1 hippocampal stratum oriens-alveus interneurons. *J Physiol* 497: 119–130, 1996. doi:10.1113/jphysiol.1996.sp021754.
- Magee JC. Dendritic hyperpolarization-activated currents modify the integrative properties of hippocampal CA1 pyramidal neurons. *J Neurosci* 18: 7613–7624, 1998. doi:10.1523/JNEUROSCI.18-19-07613.1998.
- Marder E. Electrical synapses: beyond speed and synchrony to computation. *Curr Biol* 8: R795–R797, 1998. doi:10.1016/S0960-9822(07)00502-7.
- McCormick DA, Pape HC. Noradrenergic and serotonergic modulation of a hyperpolarization-activated cation current in thalamic relay neurones. *J Physiol* 431: 319–342, 1990a. doi:10.1113/jphysiol.1990.sp018332.
- McCormick DA, Pape HC. Properties of a hyperpolarization-activated cation current and its role in rhythmic oscillation in thalamic relay neurones. *J Physiol* 431: 291–318, 1990b. doi:10.1113/jphysiol.1990.sp018331.
- Mendell LM, Henneman E. Terminals of single Ia fibers: location, density, and distribution within a pool of 300 homonymous motoneurons. *J Neurophysiol* 34: 171–187, 1971. doi:10.1152/jn.1971.34.1.171.
- Mercer A, Bannister AP, Thomson AM. Electrical coupling between pyramidal cells in adult cortical regions. *Brain Cell Biol* 35: 13–27, 2006. doi:10.1007/s11068-006-9005-9.
- Migliore M, Migliore R. Know your current I(h): interaction with a shunting current explains the puzzling effects of its pharmacological or pathological modulations. *PLoS One* 7: e36867, 2012. doi:10.1371/journal.pone.0036867.
- Morquette P, Lavoie R, Fhima MD, Lamoureux X, Verdier D, Kolta A. Generation of the masticatory central pattern and its modulation by sensory feedback. *Prog Neurobiol* 96: 340–355, 2012. doi:10.1016/j.pneurobio.2012.01.011.
- Müller F, Scholten A, Ivanova E, Haverkamp S, Kremmer E, Kaupp UB. HCN channels are expressed differentially in retinal bipolar cells and concentrated at synaptic terminals. *Eur J Neurosci* 17: 2084–2096, 2003. doi:10.1046/j.1460-9568.2003.02634.x.
- Nagy JI, Buss M, Daddona PE. On the innervation of trigeminal mesencephalic primary afferent neurons by adenosine deaminase-containing projections from the hypothalamus in the rat. *Neuroscience* 17: 141–156, 1986. doi:10.1016/0306-4522(86)90232-0.
- Notomi T, Shigemoto R. Immunohistochemical localization of I<sub>h</sub> channel subunits, HCN1–4, in the rat brain. *J Comp Neurol* 471: 241–276, 2004. doi:10.1002/cne.11039.
- Otsuka T, Kawaguchi Y. Common excitatory synaptic inputs to electrically connected cortical fast-spiking cell networks. *J Neurophysiol* 110: 795–806, 2013. doi:10.1152/jn.00071.2013.
- Pál B, Pór A, Szucs G, Kovács I, Rusznák Z. HCN channels contribute to the intrinsic activity of cochlear pyramidal cells. *Cell Mol Life Sci* 60: 2189–2199, 2003. doi:10.1007/s00018-003-3187-4.
- Pape HC. Queer current and pacemaker: the hyperpolarization-activated cation current in neurons. *Annu Rev Physiol* 58: 299–327, 1996. doi:10.1146/annurev.ph.58.030196.001503.
- Pedroarena CM, Pose IE, Yamuy J, Chase MH, Morales FR. Oscillatory membrane potential activity in the soma of a primary afferent neuron. *J Neurophysiol* 82: 1465–1476, 1999. doi:10.1152/jn.1999.82.3.1465.
- Perez Velazquez JL, Carlen PL. Gap junctions, synchrony and seizures. *Trends Neurosci* 23: 68–74, 2000. doi:10.1016/S0166-2236(99)01497-6.



- Poolos NP, Migliore M, Johnston D. Pharmacological upregulation of h-channels reduces the excitability of pyramidal neuron dendrites. *Nat Neurosci* 5: 767–774, 2002. doi:10.1038/nn891.
- Pose I, Sampogna S, Chase MH, Morales FR. Mesencephalic trigeminal neurons are innervated by nitric oxide synthase-containing fibers and respond to nitric oxide. *Brain Res* 960: 81–89, 2003. doi:10.1016/S0006-8993(02)03776-9.
- Publio R, Oliveira RF, Roque AC. A computational study on the role of gap junctions and rod Ih conductance in the enhancement of the dynamic range of the retina. *PLoS One* 4: e6970, 2009. doi:10.1371/journal.pone.0006970.
- Rabinowitch I, Chatzigeorgiou M, Schafer WR. A gap junction circuit enhances processing of coincident mechanosensory inputs. *Curr Biol* 23: 963–967, 2013. doi:10.1016/j.cub.2013.04.030.
- Rateau Y, Ropert N. Expression of a functional hyperpolarization-activated current ( $I_h$ ) in the mouse nucleus reticularis thalami. *J Neurophysiol* 95: 3073–3085, 2006. doi:10.1152/jn.00922.2005.
- Rela L, Szczupak L. Gap junctions: their importance for the dynamics of neural circuits. *Mol Neurobiol* 30: 341–357, 2004. doi:10.1385/MN:30:3:341.
- Reyes AD, Rubel EW, Spain WJ. In vitro analysis of optimal stimuli for phase-locking and time-delayed modulation of firing in avian nucleus laminaris neurons. *J Neurosci* 16: 993–1007, 1996. doi:10.1523/JNEUROSCI.16-03-00993.1996.
- Robinson RB, Siegelbaum SA. Hyperpolarization-activated cation currents: from molecules to physiological function. *Annu Rev Physiol* 65: 453–480, 2003. doi:10.1146/annurev.physiol.65.092101.142734.
- Rörig B, Sutor B. Nitric oxide-stimulated increase in intracellular cGMP modulates gap junction coupling in rat neocortex. *Neuroreport* 7: 569–572, 1996. doi:10.1097/00001756-199601310-00046.
- Rosenkranz JA, Johnston D. Dopaminergic regulation of neuronal excitability through modulation of Ih in layer V entorhinal cortex. *J Neurosci* 26: 3229–3244, 2006. doi:10.1523/JNEUROSCI.4333-05.2006.
- Roy SA, Alloway KD. Coincidence detection or temporal integration? What the neurons in somatosensory cortex are doing. *J Neurosci* 21: 2462–2473, 2001. doi:10.1523/JNEUROSCI.21-07-02462.2001.
- Saito M, Murai Y, Sato H, Bae YC, Akaike T, Takada M, Kang Y. Two opposing roles of 4-AP-sensitive  $K^+$  current in initiation and invasion of spikes in rat mesencephalic trigeminal neurons. *J Neurophysiol* 96: 1887–1901, 2006. doi:10.1152/jn.00176.2006.
- Schoppa NE, Westbrook GL. AMPA autoreceptors drive correlated spiking in olfactory bulb glomeruli. *Nat Neurosci* 5: 1194–1202, 2002. doi:10.1038/nn953.
- Schweighofer N, Doya K, Kawato M. Electrophysiological properties of inferior olive neurons: A compartmental model. *J Neurophysiol* 82: 804–817, 1999. doi:10.1152/jn.1999.82.2.804.
- Shin KS, Rothberg BS, Yellen G. Blocker state dependence and trapping in hyperpolarization-activated cation channels: evidence for an intracellular activation gate. *J Gen Physiol* 117: 91–101, 2001. doi:10.1085/jgp.117.2.91.
- Smith RG, Vardi N. Simulation of the AII amacrine cell of mammalian retina: functional consequences of electrical coupling and regenerative membrane properties. *Vis Neurosci* 12: 851–860, 1995. doi:10.1017/S095252380000941X.
- Stanek E IV, Cheng S, Takatoh J, Han BX, Wang F. Monosynaptic premotor circuit tracing reveals neural substrates for oro-motor coordination. *eLife* 3: e02511, 2014. doi:10.7554/eLife.02511.
- Sterling P, Demb JB. Retina, in *The Synaptic Organization of the Brain*, edited by Shepherd GM. New York: Oxford University Press, 2004, p. 217–269.
- Sterratt DC. Q10: the effect of temperature on ion channel kinetics. In: *Encyclopedia of Computational Neuroscience*, edited by Jaeger D, Jung R. New York: Springer, 2014, p. 2551–2552.
- Stuart G, Spruston N. Determinants of voltage attenuation in neocortical pyramidal neuron dendrites. *J Neurosci* 18: 3501–3510, 1998. doi:10.1523/JNEUROSCI.18-10-03501.1998.
- Tanaka S, Chandler SH. Serotonergic modulation of persistent sodium currents and membrane excitability via cyclic AMP-protein kinase A cascade in mesencephalic V neurons. *J Neurosci Res* 83: 1362–1372, 2006. doi:10.1002/jnr.20822.
- Tanaka S, Wu N, Hsiao CF, Turman J Jr, Chandler SH. Development of inward rectification and control of membrane excitability in mesencephalic V neurons. *J Neurophysiol* 89: 1288–1298, 2003. doi:10.1152/jn.00850.2002.
- Tang ZQ, Trussell LO. Serotonergic regulation of excitability of principal cells of the dorsal cochlear nucleus. *J Neurosci* 35: 4540–4551, 2015. doi:10.1523/JNEUROSCI.4825-14.2015.
- Trenholm S, McLaughlin AJ, Schwab DJ, Awatramani GB. Dynamic tuning of electrical and chemical synaptic transmission in a network of motion coding retinal neurons. *J Neurosci* 33: 14927–14938, 2013. doi:10.1523/JNEUROSCI.0808-13.2013.
- Tsay D, Dudman JT, Siegelbaum SA. HCN1 channels constrain synaptically evoked  $Ca^{2+}$  spikes in distal dendrites of CA1 pyramidal neurons. *Neuron* 56: 1076–1089, 2007. doi:10.1016/j.neuron.2007.11.015.
- Tsien JZ. Linking Hebb's coincidence-detection to memory formation. *Curr Opin Neurobiol* 10: 266–273, 2000. doi:10.1016/S0959-4388(00)00070-2.
- Tu H, Deng L, Sun Q, Yao L, Han J-S, Wan Y. Hyperpolarization-activated, cyclic nucleotide-gated cation channels: roles in the differential electrophysiological properties of rat primary afferent neurons. *J Neurosci Res* 76: 713–722, 2004. doi:10.1002/jnr.20109.
- Usrey WM, Alonso JM, Reid RC. Synaptic interactions between thalamic inputs to simple cells in cat visual cortex. *J Neurosci* 20: 5461–5467, 2000. doi:10.1523/JNEUROSCI.20-14-05461.2000.
- van Welie I, Roth A, Ho SSN, Komai S, Häusser M. Conditional spike transmission mediated by electrical coupling ensures millisecond precision-correlated activity among interneurons in vivo. *Neuron* 90: 810–823, 2016. doi:10.1016/j.neuron.2016.04.013.
- Verdier D, Lund JP, Kolta A. Synaptic inputs to trigeminal primary afferent neurons cause firing and modulate intrinsic oscillatory activity. *J Neurophysiol* 92: 2444–2455, 2004. doi:10.1152/jn.00279.2004.
- Veruki ML, Hartveit E. AII (Rod) amacrine cells form a network of electrically coupled interneurons in the mammalian retina. *Neuron* 33: 935–946, 2002a. doi:10.1016/S0896-6273(02)00609-8.
- Veruki ML, Hartveit E. Electrical synapses mediate signal transmission in the rod pathway of the mammalian retina. *J Neurosci* 22: 10558–10566, 2002b. doi:10.1523/JNEUROSCI.22-24-10558.2002.
- Vervaeke K, Lőrincz A, Gleeson P, Farinella M, Nusser Z, Silver RA. Rapid desynchronization of an electrically coupled interneuron network with sparse excitatory synaptic input. *Neuron* 67: 435–451, 2010. doi:10.1016/j.neuron.2010.06.028.
- Wang LY, Gan L, Forsythe ID, Kaczmarek LK. Contribution of the Kv3.1 potassium channel to high-frequency firing in mouse auditory neurons. *J Physiol* 509: 183–194, 1998. doi:10.1111/j.1469-7793.1998.183bo.x.
- Wang M, Ramos BP, Paspalas CD, Shu Y, Simen A, Duque A, Vijayraghavan S, Brennan A, Dudley A, Nou E, Mazer JA, McCormick DA, Arnsten AF.  $\alpha 2A$ -adrenoceptors strengthen working memory networks by inhibiting cAMP-HCN channel signaling in prefrontal cortex. *Cell* 129: 397–410, 2007. doi:10.1016/j.cell.2007.03.015.
- Wang Y, Barakat A, Zhou H. Electrotonic coupling between pyramidal neurons in the neocortex. *PLoS One* 5: e10253, 2010. doi:10.1371/journal.pone.0010253.
- Williams SR, Stuart GJ. Site independence of EPSP time course is mediated by dendritic  $I_h$  in neocortical pyramidal neurons. *J Neurophysiol* 83: 3177–3182, 2000. doi:10.1152/jn.2000.83.5.3177.
- Wilson GW, Garthwaite J. Hyperpolarization-activated ion channels as targets for nitric oxide signalling in deep cerebellar nuclei. *Eur J Neurosci* 31: 1935–1945, 2010. doi:10.1111/j.1460-9568.2010.07226.x.
- Wu N, Enomoto A, Tanaka S, Hsiao CF, Nykamp DQ, Izhikevich E, Chandler SH. Persistent sodium currents in mesencephalic v neurons participate in burst generation and control of membrane excitability. *J Neurophysiol* 93: 2710–2722, 2005. doi:10.1152/jn.00636.2004.
- Wu N, Hsiao CF, Chandler SH. Membrane resonance and subthreshold membrane oscillations in mesencephalic V neurons: participants in burst generation. *J Neurosci* 21: 3729–3739, 2001. doi:10.1523/JNEUROSCI.21-11-03729.2001.
- Wu S, Gao W, Xie C, Xu X, Vorvis C, Marni F, Hackett AR, Liu Q, Zhou L. Inner activation gate in S6 contributes to the state-dependent binding of cAMP in full-length HCN2 channel. *J Gen Physiol* 140: 29–39, 2012. doi:10.1085/jgp.201110749.
- Yamamoto T, Matsuo R, Kiyomitsu Y, Kitamura R. Sensory and motor responses of trigeminal and reticular neurons during ingestive behavior in rats. *Exp Brain Res* 76: 386–400, 1989. doi:10.1007/BF00247896.
- Yang J, Xing JL, Wu NP, Liu YH, Zhang CZ, Kuang F, Han VZ, Hu SJ. Membrane current-based mechanisms for excitability transitions in neurons of the rat mesencephalic trigeminal nuclei. *Neuroscience* 163: 799–810, 2009. doi:10.1016/j.neuroscience.2009.07.007.
- Yang QZ, Hatton GL. Nitric oxide via cGMP-dependent mechanisms increases dye coupling and excitability of rat supraoptic nucleus neurons. *J Neurosci* 19: 4270–4279, 1999. doi:10.1523/JNEUROSCI.19-11-04270.1999.

## Chapter 4

# Activity-induced gap junctions plasticity

In this chapter, we show that the coupling coefficient presents a large variety in the population of mesencephalic trigeminal (MesV) neurons, and that part of this diversity can be explained by the heterogeneity of their gap junction (GJ) conductances  $g_J$ , suggesting that these electrical synapses are regulated in the living animal. Indeed, the firing activity of MesV neurons triggers the plasticity of these contacts, that leads to a decrease of the coupling coefficient and  $g_J$ . The plasticity of  $g_J$  was thoroughly characterized while keeping the cells in the whole-cell voltage clamp configuration, stimulating them with an activity-like protocol. We found that the depression of  $g_J$  is accumulative during the repetitive stimulation and saturates to  $\sim 30\%$  in approximately 5 minutes. This effect is mainly transient, with a long-term component of  $\sim 10\%$ . After partial (but stable) recovery of  $g_J$ , a second repetitive stimulation provokes a deeper decrease in  $g_J$ , with similar qualitative characteristics. Interestingly, stimulation of only one cell does not affect the non-rectifying properties of the synaptic contact and produced half of the  $g_J$  depression, suggesting a side-additive effect. Moreover, activity-like stimulation at physiological temperature elicits a long-term synaptic depression of 30%. Free  $\text{Ca}^{2+}$  is involved in the induction of the plasticity, but its absence does not completely abolish it. Furthermore, calcium current through the hyperpolarization-activated cyclic nucleotide-gated channels and NMDA receptors is sufficient to modify  $g_J$ , even without electrical stimulation. The repeated activity seems to trigger the synthesis of endocannabinoids, which bind to the cannabinoid receptor 1, preventing a more drastic drop of  $g_J$ . At the intracellular level, activation of protein kinase A also decreases  $g_J$ , but does not participate in the activity-induced plasticity. Finally, by blocking exocytosis, we show that there is a basal turnover of GJ, with a time constant compatible with the activity-induced plasticity.



## 4.1 Introduction

The operation of the electrical synapses is dictated by the GJ and the intrinsic properties of the coupled neurons (see section 2.3). In the previous chapter, we analyzed the impact of the  $I_H$  current -and its modulation by cGMP- on the electrical synaptic transmission between MesV neurons. Here, we focus on the regulation and plasticity of mammalian Cx36-based GJ, which has been extensively studied in expression systems (Srinivas et al., 1999; Alev et al., 2008; González-Nieto et al., 2008; Li et al., 2009; del Corso et al., 2012; Siu et al., 2016; Aseervatham et al., 2020; Kotova et al., 2020), and in native systems as well (Urschel et al., 2006; Zsiros and Maccaferri, 2008; Haas et al., 2011; Turecek et al., 2014; Mathy et al., 2014; Wang et al., 2015; Sevetson et al., 2017; Bazzigaluppi et al., 2017; Fricker et al., 2021), shedding light on their mechanisms and functional impact (see sections 2.2.2 and 2.5). However, while both approaches have strenghts, they also present severe drawbacks: while the expression systems lack signaling pathways present in native systems, they are amenable to accurate measurements of relevant variables, such as  $g_J$ . Native systems render important information on the functional impact of the regulation and plasticity of electrical synapses, but it is technically difficult to monitor and control key experimental variables, like the transjunctional potential  $V_J$  across the GJ. In contrast, the MesV nucleus constitutes an optimal model to study electrical synapses, given that it is a native system where both components of the electrical synapse can be electrophysiologically dissected, due to the simple morphology of its neurons (Dessem and Taylor, 1989) and somatic GJ (Curti et al., 2012). These primary afferents receive sensory information from the jaw closing muscles (Shigenaga et al., 1988a; Luo et al., 1995) and the periodontal ligament (Shigenaga et al., 1988b), and fire trains of action potential during eating behaviors (Yamamoto et al., 1989; Westberg et al., 2000). The aim of the present study was to understand the mechanisms involved in the induction and expression of the electrical synaptic plasticity triggered by activity in the MesV nucleus of rodents. Electrical coupling strength depends on both  $g_J$  and the intrinsic properties (see section 2.3), which will be analyzed in this chapter and the next one, respectively.

## 4.2 Materials and methods

The experimental protocol was approved by the local animal ethics committee of Facultad de Medicina, according to the guidelines of Comisión Honoraria de Experimentación Animal of Universidad de la República (Uruguay), with minimization of the numbers of animals used.

### 4.2.1 Experimental design

Transverse brain stem slices were prepared from C57 mice, Sprague-Dawley rats or Pan-nexin 1 knock-out mice (donated by Verónica Abudara) of either sex (age: postnatal days 11 to 21), which were decapitated without anesthesia. Their brains were quickly removed and placed in cold ( $\sim 4^{\circ}\text{C}$ ) sucrose solution containing the following (in mM): 213 sucrose, 2.69 KCl, 1.25  $\text{NaH}_2\text{PO}_4$ , 26  $\text{NaHCO}_3$ , 10 glucose, 1  $\text{CaCl}_2$ , 2  $\text{MgSO}_4$ , 0.35 ascorbic acid and 0.3 pyruvic acid, bubbled with 95%  $\text{O}_2$ -5%  $\text{CO}_2$  ( $\text{pH} \sim 7.4$ ). The portion of the brainstem containing the MesV was glued, by its rostral face, to the stage of a vibratome DSK DTK-1000, and transversally sliced at 170-250  $\mu\text{m}$ . The slices were then quickly transferred to an incubation chamber -at  $\sim 34^{\circ}\text{C}$ - with physiological solution (ACSF) containing the following (in mM): 122.75 NaCl, 3.94 KCl, 1.25  $\text{NaH}_2\text{PO}_4$ , 26  $\text{NaHCO}_3$ , 10 glucose, 2  $\text{CaCl}_2$ , and 2  $\text{MgSO}_4$  bubbled with 95%  $\text{O}_2$ -5%  $\text{CO}_2$  ( $\text{pH} \sim 7.4$ ), where they were kept for 30 minutes. After the heat shock, we leave them to converge to room temperature ( $\sim 20$ - $25^{\circ}\text{C}$ ) until they were transferred to the recording chamber, which has perfused with ACSF. The materials and methods used to identify and electrically record MesV neurons were the same already reported in chapter 3. Only neurons with stable resting membrane potential (RMP) below -48 mV were recorded, using the Multiclamp 700B amplifier (Molecular Devices, Sunnyvale, CA). Recoding pipettes were pulled from borosilicate glass (4-8  $\text{M}\Omega$ ), using Sutter P-87 or Narishige PC-100 pullers. Data were analyzed in the scientific Python development environment Spyder, using the following Python libraries: Numpy, Scipy, Axographio, Stfio, Pandas, Matplotlib and Seaborn.

Experimental drugs were either added to the intracellular recording solution [10  $\mu\text{M}$  KN93; 250 nM Botulinum toxin light chain E; 10 mM 1,2-Bis(o-aminophenoxy)ethane-N,N,N',N'-tetraacetic acid (BAPTA, donated by Gonzalo Pizarro); 1 mM SQ22536] or in the bath [5  $\mu\text{M}$  AM251; 40  $\mu\text{M}$  Forskolin; 50-300  $\mu\text{M}$  N-Methyl-D-aspartate (NMDA); 1-10  $\mu\text{M}$  glycine; CsCl 2-5 mM].

## 4.2.2 Data processing

Except the gap junction conductance, the remaining parameters (coupling coefficient, input resistance, RMP, etc.) were calculated according to procedures reported elsewhere (Curti et al., 2012; Davoine and Curti, 2019).

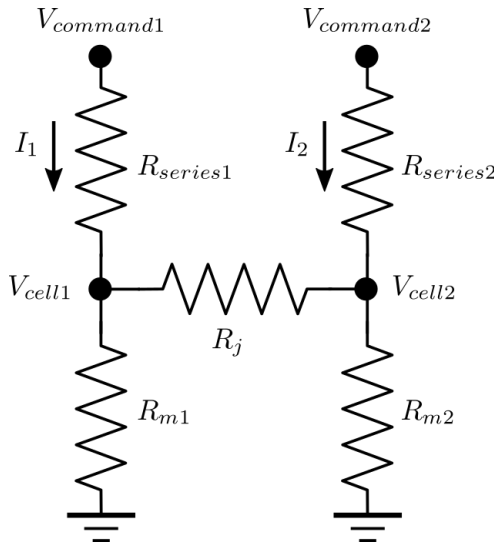
## 4.2.3 Calculation of the gap junction conductance

The gap junction conductance  $g_J$  between MesV neurons was estimated from current clamp traces according to the procedure detailed in chapter 3 (Bennett, 1966). In the voltage clamp configuration, we applied to one cell voltage steps of -5 to -50 mV of amplitude during 10-20 ms, while keeping its coupled partner at a holding potential close to the RMP. The series resistance  $R_s$  ( $\sim 4$ -5 M $\Omega$ ) was 80% online compensated, and the remaining 20% was done offline, according to the following procedure:

Given two coupled cells in voltage clamp, their membrane potentials  $V_{cell}$  are:

$$\begin{aligned} V_{cell1} &= V_1 = V_{comm1} - I_1 R_{s1} \\ V_{cell2} &= V_2 = V_{comm2} - I_2 R_{s2} \end{aligned}$$

where, for each cell,  $V_{comm1,2}$  are the corresponding amplifier's commands,  $I_{1,2}$  are the currents through each pipette (positive is going from the amplifier to the cell) and  $R_{s1,2}$  are their uncompensated series resistances (20% of their nominal values).



Schematic representation of the electrical circuit during simultaneous voltage-clamp recordings from a coupled pair.  $R_J = \frac{1}{g_J}$  denotes the junctional resistance of the GJ.

Suppose that the cell 1 is stepped and cell 2 remains clamped at a holding potential. The differential equation for the voltage  $V_2$  on cell 2 is:

$$C_2 \frac{dV_2}{dt} = I_2 - \sum_i g_i (V_2 - E_i) - g_J (V_2 - V_1) = 0 \Rightarrow I_2 = \sum_i g_i (V_2 - E_i) + g_J (V_2 - V_1)$$

given that  $V_2$  is held constant before and during the pulse (after the transient response to the change).  $g_i$  denote the ionic channel conductances and  $E_i$  their reverse potentials.

Therefore, the current response in cell 2  $\Delta I_2$  due to the voltage step  $\Delta V_{comm1}$  in cell 1 is<sup>1</sup>:

$$\Delta I_2 \approx g_J (\Delta V_2 - \Delta V_1) = g_J (-\Delta I_2 R_{s2} - \Delta V_{comm1} + \Delta I_1 R_{s1}) \quad (4.1)$$

Thus, the gap junction conductance  $g_J$  obtained from voltage clamp recordings is:

$$g_J = \frac{\Delta I_2}{-\Delta I_2 R_{s2} - \Delta V_{comm1} + \Delta I_1 R_{s1}} \quad (4.2)$$

#### 4.2.4 Temperature dependence of $g_J$ in MesV neurons

A TC2BIP controller with HI-25p heater and HPRE2 pre-heater (Cell MicroControls, Norfolk, VA) were used to modify the temperature of the recording chamber, always in the ascending direction. Immediately after reaching the set temperature, series resistance was online compensated by 80% and then  $g_J$  recordings were performed.

We characterized the temperature dependence of  $g_J$  in the population of MesV neurons, between 20 and 36°C. We found that the GJ  $Q_{10} = 2.04$  (Fig. 4.1), well above the values reported for GJ composed by Cx43 (Bukauskas and Weingart, 1993), Cx40 and Cx45 (Santos-Miranda et al., 2019), but smaller than the  $Q_{10}$  measured in the lateral giant axon of the crayfish (Payton et al., 1969). Given that we measured a  $Q_{10} > 1.5$ , the temperature-increase of the GJ conductance could not be attributed only to the thermal component of the aqueous diffusion of ions and viscosity of water (Hille, 2001). However, more thorough work<sup>2</sup> should be done to discern if the steep temperature-dependence of  $g_J$  was mostly due to structural changes on its conformation or to up/down regulations of intracellular cascades that are involved in Cx36 regulation (see section 2.2.2).

For our objectives, the measured  $Q_{10}$  represents the net temperature coefficient for the GJ in MesV neurons, and was used in section 4.3.2 to normalize the  $g_J$  measurements

---

<sup>1</sup>Here, we neglect the modifications of the postsynaptic ionic conductances  $g_i$  due to the small change in membrane potential  $\Delta V_2$ .

<sup>2</sup>For example, measure macroscopic  $I_J$  in the presence of inhibitors of regulatory proteins (such as CaMKII, PKA, etc.) and/or single channel conductance  $\gamma_J$  recordings, at different temperatures.

made in control conditions to the same temperature:  $T = 25^{\circ}\text{C}$ .

#### **4.2.5 Statistical analysis**

Results were expressed as average value  $\pm$  standard error of the mean (SEM). Two-tailed Student t-test from the Scipy library was used to quantify the statistical difference between data distributions. Statistical significance was established when the p-value  $P$  was below 0.05. Except explicitly noted, the data is presented in terms of cells or coupling directions.

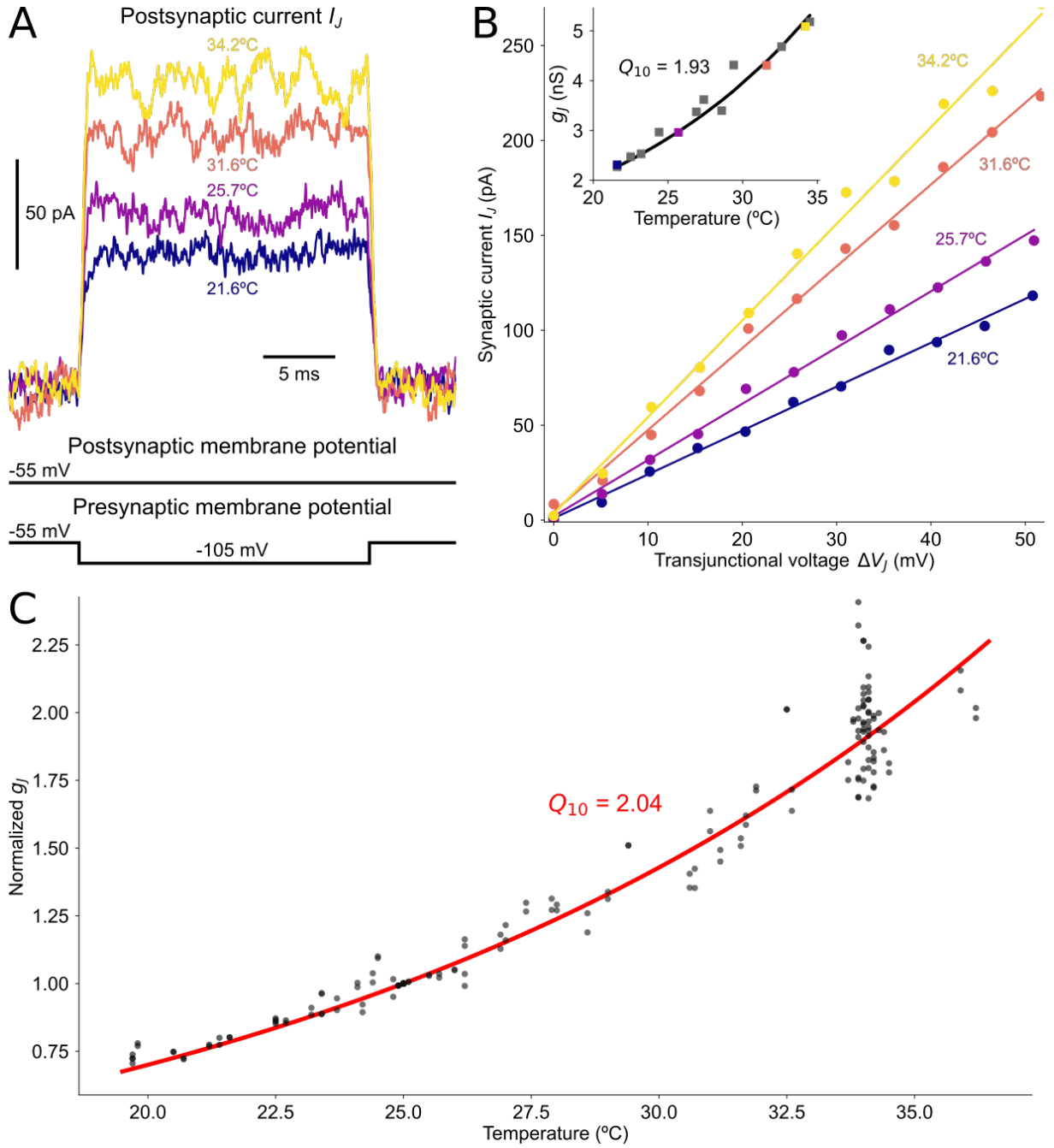


**Figure 4.1: Temperature dependence of  $g_J$  in MesV neurons.** *A*: synaptic current  $I_J$  increases with temperature. *B*: average  $I_J$  plotted against transjunctional voltage  $\Delta V_J$ , for different temperatures. Inset: the exponential fit of  $g_J$  against temperature resulted on  $Q_{10} = 1.93$ . *C*: the  $g_J$  measurements for each direction were normalized to 25°C and fitted to an exponential, obtaining  $Q_{10} = 2.04 \pm 0.03$  (range 1.61-2.58,  $n = 40$  directions from 11 animals).

## 4.3 Results

### 4.3.1 Characteristics and impact of electrical coupling between MesV neurons

In general terms, the electrical coupling between mice MesV neurons has similar characteristics to those described in rats (Curti et al., 2012): the cells are mostly coupled in pairs, by somatic gap junctions (GJ) (Fig. 4.2A). The injection of a negative current in one cell produced an hyperpolarizing voltage deflection in it and its coupled neighbor (Fig. 4.2B). The ratio between these voltage responses (see Materials and methods) defines the coupling coefficient (CC) for each direction, which averaged  $0.292 \pm 0.010$  for  $n = 264$  directions (Fig 4.2C), remarkably similar to that reported in rats (0.28) (Curti et al., 2012). Given that the CC depends on both intrinsic and synaptic properties (see 2.4), which could be different for each cell in a coupled pair, asymmetries of the CC between directions can be expected, with a preferred one whose CC is larger than in the opposite direction. However, no significant asymmetry could be found, as indicated by the plot of the larger CC against the lower CC for each pair (slope of linear regression of 1.089,  $R^2 = 0.8$ ,  $n = 132$  pairs; Fig. 4.2D). Despite its large average value for the population of recorded pairs, the CC displayed a broad distribution: ranging from 0.015 to 0.664 (Fig. 4.2E). One possible cause for this heterogeneity could be the different electrophysiological and/or morphological properties of the recorded MesV neurons, due to the dispersion of the animals' age range. Nonetheless, Figure 4.2F shows that the coupling coefficient spread was quite underlying from 12 to 18 postnatal days of age (P12 to P18, respectively). Another factor behind the heterogeneity of CC could be the recording temperature (see color reference for each data point on the right of Fig. 4.2F). However, CC from animals of 15 days (P15) obtained at 25°C was still very widely varied. Consistently, we also found a large variability in the spike transmission (Fig. 4.3). Therefore, we conclude that the CC is very heterogeneous in the mice MesV neurons' population.

The electrical coupling also affects the behavior of individual neurons, because of the “loading effect” (see chapter 3). In the current clamp configuration, the input resistance  $R_{in}$  of a single neuron was measured by applying several negative current steps and measuring the corresponding membrane potentials at the time of the peak of the most hyperpolarized response (Fig. 4.4A).  $R_{in}$  was obtained as the slope of this relationship (Fig. 4.4B), averaging  $123.99 \pm 5.17 \text{ M}\Omega$  for uncoupled neurons, ranging from 36.89 to 223.71  $\text{M}\Omega$  (Fig. 4.4C;  $n = 77$  neurons from 46 animals). In electrically coupled cells, the leak of current through the GJ diminished their effective  $R_{in}$  due to the loading effect (displayed in green in Fig. 4.4D). There was a remarkable similarity between the effective



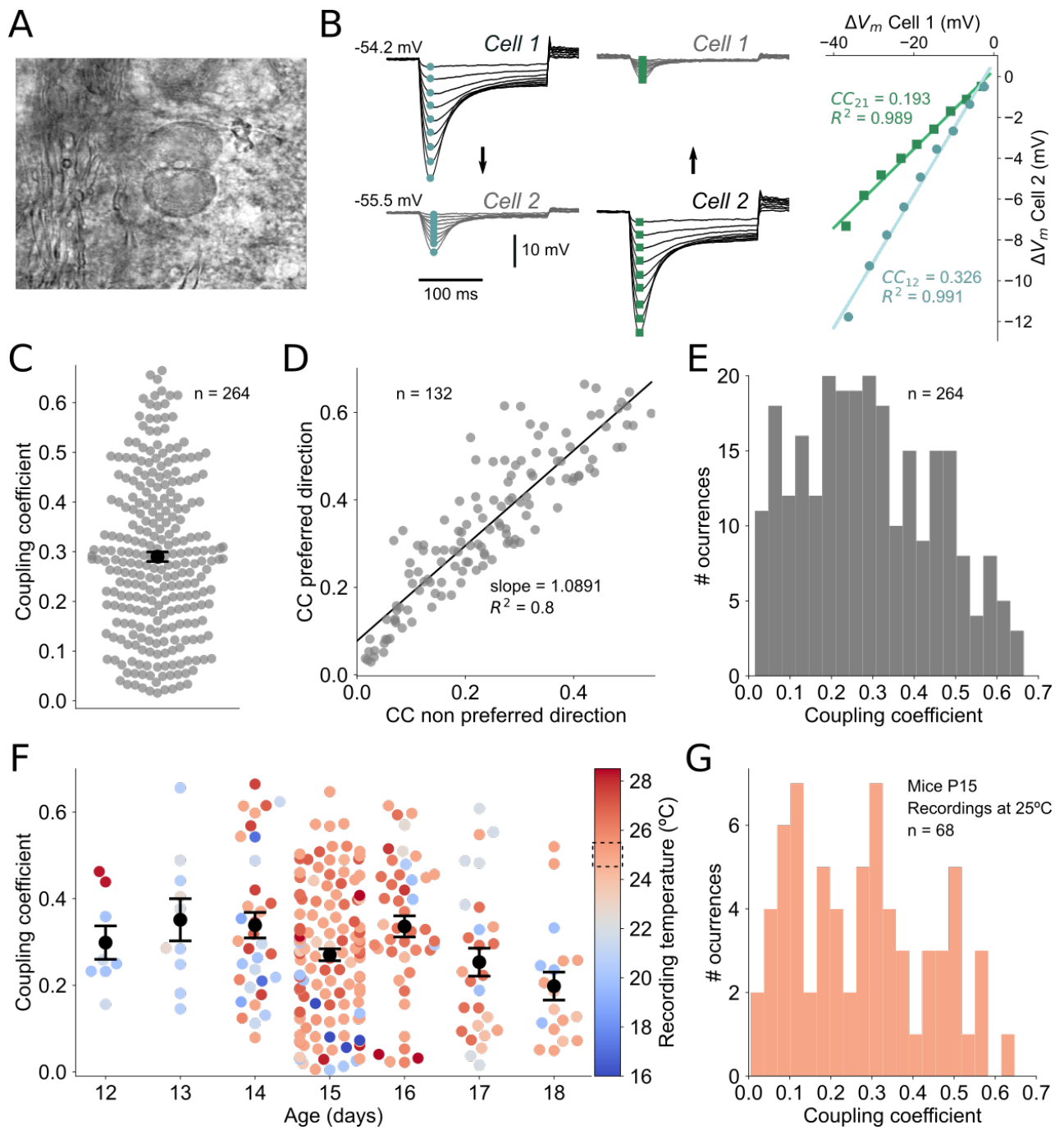


**Figure 4.2:** (Continued on the following page.)

**Figure 4.2: Coupling coefficient is heterogeneous in the population of MesV neurons.** *A*: IR-DIC image of two MesV neurons electrically coupled at their somas. *B*: left: a negative current injection (not shown) into one MesV neuron produced a hyperpolarizing voltage response in it (black trace) and in the coupled one (gray), in either direction. Right: the coupling coefficient (CC) was measured as the slope of the ratio between the pre and postsynaptic responses (left: turquoise circles on one direction, dark green squares in the other one). *C*: the CC of coupled MesV neurons was  $0.292 \pm 0.010$ . *D*: even defining, for each coupled pair, a preferred direction whose CC was larger, the CC was very symmetrical (slope of linear regression of 1.089,  $R^2 = 0.8$ ). *E*: histogram representing the broad distribution of CC in the MesV neurons' population, that ranges from 0.015 to 0.664. *F*: mean CC was quite constant for animals between 12 and 18 days old: P12  $0.298 \pm 0.039$  ( $n = 8$  directions), P13  $0.351 \pm 0.049$  ( $n = 10$ ), P14  $0.339 \pm 0.030$  ( $n = 34$ ), P15  $0.273 \pm 0.014$  ( $n = 124$ ), P16  $0.34 \pm 0.024$  ( $n = 44$ ), P17  $0.253 \pm 0.032$  ( $n = 28$ ), P18  $0.198 \pm 0.032$  ( $n = 18$ ). Note that the CC was measured at different temperatures (from 19 to 28°C, see color bar on the right), so statistical comparisons may not be informative. *G*: the CC heterogeneity even manifests even when we only consider recordings made at 25°C from P15 mice ( $n = 68$  directions). From *C* to *E*,  $n = 264$  directions were considered (132 pairs in *D*), from 76 animals. In *F*, data from p11 animals were omitted, because of their scarcity (4 directions from 2 pairs, from 2 animals).

$R_{in}$  of coupled neurons: linear regression slope = 1.0064,  $R^2 = 0.62$ ,  $n = 238$  neurons (not shown). However, the loading effect disappeared if the current steps were injected simultaneously to both coupled cells (blue in Fig. 4.4D), as their membrane potentials tend to be similar, almost eliminating the transjunctional voltage  $V_J$ . Interestingly, the  $R_{in}$  recorded when cells were “unloaded” displayed non significant difference to those obtained for isolated uncoupled cells ( $P = 0.229$  unpaired t-test, for  $n = 77$  uncoupled vs 228 unloaded coupled neurons, not shown). For  $n = 232$  neurons (from 73 animals), the decrease of the  $R_{in}$  caused by the loading effect was significant ( $P < 1 \times 10^{-3}$ , paired t-test): when the cells were unloaded,  $R_{in}$  was  $118.12 \pm 2.34 \text{ M}\Omega$  (range 59.23-254.46 M $\Omega$ ) and  $94.46 \pm 2.28 \text{ M}\Omega$  (range 36.93-246.26 M $\Omega$ ) when they were loaded. The difference of the  $R_{in}$  of both cases divided by the loaded  $R_{in}$  defines the loading effect, that was quite large in average ( $28.46 \pm 1.13\%$ ) and extremely variable for MesV neurons (range 0.01-111.02%). Note that a loading of 100% means that electrical coupling diminishes the  $R_{in}$  by half. In summary, electrical coupling is very important in setting the input resistance of MesV neurons.

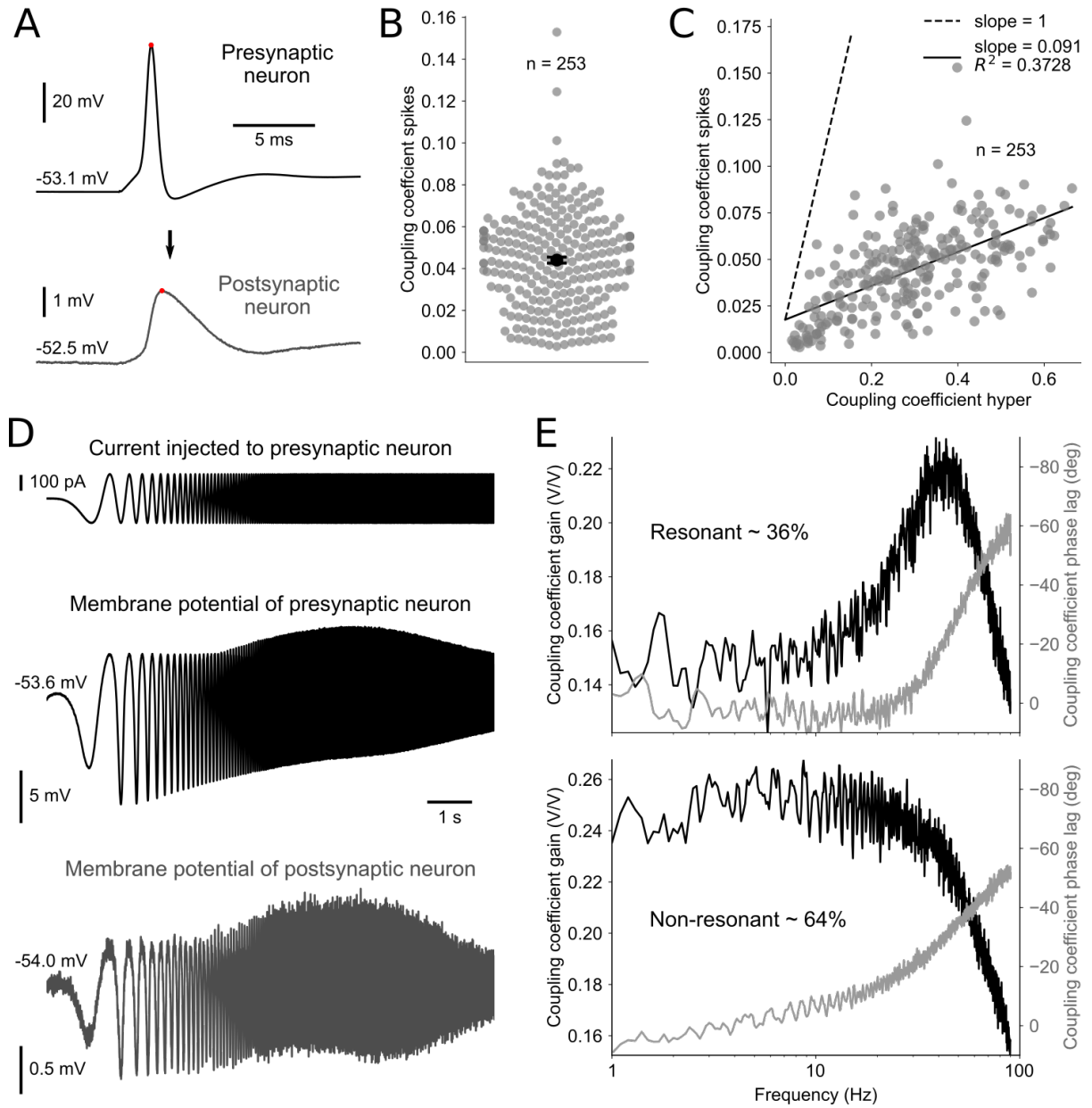


**Figure 4.3: Characteristics of spike transmission.** *A*: a presynaptic spike in a MesV neuron (black trace) elicits a subthreshold response in the coupled one (gray). The ratio between the peaks (red points) of the post and presynaptic voltage traces define the coupling coefficient for spikes. *B*: the CC mean was  $0.044 \pm 0.001$  (range 0.003-0.153). *C*: the CC for spikes correlated poorly with the CC defined by hyperpolarizing peaks (Fig. 4.2,  $R^2 = 0.33$ ).  $n = 253$  directions and 76 animals were used for *B* and *C*. *D*: CC below 0.001 were not considered in this analysis. *D*: the frequency properties of the CC were determined by injecting a ZAP current in the presynaptic neuron and recording the membrane potentials of both coupled neurons. *E*: the ratio of the FFT of the post and presynaptic membrane potentials gave the attenuation (black) and phase lag (gray) of the CC(f), which can be qualitatively classified as resonant (13 in 36 directions) or non-resonant (23 in 36).

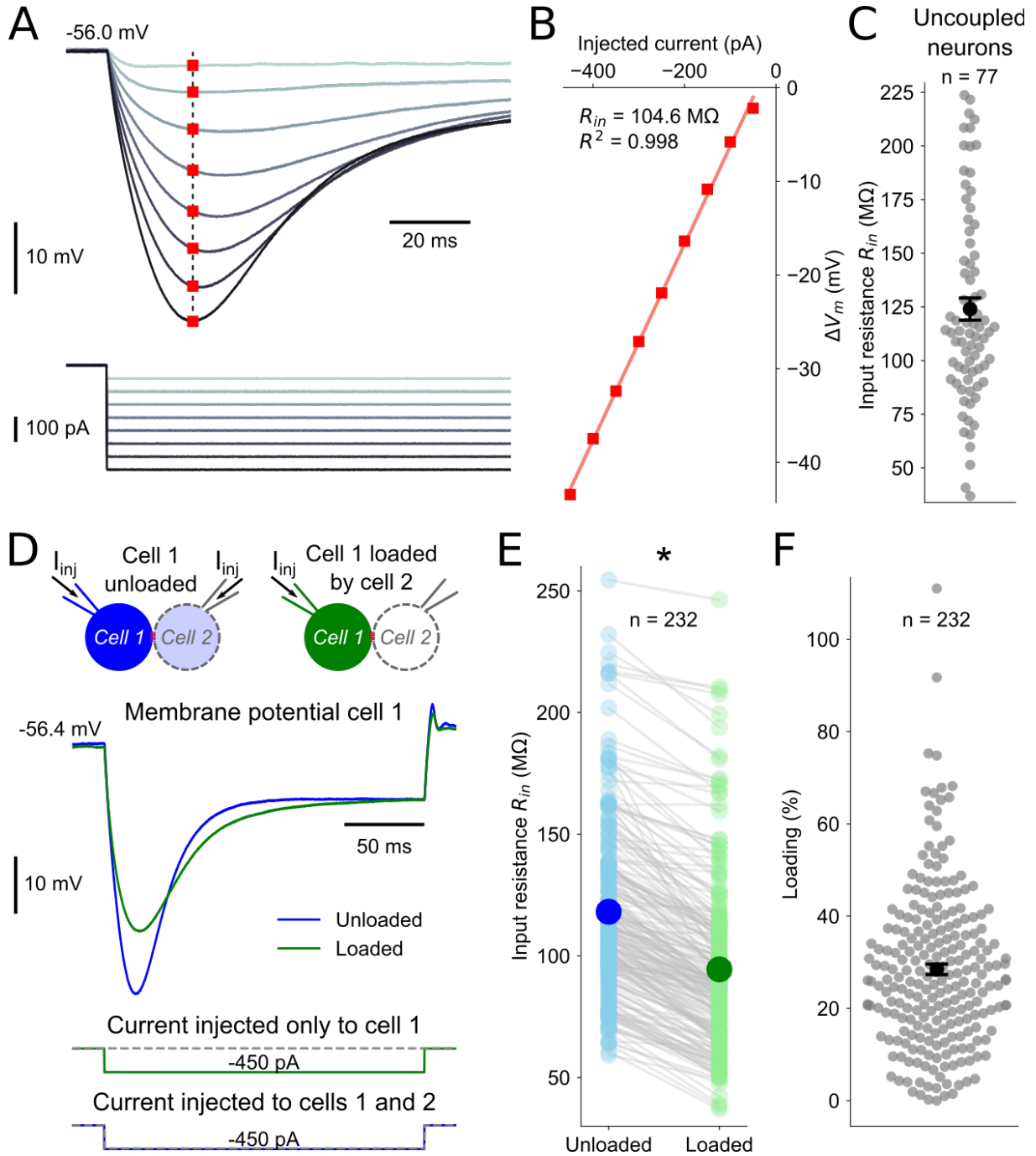


**Figure 4.4: The impact of electrical coupling on the effective input resistance is extremely varied.** *A*: the input resistance  $R_{in}$  of a neuron was measured by recording the voltage responses to the injection of hyperpolarizing current pulses. *B*: the voltage values isochronous to the peak of the most negative response (see red squares in *A*) are fitted to a line, whose slope was the  $R_{in}$ . *C*: for uncoupled MesV neurons,  $R_{in} = 123.99 \pm 5.17 \text{ M}\Omega$  ( $n = 77$  neurons from 46 animals). *D*: the voltage response to a current injection in cell 1 was smaller if its coupled partner cell 2 was not simultaneously stimulated, due a leak of current through the GJ. That was designated “loading effect”. *E*: the  $R_{in}$  of neurons loaded were significantly larger than when they are unloaded:  $118.12 \pm 2.34 \text{ M}\Omega$  versus  $94.46 \pm 2.28 \text{ M}\Omega$  ( $P < 1 \times 10^{-3}$ , paired t-test). *F*: the loading effect can be quantified as the difference between the unloaded and loaded  $R_{in}$ , divided by the loaded one, was  $28.46 \pm 1.13\%$ . For both *E* and *F*, the same  $n = 232$  neurons from 73 animals were used.

### 4.3.2 Gap junction conductance $g_J$ is heterogeneous in the MesV neurons population

Next, we asked if the variability of both CC and loading effect could be an indicator of mechanisms under regulation in the MesV neurons population. The gap junction conductance  $g_J$  plays a critical role in determining both, so we systematically measured it, by applying voltage steps to one cell, while keeping its coupled partner at a holding potential close to the RMP (Fig. 4.5A). In this and all the remaining voltage clamp experiments, the series resistances of both cells were continuously monitored, compensated online by 80%, and offline by 20% (see Materials and methods).  $g_J$  was obtained as the slope of the relationship between the mean synaptic current  $I_J$  -which was identical to the postsynaptic membrane current- and the transjunctional voltage difference  $V_J$  (Fig. 4.5B).  $g_J$  can also be inferred from current clamp traces (Bennett, 1966), but we found that this method overestimates by 10% (Fig. 4.5C) and was less precise, producing a 28% asymmetry of  $g_J$  between directions (linear regression slope 1.2763,  $R^2 = 0.858$ ,  $n = 268$  neurons, not shown). Thus, voltage clamp recordings will be used to compute  $g_J$  along this paper, unless specifically noted. There was no rectification in  $g_J$  (slope of linear correlation 1.01,  $R^2 = 0.996$ ; Fig. 4.5C), as expected from the homotypic GJ in MesV formed by Cx36 (Curti et al., 2012; Nagy and Lynn, 2018).

Figure 4.5E shows that  $g_J$  spans a large range of values, even after this temperature normalization: from 0.03 to 10.40 nS ( $n = 602$  directions). The wide spread of  $g_J$  was present for animals of the same age (Fig. 4.5F) and even within the same animal (examples from 3 animals in Fig. 4.5G). Another key observation was that the distribution of  $g_J$  displays not significant difference between ages, suggesting that the GJ was already completely developed at 11 days of age. This was consistent with the reported incidence of tracer coupling between rat MesV neurons, which was almost constant after 8-9 days of age (Curti et al., 2012). Therefore, the most parsimonious line of thinking states that the diversity would not arise from developmental stages, but from intrinsic  $g_J$  variability, which suggests that electrical coupling could be under regulatory control.

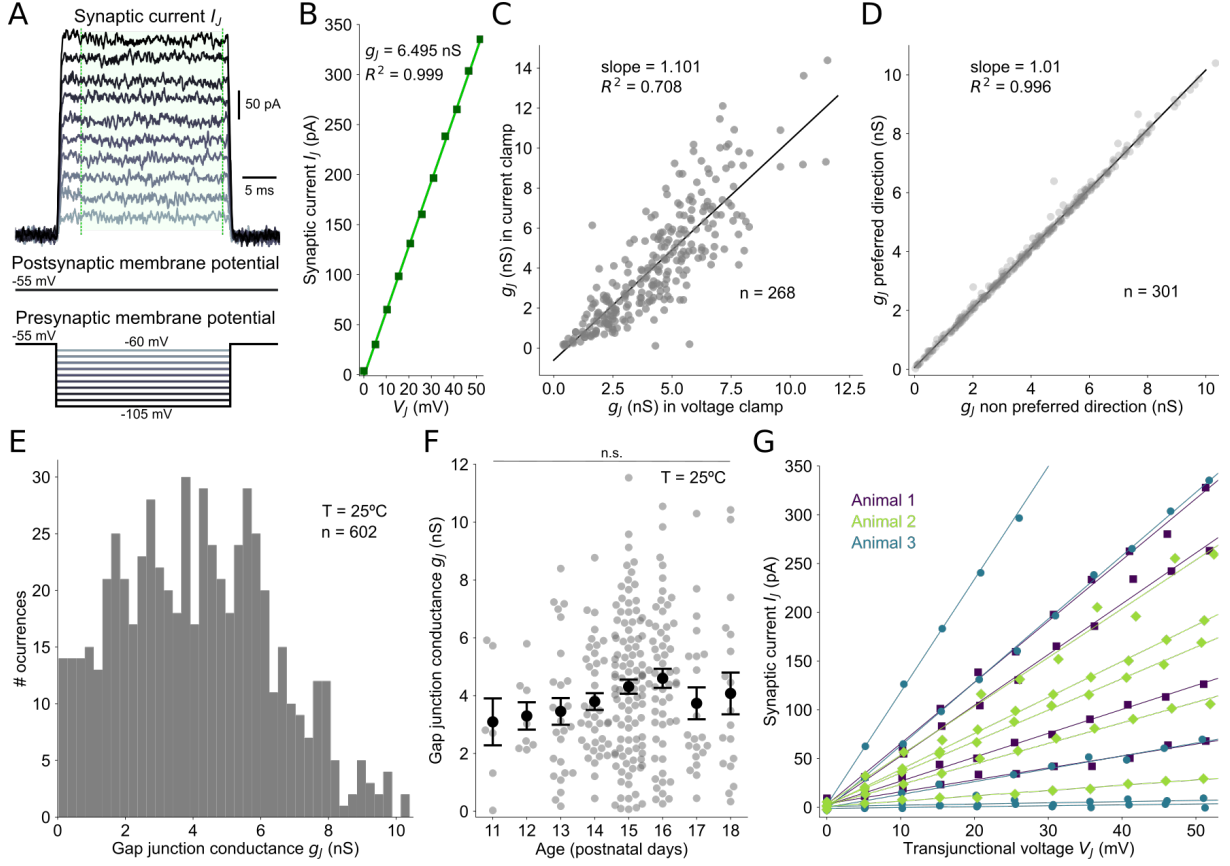


**Figure 4.5: Gap junction conductance is heterogeneous.** *A:* GJ conductance  $g_J$  was measured by recording the average (green window) postsynaptic current responses  $I_J$  to presynaptic voltage stimulation, while clamping the postsynaptic membrane potential. *B:*  $g_J$  was the slope of the relationship between  $I_J$  and the transjunctional voltage  $V_J$ . *C:*  $g_J$  estimations in current clamp correlate to those obtained in voltage clamp ( $n = 268$  directions from 77 animals). *D:* The GJ are non-rectifying in MesV neurons ( $n = 301$  coupled pairs from 140 animals). *E:* distribution of  $g_J$  in the neurons' population was very broad, spanning from 0.029 to 10.397 nS ( $g_J = 4.08 \pm 0.09$  nS,  $n = 602$  directions from 140 animals). *F:*  $g_J$  heterogeneity does not depend on the animals' age: P11  $3.09 \pm 0.81$  nS ( $n = 7$  pairs), P12  $3.30 \pm 0.47$  nS ( $n = 8$ ), P13  $3.45 \pm 0.46$  nS ( $n = 26$ ), P14  $3.79 \pm 0.29$  nS ( $n = 40$ ), P15  $4.31 \pm 0.24$  nS ( $n = 101$ ), P16  $4.60 \pm 0.33$  nS ( $n = 57$ ), P17  $3.73 \pm 0.55$  nS ( $n = 21$ ), P18  $4.08 \pm 0.72$  nS ( $n = 18$ ).  $P > 0.1$  between ages, except when comparing P13 vs P16 and P14 vs P16 ( $P > 0.05$ ), unpaired t-tests. *G:*  $g_J$  was heterogeneous, even for coupled pairs from the same animal (examples from 3 different animals, identified by color). In *D*, *E* and *F*,  $g_J$  measurements were normalized to  $25^\circ\text{C}$ , using  $Q_{10} = 2.04$  (Fig. 4.1).



### 4.3.3 *In vivo*-like firing diminishes $g_J$

Long-term plasticity of GJ may be behind the heterogeneity of  $g_J$ , as different pairs of neurons are subject to diverse inputs, linked to the animals' behavior. Indeed, activity-dependent plasticity of GJ has been extensively reported, first in the Mauthner cell (Yang et al., 1990; Pereda et al., 1998) and then in mammalian brain regions, such as the Thalamic Reticular Nucleus (Landisman and Connors, 2005; Haas et al., 2011; Sevetson et al., 2017) and the Inferior Olive (Mathy et al., 2014; Turecek et al., 2014) (see section 2.5). In order to test our hypothesis, we designed a stimulation protocol in current clamp, inspired by the descriptions of the firing patterns of MesV neurons during masticatory behaviors in rodents (Yamamoto et al., 1989; Westberg et al., 2000). The protocol consisted on 200-ms trains of 1-ms depolarizing pulses at 100 Hz, with 50 ms pauses between them, during 10 seconds. Based on the fact that pairs of coupled MesV neurons tend to present strong synchronization of their firing (Curti et al., 2012), protocols were simultaneously applied to both cells of a coupled pair, 25 times, every 29-30 seconds, totalizing about 12 minutes of duration. The intensity of the stimulation was set to elicit action potentials, as shown in figure 4.6A. The protocol was applied after the  $g_J$  values attained a stable baseline, usually 15 minutes after the break-in of the cell membrane patch. After the stimulation,  $g_J$  fell and then partially recovered 5 minutes later (see example in Fig. 4.6B).  $g_J$  dropped from  $2.76 \pm 0.51$  nS to  $2.01 \pm 0.54$  nS ( $n = 8$  directions,  $P < 0.001$ , paired t-test; Fig. 4.6C). These results show that repetitive firing activity elicits a 27% decrease of  $g_J$ .

### 4.3.4 Activity-like voltage clamp stimulation decreases the coupling coefficient and $g_J$

To further characterize the activity-induced plasticity, we created a voltage clamp protocol, that would allow to accurately control the membrane potentials and the transjunctional voltage  $V_J$ . Given that low-threshold  $\text{Ca}^{2+}$  current  $I_T$  (Huguenard and McCormick, 1992) has been involved in  $g_J$  depression triggered by activity (Sevetson et al., 2017), and that a membrane current with characteristics consistent to that of the  $I_T$  was reported in MesV neurons (Connor et al., 2005), we set the membrane potential command to maximize the activation of  $I_T$  of the coupled cells. Hence, to remove  $I_T$  inactivation, the protocol went from the holding potential ( $-55$  mV) to  $-90$  mV for around 400 ms, going then to 0 mV during 10 ms (to activate  $I_T$  (Connor et al., 2005), which also would inactivate), and finally returning to  $-90$  mV again for 50 ms to reset  $I_T$  (Fig. 4.7A). As in the current clamp stimulation, the duration of the protocol was 10 seconds, and it was repeated every 29-30 seconds, 25 times. Also, the protocol was applied simultaneously to

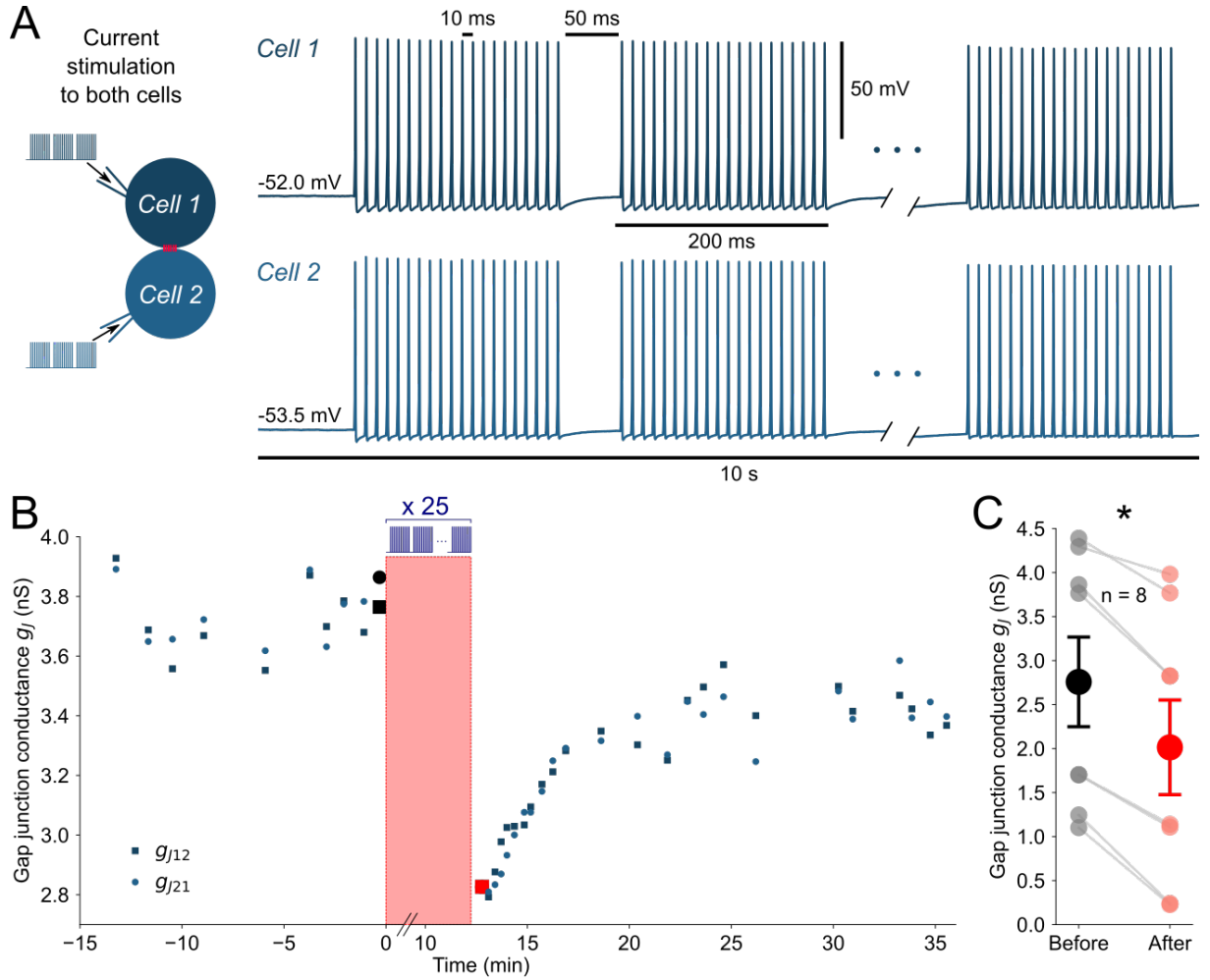


**Figure 4.6: Simultaneous repetitive firing elicits GJ short-term depression** *A*: two coupled neurons were simultaneously stimulated, during 10 seconds, by repeated 200-ms trains of current pulses at 100 Hz, with 50 ms between consecutive trains. Each stimulation was applied 25 times to the neurons, every 29-30 seconds, adding up 12 minutes, approximately. *B*: example of the  $g_J$  measured from cell 1 to 2 ( $g_{J12}$ , squares) and viceversa ( $g_{J21}$ , circles). After the application of the stimulation protocol,  $g_J$  fell from around 3.8 (black) to 2.8 nS (red) and quickly recovered to a new baseline of 3.4 nS. *C*:  $g_J$  went from  $2.76 \pm 0.51$  nS to  $2.01 \pm 0.54$  nS after the stimulation protocol.  $n = 8$  directions from 4 animals;  $P < 0.001$ , paired t-test.

both neurons, which remain isopotential during the whole time ( $V_J = 0$  mV). Figure 4.7B displays membrane voltage responses of a pair of coupled neurons when current pulses were injected in one of them (cell 1) before and after the activity-like protocol. In this case, the CC varied from 0.33 before the protocol to 0.22 after it (Fig. 4.7C). Concomitantly to the reduction in CC, the activity-like protocol also induced a significant hyperpolarization of the RMP and a reduction of the  $R_{in}$ . In fact, for the recorded  $n = 28$  directions, the CC went from  $0.34 \pm 0.03$  to  $0.18 \pm 0.02$ , whereas  $R_{in}$  went from  $83.16 \pm 3.90$  M $\Omega$  to  $57.01 \pm 4.03$  M $\Omega$  (Fig. 4.7D and E respectively;  $P < 1 \times 10^{-5}$ , paired t-tests). In order to determine if the change in CC was just a consequence of the  $R_{in}$  reduction, the  $g_J$  was estimated from current clamp recordings, before and after the protocol. Notheworthy,  $g_J$  also showed a significant reduction, from  $5.17 \pm 0.46$  nS to  $3.52 \pm 0.32$  nS ( $P < 1 \times 10^{-5}$ , paired t-test; Fig. 4.7F), indicating that the reduction in synaptic strength result from the concomitant/sinergistic reduction of  $g_J$  and  $R_{in}$ . In this chapter, we will focus on the depression of  $g_J$ , while chapter 5 will deal with  $R_{in}$  reduction.

In order to confirm our estimations in current clamp, we conducted voltage clamp experiments, which yield more accurate estimations of the  $g_J$  (Welzel and Schuster, 2019). Figure 4.8A displays the evolution of  $g_J$  measured in both directions for a coupled pair. Similarly to what we saw in the repetitive firing experiment (Fig. 4.6B), the conductance falls  $\sim 1$  nS after stimulation (note the broken time axis), recovering partially later. In order to summarize the results from multiple coupled pairs, we resampled them into a common time base, using linear interpolation between data points, and normalize them with their corresponding value of  $g_J$  before the protocol. The figure 4.8B clearly shows that there was a stable baseline in the 15 minutes before the activity-like stimulation and that  $g_J$  fell in all pairs afterwards, averaging  $4.88 \pm 0.28$  nS before the protocol, and  $3.60 \pm 0.24$  nS after its application ( $n = 54$  directions,  $P < 0.001$ , paired t-test; Fig. 4.8C). Interestingly, a linear regression analysis did not indicate any correlation between the percentual decrease of  $g_J$  and its value in control conditions [slope =  $-2.788$ ,  $R^2 = 0.261$ ].

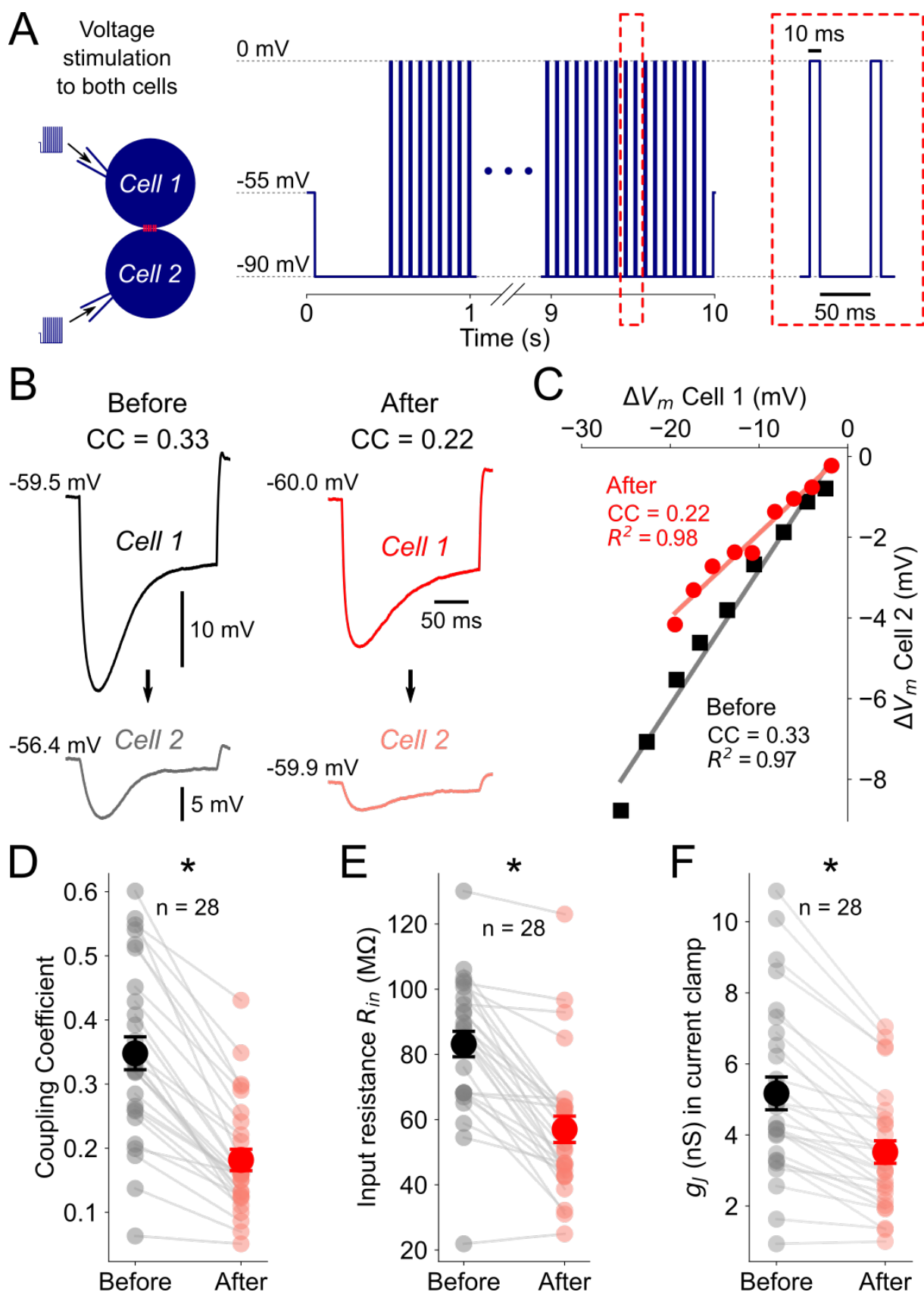
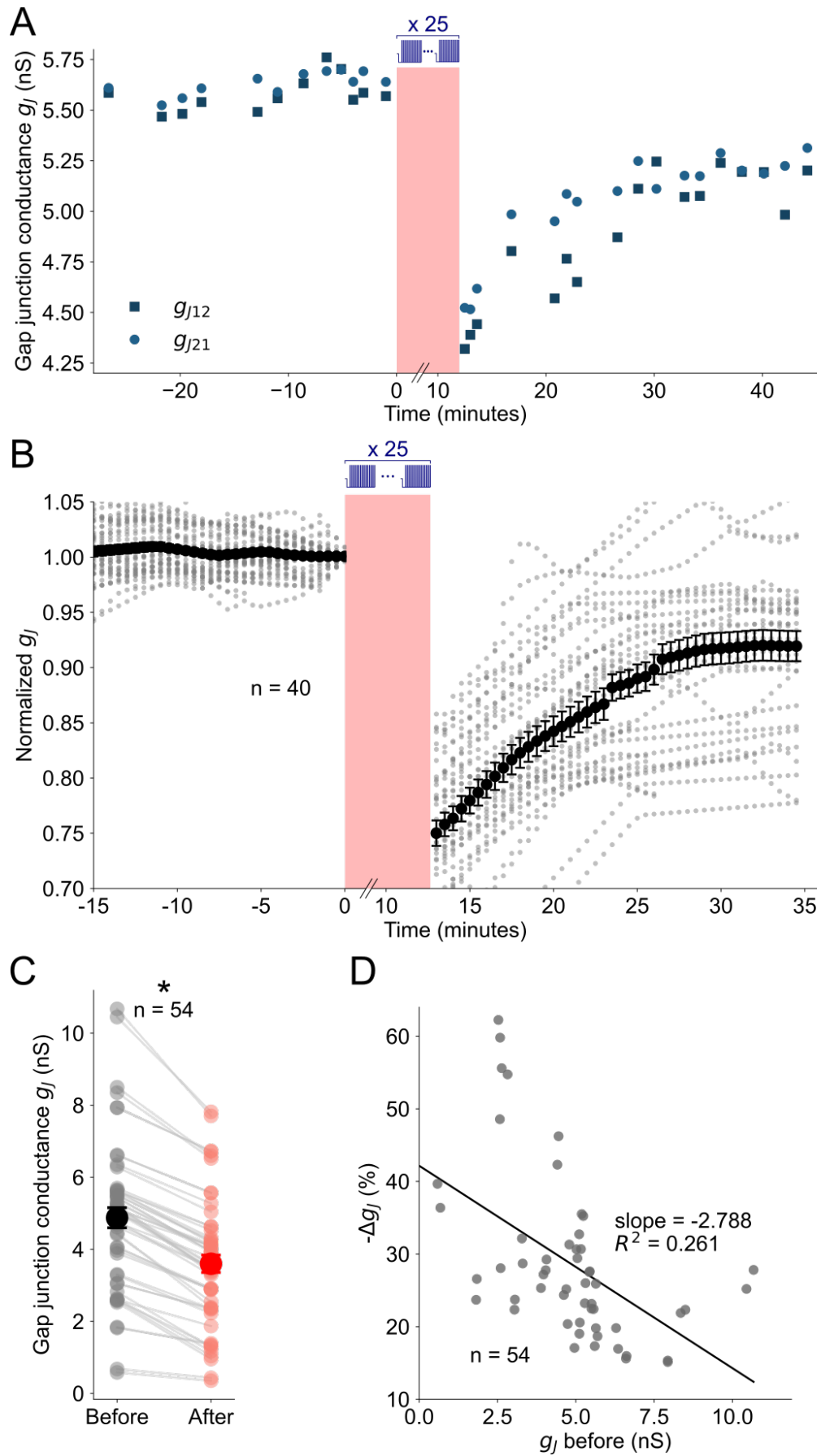


Figure 4.7: (See next page).

**Figure 4.7: Coupling coefficient decreases after repeated stimulation.** *A*: the voltage stimulation protocol, simultaneously applied to coupled neurons, consists on an hyperpolarization to  $-90$  mV, followed by repeated depolarizations to  $0$  mV, separated by 50-ms intervals, during 10 seconds. This protocol was applied 25 times to the cells, every 29-30 seconds, adding up to 12 minutes, approximately. *B*: sample voltage responses to the same current pulse to cell 1, before and after protocol. *C*: the coupling coefficient (CC) from the cell 1 to 2 in *B* decreases from 0.33 to 0.22. *D*: the CC decreases from  $0.34 \pm 0.03$  to  $0.18 \pm 0.02$ . The CC was defined by the input resistance  $R_{in}$  (*E*), which went from  $83.16 \pm 3.90$  M $\Omega$  to  $57.01 \pm 4.03$  M $\Omega$ , and the gap junction conductance  $g_J$  (*F*), which, measured in current clamp, went from  $5.17 \pm 0.46$  nS to  $3.52 \pm 0.32$  nS. In *D*, *E* and *F*,  $n = 28$  directions from 12 animals were used; comparisons between before and after stimulation are statistically significant in all the cases:  $P < 1 \times 10^{-5}$ , paired t-test.

**Figure 4.8:  $g_J$  decreases after repeated stimulation** (see next page). *A*: the application of the activity-like protocol presented in Fig. 4.7 (marked by the light-red box at  $t = 0$ ) leads to a transient decrease of  $g_J$ , measured in the voltage clamp configuration, in both directions. *B*: summary of the  $g_J$  depression induced by the activity-like protocol. The black points and bars indicate mean and SEM values, while the gray ones corresponds to recordings from individual directions ( $n = 40$  directions from 19 animals). For this and similar data crunches in the following figures, the experimental data was linearly interpolated to a common time-grid, in order to compute the mean and SEM for the whole population. *C*: individual  $g_J$  values before and after the protocol: from  $4.88 \pm 0.28$  nS to  $3.60 \pm 0.24$  nS, respectively ( $P < 0.001$ , paired t-test). *D*: there was no clear correlation between the decrease of  $g_J$  and its value before the protocol: slope of linear regression = -2.788,  $R^2 = 0.261$ . For both *C* and *D*,  $n = 54$  directions from 23 animals.



**Figure 4.8:** (Caption in the previous page).



### 4.3.5 The depression of $g_J$ has transient and long-term components

Next, we sought to characterize the time course of this activity-dependant plasticity of electrical transmission between MesV neurons. To assess  $g_J$  during the stimulation, we introduced a brief 10-ms hyperpolarizing voltage pulse ( $-50$  mV of amplitude) before each train of pulses. This pulse was applied to both neurons at different times, in order to get the synaptic current in both directions. The series resistance was compensated once by 80%, before the beginning of the stimulation. Hence, we obtained 25 measurements of  $g_J$  before the application of each train of pulses, each with a sample period of 29-30 seconds (Fig. 4.9A). The evolution of the average normalized  $g_J$  ( $n = 40$  directions) was fitted by a exponential function whose time constant  $\tau = 4.79$  minutes and asymptotic  $g_J$  decrease of 32.5% of the initial value, consistent with the net drop shown in figure 4.8C.

The evolution of  $g_J$  after the activity-like stimulation can be split in two phases: recovery from the short-term depression (STD) and long-term depression (LTD). Figure 4.9B focuses on the recovery phase, which was best fit by a double exponential function, with two time constants: a fast  $\tau_1 = 0.18$  minutes and a slow one  $\tau_2 = 9.41$  minutes, which account for 3% and 19% of the recovery, respectively. This suggests that there are two mechanisms responsible of the recovery, with different time scales.

Following the STD,  $g_J$  did not return to its value before the activity-like protocol, but remained below it (Fig. 4.9C), in a new baseline that can be properly described as LTD. 20 minutes after the end of the stimulation,  $g_J$  was  $4.72 \pm 0.29$  nS, compared with  $5.26 \pm 0.27$  nS before it ( $P < 0.001$  paired t-test; Fig. 4.9D), resulting in a LTD of  $\sim 10\%$ .

---

**Figure 4.9: Time courses of the  $g_J$  depression and recovery** (see next page). *A*: a brief voltage pulse of  $-50$  mV was applied to each neuron before applying the activity protocol presented in Fig. 4.7, in order to estimate the  $g_J$  during the stimulation (light-red box on the left, expanded on the right), which displays an exponential decrease with a time constant of 4.79 minutes. *B*: the recovery phase of  $g_J$  during the first 10 minutes (sky-blue box) after the activity protocol can be fitted by a double exponential (inset), characterized by a fast ( $\tau_1 = 0.18$  minutes) recuperation of 3% and a slower one ( $\tau_2 = 9.41$  minutes) of 19%. *C*: after the first 20 minutes post-protocol,  $g_J$  reaches a stable value, marked by the dotted blue line. *D*: the comparison between the  $g_J$  before the activity-like protocol and 20 minutes after its end (vertical blue line in *C*) results on long-term depression:  $g_J$  went from  $5.26 \pm 0.27$  nS to  $4.72 \pm 0.29$  nS ( $P < 0.001$  paired t-test).  $n = 40$  directions from 19 animals were used in all panels.

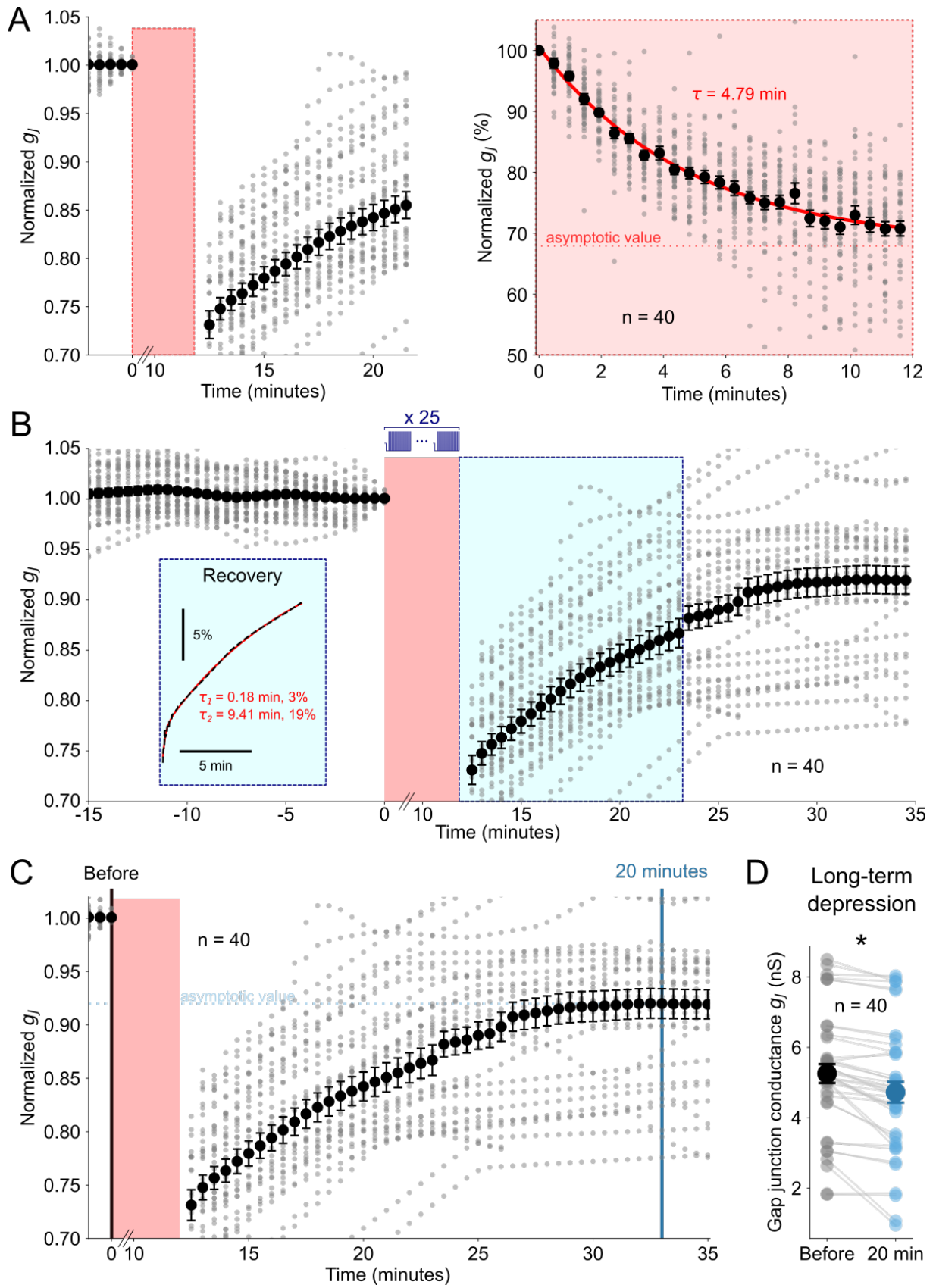
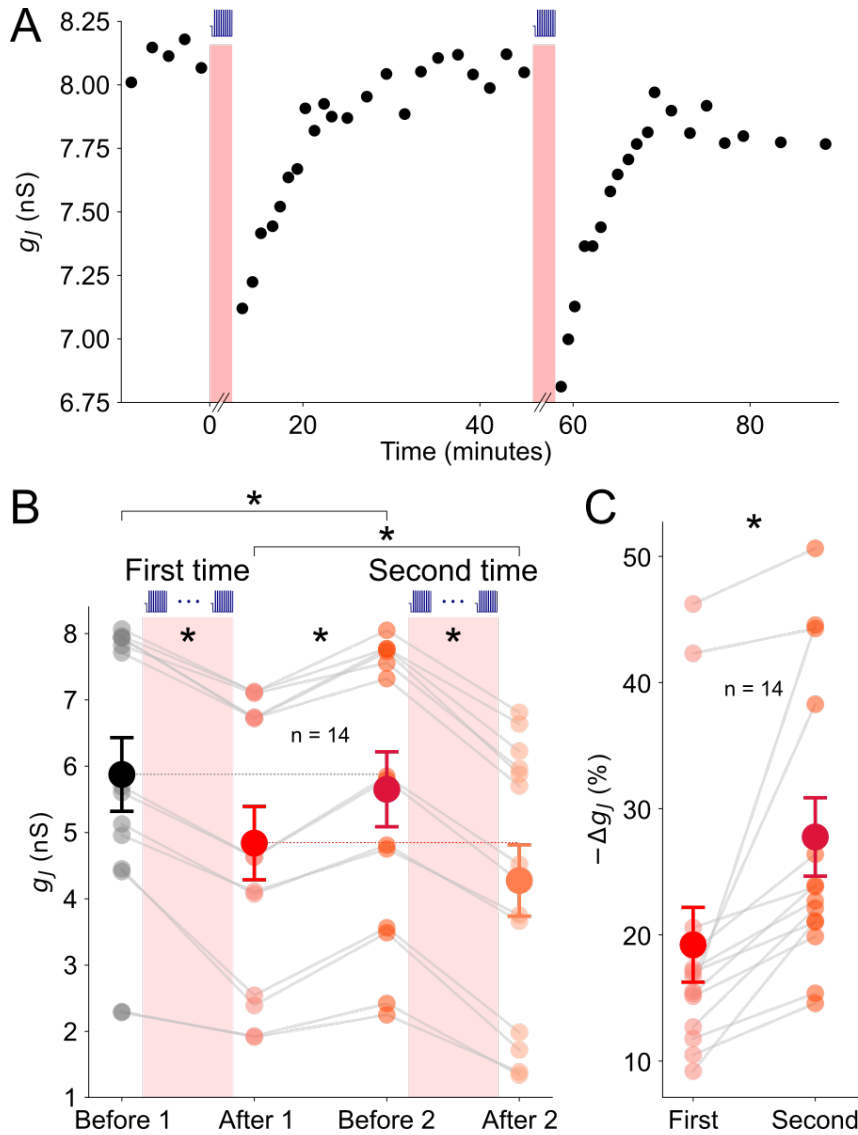


Figure 4.9: (Caption in the previous page).

### 4.3.6 Activity-induced $g_J$ plasticity is primed by previous stimulation

Application of the activity-like stimulation, for a second time, in 7 pairs of neurons, after a new stable baseline was reached, resulted in an even deeper drop of  $g_J$  (Fig. 4.10A). Indeed, for  $n = 14$  directions,  $g_J$  changed from  $5.88 \pm 0.55$  nS to  $4.84 \pm 0.55$  nS after the first protocol, recovered to  $5.65 \pm 0.56$  nS, and fell to  $4.28 \pm 0.54$  nS after the second one (Fig. 4.10B). Thus, for this set of experiments, the first stimulation induced a depression of  $19.22 \pm 2.96\%$ , while the second one generated a drop of  $27.76 \pm 3.11\%$  from the new baseline ( $P < 0.01$ , paired t-test). Thus, there was an accumulative effect that leads the activity-induced plasticity to be primed by a previous presentation of the stimulation protocol.



**Figure 4.10: Repeated stimulation induces stronger plasticity.** *A*: a second application of the activity-like protocol after recovery from the first one, elicits a stronger short-term depression. *B*: for a set of  $n = 14$  directions from 7 animals that were twice stimulated, the  $g_J$  decreases from  $5.88 \pm 0.55$  nS to  $4.84 \pm 0.55$  nS after the first protocol, recovering to  $5.65 \pm 0.56$  nS, and falling to  $4.28 \pm 0.54$  nS after the second one. Paired t-tests indicate statistical significance between all the distributions:  $P < 0.001$  in all the cases, except by the comparison between Before 1 and Before 2 ( $P = 0.028$ ). *C*:  $g_J$  diminution due to the first stimulation was  $19.22 \pm 2.96\%$ , while the second provokes a  $27.76 \pm 3.11\%$  decrease ( $P < 0.01$ , paired t-test).

### 4.3.7 $g_J$ plasticity results from side-additive contribution of each coupled partner

Until now, we showed that simultaneous activity-like stimulation of coupled MesV neurons diminishes the GJ conductance between them. It may also be possible that only one neuron from a coupled pair gets repeatedly activated, while the other keeps quiescent. We simulated this scenario, by applying the same stimuli shown in Fig. 4.7A to only one neuron, clamping its coupled partner at  $-55$  mV. As a result,  $g_J$  went from  $3.24 \pm 0.29$  nS to  $2.81 \pm 0.27$  nS ( $n = 22$  directions,  $P < 0.001$ , paired t-test; Fig. 4.11A). Even though homotypic Cx36 GJ are non-rectifying (see section 2.2.1), a similar stimulation protocol applied on TRN neurons was reported to increase  $g_J$  asymmetry between directions (Haas et al., 2011). We tested this possibility in MesV neurons, finding that their GJ displayed no rectification either before or after the unilateral stimulation, as the ratio between directions of  $g_J$  averaged  $0.996 \pm 0.010$  and  $1.004 \pm 0.010$ , respectively ( $P = 0.373$ , paired t-test; Fig. 4.11B).

Remarkably, the  $g_J$  percentual decrease due to simultaneous bilateral stimulation doubled the obtained by the unilateral protocol: 28.57% versus 14.65% ( $P < 0.001$ , unpaired t-test; Fig. 4.11C). A close inspection of both kinds of experiments suggests that the unilateral results distribution was similar to what we see in the bilateral ones. Figure 4.11D illustrates this hypothesis more rigorously: we mathematically doubled the value of each  $g_J$  depression obtained by the unilateral stimulation, getting a distribution which has now no significant difference with that of the bilateral ones ( $P = 0.833$ , unpaired t-test). This surprising result may be just a statistical anomaly, but may also suggest a side-additive effect of the stimulation. For example, the plasticity could be caused by an intracellular mechanism that was elicited by the repeated stimulation but does not permeate through the GJ, like large protein kinases (see section 2.2.2).

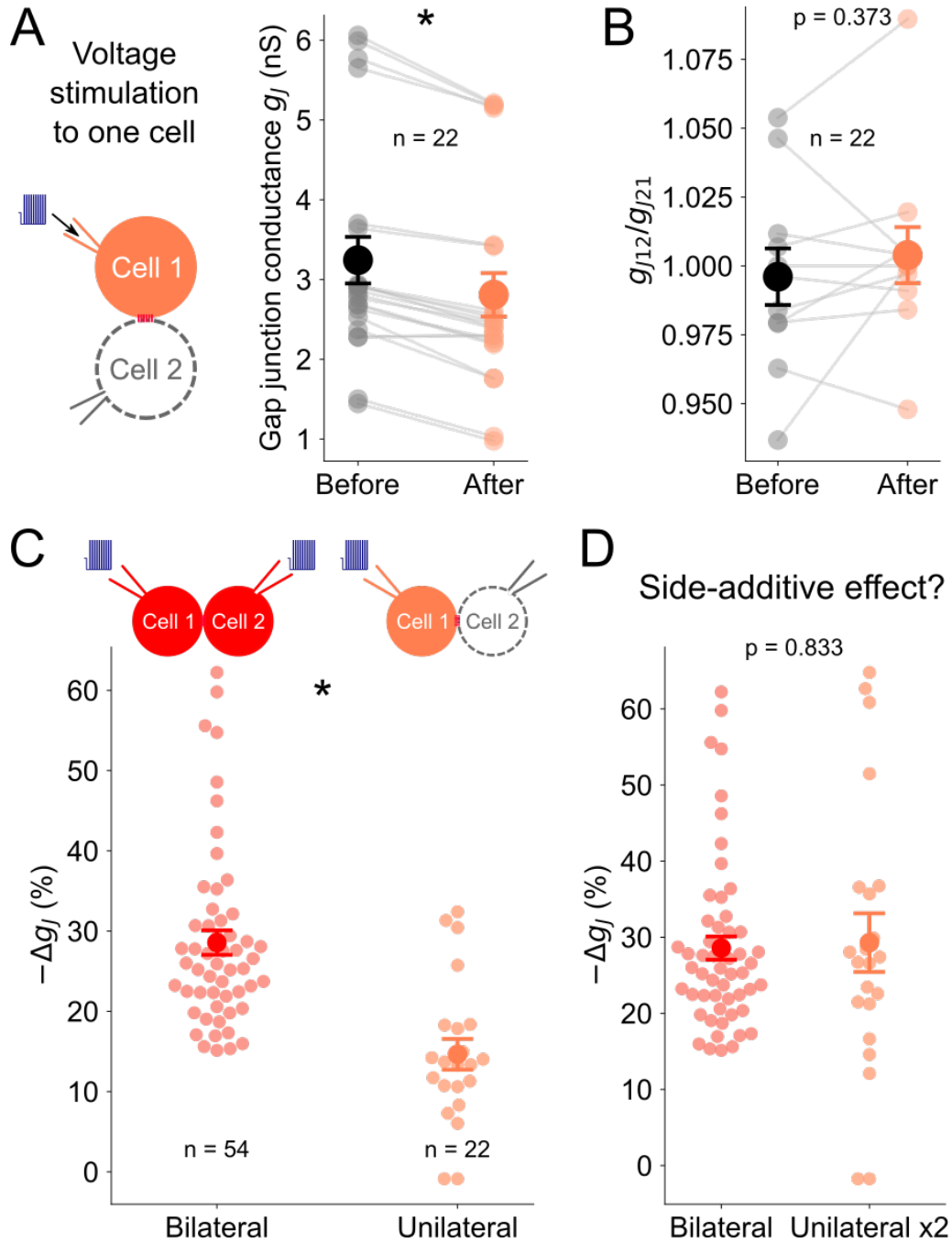


**Figure 4.11: Unilateral stimulation induces half of the plasticity.** **A:** applying the activity-like protocol to only one cell, while keeping the other clamped at  $-55$  mV, induces a decrease of  $g_J$ : from  $3.24 \pm 0.29$  nS to  $2.81 \pm 0.27$  nS ( $P < 0.001$ , paired t-test). **B:** the plasticity does not modify the non-rectifying properties of the GJ, as described by the ratio of the  $g_J$  in the two directions:  $g_{J12}/g_{J21}$  went from  $0.996 \pm 0.010$  to  $1.004 \pm 0.010$  ( $P = 0.373$ , paired t-test). **C:** whereas the bilateral stimulation induces a  $g_J$  decrease of 28.57% (see Fig. 4.8), unilateral activation only induces half as much: 14.65% ( $P < 0.001$ , unpaired t-test). **D:** the distribution of the  $g_J$  decrease obtained by unilateral stimulation, mathematically multiplied by 2, was not significantly different from the  $g_J$  decrease distribution obtained by bilateral stimulation ( $P = 0.833$ , unpaired t-test). This suggests that the stimulation from each side of the GJ was responsible for half of the plasticity, and was independent from what happens on the other side. For all panels, the unilateral  $g_J$  were measured for  $n = 22$  directions from 6 animals.



### 4.3.8 Activity-like stimulation at physiological temperature elicits long-term depression of $g_J$

To validate the physiological plausibility of the activity-induced plasticity, we performed an experimental series at  $T = 34^\circ\text{C}$  throughout the experiment. We also modified the stimulation protocol, inspired by the activity patterns during eating behaviors in rodents (Yamamoto et al., 1989; Westberg et al., 2000), similarly to what we presented in figure 4.6A, but in voltage clamp. As the electrophysiological properties of neurons change with temperature, we set the holding potential to  $-60$  mV, close to their RMP at  $34^\circ\text{C}$  (Fig. 4.12A). After application of the activity-like protocol, there was a significant reduction in the CC: from  $0.29 \pm 0.04$  to  $0.19 \pm 0.03$  ( $n = 16$  direction,  $P < 0.001$  paired t-test, Fig. 4.12B). However, there was not any significant modification of  $R_{in}$ , which went from  $48.49 \pm 3.65$  M $\Omega$  to  $44.96 \pm 3.25$  M $\Omega$  ( $P = 0.426$  paired t-test; Fig. 4.12C), contrasting with what happened with the stimulation from  $-90$  mV at room temperature (Fig. 4.7E; note that  $R_{in}$  was already low before the stimulation). Hence, the CC drop was caused by the fall in  $g_J$ :  $6.98 \pm 1.03$  nS to  $4.53 \pm 0.88$  nS and from  $5.73 \pm 0.64$  nS to  $3.98 \pm 0.56$  nS, when measured in current and voltage clamp, respectively ( $P < 0.001$  paired t-test; Fig. 4.12D and E).

Figure 4.12F reveals a major qualitative difference with the plasticity induced at room temperature:  $g_J$  remained depressed after the stimulation, without any signs of recovery during the first 15 minutes. One possible explanation could be that the STD phase was extremely fast at  $34^\circ\text{C}$  and cannot be accurately measured. But, the evolution of  $g_J$  during the induction of the plasticity (Fig. 4.12G) displayed an exponential time course, whose asymptotic  $g_J$  decrease was 36.3%, that was compatible with the net drop of 30.5% measured after the end of the protocol. Thus, the application of the activity-like stimulation at physiological temperature produced LTD of the GJ.

**Figure 4.12: Long-term depression induced by activity-like stimulation at physiological temperature** (see next page). *A*: characteristics of the stimulus protocol applied to coupled neurons at  $34^\circ\text{C}$ . This protocol was applied 25 times to both cells, producing the following outcomes: (*B*) the coupling coefficient falls from  $0.29 \pm 0.04$  to  $0.19 \pm 0.03$ , (*C*) without significant changes in the input resistance  $R_{in}$  (from  $48.49 \pm 3.65$  M $\Omega$  to  $44.96 \pm 3.25$  M $\Omega$ ,  $P = 0.426$  paired t-test), while  $g_J$  decreases from  $6.98 \pm 1.03$  nS to  $4.53 \pm 0.88$  nS and from  $5.73 \pm 0.64$  nS to  $3.98 \pm 0.56$  nS, when measured in current and voltage clamp, respectively.  $P < 0.001$  for *B*, *C* and *D* paired t-tests. *F*: time course of  $g_J$  normalized to the value before the stimulation. Note that there was no recovery in the first 20 minutes. *G*: during the activity-like protocol,  $g_J$  decrease can be fitted by a single exponential with time constant  $\tau = 5.13$  minutes. For panels *B*, *C* and *D*,  $n = 16$  directions from 6 animals; whereas for *E*, *F* and *G*,  $n = 18$  directions from 6 animals.

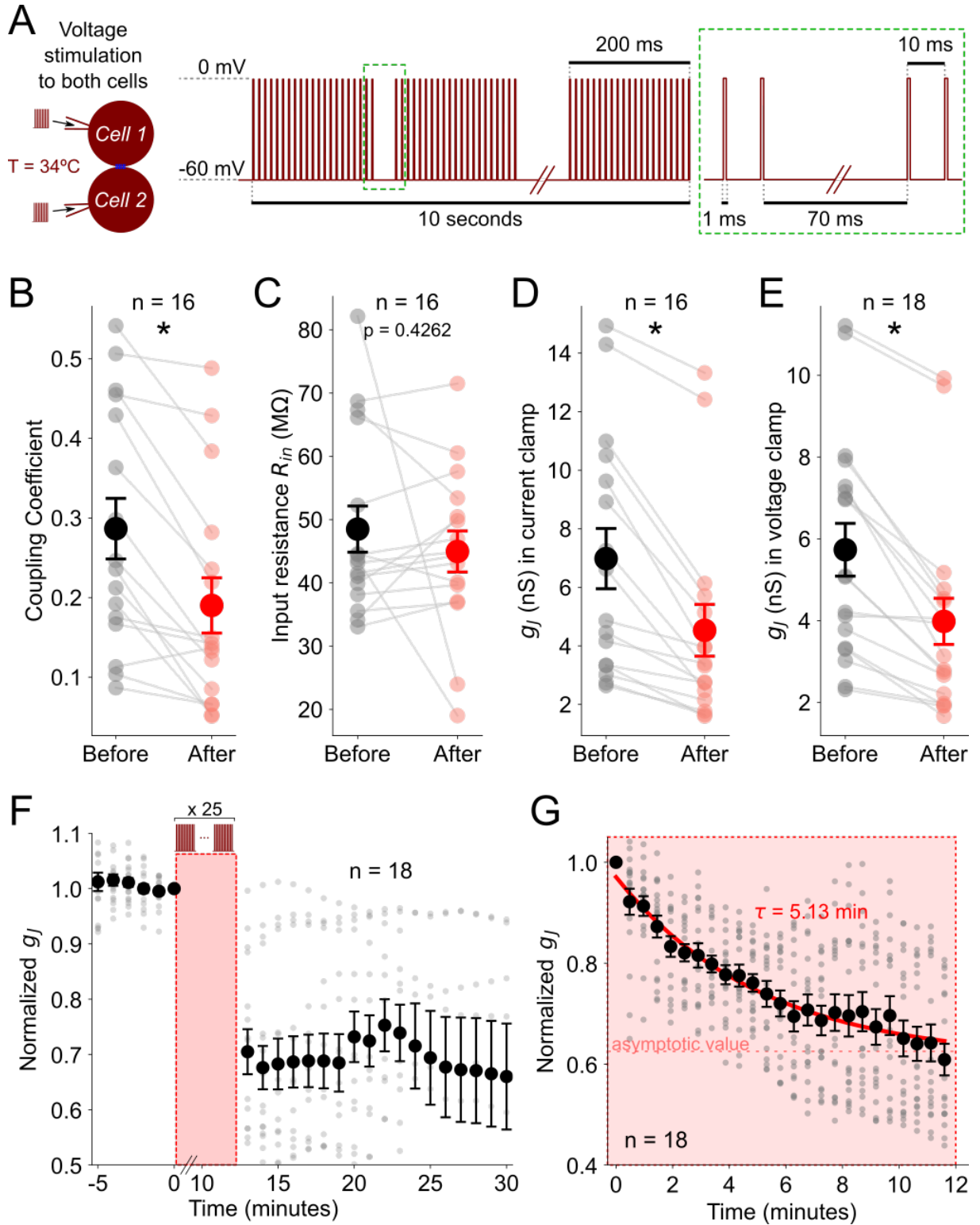


Figure 4.12: (Caption in the previous page.)

### 4.3.9 Calcium weakens, but does not prevent, the activity-induced $g_J$ depression

$\text{Ca}^{2+}$  is usually involved in the induction of synaptic plasticity (see section 2.5), but the blockade of voltage-gated  $\text{Ca}^{2+}$  channels was not enough to avert the activity-induced plasticity, both in the TRN (Sevetson et al., 2017) and in the MesV (data not shown), probably due to the involvement of other  $\text{Ca}^{2+}$  sources. On the other hand, the chelation of intracellular  $\text{Ca}^{2+}$  by BAPTA prevented the induction of activity-dependent plasticity of electrical synapses in the IO (Mathy et al., 2014) and the TRN (Sevetson et al., 2017). Therefore, we applied the activity-like stimulation (see Fig. 4.7A), in the presence of intracellular 10 mM BAPTA. Surprisingly, we found that  $g_J$  depression was not completely abolished, but just weakened in comparison with the control condition (Fig. 4.13A). Indeed, figure 4.13B shows that  $g_J$  dropped from  $3.98 \pm 0.49$  nS to  $3.28 \pm 0.39$  nS ( $n = 22$  directions,  $P < 0.001$ , paired t-test).

As  $\text{Ca}^{2+}$  microdomains were shown to be involved in the electrical synaptic plasticity in the IO (Turecek et al., 2014), we reasoned that BAPTA might not be fast enough to buffer  $\text{Ca}^{2+}$  in similar sites in the MesV neurons. In consequence, we tested removing extracellular  $\text{Ca}^{2+}$ , substituting  $\text{CaCl}_2$  by  $\text{MgCl}_2$ , while using the intracellular solution from the control condition. Again, we could not prevent the plasticity in the presence of ACSF without  $\text{Ca}^{2+}$ :  $g_J$  fell from  $2.36 \pm 0.53$  nS before to  $2.10 \pm 0.48$  nS after the activity-like stimulation protocol ( $n = 12$  directions,  $P < 0.002$  paired t-test; 4.13C). In fact, the  $g_J$  depression under this condition or with intracellular BAPTA were not statistically different between them ( $P = 0.068$ ), but clearly smaller than control. Figure Fig. 4.13D displays the distribution of the percentual  $g_J$  decrease for each condition:  $28.57 \pm 1.52\%$  in control,  $15.99 \pm 1.67\%$  with BAPTA and  $11.16 \pm 1.60\%$  without  $\text{Ca}^{2+}$  in the bath ( $P < 0.001$  between control and both other conditions, unpaired t-test).

Given that the difference between the plasticity in the presence of intracellular BAPTA and without extracellular  $\text{Ca}^{2+}$  was not markedly strong (the P-value was just above 0.05), we repeated the activity-like stimulation under both conditions simultaneously. Unluckily, most cells did not remain viable during all the plasticity induction, probably due to the lack (or deep reduction, at least) of free extracellular  $\text{Ca}^{2+}$ . However, we were able to measure  $g_J$  during the application of the activity-like protocol (Fig. 4.13E), finding that the plasticity was weaker under these combined conditions, but it was still not completely abolished. A comparison after 10 minutes of induction (Fig. 4.13F) revealed that the decrease of  $g_J$  was  $27.04 \pm 1.52\%$  in control conditions ( $n = 40$  directions),  $18.32 \pm 1.80\%$  with BAPTA ( $n = 22$ ), and  $9.21 \pm 7.52\%$  with both intracellular BAPTA and ACSF

without  $\text{Ca}^{2+}$  ( $n = 6$ ). Although there was a diminution of the induced plasticity in the combined condition, it was not statistically different from the BAPTA alone condition ( $P = 0.086$ , unpaired t-test). Therefore, while our results clearly show the involvement of  $\text{Ca}^{2+}$  in the induction of this activity-dependent plasticity, it is not possible to rule out the involvement of a  $\text{Ca}^{2+}$  independent mechanism too.

---

**Figure 4.13: Lack of free  $\text{Ca}^{2+}$  weakens the activity-induced  $g_J$  plasticity, but does not prevent it** (see next page). *A*: repeated activity also diminished  $g_J$  of coupled cells with intracellular 10 mM BAPTA 10 mM, but the magnitude of the depression and its time course are different from those in control conditions. *B*:  $g_J$  decreased from  $3.98 \pm 0.49$  nS to  $3.28 \pm 0.39$  nS ( $n = 22$  directions from 8 animals,  $P < 0.001$ , paired t-test). *C*: removing  $\text{Ca}^{2+}$  from the ACSF (with standard intracellular solution) did not impede the activity-induced depression:  $g_J$  went from  $2.36 \pm 0.53$  nS before to  $2.10 \pm 0.48$  nS after the activity-like stimulation protocol ( $n = 12$  directions from 6 animals;  $P < 0.002$  paired t-test). *D* there was no significant difference in the activity-induced depression between the ACSF without  $\text{Ca}^{2+}$  and the intracellular BAPTA conditions ( $P = 0.068$ , unpaired t-test). However, between these conditions are significantly different from control:  $28.57 \pm 1.52\%$  in control,  $15.99 \pm 1.67\%$  with BAPTA and  $11.16 \pm 1.60\%$  without  $\text{Ca}^{2+}$  in the bath.  $P < 0.001$  between each one of them and control, unpaired t-test. *E*: during the repetitions of the activity protocol, there seemed to be less  $g_J$  depression when there was BAPTA in the intracellular solution and no  $\text{Ca}^{2+}$  in the perfusion. *F*: however, after 10 minutes of stimulation, there was no significant difference in the depression when  $\text{Ca}^{2+}$  was absent in the extracellular solution ( $P = 0.086$  unpaired t-test;  $n = 6$  directions from 2 animals). All the data in the presence of BAPTA were obtained from  $n = 22$  directions from 8 animals.

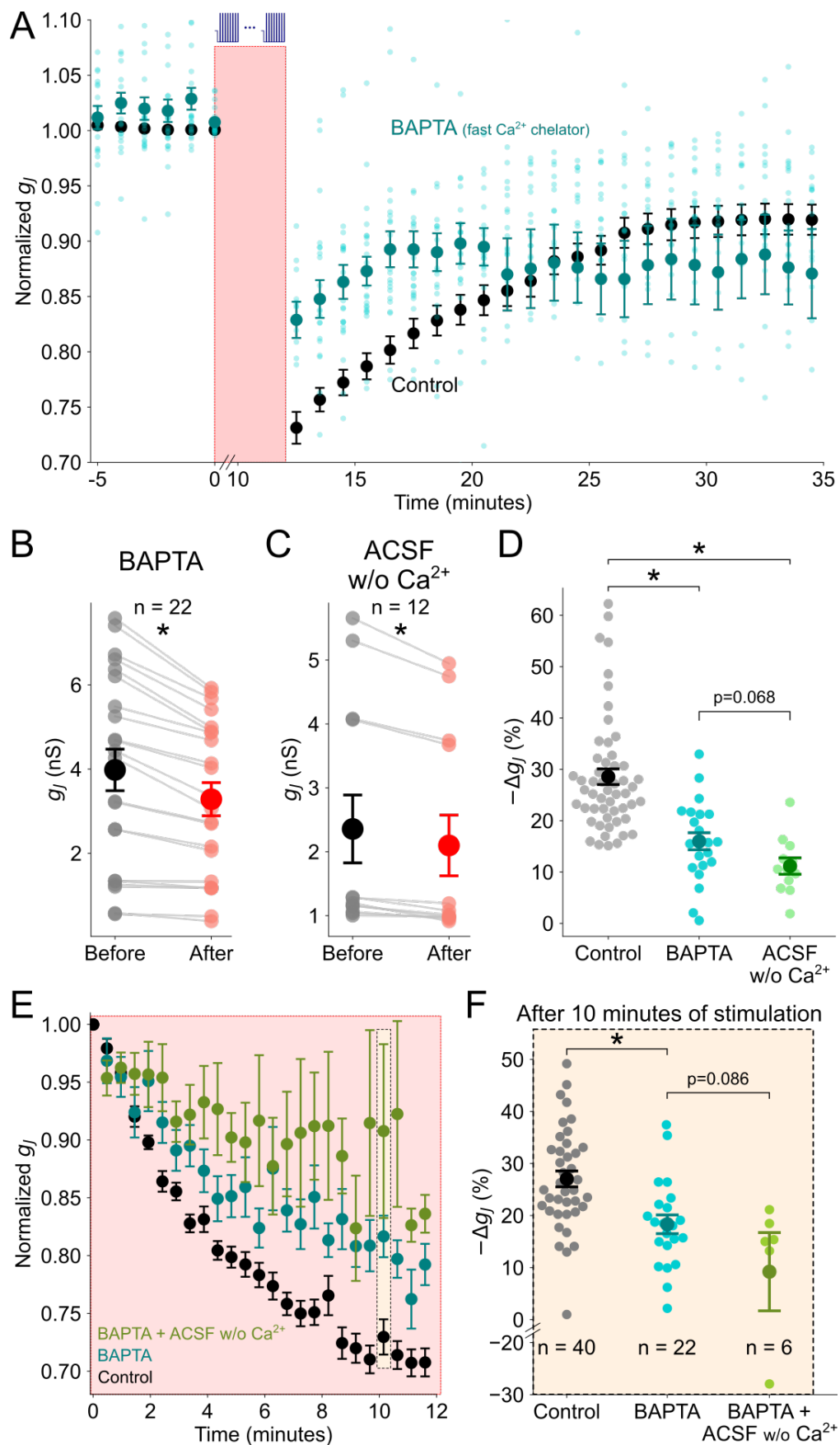


**Figure 4.13:** (Caption in the previous page.)

#### 4.3.10 Bath application of NMDA produced $g_J$ depression

In the previous section, we concluded that an increase in cytosolic free  $\text{Ca}^{2+}$  is necessary, at least in part, for the induction of this phenomenon of activity-dependent plasticity. We next asked whether an increase of intracellular  $\text{Ca}^{2+}$  was enough for triggering  $g_J$  depression. We took advantage from the fact that MesV neurons express NMDA receptors (Turman Jr. et al., 1999; Verdier et al., 2004), which are permeable to  $\text{Ca}^{2+}$  and whose activation triggered electrical synaptic plasticity in the M-cell (Yang et al., 1990) and the IO (Mathy et al., 2014; Turecek et al., 2014).

To activate these receptors, we applied NMDA 50-300  $\mu\text{M}$  in the bath, along with 1-10  $\mu\text{M}$  glycine as a coagonist to enhance their current and slow their desensitization (Cummings and Popescu, 2015). Coupled MesV neurons were held at a slightly depolarized potential ( $-50$  or  $-45$  mV), in order to reduce pore blockade by  $\text{Mg}^{2+}$ . Figures 4.14A-B illustrate the membrane currents and the consequent gradual decrease of  $g_J$  in both directions. Although the elicited currents were of small amplitude and short duration (few minutes), and  $\text{Ca}^{2+}$  represents only a fraction of it (Schneggenburger, 1996; Dingledine et al., 1999), they were enough to induce a decrease of  $g_J$  (Fig. 4.14C-D). The effect was consistent for  $n = 16$  directions, as  $g_J$  went from  $2.64 \pm 0.37$  nS to  $2.44 \pm 0.36$  nS,  $P < 1 \times 10^{-3}$ , paired t-test (Fig. 4.14E). Thus, the raise of intracellular  $\text{Ca}^{2+}$ , without activity-like electrical stimulation, was enough to trigger  $g_J$  plasticity.



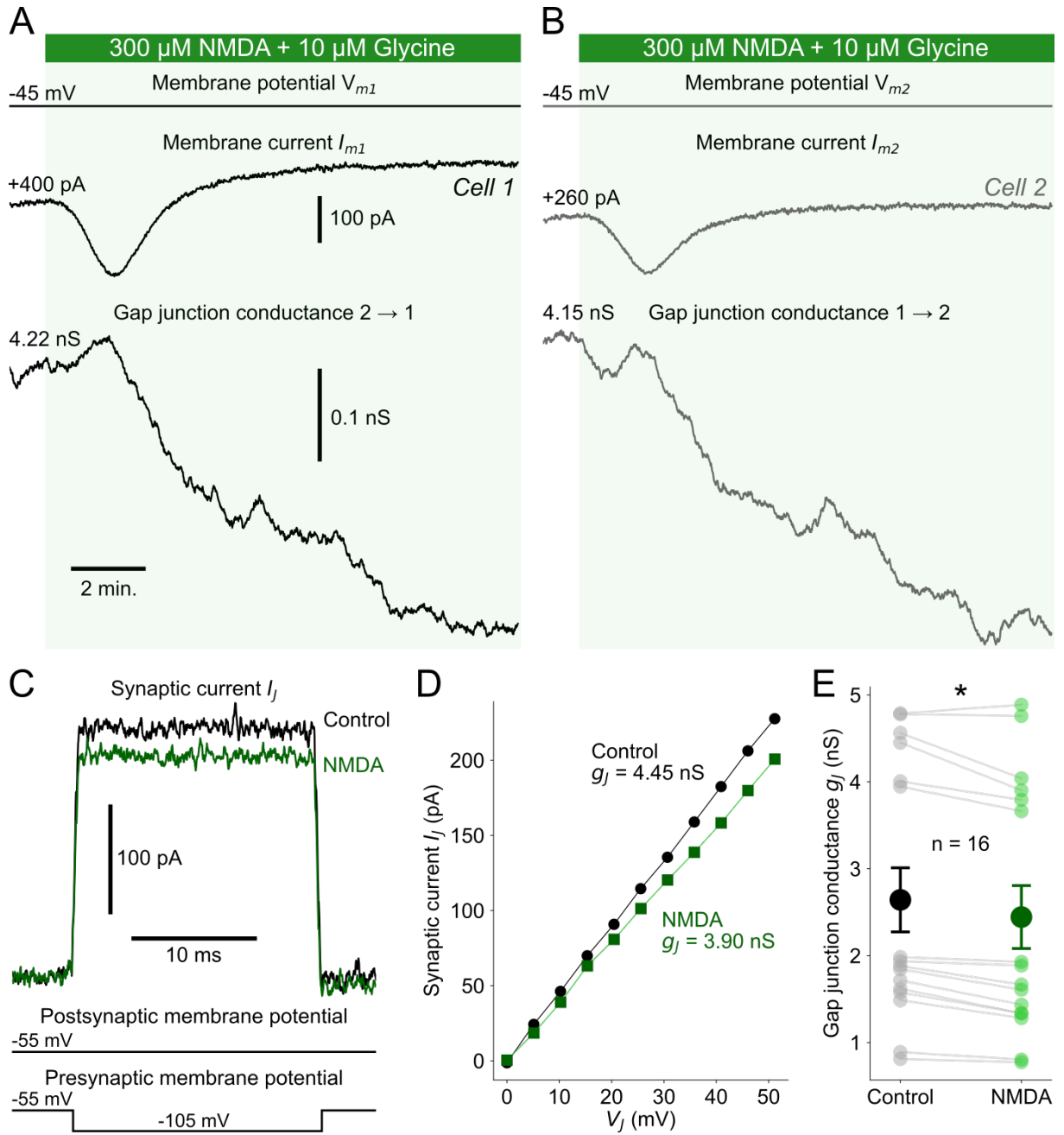


**Figure 4.14: Current through NMDA receptors decreases  $g_J$  without firing activity.** *A-B*: NMDA 300  $\mu$ M and glycine 10  $\mu$ M were applied (indicated by the green color) to two coupled cells, which were voltage clamped at  $-45$  mV, eliciting an inward current of small amplitude that inactivated in few minutes.  $g_J$  gradually reduced, in both directions, after the activation of the NMDA receptors, illustrated by the electrical synaptic current  $I_J$  responses for a transjunctional potential  $V_J$  of 50 mV (*C*) and by the slope of the I-V relationship (*D*). *E*: NMDA application without firing induced a consistent decrease of  $g_J$ , which went from  $2.64 \pm 0.37$  nS to  $2.44 \pm 0.36$  nS,  $n = 16$  directions,  $P < 1 \times 10^{-3}$ , paired t-test.

#### 4.3.11 $I_H$ participates in setting basal $g_J$ and in the activity-induced plasticity

Despite the fact that voltage-gated calcium channels are typical candidates to mediate  $\text{Ca}^{2+}$  entry during activity-like protocols,  $\text{Ca}^{2+}$  current of MesV neurons are of small amplitude and their activation strongly curtailed by large and fast voltage-dependent  $\text{K}^+$  outward currents (Del Negro and Chandler, 1997). Based on that, we focused our attention on alternative mechanisms, like other membrane currents activated during the protocols. In that sense, although  $\text{Ca}^{2+}$  represents a minor fraction of the total  $I_H$  current (Yu et al., 2004), it is highly expressed in this neuronal population, suggesting the possibility of its involvement in the induction of this plasticity. Consistently, voltage commands during activity-like protocols elicited a large inward current, whose amplitude and time course was consistent with the  $I_H$  current. Accordingly, this inward current is strongly reduced after application of CsCl 5 mM, confirming the activation of the  $I_H$  during these protocols (Fig. 4.15A).

To directly test the possible involvement of the  $I_H$  current in the induction of activity-dependent  $g_J$  plasticity, we measured the effect of the stimulation on  $g_J$  in the presence of CsCl 2-5 mM (Fig. 4.15B), finding that  $g_J$  plasticity was substantially reduced. In fact,  $g_J$  went from  $6.05 \pm 0.40$  nS before to  $5.04 \pm 0.39$  nS after the activity-like protocol ( $P < 0.001$  paired t-test,  $n = 14$  directions; Fig. 4.15C). Consequently, the  $g_J$  decrease with CsCl was smaller than in the control condition: (Fig. 4.15D):  $17.34 \pm 2.33\%$  and  $28.57 \pm 1.53\%$ , respectively ( $P < 0.001$ , paired t-test). The most parsimonious explanation for the reduction of the activity-induced plasticity was that some  $\text{Ca}^{2+}$  was being conveyed through the HCN channels.

Despite the very hyperpolarized activation of  $I_H$  (see chapter 3), its large amplitude allows it to be a substantial current at the RMP. Indeed, recordings of  $I_H$  currents from a coupled pair of MesV neurons (Fig. 4.16A) shows that the maximum  $I_H$  current was above 5 nA, while at  $-55$  mV, the  $I_H$  represents an inward current of  $\sim 200$  pA (Fig. 4.16B). Then, there was a basal  $I_H$  at the RMP, carrying some  $\text{Ca}^{2+}$  into the cells. We asked if this constitutive  $\text{Ca}^{2+}$  current could enough to modulate  $g_J$  in control conditions. Indeed, we found that the synaptic current got increased when  $I_H$  was blocked (Fig. 4.16C), which translated into an augmentation of  $g_J$  (Fig. 4.16D). In general, after the bath application of CsCl 2-5 mM,  $g_J$  went from  $6.08 \pm 0.35$  nS to  $6.57 \pm 0.34$  nS ( $n = 22$  directions,  $P < 0.001$ , paired t-test; Fig. 4.16E). Therefore, the  $I_H$  current does not only play a role on setting  $g_J$  during the activity-like stimulation, but also at basal conditions.

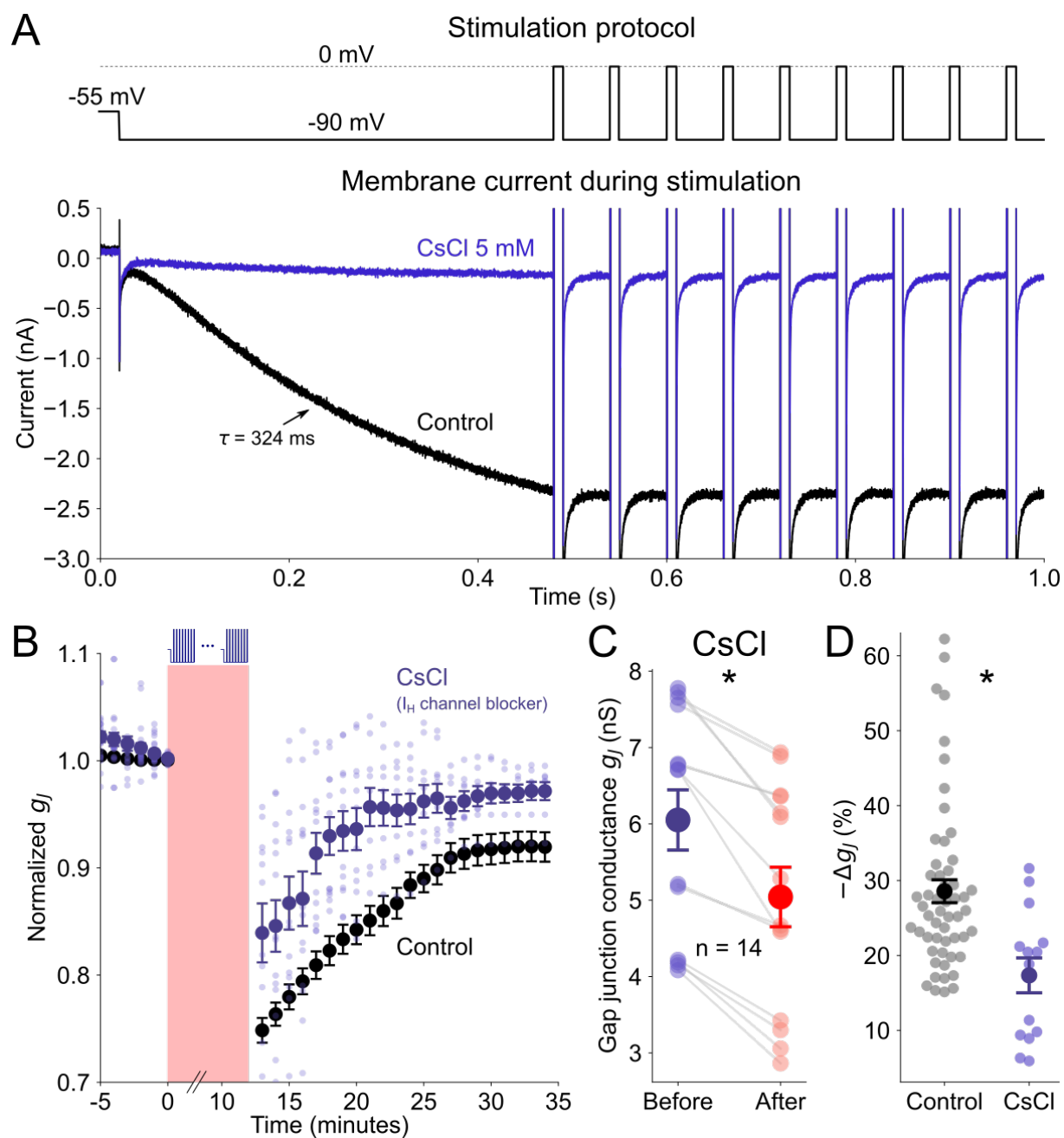


**Figure 4.15:** (Continued on the following page.)

**Figure 4.15:  $I_H$  constitutes a major inward current during the plasticity-inducing stimulation and its blockade diminished  $g_J$  depression.** *A*: two different examples of the membrane current during at the beginning of the stimulation protocol (schematic representation above; also see Fig.4.7A), in control conditions (black trace) and with CsCl 5 mM in the bath (purple). As the protocol first drives the membrane potential to  $-90$  mV, a large inward current activates with a time constant of  $\sim 300$  ms, compatible with the hyperpolarization-activated  $I_H$  current (see Fig. 3H from chapter 3). The hyperpolarization-activated inward current was completely absent when there was CsCl 5 mM in the perfusion. *B*: the plasticity induced in the presence of CsCl 2-5 mM (purple) was smaller than in control conditions (black). *C*:  $g_J$  went from  $6.05 \pm 0.40$  nS before to  $5.04 \pm 0.39$  nS after the stimulation protocol ( $P < 0.001$  paired t-test,  $n = 14$  directions from 8 animals). *D*: the depression of  $g_J$  was significantly smaller with CsCl ( $17.34 \pm 2.33\%$ ,  $n = 14$  directions from 8 animals) than in control conditions ( $28.57 \pm 1.53\%$ ;  $n = 54$  directions from 23 animals).  $P < 0.001$ , paired t-test.

**Figure 4.16: Blocking basal  $I_H$  current enhances  $g_J$**  (see next page). *A*:  $I_H$  current elicited by simultaneous long voltage pulses (from  $-45$  to  $-105$  mV) in a coupled pair. Each trace was obtained by subtracting the responses in control conditions and with CsCl 5 mM. *B*: the steady-state  $I_H$  currents and sigmoidal fits for each cell. Note that, even though there was little activation of  $I_H$  at the holding voltage ( $-55$  mV), the amount of  $I_H$  was not negligible:  $I_{H@V \text{ holding}} \sim -200$  pA. *C*: a brief hyperpolarized pulse applied to cell 1, while cell 2 voltage was held, provokes an outward current in cell 2 (the synaptic current  $I_J$ ), that augments in the presence of CsCl 5 mM. Note also the large inward current in cell 1, that was blocked by CsCl. *D*: the increase in  $g_{J21}$  was confirmed by repeating the procedure of *C* with several voltage amplitudes on cell 1. *E*:  $g_J$  went from  $6.08 \pm 0.35$  nS in control to  $6.57 \pm 0.34$  nS with CsCl 2-5 mM,  $P < 0.001$  paired t-test,  $n = 22$  directions from 8 animals.

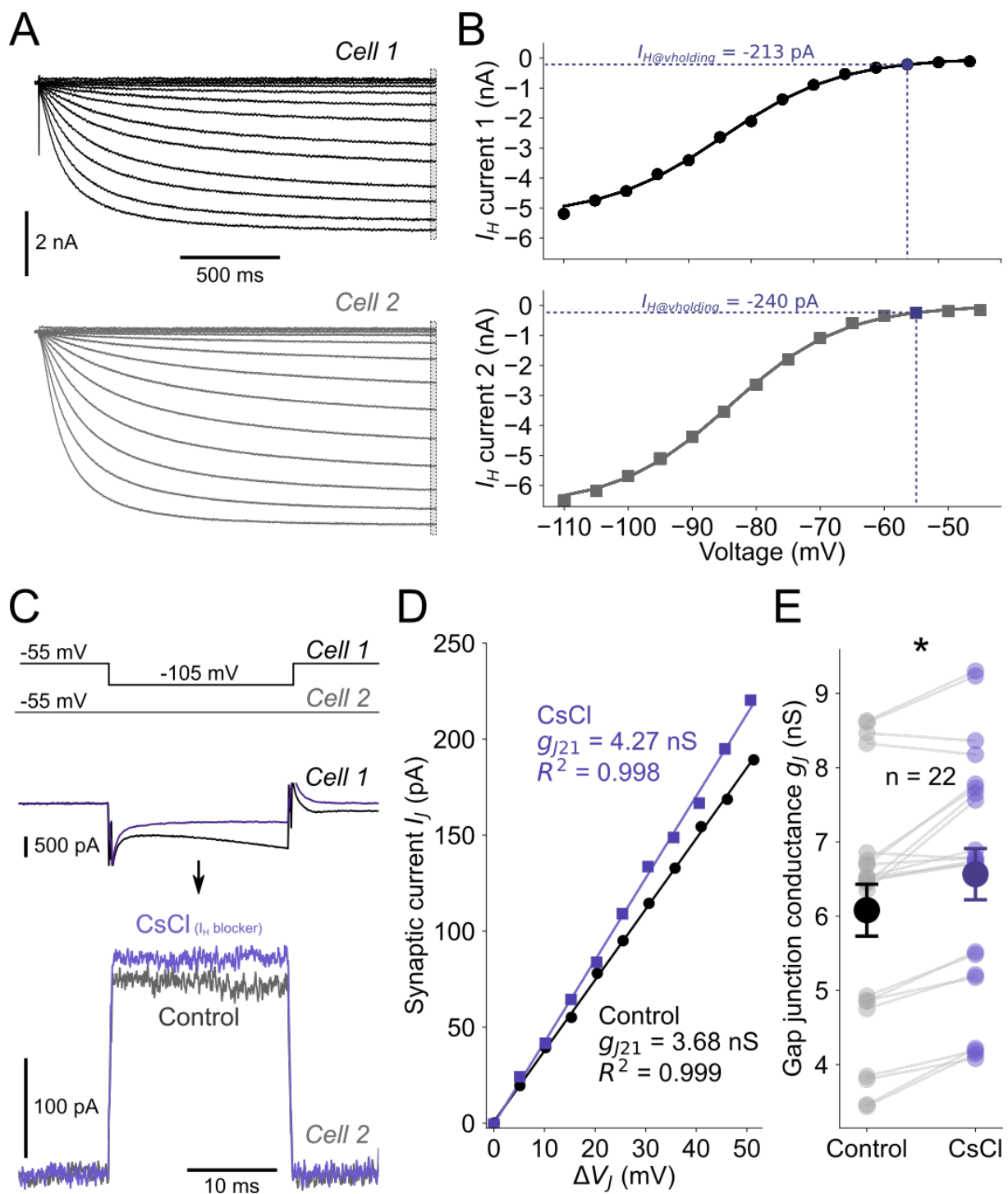


Figure 4.16: (Caption in the previous page).

#### 4.3.12 Blockade of cannabinoid type 1 receptors enhances activity-induced plasticity

Endocannabinoids (eCB) are lipid messengers, that have been reported to mediate both autocrine (Bacci et al., 2004; Marinelli et al., 2009) and retrograde (Wilson and Nicoll, 2001; Castillo et al., 2012) actions upon depolarization of the membrane potential. The accompanying increase of intracellular  $\text{Ca}^{2+}$  during depolarization promotes the synthesis of eCB (Tanimura et al., 2010), which then can diffuse to the presynaptic membrane, inhibiting  $\text{Ca}^{2+}$  channels and activating  $\text{K}^{+}$  ones (Chevalleyre et al., 2006; Fletcher-Jones et al., 2020). In this way, eCB are responsible for a phenomenon called depolarization-induced suppression of inhibition (Brenowitz and Regehr, 2003), that has been observed in MesV neurons (Zhang et al., 2012). On the other hand, eCB can also potentiate synaptic transmission (Piette et al., 2020), for example through interactions with astrocytes (Gómez-Gonzalo et al., 2014; Navarrete et al., 2014). Interestingly, in some circuits, eCB can mediate both potentiation or depression of chemical synaptic transmission, depending on their timing and concentration (Cui et al., 2016). For electrical synapses, eCB have been shown to potentiate the synaptic transmission at mixed synapses onto M-cell of the fish (Cachope et al., 2007).

We asked if eCB released due to the activity-like stimulation participate on the regulation and plasticity of electrical synapses. As cannabinoid receptor type 1 ( $\text{CB}_1\text{R}$ ) is the most prevalent endocannabinoid receptor in the brain (Wilson and Nicoll, 2002; Zou and Kumar, 2018), we applied the plasticity-inducing protocol to coupled pairs in the presence of the specific antagonist AM251 5  $\mu\text{M}$  in the bath. Surprisingly, the activity-induced depression was augmented in this condition compared with control (Fig. 4.17A). In addition, just the application of AM251 had a small, but significant, diminishing effect on  $g_J$  (Fig. 4.17B), which varied from  $7.08 \pm 0.44$  nS in control to  $6.72 \pm 0.49$  nS ( $n = 18$  directions,  $P = 0.006$  paired t-test), reversing a slightly upwards basal trend after 10 minutes in the whole cell configuration. The drop of  $g_J$  caused by the activity-like stimulation was  $35.04 \pm 2.32\%$  in the presence of AM251, versus  $28.57 \pm 1.53\%$  in control ( $P = 0.03$ , unpaired t-test; Fig. 4.17C). These results suggest that  $\text{CB}_1$  receptors are activated by the activity-like stimulation and are involved in setting  $g_J$ , even though we do not know their cellular location yet.



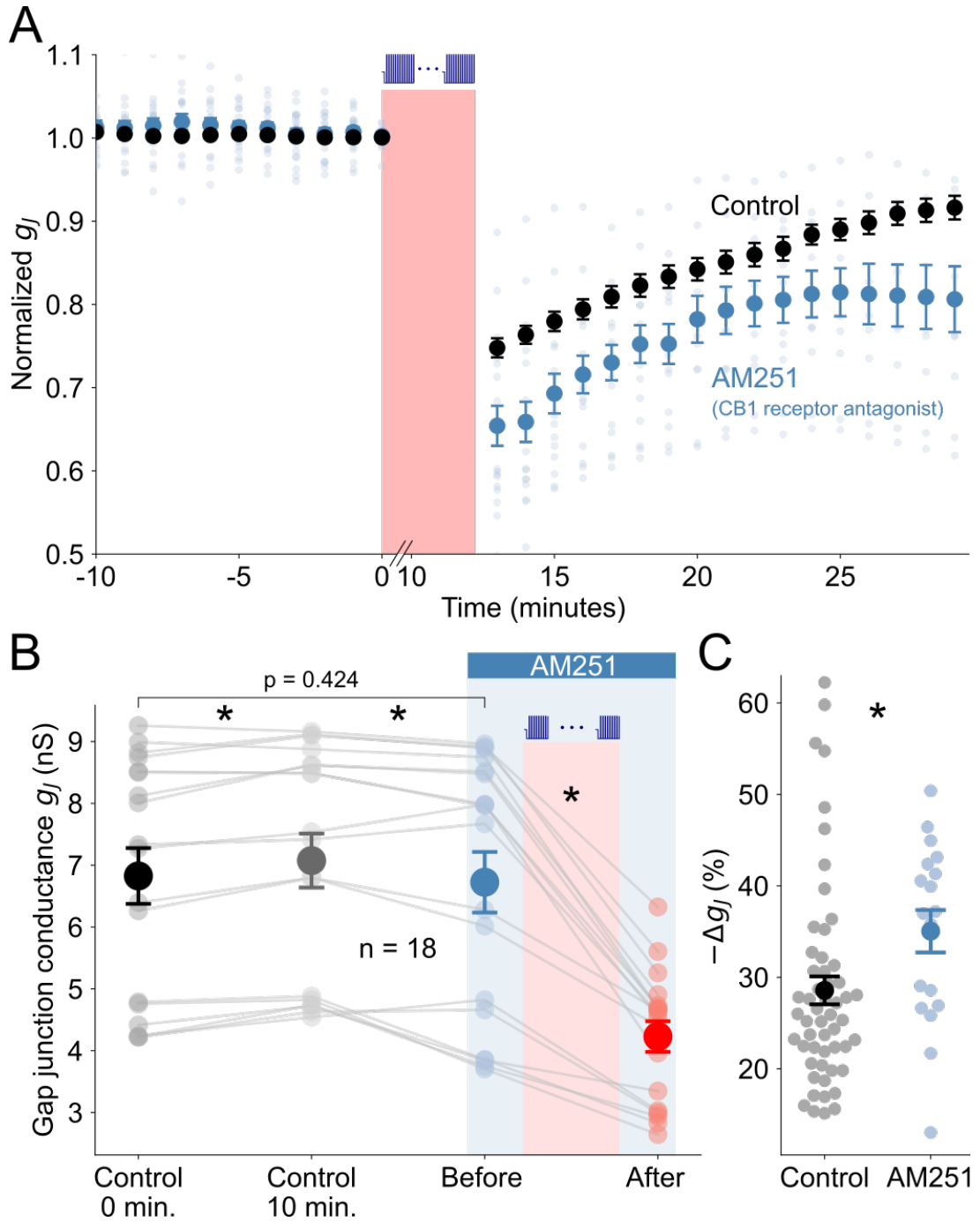


**Figure 4.17: Inhibition of the CB<sub>1</sub> receptor augments the  $g_J$  depression after the activity-like stimulation.** *A*: repeated stimulation provokes a larger decrease of  $g_J$  in the presence of AM251 5  $\mu$ M, a CB<sub>1</sub> receptors antagonist. *B*: in control conditions, there was a weak increase of  $g_J$  after 10 minutes of opening the membrane patch: from  $6.83 \pm 0.45$  nS to  $7.08 \pm 0.44$  nS ( $P < 0.001$ , paired t-test). This augmentation was reversed by the application of AM251 in the bath:  $g_J = 6.72 \pm 0.49$  nS ( $P = 0.006$  compared with Control 10 minutes condition, but  $P = 0.424$  compared to Control 0 minutes, paired t-tests). The activity-like stimulation further decreased the conductance to  $4.23 \pm 0.25$  nS ( $P < 0.001$ , paired t-test). *C*: the decrease in  $g_J$  due to the activity-like stimulation was  $35.04 \pm 2.32\%$  in the presence of the antagonist of CB<sub>1</sub> receptors, and  $28.57 \pm 1.53\%$  in control ( $n = 54$  directions from 23 animals;  $P = 0.03$ , unpaired t-test). All the data with AM251 5  $\mu$ M was obtained from  $n = 18$  directions from 4 animals.

#### 4.3.13 Neither CaMKII nor PKA are involved in the activity-induced plasticity in MesV neurons

$\text{Ca}^{2+}$ /calmodulin-dependent kinase II (CaMKII) has been reported to mediate  $\text{Ca}^{2+}$ -signaling in both chemical (Lisman et al., 2012; Herring and Nicoll, 2016) and electrical (Pereda et al., 1998; Mathy et al., 2014; Turecek et al., 2014) synaptic plasticity. For this reason, we applied the activity-like protocol to coupled neurons, using the CaMKII inhibitor KN-93 10  $\mu\text{M}$  in the patch solution, finding that the activity-like protocol was still able to induce a significant reduction of  $g_J$  (Fig. 4.18A). In fact,  $g_J$  varied from  $4.15 \pm 0.59$  nS before the protocol, to  $2.90 \pm 0.37$  nS after its application,  $n = 16$  directions,  $P < 0.001$  paired t-test (Fig. 4.18B). Moreover, inhibition of the CaMKII had no significant effect in the plasticity:  $28.57 \pm 1.53\%$  in control and  $28.07 \pm 1.79\%$  in the presence of KN-93,  $P = 0.868$ , unpaired t-test (Fig. 4.18C).

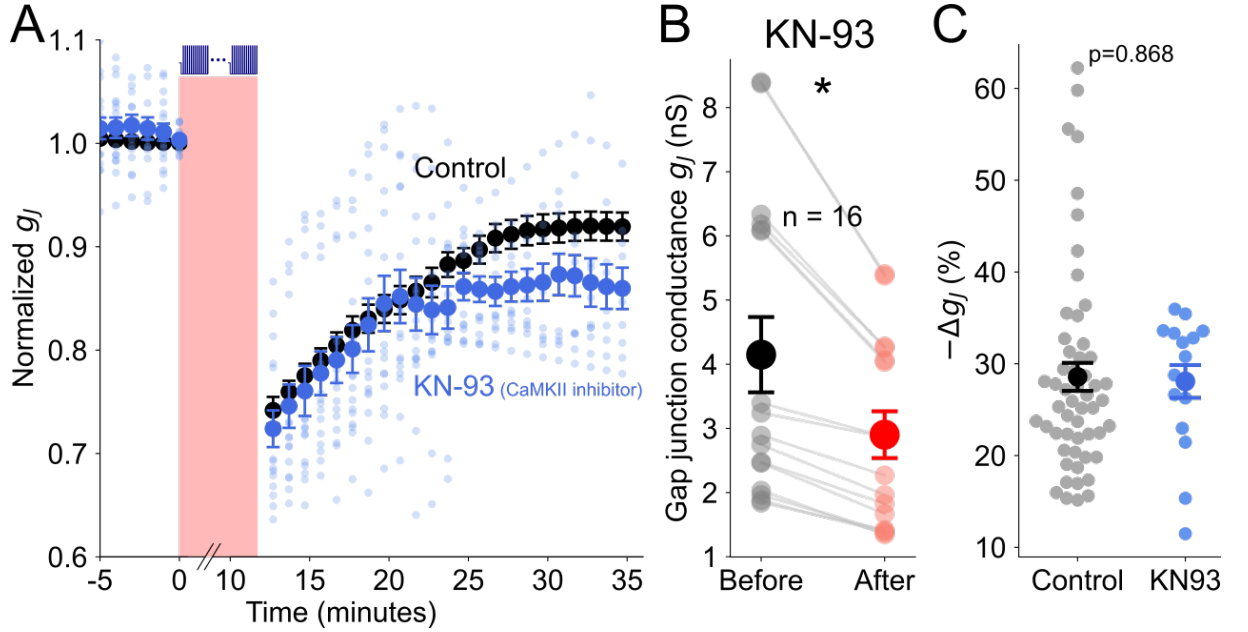


**Figure 4.18: CaMKII is not involved in the activity-induced  $g_J$  plasticity.** *A*: the inhibition of CaMKII by intracellular KN-93 10  $\mu\text{M}$  does not prevent the plasticity. *B*:  $g_J$  went from  $4.15 \pm 0.59$  nS to  $2.90 \pm 0.37$  nS,  $P < 0.001$  paired t-test. *C*: the  $g_J$  depression was  $28.57 \pm 1.53\%$  in control and  $28.07 \pm 1.79\%$  with KN-93,  $P = 0.868$ , unpaired t-test. All the data using KN-93 was obtained from  $n = 16$  directions from 4 animals.

Since our results suggest the existence of a  $\text{Ca}^{2+}$ -independent mechanism in mediating part of the plasticity of  $g_J$ , we sought to identify such hypothetical pathways. Adenyl cyclase (AC) is a good candidate, as it catalyzes the conversion of ATP into cAMP, promoting protein kinase A (PKA) activation. Furthermore, PKA has been reported to directly regulate Cx36 GJ (Kothmann et al., 2007; Bazzigaluppi et al., 2017; Zsiros and Maccaferri, 2008) (see section 2.2.2). In addition, the activity of several AC can be regulated by calmodulin (Neil et al., 1985; Ferguson and Storm, 2004; Halls and Cooper, 2011). Then, we postulated that the electrical activity of coupled MesV neurons might be promoting the AC, which could be boosted by calmodulin due to intracellular  $\text{Ca}^{2+}$  increase.

Firstly, we tested the ability of the cAMP pathway to modulate  $g_J$  by using the AC activator Forskolin  $40\ \mu\text{M}$  in the bath, monitoring  $g_J$  in coupled MesV neurons from Sprague Dawley rats (ages: P11 to P16). Figures 4.19A,B illustrate the effect of Forskolin in either direction in a coupled pair, where the synaptic current decreased compared with control (see example of the response to several voltage steps in Fig. 4.19C). Forskolin produced a decrease in  $g_J$ , which dropped from  $8.56 \pm 1.16\ \text{nS}$  in control conditions to  $6.61 \pm 1.21\ \text{nS}$  after its application,  $P = 0.02$  paired t-test,  $n = 14$  directions (Fig. 4.19D). Note that the increase of cAMP concentration also augmented the membrane current in the presynaptic neuron (more markedly in cell 1 in Fig. 4.19A), due to the expected upregulation of the  $I_H$  current, which might introduce a larger series resistance error in voltage clamp (even though it was compensated 80% online and 20% offline). In order to circumvent this possible problem, we independently measured  $g_J$  in current clamp (with bridge balance) in both conditions, finding a similar result:  $g_J$  changed from  $6.91 \pm 0.92\ \text{nS}$  before to  $4.75 \pm 0.68\ \text{nS}$  after Forskolin application,  $P < 0.001$  paired t-test,  $n = 38$  (Fig. 4.19E). Thus, electrical synapses between MesV neurons can be modulated by changes in intracellular levels of cAMP, even without electrical stimulation.

**Figure 4.19: Stimulation of adenylyl cyclase elicits  $g_J$  decrease without electrical activity** (see next page). *A*: Forskolin 40  $\mu\text{M}$  increases the activity of the adenylyl cyclase which raises cAMP, upregulating the PKA, producing a reduction in the synaptic current from cell 2 to cell 1, due to a brief hyperpolarizing voltage pulse in cell 1. Note that the membrane current in the cell 1 was increased by Forskolin, due to the cAMP-regulation of its  $I_H$  current. *B*: the same as in (*A*), but in the opposite direction. *C*: linear fit of the synaptic current against different transjunctional voltages (average of the two directions) evidences the diminution in  $g_J$ . *D*:  $g_J$  measured in voltage clamp went from  $8.56 \pm 1.16$  nS to  $6.61 \pm 1.21$  nS ( $P = 0.02$  paired t-test,  $n = 14$  directions from 6 animals). *E*: given that Forskolin also upregulates the presynaptic current (which could lead to a larger voltage clamp error),  $g_J$  reduction was also measured in the current clamp configuration. It went from  $6.91 \pm 0.92$  nS to  $4.75 \pm 0.68$  nS ( $P < 0.001$  paired t-test,  $n = 38$  directions from 17 animals).

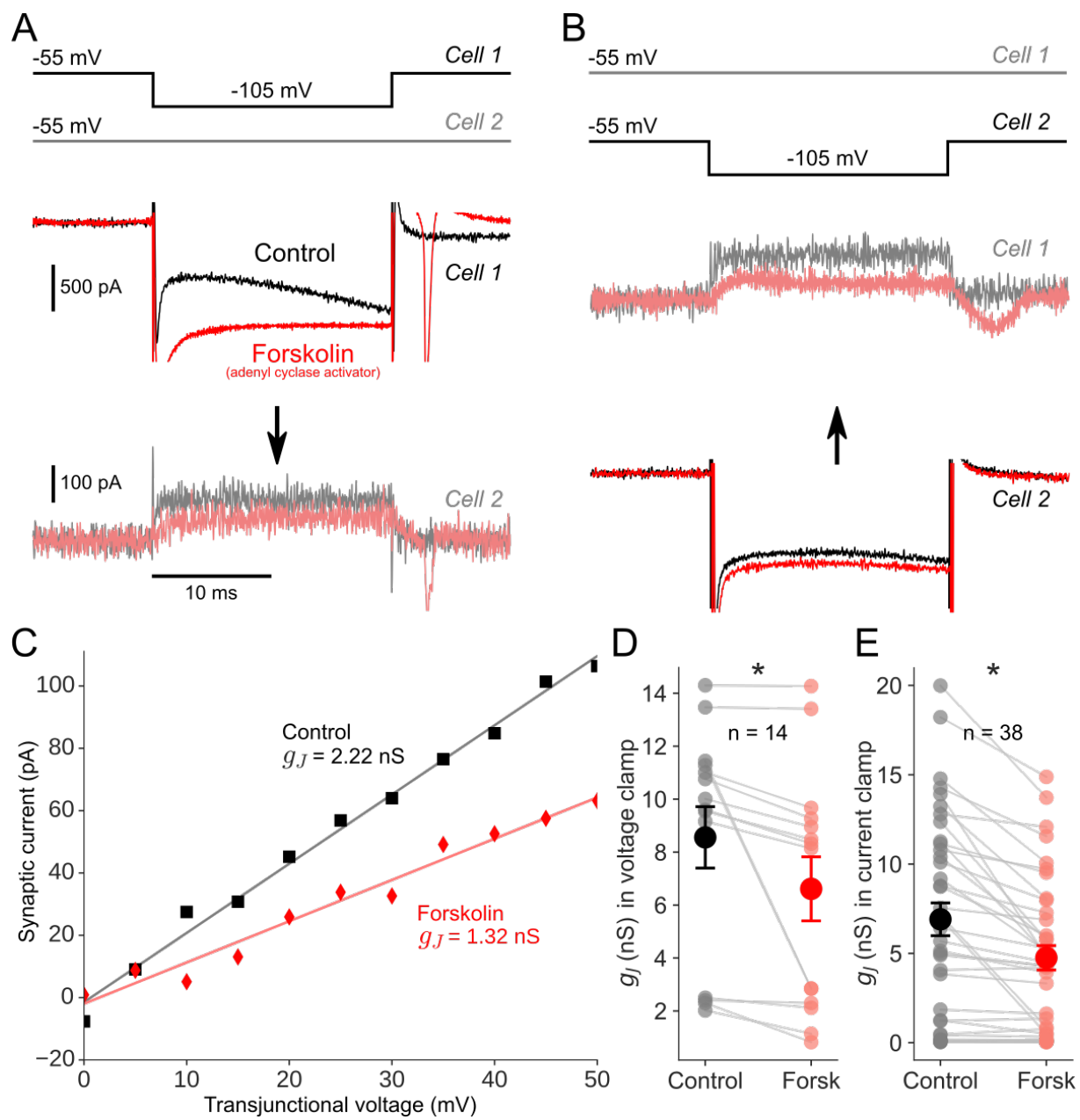


**Figure 4.19:** (Caption in the previous page.)

The reduction of  $g_J$  due to the activation of AC encouraged us to further investigate its possible role in the activity-induced plasticity. We applied the activity-like protocol in coupled pairs of mice MesV neurons, using an intracellular solution that included the AC inhibitor SQ22536 1 mM. In this condition, we found that the time course of the  $g_J$  depression was not different from control (Fig. 4.20A). The net  $g_J$  drop was from  $3.95 \pm 0.68$  nS to  $2.77 \pm 0.46$  nS,  $n = 8$ ,  $P = 0.003$  paired t-test (Fig. 4.20B) and it was not different from control:  $28.57 \pm 1.53\%$  in control and  $30.23 \pm 2.94\%$  with SQ22536,  $P = 0.690$ , unpaired t-test (Fig. 4.20C). Hence, it seems that the signaling pathway that involves AC and PKA is not involved in the activity-induced plasticity.

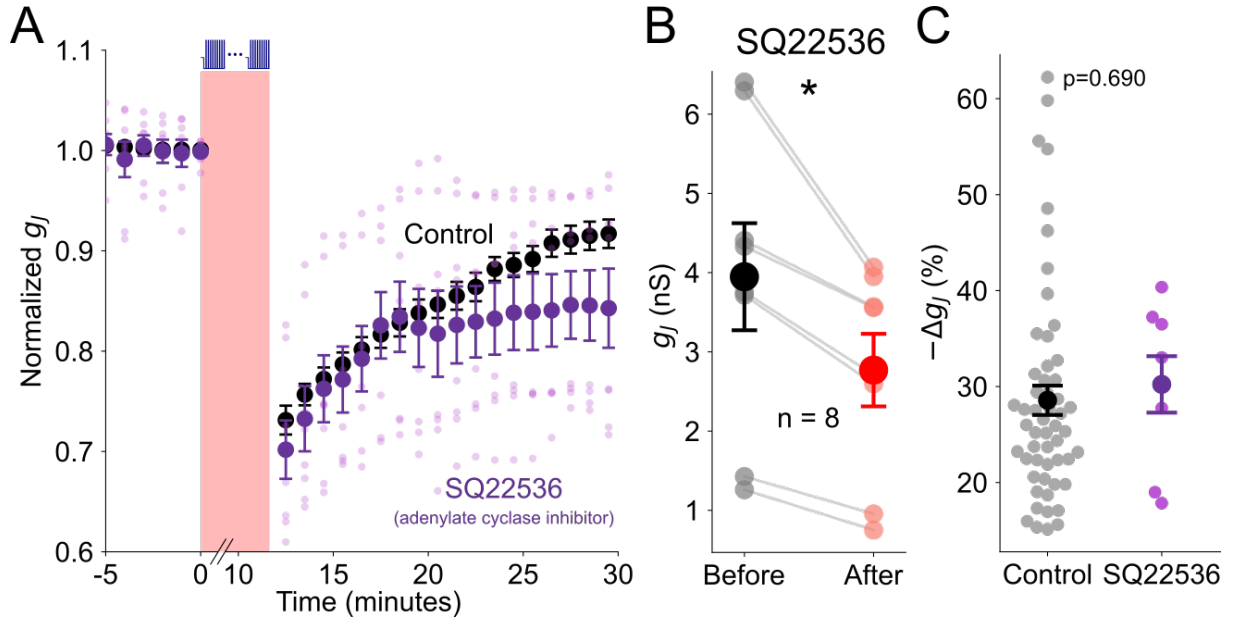


**Figure 4.20: Inhibition of adenylyl cyclase does not impair the activity-induced  $g_J$  plasticity.** *A*: inhibiting the adenylyl cyclase by intracellular SQ22536 1 mM does not alter the  $g_J$  depression due to repeated electrical stimulation. *B*:  $g_J$  went from  $3.95 \pm 0.68$  nS to  $2.77 \pm 0.46$  nS,  $P = 0.003$  paired t-test. *C*: the  $g_J$  depression was  $28.57 \pm 1.53\%$  in control and  $30.23 \pm 2.94\%$  with SQ22536,  $P = 0.690$ , unpaired t-test. All the data using SQ22536 was obtained from  $n = 8$  directions from 3 animals.



#### 4.3.14 Fast gap junction turnover rate in control conditions

The activity-induced reduction of  $g_J$  may be the consequence of the decrease of the unitary GJ channel conductance  $\gamma_J$ , the open probability and/or the total number of channels. Given that Cx36 has a lifetime of only few hours (Wang et al., 2015) (see section 2.2.2), it is possible that the activity-induced plasticity might be expressed as an imbalance between internalization and externalization of Cx36. In order to unveil the turnover of Cx36 in control conditions, we monitored  $g_J$  in coupled neurons, while blocking the exocytosis with Botulinum Toxin C (Botox) 250 nM in the patch pipettes. Figure 4.21A displays an example of the time course of  $g_J$  during the first 7 minutes after establishing the whole-cell configuration, with and without Botox in the internal solution (maroon and black dots, respectively). After a 2-minutes baseline of  $\sim 5.3$  nS, in presence of Botox  $g_J$  fell by 1 nS to a new stable value.

We measured  $g_J$  for coupled MesV neurons for longer times, without any other electrical or pharmacological stimulation (Fig. 4.21B). We found that, whereas  $g_J$  remained pretty stable in control conditions (in fact, there is a bit of upregulation), it decreased in few minutes for the coupled cells with Botox. These modifications are already noticeable after 15 minutes in the whole cell configuration:  $g_J$  went from  $4.58 \pm 0.33$  nS to  $4.70 \pm 0.34$  nS in control conditions ( $n = 58$  directions,  $P < 1 \times 10^{-4}$  paired t-test), whereas in pairs recorded with Botox-containing electrodes,  $g_J$  varied from  $3.74 \pm 0.37$  nS upon establishment of the whole cell configuration to  $2.97 \pm 0.29$  nS 15 minutes later ( $n = 16$ ,  $P < 0.001$  paired t-test; Fig. 4.21C and E, respectively). In summary,  $g_J$  changes by  $4.18 \pm 0.82\%$  in control and  $-19.59 \pm 3.19\%$  with intracellular Botox ( $P < 1 \times 10^{-15}$  unpaired t-test). Thus, these results strongly suggest that the GJ between MesV neurons are sustained by a continuous Cx36 turnover, where  $\sim 20\%$  of the open GJ channels are internalized in 15 minutes. This time course is compatible to the activity-induced plasticity, suggesting that an imbalance between exo- and endocytosis might explain, at least part, of the  $g_J$  reduction.

**Figure 4.21: Fast turnover rate of MesV gap junctions** (see next page). *A*: in control conditions  $g_J$  remained stable (black dots). However, blockade of exocytosis by intracellular Botulinum toxin C 250 nM (Botox; maroon dots) elicits a fast decrease of  $g_J$  in another pair of cells. *B*: the same as in (*A*) for several cells in control conditions (black) or with Botox (maroon), summarized in *C* and *D*, respectively. Comparing the values at the beginning and 15 minutes after,  $g_J$  went from  $4.58 \pm 0.33$  nS to  $4.70 \pm 0.34$  nS in control conditions (*C*;  $n = 58$  directions from 16 animals) and from  $3.74 \pm 0.37$  nS to  $2.97 \pm 0.29$  nS (*D*;  $n = 16$  directions from 4 animals) with Botox. In both cases, the changes of  $g_J$  are statistically significant:  $P < 0.001$ , paired t-tests. *E*: whereas  $g_J$  displays a small basal potentiation in control conditions ( $4.18 \pm 0.82\%$ ), it decreases by  $-19.59 \pm 3.19\%$  with intracellular Botox ( $P < 1 \times 10^{-15}$  unpaired t-test).

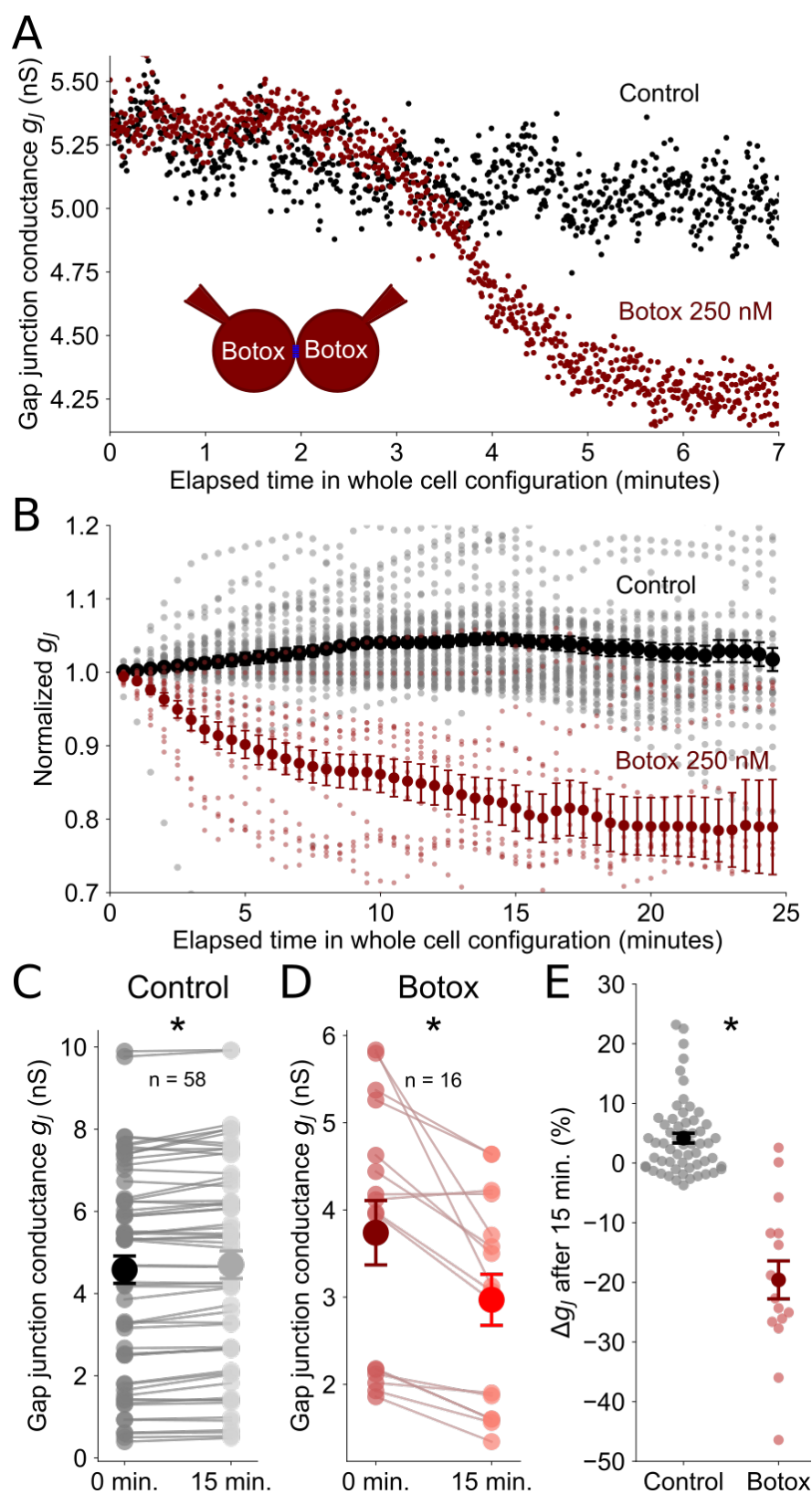


**Figure 4.21:** (Caption in the previous page.)

### 4.3.15 Somatic exocytosis is not involved in the activity-induced plasticity

Firing activity of MesV neurons can trigger  $\text{Ca}^{2+}$ -dependent somatic exocytosis (Zhang et al., 2012), which might be releasing signaling molecules, such as ATP (Chai et al., 2017), that could be participating in the induction of the electrical synaptic plasticity, through ionotropic (permeable to  $\text{Ca}^{2+}$  (Robertson et al., 1999)) and/or metabotropic purinergic receptors (Khakh and Henderson, 1998; Patel et al., 2001; Huang et al., 2010). Hence, we applied the activity-like stimulation in coupled neurons in the presence of intracellular Botox 250 nM (Fig. 4.22A). The activity-like stimulation protocol induced a drop of  $g_J$  from  $2.56 \pm 0.29$  nS before to  $1.77 \pm 0.23$  nS after the protocol,  $n = 12$  directions,  $P < 0.001$  paired t-test (Fig. 4.22B). This  $g_J$  depression is not statistically different from that obtained in control conditions:  $31.54 \pm 4.18\%$  with Botox,  $28.57 \pm 1.53\%$  in control,  $P = 0.434$ , unpaired t-test, ruling out the involvement of somatic release mechanisms in the activity-induced plasticity.

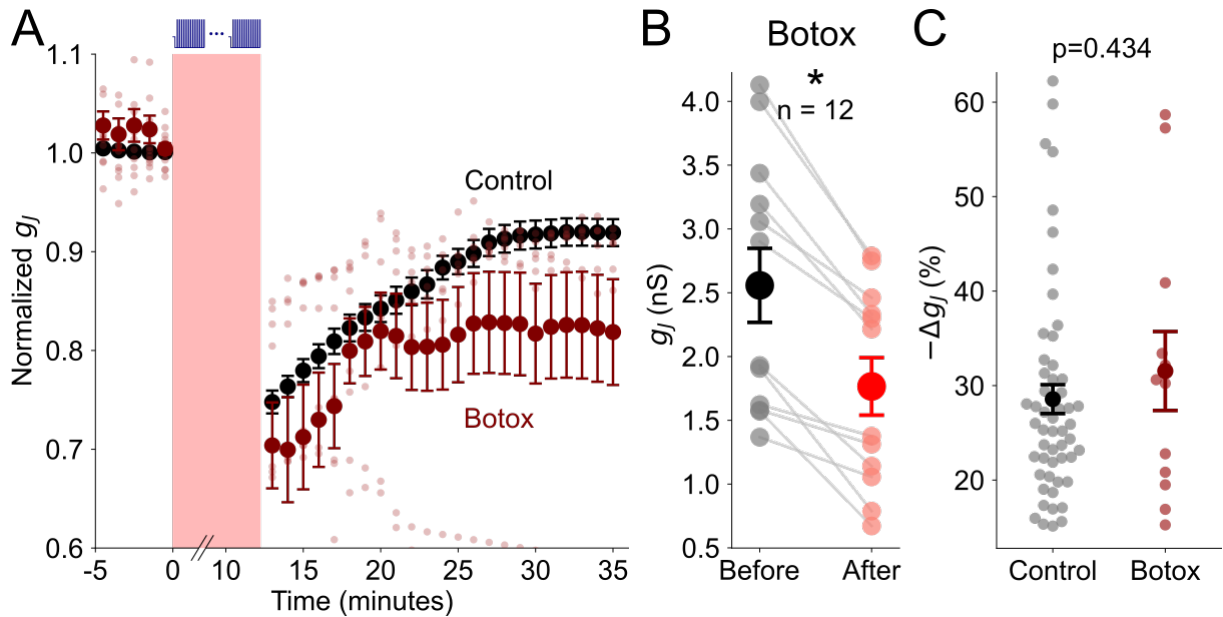


**Figure 4.22: Inhibition of exocytosis does not impair the activity-induced  $g_J$  plasticity.** *A*: inhibiting the exocytosis using intracellular Botulinum toxin (Botox) 250 nM does not alter the  $g_J$  depression due to repeated electrical stimulation. *B*:  $g_J$  went from  $2.56 \pm 0.29$  nS to  $1.77 \pm 0.23$  nS,  $P < 0.001$  paired t-test. *C*: the  $g_J$  depression is  $28.57 \pm 1.53\%$  in control and  $31.54 \pm 4.18\%$  with Botox,  $P = 0.434$ , unpaired t-test. All the data using Botox was obtained from  $n = 12$  directions from 4 animals.

## 4.4 Discussion

### 4.4.1 Heterogeneity of electrical synapses in the MesV nucleus can be explained by activity-dependent plasticity

We have characterized the impact of coupling in the synaptic transmission and in neuronal behavior in the MesV nucleus, through the CC and the loading effect. Remarkably, both functional features are very heterogeneous across the population of MesV neurons. This diversity could be explained in terms of the variability of both GJ and the intrinsic properties of the coupled neurons, as the operation of electrical synapses is determined by the interaction between them (see section 2.3). Here, we focused on the GJ, as they are the structural basis of the electrical synapses. Their conductances  $g_J$  were extremely varied too, suggesting that the GJ might be regulated in the living animal, according to behavioral needs. We found that electrical activity of MesV neurons, similar to that observed during feeding behavior (Yamamoto et al., 1989; Westberg et al., 2000), was enough to trigger a sharp decrease of  $g_J$  and the CC. The depression of  $g_J$  had short- and long-term components and was accentuated by a subsequent stimulation. Moreover, the induction of the plasticity had an exponential time course, which could give rise to further heterogeneity. Therefore, differential activity within the MesV neurons' population could be involved in setting the large diversity of electrical coupling strength.

### 4.4.2 Unilateral stimulation produced half of the plasticity

Mitral cells in the olfactory bulb are electrically coupled between themselves within each glomerulus, where they receive the same sensory information and fire synchronously (Christie et al., 2005; Maher et al., 2009; Pouille et al., 2017). The spatial organization of the retina (Fig. 2.8) and the dorsal cochlear nucleus (Apostolides and Trussell, 2013) determine that neighboring coupled neurons share a common sensory input too. Hence, it would not be surprising that coupled MesV neurons convey similar sensory information too, even though we do not know that yet. For that reason, we also tested applying the activity-like protocol to only one neuron (unilateral stimulation), while keeping its coupled partner at a fixed potential. The  $g_J$  depression was half that when the two cells were simultaneously stimulated (bilateral). However, unilateral stimulation in coupled TRN neurons resulted in the same synaptic depression as in the bilateral case (Haas et al., 2011). In addition, we found no rectification neither before nor after the stimulation -as expected from homotypic GJ-, while it increased in TRN neurons after unilateral stimulation (Haas et al., 2011; Sevetson and Haas, 2015). The main difference between these two

sets of results may rely on the measurement technique: the dendritic location of TRN GJ hinders accurate  $g_J$  recordings, due to poor space clamp. Furthermore,  $g_J$  in TRN was indirectly estimated from current clamp responses, using an approximation that assumes two isopotential cells (Bennett, 1966), introducing errors when not used in that context (Welzel and Schuster, 2019).

#### 4.4.3 $\text{Ca}^{2+}$ participates in the basal regulation and activity-dependent plasticity of GJ in the MesV nucleus

Plasticity of electrical coupling induced by activity has been reported in other brain regions, usually associated with an increase of intracellular  $\text{Ca}^{2+}$  concentration and prevented by BAPTA (Yang et al., 1990; Sevetson et al., 2017; Mathy et al., 2014). However, in our experiments, the depression of  $g_J$  was only partially blocked in the presence of intracellular BAPTA, suggesting that some of the induction occurs in nanodomains, where GJ are in close proximity to voltage-activated  $\text{Ca}^{2+}$  sources, such as CaV channels (Gandini and Zamponi, 2021).  $\text{Ca}^{2+}$  microdomains were already described in the IO, where there are few hundreds of nanometers between the Cx36 and the NR1 subunit of extrasynaptic NMDA receptors (Turecek et al., 2014). More detailed experiments should be done, in order to confirm a similar arrangement close to the Cx36 puncta between MesV neurons (see chapter 5).

Activation of CaMKII, triggered by increments of intracellular  $\text{Ca}^{2+}$  concentration after NMDA receptor activation, has been shown to be involved in GJ plasticity in the M-cell (Pereda et al., 1998) and the IO (Mathy et al., 2014; Turecek et al., 2014; Bazzigaluppi et al., 2017). However, it does not participate in the activity-induced plasticity in the MesV, because its inhibition did not alter the  $g_J$  drop. Another potential candidate as  $\text{Ca}^{2+}$  effector is Calcineurin, a phosphatase involved in the LTD induced by activity of GJ in the TRN (Sevetson et al., 2017).

Surprisingly, the activity-like protocol elicited electrical synaptic plasticity, even after the equimolar substitution of  $\text{Ca}^{2+}$  by  $\text{Mg}^{2+}$  in the extracellular solution and with intracellular BAPTA. This could be adjudicated to a poor control of the extracellular  $\text{Ca}^{2+}$  concentration in the slices or to a  $\text{Ca}^{2+}$ -independent pathway of the plasticity. Indeed, we showed that the GJ conductance in the MesV nucleus is depressed by the activation of the adenylyl cyclase (AC), which induces an increase of PKA activity, in accordance with previous results from the hippocampus (Zsiros and Maccaferri, 2008). Moreover, as  $\text{Ca}^{2+}$  regulates several AC (Neil et al., 1985; Ferguson and Storm, 2004; Halls and Cooper,



2011), it seemed plausible that the electrical activity was promoting AC, which was further boosted by the increase of intracellular  $\text{Ca}^{2+}$ . Nevertheless, the activity-induced depression was not affected by the inhibition of AC.

Seeking an alternative hypothesis for a  $\text{Ca}^{2+}$ -independent pathway, we postulated that the somatic exocytosis triggered by activity in MesV neurons (Zhang et al., 2012) was releasing a signaling molecule that acted in an autocrine way or on other neuron or glia. In fact, dorsal root ganglion (DRG) neurons also secrete vesicles filled by ATP, without depending on the intracellular  $\text{Ca}^{2+}$  concentration, but on the voltage activation of N-type CaV channels (Chai et al., 2017). Nonetheless, the plasticity was not impacted by the blockade of exocytosis during its induction.

Membrane hemichannels of Panx and or Cx in MesV neurons might be another possible source of signaling molecules, such as ATP (Anselmi et al., 2008; Dahl, 2015). In fact, non-synaptic Cx36 expression was reported for MesV neurons from animals of 15 days of age (Curti et al., 2012). Even more fittingly, Panx1 hemichannels can be opened by voltage and intracellular  $\text{Ca}^{2+}$  (Whyte-Fagundes and Zoidl, 2018) but, as figure 4.23 shows, the plasticity was not altered in Panx1 knock-out mice. The involvement of connexons has not been tested yet, but the most parsimonious hypothesis seems to be the non-existence of a  $\text{Ca}^{2+}$ -independent pathway regulating  $g_J$ , but a lack of accurate control of  $\text{Ca}^{2+}$  concentration in our experimental setup.

#### 4.4.4 HCN channels participate in the regulation of $g_J$

The participation of HCN channels in the activity-induced plasticity and basal regulation of  $g_J$  were unexpected, as they are traditionally described carrying mixed  $\text{Na}^+/\text{K}^+$  currents. However, the pore of HCN channels allows the flow of  $\text{Ca}^{2+}$  ions (Zhong et al., 2004; Yu et al., 2007; Michels et al., 2008), which can be blocked by  $\text{Cs}^+$  (Yu et al., 2004). In MesV neurons, HCN1 and HCN2 channels (Kang et al., 2004; Notomi and Shigemoto, 2004) constitute the molecular substrate of a large  $I_H$  current (see chapter 3). Then, even though the 0.5% of  $\text{Ca}^{2+}$  permeability through HCN2 channels (Yu et al., 2007) is an order the magnitude smaller than through NMDA receptors (Schneggenburger et al., 1993), the large density of the  $I_H$  makes it a substantial source of  $\text{Ca}^{2+}$  current for MesV neurons. Something similar happens in the DRG, where the  $\text{Ca}^{2+}$  component of  $I_H$  is equivalent to  $\sim 20\%$  of the current through voltage-gated  $\text{Ca}^{2+}$  channels, affecting the exocytosis triggered by action potentials (Yu et al., 2004). Our results suggest that  $\text{Ca}^{2+}$  flow through  $I_H$  is relevant to the regulation of  $g_J$ , but more evidence is still needed (see chapter 5), as more complex interactions between subunits HCN2 and voltage-gated  $\text{Ca}^{2+}$

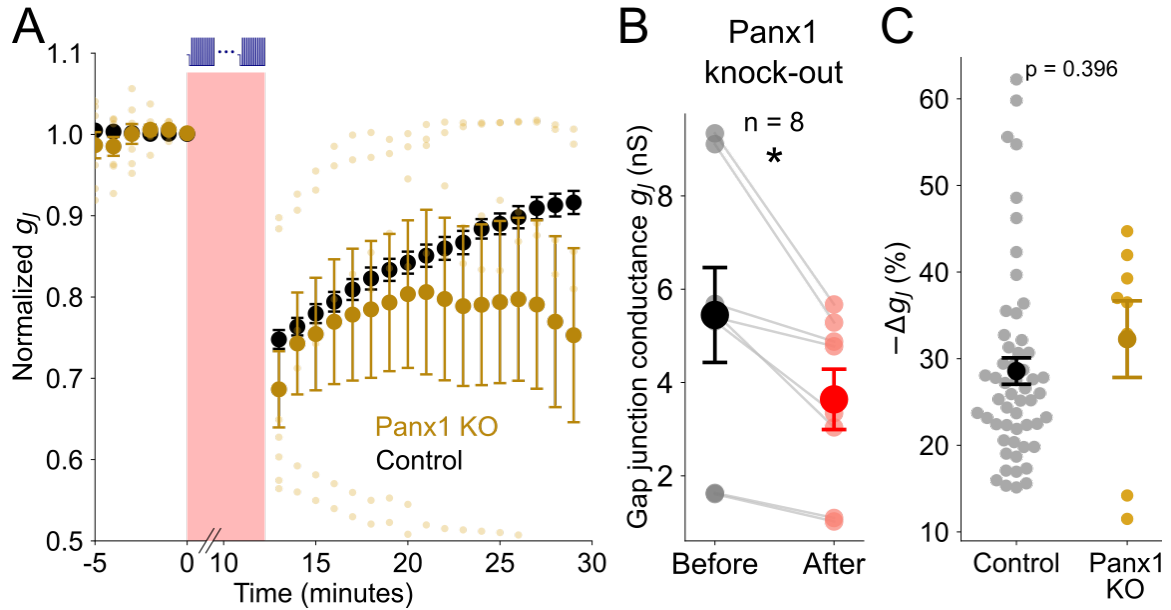


**Figure 4.23: Knock-out of Pannexin 1 (Panx1) does not alter the activity-induced  $g_J$  plasticity.** *A*: repeated stimulation provoked a similar decrease of  $g_J$  similar in Panx1 knock-outs (KO) and wild-type (WT) mice. *B*: in the Panx1 KO mice, the stimulation drives  $g_J$  from  $5.45 \pm 1.02$  nS to  $3.64 \pm 0.65$  nS ( $n = 8$  directions from 2 animals). *C*: the decrease in  $g_J$  was  $32.25 \pm 4.42\%$  in Panx1 KO ( $n = 8$  directions from 2 animals) and  $28.57 \pm 1.53\%$  in WT mice ( $n = 54$  directions from 23 animals). The two distributions did not display any significant difference:  $P = 0.396$ , unpaired t-test.

channels are possible too (Lin et al., 2010).

#### 4.4.5 Endocannabinoids are involved in the $g_J$ plasticity induced by activity

Previously, Zhang and coworkers have found that depolarization of MesV neurons produced a transient diminution of its GABAergic inputs, which was avoided by pharmacological blockade of CB<sub>1</sub> receptors (Zhang et al., 2012), suggesting a retrograde signaling by eCB produced in the MesV to presynaptic terminals. Indeed, MesV neurons display abundant expression of the fatty acid amide hydrolase, a molecule that catalyzes the hydrolysis of eCB and is characteristic in neurons that synthesize them (Egertová et al., 2003).<sup>1</sup> We found that the blockade of CB<sub>1</sub> receptors during the activity-like protocol enhanced the  $g_J$  depression, suggesting that in control conditions these receptors are activated by eCB during the stimulation, partially forestalling the induction of the electrical synaptic depression.

<sup>1</sup>eCB also activate transient receptor potential vanilloid type 1 receptors (De Petrocellis et al., 2001; Ahluwalia et al., 2003), which inhibit high-voltage activated Ca<sup>2+</sup> channels in trigeminal ganglion neurons (Zhang et al., 2014). However, we can rule out their involvement in the activity-induced plasticity, because they are not expressed in the MesV nucleus (Kim et al., 2010).

There are several possible signaling pathways linking the CB<sub>1</sub> receptors and the GJ, that depend on the localization of the receptors. They could be expressed in presynaptic terminals or astrocytes, which release a neurotransmitter in response to the activation of the eCB synthesized by the MesV neurons, as happens in the mixed synapses between the club endings and the M-cell (Cachope et al., 2007). There are multiple possible options for presynaptic boutons, given that MesV nucleus receive multiple chemical synaptic inputs (Lazarov, 2002). Astrocytes are another suitable option, as they are morphologically close to MesV neurons (Copray et al., 1990) and they might release glutamate (Gómez-Gonzalo et al., 2014; Navarrete et al., 2014), which stimulates NMDA and metabotropic glutamate receptors (Wang et al., 2015).

Autocrine signaling could also be possible (Bacci et al., 2004; Marinelli et al., 2009), but we still do not know if MesV neurons express CB<sub>1</sub> receptors. The effectors of CB<sub>1</sub> receptors are multiple and cell-dependant (Busquets-Garcia et al., 2018). For example, CB<sub>1</sub> receptors in hippocampal neurons are associated with the induction of LTD, by inhibiting the AC-cAMP-PKA pathway (Chevalleyre et al., 2007), a mechanism that we can rule out, given that it would cause a  $g_J$  potentiation, according to our results from section 4.3.13. Although eCB can modulate HCN channels (Maroso et al., 2016), and we showed that HCN channels participate in the  $g_J$  plasticity and regulation, this pathway may not be possible in our case, due to the fact that MesV do not display immunoreactivity for neuronal nitric oxide synthase (Pose et al., 2003), which is needed for the effect (Maroso et al., 2016). A more realistic possibility is that CB<sub>1</sub> receptors may regulate calcineurin (Heifets et al., 2008; Cui et al., 2016), which is involved in activity-dependent LTD in the TRN (Sevetson et al., 2017). CB<sub>1</sub> receptors could also be down-regulating CaV channels (Mackie et al., 1995; Twitchell et al., 1997; Huang et al., 2001; Kushmerick et al., 2004; Brown et al., 2004; Szabó et al., 2014), diminishing the inward flow of Ca<sup>2+</sup> during the activity-like stimulation.

#### 4.4.6 Trafficking of Cx36 might participate in electrical synaptic plasticity

We unveiled the basal GJ turnover in a mammal electrical synapse, that is behind the remarkable stability of  $g_J$  in control conditions. Our results are similar to those from the fish (Flores et al., 2012): the blockade of exocytosis elicited a rapid decrease of  $g_J$ , which seemingly saturated after few tens of minutes. Moreover, fluorescent tagged Cx36 has a lifetime of only few hours in expression systems (Wang et al., 2015) (see section 2.2.2). Interestingly, this fast turnover rate is compatible with the time frame of the activity-

induced plasticity, suggesting that  $g_J$  depression might be expressed as a diminution on the number of GJ, caused by an imbalance between internalization and externalization of Cx36. In fact, neuronal hyperactivity in the zebrafish produced a decrease in the expression of Cx36 orthologues in just 30 minutes (Brunal et al., 2021). In addition, the  $\text{Ca}^{2+}$ -signaling pathway has been proposed to mediate modifications of the number of Cx36 channels in the GJ (Bazzigaluppi et al., 2017). Indeed,  $\text{Ca}^{2+}$  enhances the interaction between Cx36 and Caveolin-1 in expression systems, promoting the internalization of GJ (Kotova et al., 2020).

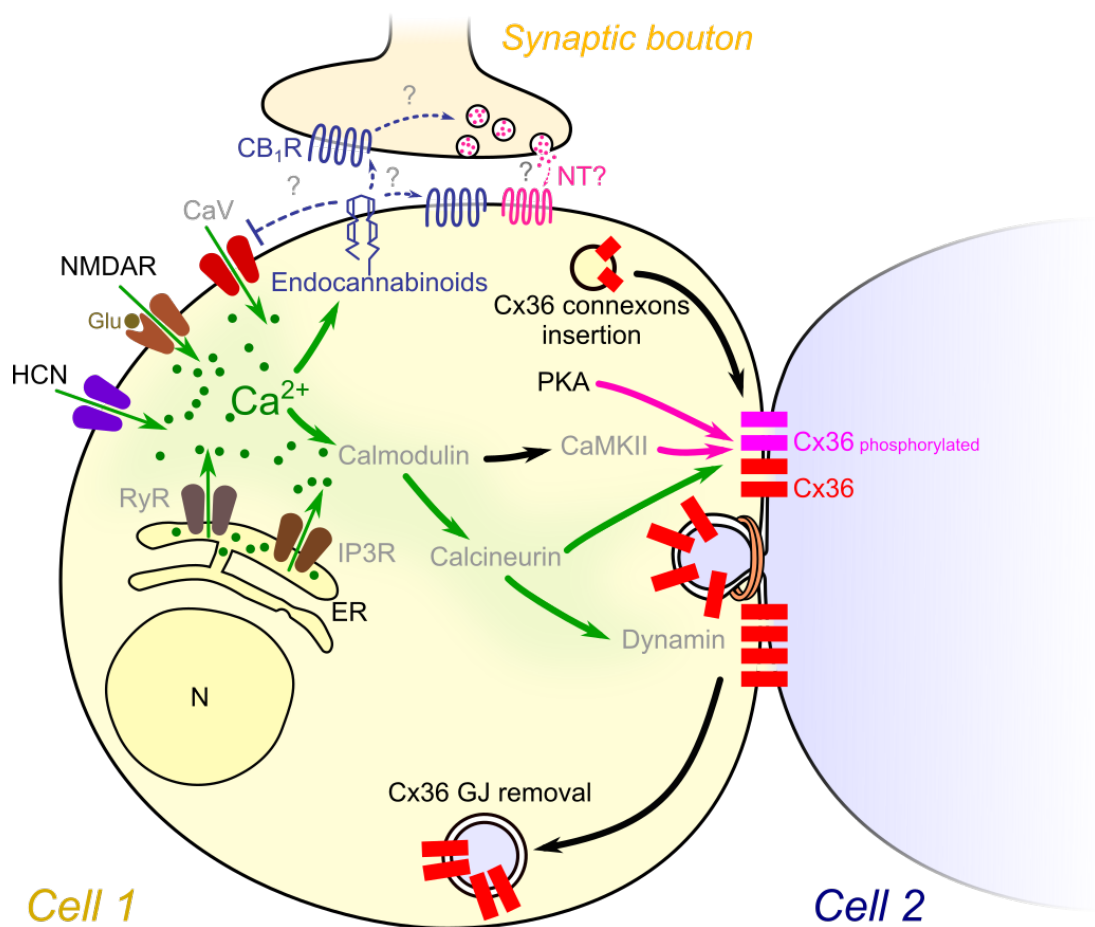


**Figure 4.24: Summary of the possible pathways involved in the plasticity of GJ between MesV neurons.** Repetitive firing may elicit  $Ca^{2+}$  going into a MesV neuron through voltage-gated  $Ca^{2+}$  and HCN channels. Another  $Ca^{2+}$  entry point are the NMDA receptors, activated by glutamatergic synaptic inputs. The increase of intracellular  $Ca^{2+}$  may activate Ryanodine and IP3 receptors, which liberate more  $Ca^{2+}$  from the endoplasmic reticulum. According to the level of intracellular  $Ca^{2+}$ , Calmodulin modifies the concentration of CaMKII and/or Calcineurin, both proteins that have been shown to participate in the regulation of electrical synapses. In addition to that, Calcineurin may also be involved in the activity of Dynamin, a GTPase that is key in the endocytotic process. Moreover, PKA participates of the regulation of the strength of electrical synapses. Furthermore, the intracellular  $Ca^{2+}$  increase promotes the synthesis of eCB, which activate  $CB_1$  receptors on the cell (inhibiting voltage-dependent  $Ca^{2+}$  channels, for example) and/or in a synaptic bouton (or astrocyte, not shown). On the other hand, GJ of MesV neurons are constantly renewed by the insertion of Cx36 hemichannels. The inhibition of this process by Botox evinced their fast turnover, with their removal probably is achieved by double-membrane vesicles, as shown in the recent literature. Green arrows signal the activity-induced plasticity studied in this chapter, while pink indicates the phosphorylation of Cx36 by regulatory kinases. The gray labels point out possible participants in the activity-induced plasticity that are still to be tested.

## Chapter 5

# Activity-induced plasticity of intrinsic properties

The intrinsic properties of neurons are as important as the GJ conductance  $g_J$  in setting the electrical coupling strength. In the chapter 4, we showed that activity-like stimulation elicited a decrease of the coupling coefficient, as a result of the reduction of both  $g_J$  and the input resistance  $R_{in}$ , focusing on the first phenomenon. Here, we will describe the later, proposing some mechanisms responsible for its induction. Cesium-sensitive potassium currents seem to be behind the sharp  $\sim 50\%$  fall of  $R_{in}$ , which is consistent with the  $\sim 100$  pA increase of the holding current in voltage clamp (effectively equivalent to an hyperpolarization in current clamp). The activity-induced  $R_{in}$  decrease is attenuated in the presence of intracellular BAPTA, indicating the possible involvement of  $\text{Ca}^{2+}$  signaling in this phenomenon. On the other hand, as  $\text{Cs}^+$  is also a blocker of HCN channels, we applied the methods from chapter 3 to characterize the  $I_H$  in MesV neurons from mice. Remarkably, we found that the  $I_H$  maximum conductance  $g_{Hmax}$  in coupled neurons was substantially larger than in the uncoupled ones, but their biophysical properties were the same. Furthermore, there was a significant relationship between  $g_{Hmax}$  and  $g_J$  in control conditions. Even more surprisingly, the  $I_H$  also experienced an activity-induced decrease, with a similar time course to the  $g_J$  depression, suggesting common mechanisms behind both phenomena.



## 5.1 Introduction

The coupling coefficient (CC) depends on both the GJ and the postsynaptic input resistances,  $R_J$  and  $R_{in2}$  respectively. Using the equation 2.1, we can easily express the CC in terms of  $g_J = \frac{1}{R_J}$ :

$$CC = \frac{g_J \cdot R_{in2}}{1 + g_J \cdot R_{in2}} \quad (5.1)$$

According to this equation, the CC can be analyzed as a monotonically increasing function of only one adimensional variable  $x$ , defined as the product between  $g_J$  and  $R_{in2}$  (Fig. 5.1A):  $CC = \frac{x}{1+x}$ . When  $x = 0$  ( $g_J = 0$  and/or  $R_{in2} = 0$ ), the CC is zero, as expected. On the other hand, when both  $g_J$  and  $R_{in2}$  are very large,  $x$  becomes even larger and  $CC \rightarrow 1$ . Note that most of the CC between mammalian neurons (section 2.3) occur in the region below 0.1, where slight changes on  $x$  have a large impact on the CC.

In the chapter 4, we characterized the  $g_J$  depression provoked by activity-like stimulation (Fig. 4.7A). In an homeostatic situation, the decrease of  $g_J$  would be mirrored by a parallel increase of  $R_{in}$ , in order to maintain the CC. However, the protocol did not only diminish  $g_J$  but also  $R_{in}$ , further reducing  $x$  and boosting the depression in the electrical synaptic transmission (Fig. 4.7D-F). Before the stimulation (black square in Fig. 5.1B), the respective average values of  $g_J$  and  $R_{in}$  were  $5.17 \times 10^{-3} \mu S$  and  $83.16 M\Omega$ , resulting in  $x_{\text{before}} = 0.43$  and  $CC = 0.30$  (experimental mean: 0.34). After (red square), they were  $3.52 \times 10^{-3} \mu S$  and  $57.01 M\Omega$ , whereas  $x_{\text{after}} = 0.20$  and  $CC = 0.17$  (experimental mean: 0.18). However, if there was only a  $g_J$ -depression, and  $R_{in}$  kept unaltered (blue circle),  $x = 0.29$  and the theoretical CC would fell to 0.23. In the opposite case (green circle), the final theoretical CC would also be 0.23 ( $x = 0.29$ ). Therefore, the reduction of  $g_J$  and  $R_{in}$  contributed equally to the reduction of the CC. In this chapter, we will present a preliminary analysis on the activity-induced decrease of  $R_{in}$  in the MesV neurons, due to its functional relevance.

The plasticity of neuronal intrinsic properties can be induced by several mechanisms, usually involving the activation of G-protein coupled receptors, or  $Ca^{2+}$  influx through voltage-dependent ion channels or ionotropic receptors (Cantrell and Catterall, 2001; Zhang and Linden, 2003; Burke and Bender, 2019). For example, the activation of muscarinic receptors inhibits  $Ca^{2+}$ -activated  $K^+$  (K(Ca)) channels in hippocampal pyramidal neurons, preventing the membrane hyperpolarization and enabling LTP mediated by NMDA receptors (Egorov et al., 1999; Buchanan et al., 2010). K(Ca) channels in fast spiking neurons are activated by the increase of intracellular  $Ca^{2+}$  concentration due to the activation of NMDA receptors, regulating their input resistance and excitability (Zhang

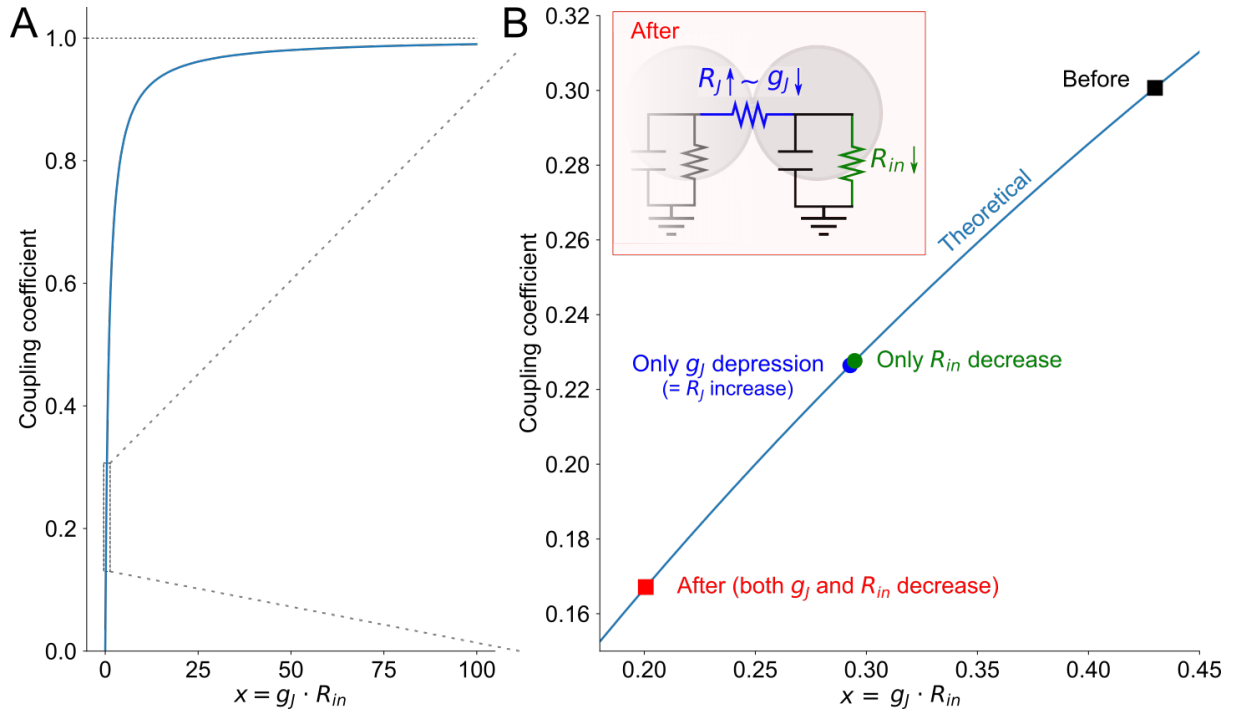


**Figure 5.1: Role of  $g_J$  and  $R_{in}$  in setting the coupling coefficient (CC).** *A*: theoretical CC for a wide range of  $x = g_J \cdot R_{in}$ . *B*: zoom of the theoretical CC within the range of  $x$  relevant for the activity-dependent electrical synaptic plasticity in MesV neurons. According to this relationship, using the mean values of  $g_J$  and  $R_{in}$  (Fig. 4.7), before the activity-like stimulation the CC was 0.30 (black point) and after 0.17 (red). But, if only  $R_{in}$  or  $g_J$  changed (green and blue, respectively), the CC would be  $\sim 0.23$  in both cases. Inset: schematic representation of the equivalent circuit modifications after the induction of the plasticity.

and Huang, 2017). Activity patterns can also reduce the number of channels available on the membrane, by promoting their endocytosis. Repetitive firing of CA3 (but not CA1) hippocampal pyramidal neurons elicits the internalization of voltage-dependent  $K^+$  channels Kv1.2, mediated by the protein tyrosine kinase (Kim et al., 2007). In CA1,  $Ca^{2+}$  influx through NMDA receptors provokes the endocytosis of another voltage-dependent  $K^+$  channels (Kv4.2) (Hyun et al., 2013).

MesV neurons express a myriad of ion channels:  $K^+$  channels (delayed rectifier, high-threshold, A-type, inward rectifier, K(Ca) (Del Negro and Chandler, 1997; Tanaka et al., 2003; Hsiao et al., 2009)),  $Na^+$  channels (generating transient, persistent and resurgent currents (Enomoto et al., 2007)),  $Ca^{2+}$  channels (low and high-threshold currents (Yoshida and Oka, 1998)), HCN (see chapter 3), among others. Some of them could be affected by the activity-like stimulation presented in chapter 4, due to  $Ca^{2+}$  influx *per se* and/or signaling cascades. Here, we will explore some of these possibilities, employing recordings performed in chapter 4 with focus on the intrinsic properties.

## 5.2 Materials and methods

The results presented in this chapter came from the experiments performed in mice in the chapter 4. All the materials and methods described there apply here. The characterization of the  $I_H$  current followed the procedures detailed in chapter 3, from a holding potential of -55 mV.

### 5.2.1 Measurement of $R_{in}$ from current traces in voltage clamp

While in chapter 3 the  $R_{in}$  was estimated in the current clamp configuration, from voltage responses, in this chapter the  $R_{in}$  is estimated from voltage clamp recordings, since the study of activity-dependent plasticity was mostly performed under this experimental condition. Taking into advantage our numerous recordings in voltage clamp, we used them to compute  $R_{in}$  by applying negative voltage steps, from a holding potential of -55 mV to -105 mV, in 5-mV steps, and recording the membrane current responses, which presented an early linear component, and a later one with strong voltage dependency (green and orange traces, respectively, in Fig. 5.2A). In fact, the linear component is defined by the minimum of the current response to the most hyperpolarized voltage step, which is equivalent to the peak voltage response used to calculate  $R_{in}$  in current clamp. Accordingly, its discrepancy to the later orange traces is a result of the hyperpolarization-activated current  $I_H$ , and disappears in the presence of CsCl (Fig. 5.2B). Therefore, we will use the minimum peak current responses to compute  $R_{in}$  from voltage clamp recordings.

For coupled neurons, we could apply the voltage steps simultaneously to both cells, eliminating the junctional current through the GJ conductance. Alternatively,  $R_{in}$  can be obtained from presynaptic currents recorded during protocols used to assess  $g_J$  in voltage clamp (Fig. 4.5A). In this protocol, the presynaptic neuron is stepped to negative voltages, while keeping the postsynaptic one at the holding potential (usually -55 mV). The corresponding equivalent circuit, drawn in Fig. 5.2C, shows that the measured current response  $I_1$  was the sum of the junctional and presynaptic membrane currents,  $I_J$  and  $I_{m1}$  respectively. As  $I_J$  was accurately recorded in the postsynaptic neuron and used to compute  $g_J$ , it was possible to subtract it to the slope of the current-voltage (I-V) relationship, obtaining the presynaptic input conductance  $g_{in1}$ :

$$g_{in1} = \frac{1}{R_{in1}} = \frac{\Delta I_1}{\Delta V_1} - g_J = \text{slope of I-V} - g_J \quad (5.2)$$

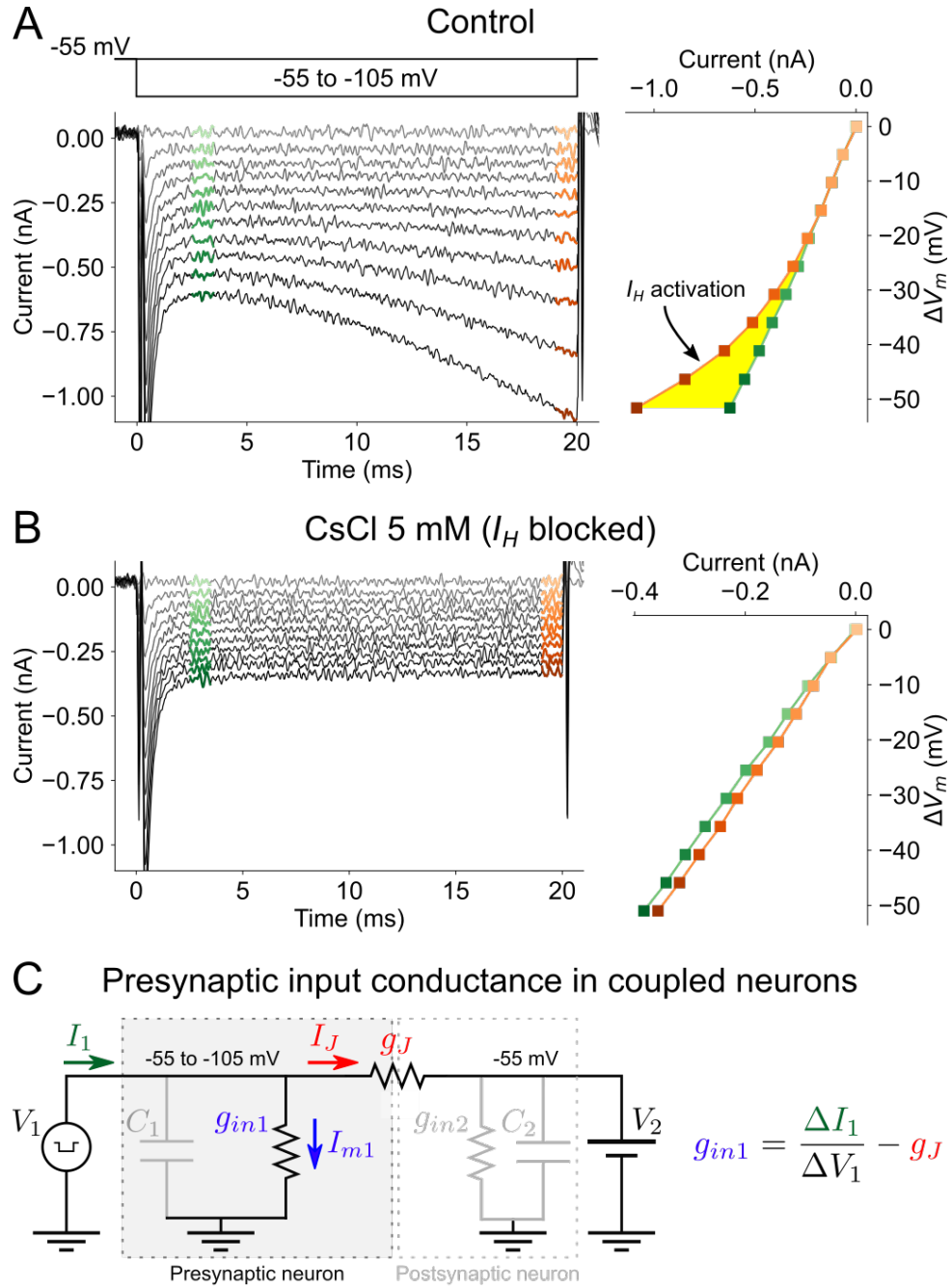


**Figure 5.2: Measurement of the input resistance  $R_{in}$  in voltage clamp.** A: voltage steps from the holding potential -55 mV to -105 mV elicit inward currents in an isolated MesV neuron. After the initial stimulation artifact, the early inward currents (green segments) behave linearly, as demonstrated by the corresponding current-voltage (I-V) plot shown on the right, whose slope is the input resistance  $R_{in}$ . Later responses (orange) present a voltage-dependent enhancement (orange), mainly due to the hyperpolarization-activated current  $I_H$  (yellow area in the I-V). B: The nonlinear behavior disappears in the presence of CsCl 5 mM, which blocks the  $I_H$ . C: For an electrically coupled presynaptic neuron,  $R_{in}$  was computed using hyperpolarizing voltage steps, while the postsynaptic cell was clamped at a fixed potential. The recorded current  $I_1$  (green) is the sum of two components: the presynaptic current  $I_{m1}$  (blue) and the junctional current  $I_J$  (red). As explained in chapter 4, in this configuration,  $I_J$  is recorded in the postsynaptic neuron, to compute  $g_J$  (Fig. 4.5). Thus, the presynaptic input conductance  $g_{in1} = \frac{1}{R_{in1}}$  is obtained by subtracting  $g_J$  to the slope of the presynaptic I-V curve.

### 5.2.2 Measurement of $I_H$

We measure the  $I_H$  current in mice MesV neurons, in control conditions, using the methods described in chapter 3. Briefly, the membrane voltage was stepped during 2 seconds, from -45 to -110 mV, in 5-mV steps, from a holding potential of -55 mV (Fig. 5.7A), followed by a test pulse to -85 mV. The series resistance was always compensated online by 80%. We stepped coupled neurons simultaneously, in order to eliminate the junctional current. We obtained the  $I_H$  by subtracting current traces in the presence of extracellular CsCl 2-5 mM to the control ones.

Given that, in the hyperpolarizing range, the  $I_H$  is several times larger than the remaining currents with CsCl (Fig. 5.7A), we asked if we could estimate its biophysical parameters directly in the raw traces in control conditions, without subtraction of CsCl traces. Actually, we found that the estimations of  $V_{H1/2}$  and the slope factor had negligible errors:  $-0.47 \pm 0.12\%$  and  $0.19 \pm 0.74\%$  respectively, whereas it was also small but larger for  $g_{Hmax}$ , as expected:  $-5.47 \pm 0.64\%$  ( $n = 23$  neurons from 16 animals; Fig. 5.3A). The time constants obtained in both conditions were almost undistinguishable in the range -110 to -60 mV (Fig. 5.3B). Thus, raw traces in control conditions can be used to precisely estimate the characteristics of  $I_H$ .

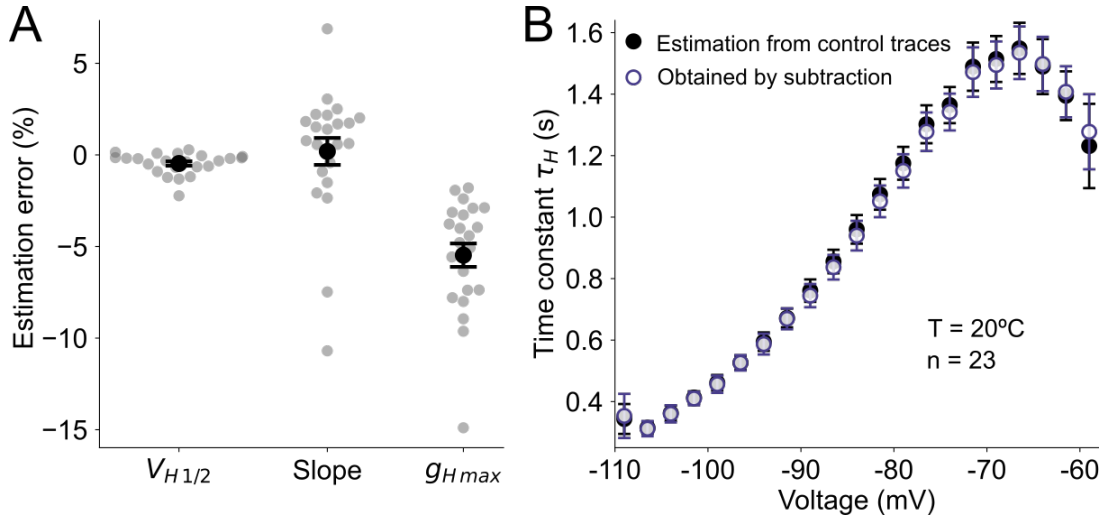


**Figure 5.3: The  $I_H$  can be accurately described without subtraction of CsCl traces.** A: estimation of  $I_H$  properties from tail currents in control conditions displayed a small error, compared to those obtained by subtracting them by traces in the presence of CsCl:  $-0.47 \pm 0.12\%$  for the half-activation voltage  $V_{H1/2}$ ,  $0.19 \pm 0.74\%$  for the slope  $k$ , and  $-5.47 \pm 0.64\%$  for the maximum conductance  $g_{Hmax}$ . B: there is an almost complete overlap for the time constants  $\tau_H$  obtained from control traces (filled circles) and subtracting CsCl traces.  $n = 23$  neurons from 16 animals in all cases.

## 5.3 Results

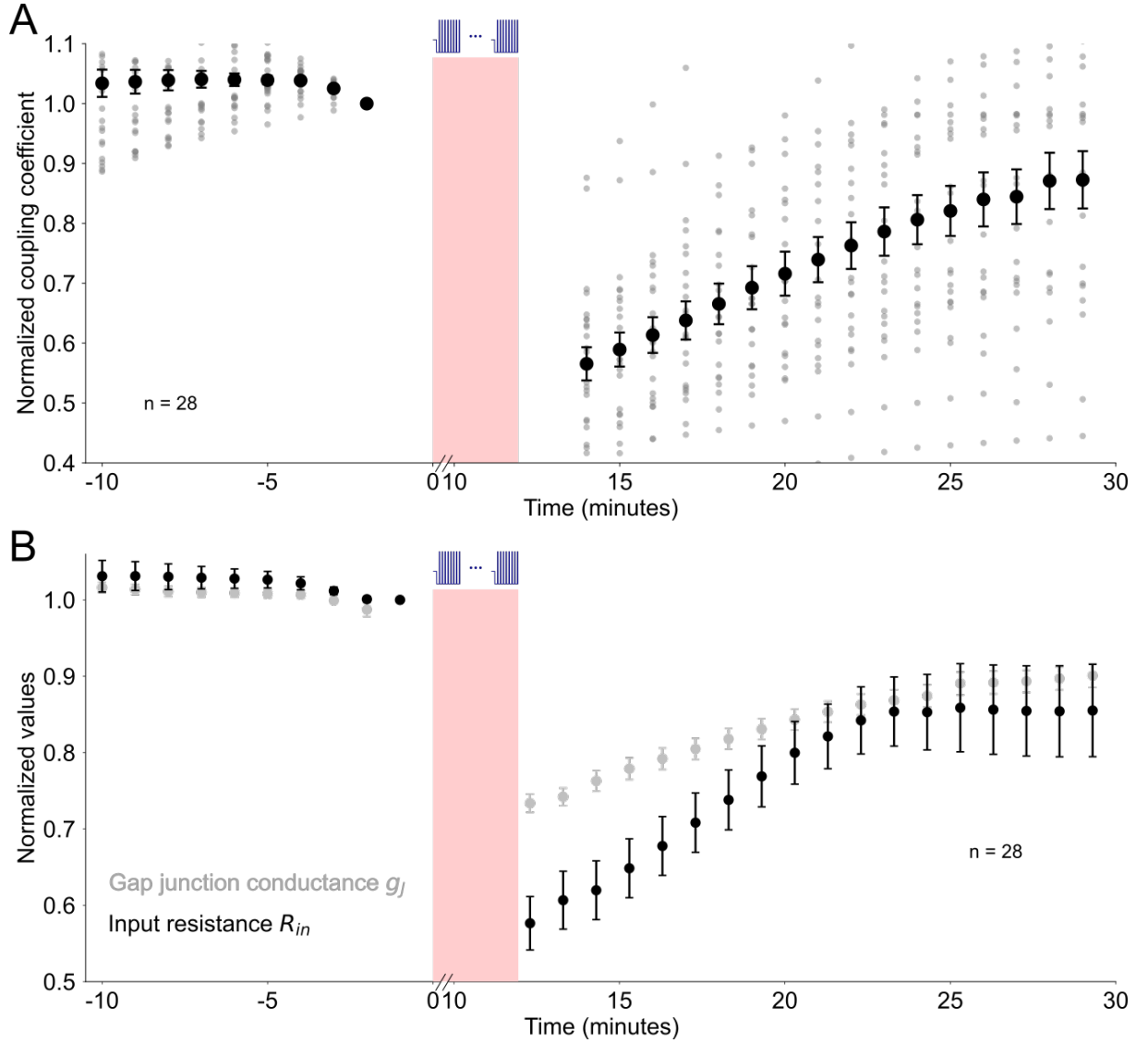
### 5.3.1 Activity-like stimulation reduces the input resistance

Figure 5.4A shows the time course of the coupling coefficient, which, after the activity-like stimulation, fell to 56.5% of its initial value, recovering to 84.5% 15 minutes later. According to our analysis, the reduction of CC results from the decrease of  $g_J$  and  $R_{in}$ , which after few minutes show a partial recovery (Fig. 5.4B). Surprisingly, the decrease in  $R_{in}$  was deeper than the  $g_J$  depression (73% versus 57% of their respective initial values, for  $n = 28$  neurons from 12 animals), emphasizing the role of the activity-induced modifications of the intrinsic properties in the electrical synaptic transmission. In addition, after  $\sim 10$  minutes of recovery, the  $R_{in}$  reached a new baseline, which is 85% of its initial value. This activity-dependent long-term decrease of  $R_{in}$  mirrored the similar (but slower) behavior of  $g_J$  depression (Fig. 4.9), further boosting the LTD and enhancing the heterogeneity of CC in control conditions (Fig. 4.2).

We wondered if the mechanisms responsible for  $g_J$  depression were also behind  $R_{in}$  reduction. As a matter of fact, the time courses of both phenomena, during the stimulation, are completely different: while  $g_J$  decay could be fitted by a single exponential (Fig. 4.9A),  $R_{in}$  showed a more complex temporal course, whose decrease is considerably faster and deeper, with a small rebound after 4 minutes (Fig. 5.5A), suggesting different mechanisms. The  $R_{in}$  was  $138.17 \pm 12.26$  M $\Omega$  before the stimulation and  $75.96 \pm 7.97$  M $\Omega$  immediately after it ( $P < 1 \times 10^{-8}$  paired t-test,  $n = 28$  neurons from 12 animals; Fig. 5.5B). Moreover, during the activity protocol the change in holding current mirrored that of the  $R_{in}$ , strongly suggesting that both phenomena are manifestations of the same mechanisms (Fig. 5.5C). The holding current at -55 mV changed from  $20.36 \pm 12.45$  pA before the protocol to  $129.75 \pm 22.8$  pA after its application ( $n = 28$  cells,  $P < 1 \times 10^{-5}$  paired t-test; Fig. 5.5D). The increase in the holding current and decrease of  $R_{in}$  suggested the opening of  $K^+$  and/or  $Cl^-$  channels, whose reverse potentials are usually below the holding potential of -55 mV.

Furthermore, we performed a systematic comparison of the decrease  $-\Delta R_{in}$  between control ( $43.01 \pm 3.49\%$ ,  $n = 28$ ) and all the conditions implemented to study  $g_J$  plasticity is shown in Fig. 5.6A. Activity-induced somatic exocytosis was reported in the MesV (Zhang et al., 2012), maybe releasing ATP (Chai et al., 2017) which could be activating purinergic receptors that modulate negatively  $I_H$  (Khakh and Henderson, 1998). Nevertheless, blockade of exocytosis by intracellular Botox 250 nM did not alter  $-\Delta R_{in}$  ( $39.35 \pm 6.67\%$ ,  $n = 12$ ,  $P = 0.60$  unpaired t-test). Somatic release of endocannabinoids could





**Figure 5.4: Time courses of the coupling coefficient CC and its components, after the activity-like stimulation.** *A*: the CC experienced a large decrease after the activity-like stimulation, due to the fall of both the gap junction conductance  $g_J$  and the input resistance  $R_{in}$  (silver and black points in *B*; see also Fig. 4.7). Note that the CC was measured from current clamp recordings, whereas  $g_J$  and  $R_{in}$  were from separate voltage clamp ones.  $n = 28$  neurons/directions in all cases, from 12 animals.

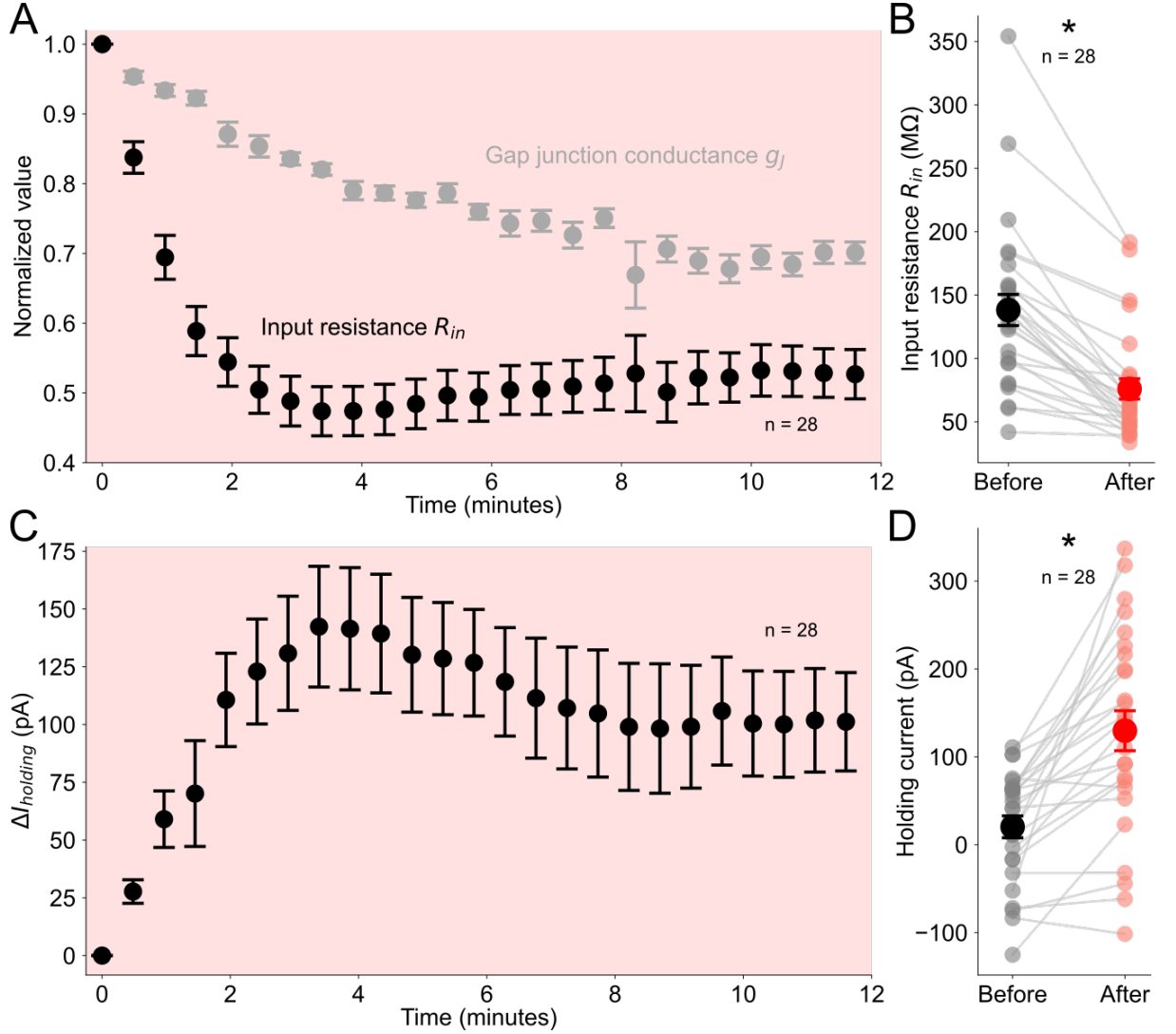


**Figure 5.5: Several non-synaptic membrane currents get affected by the activity-like stimulation.** *A*: during the stimulation, the  $g_J$  and  $R_{in}$  depressions had very different time courses: while the former was best fitted by a single exponential (Fig. 4.9), the later displayed a deeper ( $\sim 50\%$ ) and faster decay (time constant  $\sim 1$  minute), with a subsequent small rebound after  $\sim 4$  minutes. *B*: in parallel, the holding current increased with a time course similar to that of  $R_{in}$ , suggesting the activation of outward currents. *C*:  $R_{in}$  was  $138.17 \pm 12.26 M\Omega$  before the stimulation protocol and  $75.96 \pm 7.97 M\Omega$  after it ( $P < 1 \times 10^{-8}$  paired t-test).  $n = 28$  neurons from 12 animals for *A*, *B* and *C*. *D*: the intersection of the current-voltage (I-V) curves (used to measure  $R_{in}$ , see Fig. 5.2) before and after the stimulation indicates a membrane potential at which they produce the same current. If only one membrane current got altered by the activity-like protocol, the voltage of the I-V crossing would happen at its reverse potential. *E*: the I-V crossings ( $-67.56 \pm 2.99$  mV) spanned from voltages close to the reverse potentials of  $K^+$  and  $Cl^-$  ( $E_K = -92$  mV) to that of the  $I_H$  current ( $E_h = -28.7$  mV), indicating that several ion currents were modified. Data from neurons which experienced a decrease below 10% were not considered, to avoid spurious intersections from almost parallel I-V, resulting in  $n = 21$  neurons from 11 animals.

be acting on CB<sub>1</sub> receptors, activating K<sup>+</sup> channels (Mackie et al., 1995), but  $-\Delta R_{in}$  was not substantially reduced in the presence of the specific antagonist AM251 5  $\mu$ M ( $34.18 \pm 6.81$ ,  $n = 18$ ,  $P = 0.21$  unpaired t-test). We also tested blocking intracellular cascades involving adenylyl cyclase (with intracellular SQ22536 1 mM) or CaMKII (with intracellular KN93 10  $\mu$ M), with not significant difference:  $41.10 \pm 8.93\%$  ( $n = 10$ ,  $P = 0.81$  unpaired t-test) and  $35.54 \pm 4.71\%$  ( $n = 16$ ,  $P = 0.21$  unpaired t-test), respectively. As detailed before, we only found a diminution on  $-\Delta R_{in}$  with intracellular BAPTA 10 mM ( $22.70 \pm 5.37\%$ ,  $n = 16$  neurons,  $P < 0.002$  unpaired t-test) or in the presence of extracellular CsCl 2-5 mM ( $6.43 \pm 5.47\%$ ,  $n = 12$ ,  $P < 1 \times 10^{-5}$  unpaired t-test).

We analyzed the activity-induced changes of  $R_{in}$  in the presence of intracellular BAPTA 10 mM or extracellular CsCl 2-5 mM (Fig. 5.6B). With BAPTA, the  $R_{in}$  was  $117.94 \pm 10.10$  M $\Omega$  before and  $87.02 \pm 7.34$  M $\Omega$  after the stimulation ( $n = 16$  neurons from 6 animals,  $P < 0.003$ , paired t-test; Fig. 5.6C). In the presence of CsCl 2-5 mM in the bath,  $R_{in}$  was  $342.70 \pm 30.68$  M $\Omega$  and  $323.56 \pm 36.43$  M $\Omega$  after ( $n = 12$  neurons from 5 animals,  $P = 0.30$  paired t-test; Fig. 5.6D).

Thus, we conclude that the activity-induced  $R_{in}$  decrease is not related to signaling cascades involving the activation of somatic exocytosis, CB<sub>1</sub> receptors, adenylyl cyclase and/or CaMKII. On the other hand, the almost complete blockade of the phenomenon by CsCl suggests that HCN and/or K<sup>+</sup> channels are modified by the stimulation. In the hyperpolarization range, the possible K<sup>+</sup> channels involved are the inward rectifier (KIR) and the Ca<sup>2+</sup>-activated ones (K(Ca)) (Hille, 2001). Accordingly, the partial reduction on  $-\Delta R_{in}$  with BAPTA suggests that K(Ca) channels were opened due to the stimulation. We have also preliminary results ( $n = 4$  neurons from 1 mouse) in the presence of extracellular BaCl<sub>2</sub> 500  $\mu$ M, a KIR blocker, where  $R_{in}$  was  $254.13 \pm 61.81$  M $\Omega$  before and  $190.79 \pm 36.39$  M $\Omega$  after the plasticity-inducing protocol (not shown). The smaller  $-\Delta R_{in} = 21.59 \pm 5.49\%$  with BaCl<sub>2</sub> implies that KIR channels could also being affected by the stimulation. Finally, the  $I_H$  is another very versatile Cs-sensitive current, that could be modified. In the next sections, we will evaluate this hypothesis in detail.

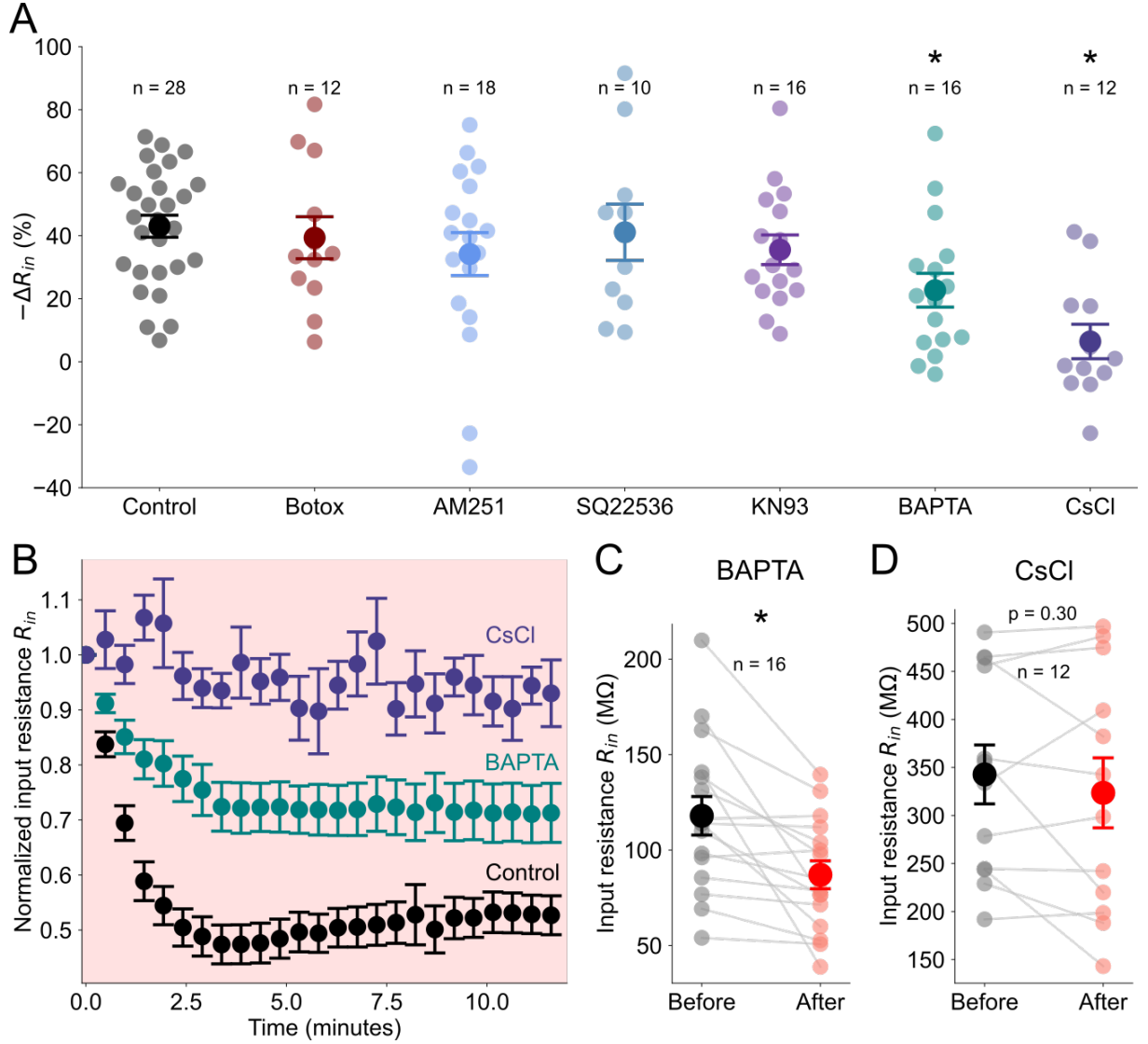


**Figure 5.6: Blockade of  $I_H$  and  $K^+$  currents abolishes activity-induced  $R_{in}$  modifications.** *A*: the activity-induced diminution of the input resistance  $-\Delta R_{in}$  was only significantly different from control ( $43.01 \pm 3.49\%$ ,  $n = 28$ ) on the BAPTA ( $22.70 \pm 5.37\%$ ,  $n = 16$  neurons,  $P < 0.002$  unpaired t-test) and CsCl ( $6.43 \pm 5.47\%$ ,  $n = 12$ ,  $P < 1 \times 10^{-5}$  unpaired t-test) conditions.  $P > 0.2$  in unpaired t-tests, for all the other conditions compared to control. Intracellular Botox 250 nM:  $39.35 \pm 6.67\%$  ( $n = 12$ ), extracellular AM251 5  $\mu$ M:  $34.18 \pm 6.81\%$  ( $n = 18$ ), intracellular SQ22536 1 mM:  $41.10 \pm 8.93\%$  ( $n = 10$ ), intracellular 10  $\mu$ M KN93:  $35.54 \pm 4.71\%$  ( $n = 16$ ). *B*: during the activity-like stimulation, the decrease in  $R_{in}$  was substantially reduced in the presence of intracellular BAPTA 10 mM, and completely abolished with CsCl 2-5 mM. *C*: with BAPTA 10 mM,  $R_{in}$  was  $117.94 \pm 10.10$  MΩ before and  $87.02 \pm 7.34$  MΩ after the stimulation ( $n = 16$  neurons from 6 animals,  $P < 0.003$ , paired t-test). *D*: in the presence of CsCl 2-5 mM in the bath,  $R_{in}$  was  $342.70 \pm 30.68$  MΩ and  $323.56 \pm 36.43$  MΩ after ( $n = 12$  neurons from 5 animals,  $P = 0.30$  paired t-test).

### 5.3.2 Characterization of $I_H$ in mice MesV neurons

The tail current, during the test pulse, was used to compute the activation curve (Fig. 5.7B), whose sigmoidal fit had a half-activation voltage  $V_{H1/2} = -79.19 \pm 0.81$  mV, slope factor  $k = 7.56 \pm 0.24$  mV and maximum conductance  $g_{Hmax} = 1.58 \pm 0.07$  nS/pF ( $n = 23$  neurons from 16 animals; Fig. 5.7C). Comparing with the results from chapter 3, the slope factor was similar to that obtained in rats ( $8.2 \pm 0.2$  mV), but the  $V_{H1/2}$  was even more depolarized in mice than in rats in the presence of cGMP ( $-82.9 \pm 20.8$  mV). The difference between  $g_{Hmax}$  is still more remarkable, as it is more than double in mice than in rats MesV neurons ( $0.68 \pm 0.05$  nS/pF). Furthermore, the time constant  $\tau_H$  also displayed a depolarizing offset compared to that from rats (the data was normalized to 20°C using  $Q_{10} = 4$  (Robinson and Siegelbaum, 2003); Fig. 5.7D). These discrepancies could not be attributed to differences in the temperature  $T$  of the recordings, as their distributions presented no significant difference ( $P > 0.05$  t-test unpaired). We conclude that, in control conditions, the  $I_H$  is more abundant in mice than in rats MesV neurons, and is more prominent at the membrane resting potential.

### 5.3.3 The maximum conductances of $I_H$ and the gap junctions may be coregulated dynamically

Using control traces to estimate the characteristics of  $I_H$  (without subtraction of traces in the presence of CsCl, see Fig. 5.3), we studied them in coupled and uncoupled MesV neurons. Remarkably, there was a substantial difference on  $g_{Hmax}$  between coupled and uncoupled cells:  $1.71 \pm 0.05$  nS/pF in the first case ( $n = 54$  neurons) and  $1.35 \pm 0.11$  nS/pF in the latter ( $n = 27$ ),  $P < 0.002$ , unpaired t-test (Fig. 5.8A). On the other hand,  $V_{H1/2}$  were not different between coupled and uncoupled neurons:  $-80.30 \pm 0.53$  mV and  $-79.53 \pm 0.96$  mV, respectively (same  $n$  as before,  $P = 0.445$ , unpaired t-test; Fig. 5.8B). There was no significant difference for the slope factor  $k$ , that was  $7.53 \pm 0.11$  mV for coupled and  $7.88 \pm 0.20$  mV for uncoupled neurons (same  $n$  as before,  $P = 0.110$ , unpaired t-test; Fig. 5.8C). Similarly, the time constant  $\tau_H$  was almost identical for coupled and isolated neurons (Fig. 5.8D). These results indicate that the  $I_H$  biophysical properties are similar among different MesV neurons, but its expression is upregulated in the coupled ones.

There was a noisy correlation between the  $g_{Hmax}$  and  $g_J$  (Fig. 5.8E) for electrically coupled MesV neurons: the slope of linear regression was 3.947,  $R^2 = 0.211$ ,  $n = 54$  neurons from 20 animals. The slope of this relationship was statistically significant:  $t = 3.73$

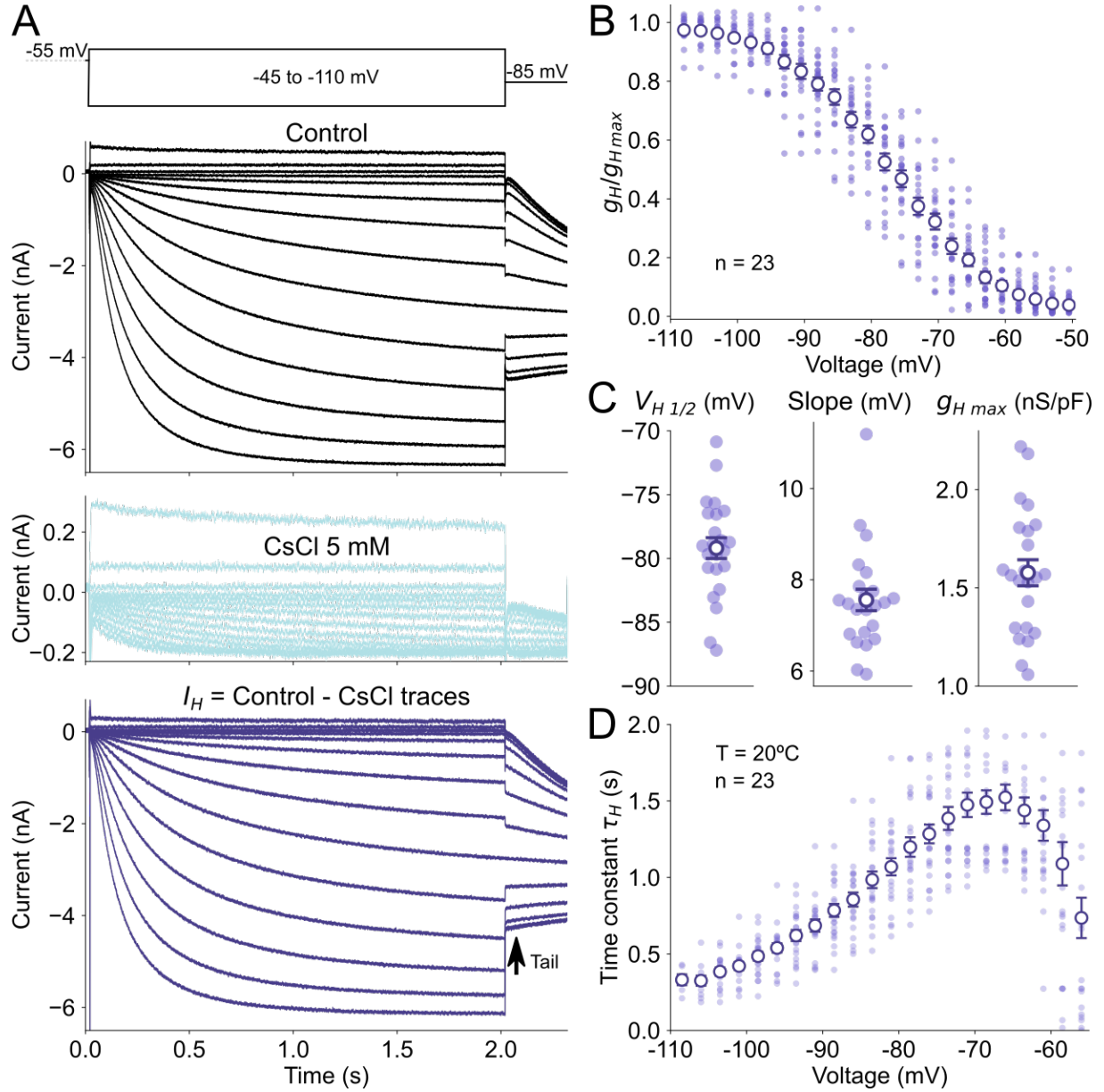


**Figure 5.7: Characterization of  $I_H$  in mice MesV neurons.** *A*: the  $I_H$  recording protocol consisted in 2-seconds voltage steps from -45 to -110 mV, from a holding potential of -55 mV, followed by a test pulse to -85 mV (see also Fig. 3.3). This protocol was applied to single or coupled neurons, recording the membrane current in control conditions (black traces) and in the presence of extracellular CsCl 5 mM (skyblue). The  $I_H$  (purple) was computed as the subtraction between these sets of traces. Notice that the remaining current in the presence of CsCl was considerably smaller than the  $I_H$ . *B*: the  $I_H$  activation curve was obtained from the initial current responses to the test pulses (tail currents, signaled by an arrow in *A*). *C*: the corresponding parameters of the activation curve were: half-activation voltage  $V_{H1/2} = -79.19 \pm 0.81$  mV, slope  $k = 7.56 \pm 0.24$  mV and maximum conductance  $g_{Hmax} = 1.58 \pm 0.07$  nS/pF. *D*: the time constant  $\tau_H$ , calculated from exponential fits to the voltage steps, normalized to 20°C, using  $Q_{10} = 4$ , as in chapter 3.  $n = 23$  neurons from 16 animals in all cases.



$> t_s = 2.01$ , t-test, further supporting that the functional interaction between electrical and the expression of  $I_H$ .

To further investigate the possible functional relationship between  $g_J$  and  $I_H$ , we assessed the effect of  $g_J$ -plasticity inducing protocol on  $I_H$ . Interestingly, this protocol also reduced the maximum conductance of this current, both in uncoupled and coupled MesV neurons (Fig. 5.9A,B). This result suggest that activity might induce parallel effects on  $g_J$  and  $I_H$ . For uncoupled neurons,  $g_{H\max}$  was  $1.30 \pm 0.13$  nS/pF before and  $1.07 \pm 0.11$  nS/pF after the stimulation ( $P < 0.001$ , paired t-test,  $n = 13$  neurons from 10 animals), whereas for coupled ones,  $g_{H\max}$  was  $1.48 \pm 0.18$  nS/pF before and  $1.34 \pm 0.18$  nS/pF after ( $P < 0.002$ , paired t-test). Moreover, the extent of regulation of these mechanisms showed a positive correlation. Although there was no significant relationship between the reduction of  $I_H$   $\Delta g_{H\max}$  and  $g_J$  depression  $\Delta g_J$ , the Figure 5.9C hints that more data would be necessary to completely discard this hypothesis.

As explained in chapter 4, the activity-like protocol had an initial step to -90 mV during  $\sim 400$  ms (Fig. 4.7A), which elicited a large inward current, blocked in the presence of CsCl (Fig. 4.15A). Taking into account these properties and that  $K^+$  currents were almost zero at -90 mV ( $E_K = -92$  mV), we conclude that the current recorded at -90 mV is mostly  $I_H$ . We fitted an exponential to the elicited current (whose baseline was subtracted), obtaining its time constant and asymptotic amplitude  $I_{H\max@-90\text{ mV}}$  for each repetition of the stimulus (25 times each 29-30 seconds), for  $n = 28$  neurons from 12 animals. While the time constant remained mostly constant during the 12 minutes of stimulation, the asymptotic current amplitude  $I_{H\max@-90\text{ mV}}$  decreased exponentially by  $\sim 30\%$  of its initial value (Fig. 5.9D), with a time constant which resembled the observed for  $g_J$  depression (Fig. 4.9A). Indeed, plotting normalized  $I_{H\max@-90\text{ mV}}$  against normalized  $g_J$ , during the stimulation in control conditions, revealed a linear relationship between them (Fig. 5.9E), whose slope was 0.885,  $R^2 = 0.959$ ,  $n = 28$  neurons from 12 animals. Furthermore, the linear relationship between these variables stood in the presence of intracellular BAPTA 10 mM: slope of linear regression 0.945,  $R^2 = 0.837$ ,  $n = 16$  neurons from 6 animals (not shown). Thus, the activity-induced modifications of  $I_H$  seems to not involve modulations of the biophysical properties of HCN channels, but only a reduction on their availability, by mechanisms that could be also behind the  $g_J$  plasticity, suggesting the co-regulation of both mechanisms.

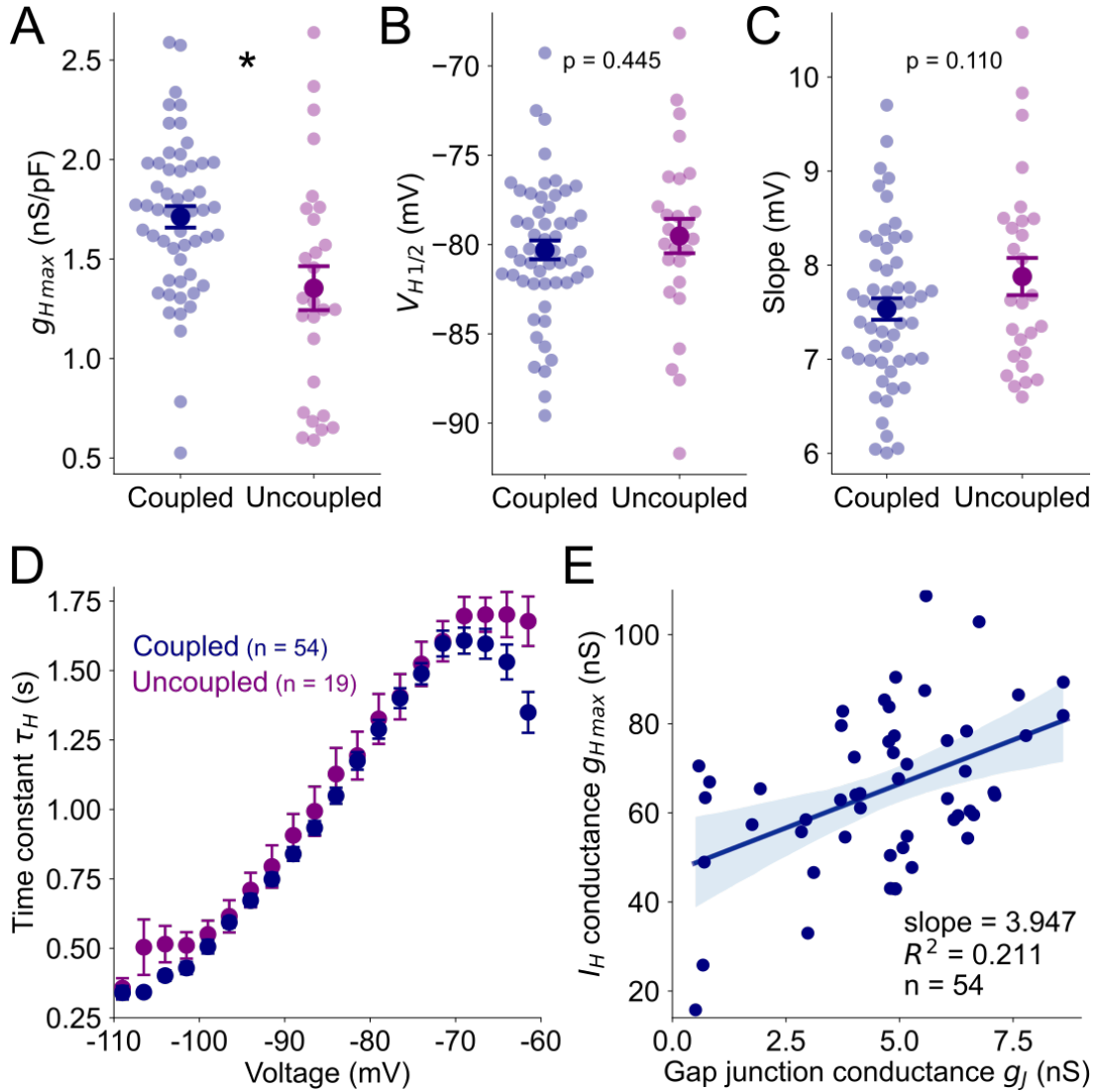


**Figure 5.8:  $I_H$  properties in coupled and uncoupled MesV neurons.** A: the maximum conductance  $g_{Hmax}$  was significantly higher for electrically coupled MesV neurons than for uncoupled ones:  $1.71 \pm 0.05$  nS/pF ( $n = 54$  neurons),  $1.35 \pm 0.11$  nS/pF ( $n = 27$ ).  $P < 0.002$ , unpaired t-test. B: the half-activation voltage  $V_{H1/2}$  for coupled and uncoupled neurons were undistinguishable:  $-80.30 \pm 0.53$  mV and  $-79.53 \pm 0.96$  mV, respectively (same  $n$  as in A),  $P = 0.445$ , unpaired t-test. C: similarly, the slope factor  $k$  were  $7.53 \pm 0.11$  mV and  $7.88 \pm 0.20$  mV, respectively (same  $n$  as in A),  $P = 0.110$ , unpaired t-test. D: time constants  $\tau_H$  for coupled and uncoupled MesV neurons overlapped from -110 to -65 mV. D: while the linear regression of  $g_{Hmax}$  against gap junction conductance  $g_J$  was quite poor ( $R^2 = 0.211$ ), its slope was statistically significant:  $t = 3.73 > t_s = 2.01$ , t-test. Light blue bands represent 95% confidence intervals.  $n = 54$  neurons from 20 animals.

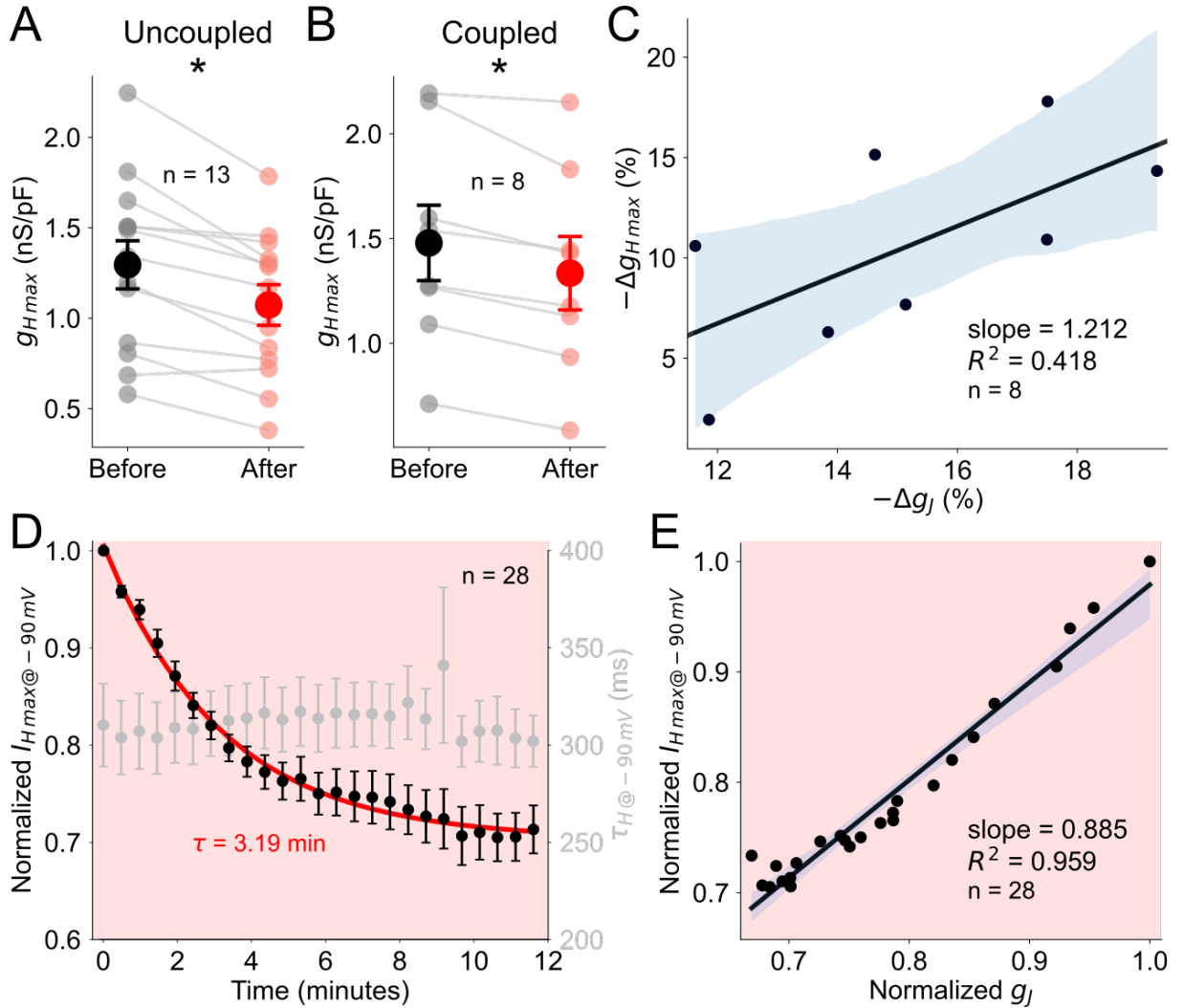


**Figure 5.9: Activity-like stimulation diminishes  $I_H$  maximum conductance, without modifying its biophysical properties.** *A*: for uncoupled neurons, the maximum conductance  $g_{Hmax}$  was  $1.30 \pm 0.13$  nS/pF before and  $1.07 \pm 0.11$  nS/pF after the activity-like protocol ( $P < 0.001$ , paired t-test,  $n = 13$  neurons from 10 animals). *B*: similarly, for coupled neurons,  $g_{Hmax}$  was  $1.48 \pm 0.18$  nS/pF before and  $1.34 \pm 0.18$  nS/pF after the stimulation ( $P < 0.002$ , paired t-test). *C*: the activity-induced diminution of  $g_{Hmax}$  correlated poorly with the depression of  $g_J$ , possibly due to the small number of observations.  $n = 8$  neurons from 3 animals for *B* and *C*. *D*: the plasticity-inducing protocol presented an initial voltage step to  $-90$  mV for  $\sim 450$  ms, which elicited a large inward current that was blocked by CsCl (Fig. 4.15A), consistent with the  $I_H$  properties. During the application of the stimuli, the asymptotic value of this exponential current  $I_{Hmax@-90mV}$  decreased, with a time constant of  $\sim 3$  minutes, while its activation time constant kept constant at  $\sim 300$  ms. *E*: during the protocol, the plot of the normalized asymptotic  $I_{Hmax@-90mV}$  correlated with the normalized  $g_J$ : slope = 0.885,  $R^2 = 0.959$ ,  $n = 28$  neurons from 12 animals. Light blue bands represent 95% confidence intervals.

## 5.4 Discussion

### 5.4.1 Activation of $K^+$ channels is most likely behind the activity-induced decrease of $R_{in}$

Although very preliminary, data presented in this chapter suggest very interesting insights into the co-regulation of mechanisms functionally interrelated determining electrical synaptic transmission efficacy. The input resistance of neuronal compartments can be modified by activity-dependent regulation of its membrane ion channels, which become a relevant factor in the context of synaptic plasticity, by boosting or attenuating postsynaptic responses (Wang et al., 2003; Shen et al., 2008; Steinert et al., 2011; Campanac et al., 2013; Cazade et al., 2017). From the increase of the holding current, we conclude that the  $R_{in}$  decrease is most likely caused by the opening of  $K^+$  currents, blocked by  $Cs^+$ . The dampening of the phenomenon by BAPTA strongly suggest the participation of  $Ca^{2+}$ -activated  $K^+$  channels (Latorre and Brauchi, 2006), which are blocked by  $Cs^+$  (Cecchi et al., 1987; Hille, 2001). This current is not very conspicuous in MesV neurons in control conditions (Del Negro and Chandler, 1997; Pedroarena et al., 1999), but it might be activated by a major intracellular  $Ca^{2+}$  increase during the stimulation. The fast decrease of  $R_{in}$  during the stimulation is consistent with this idea.

Given that even with BAPTA there was still a  $\sim 23\%$  decrease in  $R_{in}$ , several possibilities should be considered. There could be nanodomains where  $Ca^{2+}$ -sources interact with high-affinity  $Ca^{2+}$ -activated small-conductance  $K^+$  channels (Fakler and Adelman, 2008). For example, intracellular BAPTA could not completely abolish the  $K(Ca)$ -mediated activity-induced decrease of  $R_{in}$  in hippocampal pyramidal neurons (Borde et al., 1995, 2000). Another possibility is the involvement of other more  $K^+$  channels. Certain  $K^+$  currents can undergo activity-dependent but  $Ca^{2+}$ -independent facilitation, only by virtue of their own biophysical properties (Yang et al., 2014). KIR channels are a possible participant, as indicated by our preliminary experiments with  $Ba^{2+}$ , even though their half-activation voltage is very hyperpolarized (Tanaka et al., 2003). Another candidate would be a  $Ba^{2+}$ -sensitive  $K^+$  leak current, which has not been well studied yet (Tanaka and Chandler, 2006)<sup>1</sup>. Although low-threshold Kv1 channels produce prominent currents that control the excitability (Del Negro and Chandler, 1997; Hsiao et al., 2009) and electrical synaptic transmission in MesV neurons (Curti et al., 2012), their involvement is not probable, as they are not blocked by extracellular  $Cs^+$  (Hille, 2001). Experiments in the presence of TEA should be performed to fully characterize the role of  $K^+$  currents,

---

<sup>1</sup>Note that  $Ba^{2+}$  blockade is not restricted to  $K^+$  channels. For example, HCN channels can be partially blocked by  $Ba^{2+}$  too (Biel et al., 2009).

without affecting HCN channels (Biel et al., 2009).

Whereas the opening of K(Ca) channels by electrical activity is straightforward, the facilitation of the remaining  $K^+$  currents are more complex, usually requiring the phosphorylation of the channels (Fernández-Fernández and Lamas, 2021). We already tested and dismissed the PKA (Connors et al., 2008; Brignell et al., 2015) and CaMKII (Varga et al., 2004; van Welie and du Lac, 2011) pathways, but other kinases (PKC, MAPK, etc. (Fernández-Fernández and Lamas, 2021)) are still unexplored. We also rejected endocannabinoids' autocrine signaling upregulating KIR channels (Mackie et al., 1995) by blocking  $CB_1$  receptors and finding no difference on  $-\Delta R_{in}$ .

A less traditional, yet possible, additional source of outward current would be a  $Na^+$ -activated  $K^+$  current, activated by the HCN-induced intracellular  $Na^+$  increase. Even though they have been studied in mammalian neurons (Budelli et al., 2009; Hage and Salkoff, 2012), their expression has not been described in MesV neurons yet. In order to test this mechanism, we should perform experiments replacing  $Na^+$  by choline in the extracellular solution.

## 5.4.2 Co-regulation of the abundance of HCN and GJ channels

Most reported regulations of  $I_H$  involve the voltage-shift of its biophysical properties (activation curve and time constant), due to changes in the activity of cyclic nucleotides (see chapter 3 and Khakh and Henderson (1998); Tanaka et al. (2019); Won et al. (2019)). Nevertheless, the time constant of the  $I_H$  at -90 mV did not display any significant change during the activity-like stimulation, while the maximum current consistently decreased, indicating a diminution on the available channels, without modulatory actions on its biophysical properties.

Our results from chapters 4 and 5 seem to imply that electrical activity of MesV neurons is a major determinant of both  $g_J$  and  $g_{Hmax}$ , and could be responsible of their large variability in control conditions, even within the same animal (Figs. 3.3 and 4.5). Interestingly, there was a remarkable correlation between the maximum HCN and GJ conductances, not only in control conditions, but also during the activity-like stimulation, suggesting the existence of a set point of proportionality between them. Their activity-induced downregulations have similar time courses, possibly indicating shared regulatory mechanisms.

Even though more experiments are needed to fully characterize the activity-induced changes on HCN and their relationship with the GJ-depression, we postulate that there is an homeostatic mechanism that link  $g_{Hmax}$  and  $g_J$ . In fact, whereas the decrease of the former would enhance the CC because of the increase of  $R_{in}$ , the diminution of  $g_J$  has the opposite effect on the CC. Thus, the electrical activity of coupled MesV neurons results in two antagonistic phenomena, which counterbalance each other to stabilize the CC. On the other hand, the net reduction of  $R_{in}$  due to Cs-sensitive  $K^+$  conductances reinforces the depression of the electrical synapses between MesV neurons, even though it displays different dynamics, which might be caused by other mechanisms.

There are few examples of comparable co-regulations of GJ and membrane ionic channels, in invertebrates. In the cardiac ganglion of the crab, sustained pharmacological blockade of TEA-sensitive  $K^+$  channels produces compensatory upregulations of an A-type  $K^+$  current and  $g_J$ , in order to restore the network output (Lane et al., 2016). On the contrary, the associative learning of a compulsive eating behavior in the *Aplysia* elicits in a decrease of the leak current and increase of  $g_J$  (Nargeot et al., 2009; Sieling et al., 2014). Therefore, junctional and non-junctional mechanisms can co-regulated homeostatically to maintain the operation of vital circuits (like the cardiac ganglion (Lane et al., 2016)), or synergistically to reconfigure neural networks to adapt to new behaviors (compulsive biting movements in the presence of abundant food (Nargeot et al., 2009)).

In a longer timescale, similar relationships have been reported between the maximum conductances or levels of mRNA corresponding to different channels in the same neuron (Marder and Goaillard, 2006). For example, electrical stimulation of specific neurons from the stomatogastric ganglion of the crab promote an upregulation of  $I_{K(Ca)}$  with a parallel  $Ca^{2+}$ -dependent increase of  $I_A$  (Golowasch et al., 1999). This kind of phenomena would allow neurons to “keep memory” of their activity by altering their intrinsic properties, while maintaining their specific functional role within neural networks (Turrigiano et al., 1994; Marder et al., 1996; Temporal et al., 2014). This is biologically possible because several combinations of maximum ion conductances are able to produce the same electrical behavior (Prinz et al., 2004). Intracellular  $Ca^{2+}$  concentration has been proposed as the local controller of the levels of expression of ion channels in a neuron (O’Leary et al., 2014), with the electrical activity as a mechanism to coordinate them in neuronal circuits (Schulz et al., 2006; O’Leary et al., 2014; O’Leary and Marder, 2016; Santin and Schulz, 2019; Alonso and Marder, 2020). However, the induction of the  $g_{Hmax}$  and  $g_J$  depressions are too fast to be accomplished by the change in their expressions. In contrast, the time course of GJ endocytosis in MesV neurons (Fig. 4.21) is compatible with both



phenomena, providing a feasible mechanism to couple the abundance of HCN and GJ channels on the membrane. For voltage-dependent  $K^+$  channels in hippocampal neurons, similar activity-induced reductions on the maximum current have been attributed to their enhanced internalization in a time-span of 10-20 minutes (Kim et al., 2007; Hyun et al., 2013). Figure 5.10 summarizes our findings.

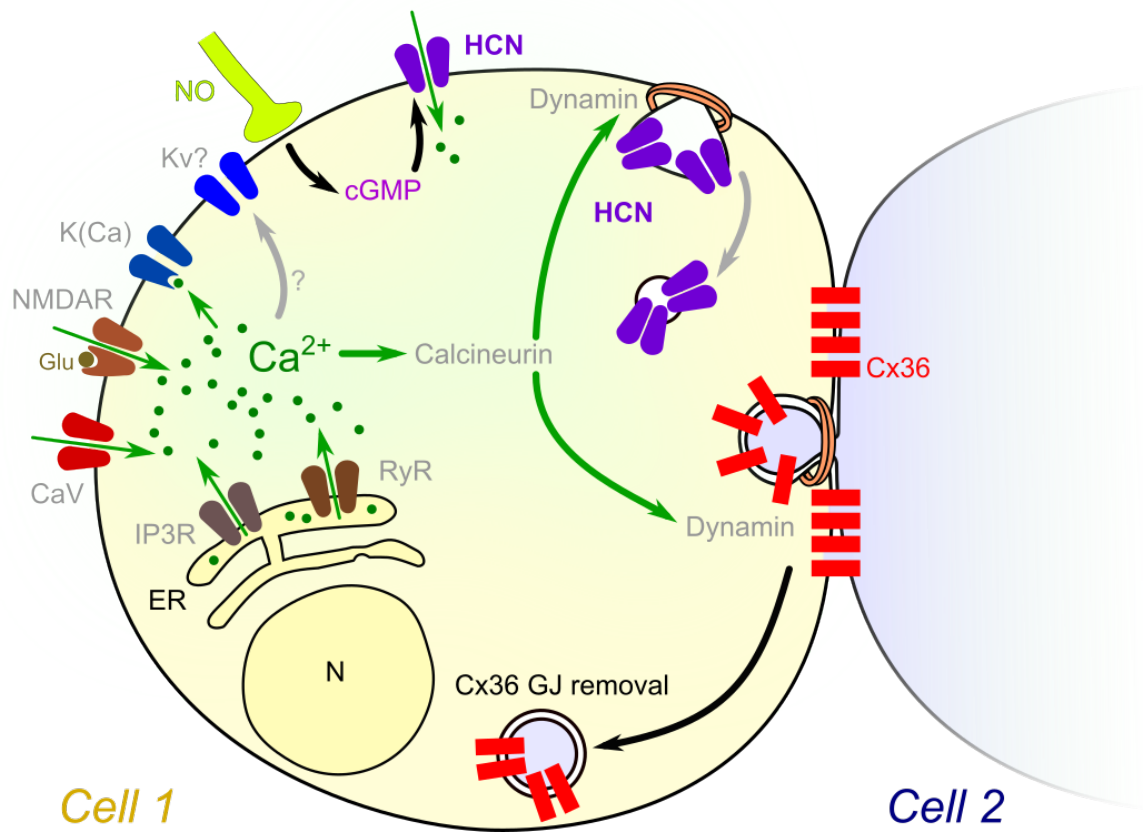


**Figure 5.10: Summary of some possible pathways involved in the regulation of intrinsic properties between MesV neurons.** This diagram represents the possible  $Ca^{2+}$  sources postulated in chapter 4, some of them elicited by repetitive firing. As in Fig. 4.24, the increase of intracellular  $Ca^{2+}$  concentration may trigger Calcineurin, which activates Dynamin, promoting the internalization of both junctional (Cx36 GJ) and non-junctional channels (HCN). We also added the regulation of HCN by cGMP studied in chapter 3, due to nitrergic inputs already reported in the MesV nucleus (Pose et al., 2003). The gray labels and arrows point out possible mechanisms that are still to be tested.

# Chapter 6

## General discussion

### 6.1 Main findings

We saw in chapter 2 that an electrical synapse is more than two cellular membranes and a GJ: it constitutes a complex system, driven by the interaction between the GJ and their scaffolding proteins, voltage-gated channels of the non-junctional membrane, the chemical synaptic receptors, the spatio-temporal features of the membrane potentials, and intra- and extracellular signaling cascades. In this thesis, we have focused only on two components: one ionic current from the non-junctional membrane ( $I_H$ ) in chapter 3 (and a bit on chapter 5), and the GJ conductance  $g_J$  in chapter 4, dissecting the mechanisms responsible for their role in the regulation and plasticity of electrical synapses. The main findings of this thesis can be summarized as follows:

1. The susceptibility to coincident inputs of electrically coupled MesV neurons is very heterogeneous.
2. The circuit operation critically depends on the GJ conductance, but also on the excitability of coupled neurons.
3. As a proof of principle of the central role of neuronal intrinsic properties, we showed that upregulation of the  $I_H$  by cGMP, which increases MesV neurons' excitability, results in an increase of the susceptibility to coincident inputs.
4. Application of *in vivo*-like activity protocols in pairs of electrically coupled neurons results in a dramatic drop of the strength of electrical coupling, with short- and long-term components.
5. The induction of such plastic changes involves changes in cytoplasmic levels of free  $\text{Ca}^{2+}$ , and each coupled partner contributes in an additive fashion.
6. Among the different origins of  $\text{Ca}^{2+}$ , HCN channels seem to contribute in a significant amount.

7. The change in the strength of electrical coupling results from a comparable reduction of the GJ conductance and the  $R_{in}$  of coupled neurons in a synergistic manner.
8. Surprisingly, even though GJ conductance can be modulated by elevations of intracellular levels of cAMP and  $\text{Ca}^{2+}$ , neither PKA nor CaMKII are involved in this activity-induced regulation of electrical transmission.
9. Endocannabinoids acting on  $\text{CB}_1$  receptors appear to be involved in the metaplasticity of the electrical synapses.
10. While the presence of electrical coupling seem to alter the expression of HCN channels, *in vivo*-like activity protocols co-regulate both mechanisms in a homeostatic fashion.
11. A fraction of intercellular channels at the GJ between MesV neurons shows a fast turn-over, with a time course comparable to that of the activity-dependent plasticity.

## 6.2 Diversity of regulation through signaling pathways

This thesis shows that electrical transmission is highly modifiable, and such plasticity arises not only from changes of gap junctions themselves, but also from regulatory actions on mechanisms of the non-junctional membrane.

In fact, modulatory actions mediated by cGMP are able to dramatically increase the susceptibility of pairs of coupled neurons through upregulation of the  $I_H$ . This result shows that electrical transmission can be regulated by modifications of electrical properties of coupled neurons, through modulatory actions of neurotransmitters. On the other hand, activation protocols, resembling MesV neurons activity in the context of feeding behaviors, strongly reduced the coupling coefficient between these neurons. Interestingly, this effect is explained by the parallel reduction of  $g_J$  and  $R_{in}$  of coupled neurons, emphasizing the interdependent relationship of junctional conductance and electrophysiological properties of neurons in determining the efficacy of electrical transmission.

MesV neurons are primary afferents that are also considered integral to the central pattern generator (CPG) responsible for the generation of jaw movements ([Morquette et al., 2012](#)). In rodents, these movements are relevant for a plethora of behaviors like feeding, grooming, pups caring as well as aggressive and defensive behaviors. This suggests that a complex regulatory control is needed in order to adapt the CPG output to such diverse motor tasks. Neuromodulatory actions mediated by changes in intracellular

levels of cGMP as shown in chapter 3, might be triggered by nitrenergic (Pose et al., 2003) or histaminergic (Inagaki et al., 1987; Lazarov and Gratzl, 2006) inputs to the MesV nucleus, among others neurotransmitters. Indeed, afferent projections from many brain regions, as well as a multiplicity of neurotransmitters and postsynaptic receptors have been described in this nucleus. It is conceivable that these actions represent general and diffuse mechanisms of regulation of the MesV nucleus aimed to adjust the network to different behaviors. For instance, hypothalamic inputs by way of histamine can exert regulatory actions in order to prepare the network for masticatory movements in the context of feeding, characterized by rhythmic patterns. On the other hand, the lateral habenula, a center of negative emotions (like pain, stress and anxiety), send direct projections to the MesV nucleus that can also influence the control of jaw movements (Ohara et al., 2016). Moreover, the locus coeruleus, a major source of noradrenaline in the brain, projects to the MesV nucleus (Takahashi et al., 2010), strongly suggesting that these afferents play an important role in stressful situations, most probably of great relevance for defensive and aggressive behaviors characterized by powerful and impulsive movements.

By contrast, activity induced plasticity seems to operate as a feedback mechanism in which pairs of strongly synchronic MesV neurons, most probably as a result of high electrical coupling, get decoupled. As this mechanism is specifically triggered by activity, it is possible that this phenomenon of synaptic plasticity contributes to establish the heterogeneity of coupling strengths typical of this neuronal population. In contrast to modulatory actions triggered by neurotransmitters, that seem to operate in an anticipatory way by preparing the CPG for different contexts, activity-dependent plasticity most probably operates as a feedback regulatory mechanism to adjust the network to behavioral needs.

As we showed previously, one of the most relevant outcomes of electrical coupling among MesV neurons is the strong synchronization of their activity. Interestingly, by regulating the ability of pairs of coupled neurons to produce synchronic bursts of action potentials, the efficacy of the MesV neurons excitatory inputs to masseteric motoneurons can be modified with relevant functional consequences. Although not well characterized, this monosynaptic pathway most probably shares similarities in its organization with the circuits that mediates spinal reflexes, particularly the great divergence of the primary afferent to motoneurons projection, as well as the convergence of inputs from different MesV neurons onto the same motoneuron. In that sense, the more synchronic the firing of MesV neurons is, the more effective will be the temporal summation of excitatory postsynaptic potentials at motoneurons. Thus, the regulation of the synchronic firing of

MesV neurons mediated by synaptic plasticity of their electrical contacts, most probably results in changes in the gain of the stretch reflex, representing an additional mechanism to control the bite force according to the demands of the system.

Our thesis provides a showcase on the diversity of signaling pathways regulating electrical coupling between neurons. In fact, we could achieve this analysis due to the extraordinary access to the electrical synapses in the MesV nucleus. Given that its neurons receive many other chemical synaptic inputs (Lazarov, 2007) and are in close proximity to astrocytes (Coprav et al., 1990), we postulate that more relevant signaling cascades will be uncovered in the near future. Even more complex pathways may be possible in other brain regions where morphology is not as simple as in the MesV nucleus, given that GJ are usually located in dendrites, whose intrinsic properties could be even more finely tuned by chemical synaptic inputs in a reduced compartment.

## 6.3 Future directions

We consider that our results, along with previous studies (Curti et al., 2012), have established the MesV nucleus as an exceptional model to understand electrical synaptic transmission in the mammalian brain. As a consequence of our work, we have produced far more questions than answers, that we hope will be studied soon by us and other researchers.

### Co-regulation of intrinsic properties in coupled neurons

The coupling coefficient of MesV neurons is very symmetrical (Fig. 4.2D), which is consistent with the non-rectification of GJ (Fig. 4.5D) and the similitude between the effective input resistances (see section 4.3.1). On the other hand, we have seen that there is a large variability in the electrophysiological properties within the MesV nucleus, even for the same animal. How do coupled neurons achieve symmetrical input resistances, while presenting a wide range in the expression of ionic currents like the  $I_H$  (Fig. 3.3)? The GJ may promote this symmetry between coupled neurons, by allowing the flow of second messengers (like cAMP and IP3, see section 2.2.1) and by transmitting the membrane potential too, as it might act as a feedback signal coordinating ion channel expressions (Santin and Schulz, 2019). Indeed, we found in chapter 5 a remarkable correlation between GJ and  $I_H$  conductances in control conditions and during the activity-like stimulation. It would be interesting to characterize the relationship between other ion channels between coupled neurons, recording their membrane currents and comparing the abundance of their associated mRNA, contrasting with pseudo-pairs of uncoupled neurons from the same an-

imal. Our computational model can also provide a complementary approach, looking for how different expression of ion channels may produce similar intrinsic properties (Prinz et al., 2004; O’Leary et al., 2014; O’Leary and Marder, 2016; Alonso and Marder, 2020; Goaillard and Marder, 2021). This study could be carried out in control conditions, as well as in the presence of neuromodulators or after activity-like stimulation.

### Temperature dependence of $g_J$

Even though the characterization of the temperature dependence of  $g_J$  was a by-product of the description of the electrical synapses in the mice MesV nucleus, we found a  $Q_{10}$  larger than expected by passive thermodynamics. However, this could also be explained by the down/upregulation of intracellular cascades involved in the regulation of GJ and their interaction with other proteins (see section 2.2.2). To evaluate these possible contributions to the temperature dependence of  $g_J$ , it should be measured in the presence of inhibitors of known regulatory proteins, such as PKA, CaMKII, etc.

### Role of $\text{Ca}^{2+}$ in the activity-induced plasticity

Our experiments with intracellular BAPTA 10 mM and without free  $\text{Ca}^{2+}$  in the ACSF show that  $\text{Ca}^{2+}$  plays a major role in the plasticity induced by activity, but there are still several unknowns to understand:

- **Spatio-temporal distribution of the intracellular  $\text{Ca}^{2+}$ :** To fully understand the impact of  $\text{Ca}^{2+}$  in the induction of the plasticity, it is necessary to characterize its dynamics during the activity-like stimulation, using a fluorometric  $\text{Ca}^{2+}$  indicator.
- **$\text{Ca}^{2+}$  sources:** Like in the TRN (Sevetson et al., 2017), the activity-induced  $\text{Ca}^{2+}$  increase in the MesV could have several sources, such as CaV and HCN channels in the membrane, and Ryanodine and IP3 receptors in the endoplasmic reticulum. The contribution of each of them has to be characterized using electrophysiology and  $\text{Ca}^{2+}$  fluorometry.
- **$\text{Ca}^{2+}$  nanodomains:** We tested several possible signaling pathways where  $\text{Ca}^{2+}$  was not essential, without identifying any clearly involved in the induction of the plasticity. Given that intracellular BAPTA 10 mM only prevented half of the  $g_J$  drop, it is possible that  $\text{Ca}^{2+}$  might be interacting with some regulatory protein (even the Cx36) within the nanometer scale. Thus, in order to test the existence of  $\text{Ca}^{2+}$  nanodomains (Wang and Augustine, 2015), we could use a low-affinity  $\text{Ca}^{2+}$  indicator (Llinas et al., 1992), in order to find regions in the soma where there is a large increase in the intracellular  $\text{Ca}^{2+}$  concentration. To find out if there is a direct interaction with the GJ, we could uncage  $\text{Ca}^{2+}$  close to it using flash photolysis.



- **Ca<sup>2+</sup> sensors:** Calmodulin is the chief candidate as the intracellular Ca<sup>2+</sup> sensor (Chin and Means, 2000; Peracchia, 2020b) triggering the induction of the plasticity, given that two of its effector molecules (CaMKII and Calcineurin; see section 2.2.2) have been reported to be key in other brain regions. PKC is also a possible Ca<sup>2+</sup> sensor (Jin et al., 2019), that is involved in the developmental regulation of Cx36 (Arumugam et al., 2005).

## Signaling by endocannabinoids in the electrical synaptic transmission

We have shown that CB<sub>1</sub> receptors participate in the activity-induced plasticity of  $g_J$ . They could be expressed on the membrane of the stimulated neuron, another cell (neuron or glia (Stella, 2010; Navarrete et al., 2014)) and/or even on intracellular organelles, such as mitochondria (Bénard et al., 2012). Thus, the first step is to identify, using immunohistochemistry, where are the CB<sub>1</sub> receptors expressed. Then, to fully characterize their involvement in the plasticity, the  $g_J$  and  $R_{in}$  could be monitored during the puff application of an agonist (like WIN 55,212 or 2-arachidonoylglycerol (Bacci et al., 2004; Cachope et al., 2007)) close to the coupled cells. As inhibition of CaV channels is a good candidate as effector mechanism of CB<sub>1</sub> receptors, activity-like stimulation should be performed in the presence of Cd<sup>2+</sup> or Ni<sup>2+</sup>, with and without AM251 as blocker of CB<sub>1</sub> receptors.

## Expression of the GJ plasticity

The activity-induced reduction of  $g_J$  could be due to an increased endocytosis of GJ. In that case, it would be interesting to investigate how basal  $g_J$  (and  $g_{H,max}$  as well) and its activity-induced plasticity are affected by Dynamin inhibitors, such as Dynasore. As GJ internalization depends on clathrin (Piehl et al., 2007; Gumpert et al., 2008; Nickel et al., 2013), the inhibitor Phenylarsine oxide could also be tested in both conditions (Dutta and Donaldson, 2012). Given that the whole GJ is endocytosed in a vesicle that includes the cytoplasm of the coupled partner (see section 2.2.3), it would be possible to use a fluorescent GJ-impermeable dye in only one cell, to monitor the endocytosis using imaging (see Fig. 2.3). An increased endocytosis should decrease the global cell capacitance too, which could be electrophysiologically monitored through the phase of its impedance, using a lock-in amplifier (Rituper et al., 2013).

## Functional role of the activity-induced plasticity

The diminution of the electrical coupling due to activity-induced plasticity probably decreases the synchronization and coincidence detection in neural circuits. However, it also

provokes a drop of  $R_{in}$  (Fig. 4.7), indicating a modification of the intrinsic properties of the neurons too. Therefore, both synchronization and coincidence detection should be assessed after the activity-like stimulation, in order to understand the functional impact of it. In addition to that, a more detailed characterization of the MesV nucleus afferences (do coupled neurons receive information from the same sensory modality? (el Manira et al., 1993)) and efferences (do coupled neurons project onto the same motoneuron?) will be great to further understand the operation of the electrical synaptic transmission within the context of the oral behaviors.

# Bibliography

- Abascal, F. and Zardoya, R. (2013). Evolutionary analyses of gap junction protein families. *Biochimica et Biophysica Acta (BBA) - Biomembranes*, 1828(1):4 – 14. The Communicating junctions, roles and dysfunctions.
- Ahluwalia, J., Urban, L., Bevan, S., and Nagy, I. (2003). Anandamide regulates neuropeptide release from capsaicin-sensitive primary sensory neurons by activating both the cannabinoid1 receptor and the vanilloid receptor1 in vitro. *European Journal of Neuroscience*, 17(12):2611–2618.
- Akopian, A., Atlasz, T., Pan, F., Wong, S., Zhang, Y., Völgyi, B., Paul, D. L., and Bloomfield, S. A. (2014). Gap junction-mediated death of retinal neurons is connexin and insult specific: A potential target for neuroprotection. *Journal of Neuroscience*, 34(32):10582–10591.
- Al-Ubaidi, M. R., White, T. W., Ripps, H., Poras, I., Avner, P., Gomès, D., and Bruzzone, R. (2000). Functional properties, developmental regulation, and chromosomal localization of murine connexin36, a gap-junctional protein expressed preferentially in retina and brain. *Journal of Neuroscience Research*, 59(6):813–826.
- Alcami, P. (2018). Electrical synapses enhance and accelerate interneuron recruitment in response to coincident and sequential excitation. *Frontiers in Cellular Neuroscience*, 12:156.
- Alcami, P. and Marty, A. (2013). Estimating functional connectivity in an electrically coupled interneuron network. *Proc. Natl Acad. Sci. USA*, 110.
- Alcamí, P. and Pereda, A. E. (2019). Beyond plasticity: the dynamic impact of electrical synapses on neural circuits. *Nature Reviews Neuroscience*, 20(5):253–271.
- Alev, C., Urschel, S., Sonntag, S., Zoidl, G., Fort, A. G., Höher, T., Matsubara, M., Willecke, K., Spray, D. C., and Dermietzel, R. (2008). The neuronal connexin36 interacts with and is phosphorylated by camkii in a way similar to camkii interaction with glutamate receptors. *Proceedings of the National Academy of Sciences*, 105(52):20964–20969.

- Alonso, L. M. and Marder, E. (2020). Temperature compensation in a small rhythmic circuit. *eLife*, 9:e55470.
- Alvarez, O., Gonzalez, C., and Latorre, R. (2002). Counting channels: A tutorial guide on ion channel fluctuation analysis. *Advances in Physiology Education*, 26(4):327–341. PMID: 12444005.
- Anselmi, F., Hernandez, V. H., Crispino, G., Seydel, A., Ortolano, S., Roper, S. D., Kessaris, N., Richardson, W., Rickheit, G., Filippov, M. A., Monyer, H., and Mammano, F. (2008). Atp release through connexin hemichannels and gap junction transfer of second messengers propagate ca<sup>2+</sup> signals across the inner ear. *Proceedings of the National Academy of Sciences*, 105(48):18770–18775.
- Antic, S. D., Baker, B. J., and Canepari, M. (2019). Editorial: New insights on neuron and astrocyte function from cutting-edge optical techniques. *Frontiers in Cellular Neuroscience*, 13:463.
- Apostolides, P. F. and Trussell, L. O. (2013). Regulation of interneuron excitability by gap junction coupling with principal cells. *Nature Neuroscience*, 16(12):1764–1772.
- Arai, I., Tanaka, M., and Tachibana, M. (2010). Active roles of electrically coupled bipolar cell network in the adult retina. *Journal of Neuroscience*, 30(27):9260–9270.
- Arumugam, H., Liu, X., Colombo, P. J., Corriveau, R. A., and Belousov, A. B. (2005). Nmda receptors regulate developmental gap junction uncoupling via creb signaling. *Nature Neuroscience*, 8(12):1720–1726.
- Aseervatham, J., Li, X., Mitchell, C. K., Lin, Y.-P., Heidelberger, R., and O’Brien, J. (2020). Calmodulin binding to connexin 35: Specializations to function as an electrical synapse. *International Journal of Molecular Sciences*, 21(17).
- Auerbach, A. A. and Bennett, M. V. L. (1969). A Rectifying Electrotonic Synapse in the Central Nervous System of a Vertebrate . *Journal of General Physiology*, 53(2):211–237.
- Bacci, A., Huguenard, J. R., and Prince, D. A. (2004). Long-lasting self-inhibition of neocortical interneurons mediated by endocannabinoids. *Nature*, 431(7006):312–316.
- Bargiello, T. A., Tang, Q., Oh, S., and Kwon, T. (2012). Voltage-dependent conformational changes in connexin channels. *Biochimica et Biophysica Acta (BBA) - Biomembranes*, 1818(8):1807 – 1822. The Communicating junctions, composition, structure and characteristics Part 1.

- Barrio, L. C., Suchyna, T., Bargiello, T., Xu, L. X., Roginski, R. S., Bennett, M. V., and Nicholson, B. J. (1991). Gap junctions formed by connexins 26 and 32 alone and in combination are differently affected by applied voltage. *Proceedings of the National Academy of Sciences*, 88(19):8410–8414.
- Bazzigaluppi, P., Isenia, S. C., Haasdijk, E. D., Elgersma, Y., De Zeeuw, C. I., van der Giessen, R. S., and de Jeu, M. T. G. (2017). Modulation of murine olivary connexin 36 gap junctions by pka and camkii. *Frontiers in Cellular Neuroscience*, 11:397.
- Beblo, D. A. and Veenstra, R. D. (1997). Monovalent Cation Permeation through the Connexin40 Gap Junction Channel : Cs, Rb, K, Na, Li, TEA, TMA, TBA, and Effects of Anions Br, Cl, F, Acetate, Aspartate, Glutamate, and NO<sub>3</sub>. *Journal of General Physiology*, 109(4):509–522.
- Bedner, P., Niessen, H., Odermatt, B., Kretz, M., Willecke, K., and Harz, H. (2006). Selective permeability of different connexin channels to the second messenger cyclic amp. *Journal of Biological Chemistry*, 281(10):6673–6681.
- Bejarano, E., Girao, H., Yuste, A., Patel, B., Marques, C., Spray, D. C., Pereira, P., and Cuervo, A. M. (2012). Autophagy modulates dynamics of connexins at the plasma membrane in a ubiquitin-dependent manner. *Molecular Biology of the Cell*, 23(11):2156–2169. PMID: 22496425.
- Bell, C. L., Shakespeare, T. I., Smith, A. R., and Murray, S. A. (2019). Visualization of annular gap junction vesicle processing: The interplay between annular gap junctions and mitochondria. *International Journal of Molecular Sciences*, 20(1).
- Belluardo, N., Mudò, G., Trovato-Salinaro, A., Le Gurun, S., Charollais, A., Serre-Beinier, V., Amato, G., Haeffliger, J.-A., Meda, P., and Condorelli, D. F. (2000). Expression of connexin36 in the adult and developing rat brain. *Brain Research*, 865(1):121 – 138.
- Belousov, A. B., Fontes, J. D., Freitas-Andrade, M., and Naus, C. C. (2017). Gap junctions and hemichannels: communicating cell death in neurodevelopment and disease. *BMC Cell Biology*, 18(1):4.
- Bénard, G., Massa, F., Puente, N., Lourenço, J., Bellocchio, L., Soria-Gómez, E., Matias, I., Delamarre, A., Metna-Laurent, M., Cannich, A., Hebert-Chatelain, E., Mulle, C., Ortega-Gutiérrez, S., Martín-Fontecha, M., Klugmann, M., Guggenhuber, S., Lutz, B., Gertsch, J., Chaouloff, F., López-Rodríguez, M. L., Grandes, P., Rossignol, R., and Marsicano, G. (2012). Mitochondrial cb1 receptors regulate neuronal energy metabolism. *Nature Neuroscience*, 15(4):558–564.

- Bennett, M. V. (1966). Physiology of electrotonic junctions. *Ann NY Acad Sci*, 137(2):509–539.
- Bennett, M. V. and Zukin, R. S. (2004). Electrical coupling and neuronal synchronization in the mammalian brain. *Neuron*, 41 (4):495–511.
- Berg, E. M., Björnfors, E. R., Pallucchi, I., Picton, L. D., and El Manira, A. (2018). Principles governing locomotion in vertebrates: Lessons from zebrafish. *Frontiers in Neural Circuits*, 12:73.
- Best, A. R. and Regehr, W. G. (2009). Inhibitory regulation of electrically coupled neurons in the inferior olive is mediated by asynchronous release of gaba. *Neuron*, 62(4):555–565.
- Bhattacharya, A., Aghayeva, U., Berghoff, E. G., and Hobert, O. (2019). Plasticity of the electrical connectome of *c. elegans*. *Cell*, 176(5):1174–1189.e16.
- Biel, M., Wahl-Schott, C., Michalakakis, S., and Zong, X. (2009). Hyperpolarization-activated cation channels: From genes to function. *Physiological Reviews*, 89(3):847–885. PMID: 19584315.
- Bloomfield, S. and Volgyi, B. (2009). The diverse functional roles and regulation of neuronal gap junctions in the retina. *Nature reviews. Neuroscience*, 10:495–506.
- Bloomfield, S. A. and Völgyi, B. (2004). Function and plasticity of homologous coupling between aii amacrine cells. *Vision Research*, 44(28):3297 – 3306. The Mouse Visual System: From Photoreceptors to Cortex.
- Bloomfield, S. A. and Xin, D. (1997). A comparison of receptive-field and tracer-coupling size of amacrine and ganglion cells in the rabbit retina. *Visual Neuroscience*, 14(6).
- Boassa, D., Solan, J. L., Papas, A., Thornton, P., Lampe, P. D., and Sosinsky, G. E. (2010). Trafficking and recycling of the connexin43 gap junction protein during mitosis. *Traffic (Copenhagen, Denmark)*, 11(11):1471–1486.
- Borde, M., Bonansco, C., Fernández de Sevilla, D., Le Ray, D., and Buño, W. (2000). Voltage-clamp analysis of the potentiation of the slow  $Ca^{2+}$ -activated  $K^{+}$  current in hippocampal pyramidal neurons. *Hippocampus*, 10(2):198–206.
- Borde, M., Cazalets, J. R., and Buno, W. (1995). Activity-dependent response depression in rat hippocampal ca1 pyramidal neurons in vitro. *Journal of Neurophysiology*, 74(4):1714–1729. PMID: 8989407.



- Brenowitz, S. D. and Regehr, W. G. (2003). Calcium dependence of retrograde inhibition by endocannabinoids at synapses onto purkinje cells. *Journal of Neuroscience*, 23(15):6373–6384.
- Brignell, J. L., Perry, M. D., Nelson, C. P., Willets, J. M., Challiss, R. A. J., and Davies, N. W. (2015). Steady-state modulation of voltage-gated  $K^+$  channels in rat arterial smooth muscle by cyclic amp-dependent protein kinase and protein phosphatase 2b. *PLOS ONE*, 10(3):1–17.
- Brown, C. A., del Corso, C., Zoidl, C., Donaldson, L. W., Spray, D. C., and Zoidl, G. (2019). Tubulin-dependent transport of connexin-36 potentiates the size and strength of electrical synapses. *Cells*, 8(10).
- Brown, E., Moehlis, J., and Holmes, P. (2004). On the phase reduction and response dynamics of neural oscillator populations. *Neural computation*, 16(4):673–715.
- Brunal, A. A., Clark, K. C., Ma, M., Woods, I. G., and Pan, Y. A. (2021). Effects of constitutive and acute connexin 36 deficiency on brain-wide susceptibility to ptz-induced neuronal hyperactivity. *Frontiers in Molecular Neuroscience*, 13:239.
- Bruzzone, R., Haefliger, J. A., Gimlich, R. L., and Paul, D. L. (1993). Connexin40, a component of gap junctions in vascular endothelium, is restricted in its ability to interact with other connexins. *Molecular Biology of the Cell*, 4(1):7–20. PMID: 8382974.
- Bruzzone, R., Hormuzdi, S. G., Barbe, M. T., Herb, A., and Monyer, H. (2003). Pannexins, a family of gap junction proteins expressed in brain. *Proceedings of the National Academy of Sciences*, 100(23):13644–13649.
- Buchanan, K. A., Petrovic, M. M., Chamberlain, S. E., Marrion, N. V., and Mellor, J. R. (2010). Facilitation of long-term potentiation by muscarinic m1 receptors is mediated by inhibition of  $SK$  channels. *Neuron*, 68(5):948–963.
- Budelli, G., Hage, T. A., Wei, A., Rojas, P., Ivy Jong, Y.-J., O’Malley, K., and Salkoff, L. (2009).  $Na^+$ -activated  $K^+$  channels express a large delayed outward current in neurons during normal physiology. *Nature Neuroscience*, 12(6):745–750.
- Bukauskas, F. F., Bukauskiene, A., and Verselis, V. K. (2002). Conductance and Permeability of the Residual State of Connexin43 Gap Junction Channels . *Journal of General Physiology*, 119(2):171–186.
- Bukauskas, F. F. and Verselis, V. K. (2004). Gap junction channel gating. *Biochimica et Biophysica Acta (BBA) - Biomembranes*, 1662(1):42 – 60. The Connexins.

- Bukauskas, F. F. and Weingart, R. (1993). Temperature dependence of gap junction properties in neonatal rat heart cells. *Pflügers Archiv*, 423(1):133–139.
- Buniello, A., Montanaro, D., Volinia, S., Gasparini, P., and Marigo, V. (2004). An expression atlas of connexin genes in the mouse. *Genomics*, 83(5):812 – 820.
- Burke, K. J. and Bender, K. J. (2019). Modulation of ion channels in the axon: Mechanisms and function. *Frontiers in Cellular Neuroscience*, 13:221.
- Burr, G. S., Mitchell, C. K., Keflemariam, Y. J., Heidelberger, R., and O’Brien, J. (2005). Calcium-dependent binding of calmodulin to neuronal gap junction proteins. *Biochemical and Biophysical Research Communications*, 335(4):1191 – 1198.
- Busquets-Garcia, A., Bains, J., and Marsicano, G. (2018). Cb1 receptor signaling in the brain: Extracting specificity from ubiquity. *Neuropsychopharmacology*, 43(1):4–20.
- Cachope, R., Mackie, K., Triller, A., O’Brien, J., and Pereda, A. E. (2007). Potentiation of electrical and chemical synaptic transmission mediated by endocannabinoids. *Neuron*, 56(6):1034 – 1047.
- Campanac, E., Gasselin, C., Baude, A., Rama, S., Ankri, N., and Debanne, D. (2013). Enhanced intrinsic excitability in basket cells maintains excitatory-inhibitory balance in hippocampal circuits. *Neuron*, 77(4):712–722.
- Cantrell, A. R. and Catterall, W. A. (2001). Neuromodulation of  $Na^+$  channels: An unexpected form of cellular plasticity. *Nature Reviews Neuroscience*, 2(6):397–407.
- Castillo, P. E., Younts, T. J., Chávez, A. E., and Hashimoto, Y. (2012). Endocannabinoid signaling and synaptic function. *Neuron*, 76(1):70–81.
- Cazade, M., Bidaud, I., Lory, P., and Chemin, J. (2017). Activity-dependent regulation of t-type calcium channels by submembrane calcium ions. *eLife*, 6:e22331.
- Cecchi, X., Wolff, D., Alvarez, O., and Latorre, R. (1987). Mechanisms of  $Ca^{2+}$  blockade in a  $Ca^{2+}$ -activated  $K^+$  channel from smooth muscle. *Biophysical Journal*, 52(5):707–716.
- Chai, Z., Wang, C., Huang, R., Wang, Y., Zhang, X., Wu, Q., Wang, Y., Wu, X., Zheng, L., Zhang, C., Guo, W., Xiong, W., Ding, J., Zhu, F., and Zhou, Z. (2017). Cav2.2 gates calcium-independent but voltage-dependent secretion in mammalian sensory neurons. *Neuron*, 96(6):1317–1326.e4.
- Chakraborty, S., Mitra, S., Falk, M. M., Caplan, S. H., Wheelock, M. J., Johnson, K. R., and Mehta, P. P. (2010). E-cadherin differentially regulates the assembly of connexin43

- and connexin32 into gap junctions in human squamous carcinoma cells. *Journal of Biological Chemistry*, 285(14):10761–10776.
- Chalfie, M., Sulston, J., White, J., Southgate, E., Thomson, J., and Brenner, S. (1985). The neural circuit for touch sensitivity in *caenorhabditis elegans*. *Journal of Neuroscience*, 5(4):956–964.
- Chen, J., Pan, L., Wei, Z., Zhao, Y., and Zhang, M. (2008). Domain-swapped dimerization of zo-1 pdz2 generates specific and regulatory connexin43-binding sites. *The EMBO Journal*, 27(15):2113–2123.
- Chevalleyre, V., Heifets, B. D., Kaeser, P. S., Südhof, T. C., and Castillo, P. E. (2007). Endocannabinoid-mediated long-term plasticity requires camp/pka signaling and rim1. *Neuron*, 54(5):801–812.
- Chevalleyre, V., Takahashi, K. A., and Castillo, P. E. (2006). Endocannabinoid-mediated synaptic plasticity in the cns. *Annual Review of Neuroscience*, 29(1):37–76. PMID: 16776579.
- Chin, D. and Means, A. R. (2000). Calmodulin: a prototypical calcium sensor. *Trends in Cell Biology*, 10(8):322–328.
- Christie, J. M., Bark, C., Hormuzdi, S. G., Helbig, I., Monyer, H., and Westbrook, G. L. (2005). Connexin36 mediates spike synchrony in olfactory bulb glomeruli. *Neuron*, 46(5):761 – 772.
- Condorelli, D. F., Parenti, R., Spinella, F., Salinaro, A. T., Belluardo, N., Cardile, V., and Cicirata, F. (1998). Cloning of a new gap junction gene (cx36) highly expressed in mammalian brain neurons. *European Journal of Neuroscience*, 10:1202–1208.
- Condorelli, D. F., Trovato-Salinaro, A., Mudò, G., Mirone, M. B., and Belluardo, N. (2003). Cellular expression of connexins in the rat brain: neuronal localization, effects of kainate-induced seizures and expression in apoptotic neuronal cells. *European Journal of Neuroscience*, 18(7):1807–1827.
- Connor, M., Naves, L. A., and McCleskey, E. W. (2005). Contrasting phenotypes of putative proprioceptive and nociceptive trigeminal neurons innervating jaw muscle in rat. *Molecular Pain*, 1:1744–8069–1–31. PMID: 16242047.
- Connors, B. W. and Long, M. A. (2004). Electrical synapses in the mammalian brain. *Annual Review of Neuroscience*, 27(1):393–418.

- Connors, E. C., Ballif, B. A., and Morielli, A. D. (2008). Homeostatic regulation of kv1.2 potassium channel trafficking by cyclic amp\*. *Journal of Biological Chemistry*, 283(6):3445–3453.
- Copray, J. C. V. M., Liem, R. S. B., and van Willigen, J. D. (1990). Morphological arrangement between astrocytes and trigeminal mesencephalic primary afferent neurons in the rat. *Experimental Brain Research*, 83(1):215–218.
- Cui, Y., Prokin, I., Xu, H., Delord, B., Genet, S., Venance, L., and Berry, H. (2016). Endocannabinoid dynamics gate spike-timing dependent depression and potentiation. *eLife*, 5:e13185.
- Cummings, K. A. and Popescu, G. K. (2015). Glycine-dependent activation of nmda receptors. *The Journal of general physiology*, 145(6):513–527. 25964432[pmid].
- Curti, S., Hoge, G., Nagy, J. I., and Pereda, A. E. (2012). Synergy between electrical coupling and membrane properties promotes strong synchronization of neurons of the mesencephalic trigeminal nucleus. *Journal of Neuroscience*, 32(13):4341–4359.
- Curti, S. and O’Brien, J. (2016). Characteristics and plasticity of electrical synaptic transmission. *BMC cell biology*, 17(1):13.
- Curti, S. and Pereda, A. E. (2004). Voltage-dependent enhancement of electrical coupling by a subthreshold sodium current. *Journal of Neuroscience*, 24(16):3999–4010.
- Dahl, G. (2015). Atp release through pannexon channels. *Philosophical Transactions of the Royal Society B: Biological Sciences*, 370(1672):20140191.
- Davoine, F. and Curti, S. (2019). Response to coincident inputs in electrically coupled primary afferents is heterogeneous and is enhanced by h-current (ih) modulation. *J Neurophysiol*, 122(1):151–175.
- Davoine, F., Curti, S., and Monzón, P. (2020). Spike transmission between electrically coupled sensory neurons is improved by filter properties. In *2020 IEEE International Symposium on Circuits and Systems (ISCAS)*, pages 1–5.
- De Petrocellis, L., Bisogno, T., Maccarrone, M., Davis, J. B., Finazzi-Agrò, A., and Di Marzo, V. (2001). The activity of anandamide at vanilloid vr1 receptors requires facilitated transport across the cell membrane and is limited by intracellular metabolism \*. *Journal of Biological Chemistry*, 276(16):12856–12863.

- de Rivero Vaccari, J. C., Corriveau, R. A., and Belousov, A. B. (2007). Gap junctions are required for nmda receptor-dependent cell death in developing neurons. *Journal of Neurophysiology*, 98(5):2878–2886.
- De Zeeuw, C. I., Chorev, E., Devor, A., Manor, Y., Van Der Giessen, R. S., De Jeu, M. T., Hoogenraad, C. C., Bijman, J., Ruigrok, T. J. H., French, P., Jaarsma, D., Kistler, W. M., Meier, C., Petrasch-Parwez, E., Dermietzel, R., Sohl, G., Gueldenagel, M., Willecke, K., and Yarom, Y. (2003). Deformation of network connectivity in the inferior olive of connexin 36-deficient mice is compensated by morphological and electrophysiological changes at the single neuron level. *Journal of Neuroscience*, 23(11):4700–4711.
- Deans, M. R., Gibson, J. R., Sellitto, C., Connors, B. W., and Paul, D. L. (2001). Synchronous activity of inhibitory networks in neocortex requires electrical synapses containing connexin36. *Neuron*, 31(3):477–485.
- Deans, M. R., Volgyi, B., Goodenough, D. A., Bloomfield, S. A., and Paul, D. L. (2002). Connexin36 is essential for transmission of rod-mediated visual signals in the mammalian retina. *Neuron*, 36(4):703–712.
- Decrock, E., Vinken, M., Bol, M., D’Herde, K., Rogiers, V., Vandenabeele, P., Krysko, D. V., Bultynck, G., and Leybaert, L. (2011). Calcium and connexin-based intercellular communication, a deadly catch? *Cell Calcium*, 50(3):310 – 321. Special issue on Ca<sup>2+</sup> signaling mechanisms of cell survival and cell death.
- Dedek, K., Schultz, K., Pieper, M., Dirks, P., Maxeiner, S., Willecke, K., Weiler, R., and Janssen-Bienhold, U. (2006). Localization of heterotypic gap junctions composed of connexin45 and connexin36 in the rod pathway of the mouse retina. *European Journal of Neuroscience*, 24(6):1675–1686.
- del Corso, C., Iglesias, R., Zoidl, G., Dermietzel, R., and Spray, D. C. (2012). Calmodulin dependent protein kinase increases conductance at gap junctions formed by the neuronal gap junction protein connexin36. *Brain Research*, 1487:69 – 77. From Electrical Synapses to the Clinics: A Translational Perspective.
- Del Negro, C. and Chandler, S. (1997). Physiological and theoretical analysis of K<sup>+</sup> currents controlling discharge in neonatal rat mesencephalic trigeminal neurons. *J Neurophysiol*, 77(2):537–553.
- Dessem, D. and Taylor, A. (1989). Morphology of jaw-muscle spindle afferents in the rat. *Journal of Comparative Neurology*, 282(3):389–403.

- Devor, A. and Yarom, Y. (2000). Gabaergic modulation of olivary oscillations. In *Cerebellar modules: Molecules, morphology and function*, volume 124 of *Progress in Brain Research*, pages 213 – 220. Elsevier.
- DeVries, S. H., Qi, X., Smith, R., Makous, W., and Sterling, P. (2002). Electrical coupling between mammalian cones. *Curr Biol*, 12(22):1900–1907.
- Dingledine, R., Borges, K., Bowie, D., and Traynelis, S. F. (1999). The glutamate receptor ion channels. *Pharmacological Reviews*, 51(1):7–62.
- Dorgau, B., Herrling, R., Schultz, K., Greb, H., Segelken, J., Ströh, S., Bolte, P., Weiler, R., Dedek, K., and Janssen-Bienhold, U. (2015). Connexin50 couples axon terminals of mouse horizontal cells by homotypic gap junctions. *Journal of Comparative Neurology*, 523(14):2062–2081.
- Dugué, G. P., Brunel, N., Hakim, V., Schwartz, E., Chat, M., Lévesque, M., Courtemanche, R., Léna, C., and Dieudonné, S. (2009). Electrical coupling mediates tunable low-frequency oscillations and resonance in the cerebellar Golgi cell network. *Neuron*, 61(1):126–39.
- Dunn, C. A. and Lampe, P. D. (2014). Injury-triggered akt phosphorylation of cx43: a zo-1-driven molecular switch that regulates gap junction size. *Journal of Cell Science*, 127(2):455–464.
- Dutta, D. and Donaldson, J. G. (2012). Search for inhibitors of endocytosis. *Cellular Logistics*, 2(4):203–208. PMID: 23538558.
- Egertová, M., Cravatt, B., and Elphick, M. (2003). Comparative analysis of fatty acid amide hydrolase and cb1 cannabinoid receptor expression in the mouse brain: evidence of a widespread role for fatty acid amide hydrolase in regulation of endocannabinoid signaling. *Neuroscience*, 119(2):481–496.
- Egorov, A. V., Gloveli, T., and Müller, W. (1999). Muscarinic control of dendritic excitability and ca2+signaling in ca1 pyramidal neurons in rat hippocampal slice. *Journal of Neurophysiology*, 82(4):1909–1915. PMID: 10515980.
- Ek-Vitorin, J. F. and Burt, J. M. (2013). Structural basis for the selective permeability of channels made of communicating junction proteins. *Biochimica et Biophysica Acta (BBA) - Biomembranes*, 1828(1):51 – 68. The Communicating junctions, roles and dysfunctions.



- el Manira, A., Cattaert, D., Wallen, P., DiCaprio, R. A., and Clarac, F. (1993). Electrical coupling of mechanoreceptor afferents in the crayfish: a possible mechanism for enhancement of sensory signal transmission. *Journal of Neurophysiology*, 69(6):2248–2251. PMID: 8394415.
- Enomoto, A., Han, J. M., Hsiao, C.-F., and Chandler, S. H. (2007). Sodium currents in mesencephalic trigeminal neurons from Nav1.6 null mice. *J Neurophysiol*, 98(2):710–719.
- Faber, D. and Pereda, A. (2011). Brain and nervous system — physiology of the mauthner cell: Function. In Farrell, A. P., editor, *Encyclopedia of Fish Physiology*, pages 73 – 79. Academic Press, San Diego.
- Fakler, B. and Adelman, J. P. (2008). Control of kca channels by calcium nano/microdomains. *Neuron*, 59(6):873–881.
- Falk, M. M., Baker, S. M., Gumpert, A. M., Segretain, D., and Buckheit, R. W. (2009). Gap junction turnover is achieved by the internalization of small endocytic double-membrane vesicles. *Molecular Biology of the Cell*, 20(14):3342–3352. PMID: 19458184.
- Falk, M. M., Bell, C. L., Kells Andrews, R. M., and Murray, S. A. (2016). Molecular mechanisms regulating formation, trafficking and processing of annular gap junctions. *BMC Cell Biology*, 17(1):S22.
- Falk, M. M., Fong, J. T., Kells, R. M., O’Laughlin, M. C., Kowal, T. J., and Thévenin, A. F. (2012). Degradation of endocytosed gap junctions by autophagosomal and endo-/lysosomal pathways: A perspective. *The Journal of Membrane Biology*, 245(8):465–476.
- Feigenspan, A., Janssen-Bienhold, U., Hormuzdi, S., Monyer, H., Degen, J., Söhl, G., Willecke, K., Ammermüller, J., and Weiler, R. (2004). Expression of connexin36 in cone pedicles and off-cone bipolar cells of the mouse retina. *Journal of Neuroscience*, 24(13):3325–3334.
- Ferguson, G. D. and Storm, D. R. (2004). Why calcium-stimulated adenylyl cyclases? *Physiology*, 19(5):271–276. PMID: 15381755.
- Fernández-Fernández, D. and Lamas, J. (2021). Metabotropic modulation of potassium channels during synaptic plasticity. *Neuroscience*, 456:4–16. Metabotropic Regulation of Synaptic Plasticity.

- Fletcher-Jones, A., Hildick, K. L., Evans, A. J., Nakamura, Y., Henley, J. M., and Wilkinson, K. A. (2020). Protein interactors and trafficking pathways that regulate the cannabinoid type 1 receptor (cb1r). *Frontiers in Molecular Neuroscience*, 13:108.
- Flores, C. E., Li, X., Bennett, M. V. L., Nagy, J. I., and Pereda, A. E. (2008). Interaction between connexin35 and zonula occludens-1 and its potential role in the regulation of electrical synapses. *Proceedings of the National Academy of Sciences*, 105(34):12545–12550.
- Flores, C. E., Nannapaneni, S., Davidson, K. G. V., Yasumura, T., Bennett, M. V. L., Rash, J. E., and Pereda, A. E. (2012). Trafficking of gap junction channels at a vertebrate electrical synapse in vivo. *Proceedings of the National Academy of Sciences*, 109(9):E573–E582.
- Fong, J. T., Kells, R. M., Gumpert, A. M., Marzillier, J. Y., Davidson, M. W., and Falk, M. M. (2012). Internalized gap junctions are degraded by autophagy. *Autophagy*, 8(5):794–811. PMID: 22635056.
- Fricker, B. A., Heckman, E. L., Cunningham, P. C., Wang, H., and Haas, J. S. (2021). Activity-dependent long-term potentiation of electrical synapses in the mammalian thalamus. *Journal of Neurophysiology*, 125(2):476–488. PMID: 33146066.
- Fukuda, T. (2009). Network architecture of gap junction-coupled neuronal linkage in the striatum. *Journal of Neuroscience*, 29(4):1235–1243.
- Furshpan, E. J. (1964). "electrical transmission" at an excitatory synapse in a vertebrate brain. *Science*, 144(3620):878–880.
- Furshpan, E. J. and Potter, D. D. (1957). Mechanism of nerve-impulse transmission at a crayfish synapse. *Nature*, 180(4581):342–343.
- Furshpan, E. J. and Potter, D. D. (1959). Transmission at the giant motor synapses of the crayfish. *J Physiol*, 145(2):289–325.
- Gaietta, G., Deerinck, T. J., Adams, S. R., Bouwer, J., Tour, O., Laird, D. W., Sosinsky, G. E., Tsien, R. Y., and Ellisman, M. H. (2002). Multicolor and electron microscopic imaging of connexin trafficking. *Science*, 296(5567):503–507.
- Galarreta, M. and Hestrin, S. (2001). Spike transmission and synchrony detection in networks of gabaergic interneurons. *Science*, 292.

- Galarreta, M. and Hestrin, S. (2002). Electrical and chemical synapses among parvalbumin fast-spiking gabaergic interneurons in adult mouse neocortex. *Proceedings of the National Academy of Sciences*, 99(19):12438–12443.
- Gandini, M. A. and Zamponi, G. W. (2021). Voltage-gated calcium channel nanodomains: molecular composition and function. *The FEBS Journal*, n/a(n/a).
- Gibson, J. R., Beierlein, M., and Connors, B. W. (2005). Functional properties of electrical synapses between inhibitory interneurons of neocortical layer 4. *J Neurophysiol*, 93(1):467–80.
- Giepmans, B. N. and Moolenaar, W. H. (1998). The gap junction protein connexin43 interacts with the second pdz domain of the zona occludens-1 protein. *Current Biology*, 8(16):931–934.
- Goaillard, J.-M. and Marder, E. (2021). Ion channel degeneracy, variability, and covariation in neuron and circuit resilience. *Annual Review of Neuroscience*, 44(1):null. PMID: 33770451.
- Gollisch, T. and Meister, M. (2008). Rapid neural coding in the retina with relative spike latencies. *Science*, 319(5866):1108–1111.
- Golowasch, J., Abbott, L. F., and Marder, E. (1999). Activity-dependent regulation of potassium currents in an identified neuron of the stomatogastric ganglion of the crab cancer borealis. *Journal of Neuroscience*, 19(20):RC33–RC33.
- González-Nieto, D., Gómez-Hernández, J. M., Larrosa, B., Gutiérrez, C., Muñoz, M. D., Fasciani, I., O’Brien, J., Zappalà, A., Cicirata, F., and Barrio, L. C. (2008). Regulation of neuronal connexin-36 channels by ph. *Proceedings of the National Academy of Sciences*, 105(44):17169–17174.
- Govindarajan, R., Chakraborty, S., Johnson, K. E., Falk, M. M., Wheelock, M. J., Johnson, K. R., and Mehta, P. P. (2010). Assembly of connexin43 into gap junctions is regulated differentially by e-cadherin and n-cadherin in rat liver epithelial cells. *Molecular Biology of the Cell*, 21(23):4089–4107.
- Gumpert, A. M., Varco, J. S., Baker, S. M., Piehl, M., and Falk, M. M. (2008). Double-membrane gap junction internalization requires the clathrin-mediated endocytic machinery. *FEBS Letters*, 582(19):2887–2892.
- Gómez-Gonzalo, M., Navarrete, M., Perea, G., Covelo, A., Martín-Fernández, M., Shigemoto, R., Luján, R., and Araque, A. (2014). Endocannabinoids induce lateral long-term

- potentiation of transmitter release by stimulation of gliotransmission. *Cerebral Cortex*, 25(10):3699–3712.
- Güiza, J., Barría, I., Sáez, J. C., and Vega, J. L. (2018). Innexins: Expression, regulation, and functions. *Frontiers in Physiology*, 9:1414.
- Haas, J. and Landisman, C. (2012). State-dependent modulation of gap junction signaling by the persistent sodium current. *Frontiers in Cellular Neuroscience*, 5:31.
- Haas, J. S., Zavala, B., and Landisman, C. E. (2011). Activity-dependent long-term depression of electrical synapses. *Science*, 334(6054):389–393.
- Hage, T. A. and Salkoff, L. (2012). Sodium-activated potassium channels are functionally coupled to persistent sodium currents. *Journal of Neuroscience*, 32(8):2714–2721.
- Halls, M. L. and Cooper, D. M. (2011). Regulation by  $Ca^{2+}$ -signaling pathways of adenylyl cyclases. *Cold Spring Harbor Perspectives in Biology*, 3(1).
- Hamzei-Sichani, F., Davidson, K., Yasumura, T., Janssen, W., Wearne, S., Hof, P., Traub, R., Gutierrez, R., Ottersen, O., and Rash, J. (2012). Mixed electrical–chemical synapses in adult rat hippocampus are primarily glutamatergic and coupled by connexin-36. *Frontiers in Neuroanatomy*, 6:13.
- Harris, A. L. (2001). Emerging issues of connexin channels: biophysics fills the gap. *Quarterly Reviews of Biophysics*, 34(3):325–472.
- Harris, A. L. and Locke, D. (2009). *Permeability of Connexin Channels*, pages 165–206. Humana Press, Totowa, NJ.
- Hartfield, E. M., Rinaldi, F., Glover, C. P., Wong, L.-F., Caldwell, M. A., and Uney, J. B. (2011). Connexin 36 expression regulates neuronal differentiation from neural progenitor cells. *PLOS ONE*, 6(3):1–10.
- Hecker, A., Schulze, W., Oster, J., Richter, D. O., and Schuster, S. (2020). Removing a single neuron in a vertebrate brain forever abolishes an essential behavior. *Proceedings of the National Academy of Sciences*, 117(6):3254–3260.
- Heifets, B. D., Chevalayre, V., and Castillo, P. E. (2008). Interneuron activity controls endocannabinoid-mediated presynaptic plasticity through calcineurin. *Proceedings of the National Academy of Sciences*, 105(29):10250–10255.
- Herring, B. E. and Nicoll, R. A. (2016). Long-term potentiation: From camkii to ampa receptor trafficking. *Annual Review of Physiology*, 78(1):351–365. PMID: 26863325.

- Hervé, J.-C., Derangeon, M., Sarrouilhe, D., and Bourmeyster, N. (2014). Influence of the scaffolding protein zonula occludens (zos) on membrane channels. *Biochimica et Biophysica Acta (BBA) - Biomembranes*, 1838(2):595 – 604. Reciprocal influences between cell cytoskeleton and membrane channels, receptors and transporters.
- Hervé, J.-C., Derangeon, M., Sarrouilhe, D., Giepmans, B. N., and Bourmeyster, N. (2012). Gap junctional channels are parts of multiprotein complexes. *Biochimica et Biophysica Acta (BBA) - Biomembranes*, 1818(8):1844 – 1865. The Communicating junctions, composition, structure and characteristics Part 1.
- Hille, B. (2001). *Ion Channels of Excitable Membranes*. Sinauer Associates, 3rd edition edition.
- Hjorth, J., Blackwell, K. T., and Hellgren Kotaleski, J. (2009). Gap junctions between striatal fast-spiking interneurons regulate spiking activity and synchronization as a function of cortical activity. *J Neurosci*, 29(16):5276–5286.
- Hoge, G. J., Davidson, K. G. V., Yasumura, T., Castillo, P. E., Rash, J. E., and Pereda, A. E. (2011). The extent and strength of electrical coupling between inferior olivary neurons is heterogeneous. *Journal of Neurophysiology*, 105(3):1089–1101. PMID: 21177999.
- Hombach, S., Janssen-Bienhold, U., Söhl, G., Schubert, T., Büssow, H., Ott, T., Weiler, R., and Willecke, K. (2004). Functional expression of connexin57 in horizontal cells of the mouse retina. *European Journal of Neuroscience*, 19(10):2633–2640.
- Hormuzdi, S. G., Filippov, M. A., Mitropoulou, G., Monyer, H., and Bruzzone, R. (2004). Electrical synapses: a dynamic signaling system that shapes the activity of neuronal networks. *BBA-Biomembranes*, 1662(1-2):113 – 137.
- Hormuzdi, S. G., Pais, I., LeBeau, F. E., Towers, S. K., Rozov, A., Buhl, E. H., Whittington, M. A., and Monyer, H. (2001). Impaired electrical signaling disrupts gamma frequency oscillations in connexin 36-deficient mice. *Neuron*, 31(3):487–495.
- Horn, K. M., Deep, A., and Gibson, A. R. (2013). Progressive limb ataxia following inferior olive lesions. *The Journal of physiology*, 591(22):5475–5489.
- Hornstein, E. P., Verweij, J., Li, P. H., and Schnapf, J. L. (2005). Gap-junctional coupling and absolute sensitivity of photoreceptors in macaque retina. *Journal of Neuroscience*, 25(48):11201–11209.
- Hsiao, C.-F., Kaur, G., Vong, A., Bawa, H., and Chandler, S. H. (2009). Participation of Kv1 channels in control of membrane excitability and burst generation in mesencephalic V neurons. *J Neurophysiol*, 101(3):1407–18.

- Hu, H. and Agmon, A. (2015). Properties of precise firing synchrony between synaptically coupled cortical interneurons depend on their mode of coupling. *Journal of Neurophysiology*, 114(1):624–637. PMID: 25972585.
- Hu, H., Ma, Y., and Agmon, A. (2011). Submillisecond firing synchrony between different subtypes of cortical interneurons connected chemically but not electrically. *Journal of Neuroscience*, 31(9):3351–3361.
- Huang, C.-C., Lo, S.-W., and Hsu, K.-S. (2001). Presynaptic mechanisms underlying cannabinoid inhibition of excitatory synaptic transmission in rat striatal neurons. *The Journal of Physiology*, 532(3):731–748.
- Huang, W., Xiu, Y., an Yan, J., juan He, W., dong Zhao, Y., an Hu, Z., and zhen Ruan, H. (2010). Facilitation of ih channels by p2y1 receptors activation in mesencephalic trigeminal neurons. *Neuroscience Letters*, 482(2):156–159.
- Huguenard, J. and McCormick, D. (1992). Simulation of the currents involved in rhythmic oscillations in thalamic relay neurons. *J Neurophysiol*, 68(4):1373–1383.
- Hyun, J. H., Eom, K., Lee, K.-H., Ho, W.-K., and Lee, S.-H. (2013). Activity-dependent downregulation of d-type k<sup>+</sup> channel subunit kv1.2 in rat hippocampal ca3 pyramidal neurons. *The Journal of Physiology*, 591(22):5525–5540.
- Inagaki, N., Yamatodani, A., Shinoda, K., Shiotani, Y., Tohyama, M., Watanabe, T., and Wada, H. (1987). The histaminergic innervation of the mesencephalic nucleus of the trigeminal nerve in rat brain: a light and electron microscopical study. *Brain Research*, 418(2):388–391.
- Izhikevich, E. M. (2006). *Dynamical Systems in Neuroscience: The Geometry of Excitability and Bursting*, volume 38. The MIT Press.
- Jabeen, S. and Thirumalai, V. (2018). The interplay between electrical and chemical synaptogenesis. *Journal of Neurophysiology*, 120(4):1914–1922. PMID: 30067121.
- Jacobson, G. A., Rokni, D., and Yarom, Y. (2008). A model of the olivo-cerebellar system as a temporal pattern generator. *Trends in Neurosciences*, 31(12):617–625.
- Janssen-Bienhold, U., Trümppler, J., Hilgen, G., Schultz, K., De Sevilla Müller, L. P., Sonntag, S., Dedek, K., Dirks, P., Willecke, K., and Weiler, R. (2009). Connexin57 is expressed in dendro-dendritic and axo-axonal gap junctions of mouse horizontal cells and its distribution is modulated by light. *Journal of Comparative Neurology*, 513(4):363–374.



- Jin, N., Zhang, Z., Keung, J., Youn, S. B., Ishibashi, M., Tian, L.-M., Marshak, D. W., Solessio, E., Umino, Y., Fahrenfort, I., Kiyama, T., Mao, C.-A., You, Y., Wei, H., Wu, J., Postma, F., Paul, D. L., Massey, S. C., and Ribelayga, C. P. (2020). Molecular and functional architecture of the mouse photoreceptor network. *Science Advances*, 6(28).
- Jin, Y.-H., Wu, X.-S., Shi, B., Zhang, Z., Guo, X., Gan, L., Chen, Z., and Wu, L.-G. (2019). Protein kinase c and calmodulin serve as calcium sensors for calcium-stimulated endocytosis at synapses. *Journal of Neuroscience*, 39(48):9478–9490.
- Jing, J. (2017). *Network Functions and Plasticity: Perspectives from Studying Neuronal Electrical Coupling in Microcircuits*. Academic Press.
- Kanaporis, G., Mese, G., Valiuniene, L., White, T. W., Brink, P. R., and Valiunas, V. (2008). Gap junction channels exhibit connexin-specific permeability to cyclic nucleotides. *Journal of General Physiology*, 131(4):293–305.
- Kandel, E. R., Schwartz, J. H., Jessell, T. M., Siegelbaum, S. A., and Hudspeth, A. J. (2012). *Principles of Neural Science*. McGraw-Hill Medical, fifth edition.
- Kandler, K. and Katz, L. C. (1998). Coordination of neuronal activity in developing visual cortex by gap junction-mediated biochemical communication. *Journal of Neuroscience*, 18(4):1419–1427.
- Kang, Y., Notomi, T., Saito, M., Zhang, W., and Shigemoto, R. (2004). Bidirectional interactions between h-channels and na<sup>+</sup>-k<sup>+</sup> pumps in mesencephalic trigeminal neurons. *J Neurosci*, 24(14):3694–3702.
- Khakh, B. S. and Henderson, G. (1998). Hyperpolarization-activated cationic currents (ih) in neurones of the trigeminal mesencephalic nucleus of the rat. *Journal of Physiology*, 510.3:695–704.
- Khan, A. K., Jagielnicki, M., McIntire, W. E., Purdy, M. D., Dharmarajan, V., Griffin, P. R., and Yeager, M. (2020). A steric “ball-and-chain” mechanism for ph-mediated regulation of gap junction channels. *Cell Reports*, 31(3):107482.
- Khosrovani, S., Van Der Giessen, R. S., De Zeeuw, C. I., and De Jeu, M. T. G. (2007). In vivo mouse inferior olive neurons exhibit heterogeneous subthreshold oscillations and spiking patterns. *Proceedings of the National Academy of Sciences*, 104(40):15911–15916.
- Kim, H. Y., Kim, K., Li, H. Y., Chung, G., Park, C.-K., Kim, J. S., Jung, S. J., Lee, M. K., Ahn, D. K., Hwang, S. J., Kang, Y., Binshtok, A. M., Bean, B. P., Woolf,

- C. J., and Oh, S. B. (2010). Selectively targeting pain in the trigeminal system. *PAIN*, 150(1):29–40.
- Kim, J., Jung, S.-C., Clemens, A. M., Petralia, R. S., and Hoffman, D. A. (2007). Regulation of dendritic excitability by activity-dependent trafficking of the a-type k<sup>+</sup> channel subunit kv4.2 in hippocampal neurons. *Neuron*, 54(6):933–947.
- Kothmann, W. W., Li, X., Burr, G. S., and O’Brien, J. (2007). Connexin 35/36 is phosphorylated at regulatory sites in the retina. *Visual Neuroscience*, 24(3):363–375.
- Kothmann, W. W., Massey, S. C., and O’Brien, J. (2009). Dopamine-stimulated dephosphorylation of connexin 36 mediates aii amacrine cell uncoupling. *J. Neurosci.*, 29.
- Kothmann, W. W., Trexler, E. B., Whitaker, C. M., Li, W., Massey, S. C., and O’Brien, J. (2012). Nonsynaptic nmda receptors mediate activity-dependent plasticity of gap junctional coupling in the aii amacrine cell network. *Journal of Neuroscience*, 32(20):6747–6759.
- Kotova, A., Timonina, K., and Zoidl, G. R. (2020). Endocytosis of connexin 36 is mediated by interaction with caveolin-1. *International Journal of Molecular Sciences*, 21(15).
- Kushmerick, C., Price, G. D., Taschenberger, H., Puente, N., Renden, R., Wadiche, J. I., Duvoisin, R. M., Grandes, P., and von Gersdorff, H. (2004). Retroinhibition of presynaptic ca<sup>2+</sup> currents by endocannabinoids released via postsynaptic mglur activation at a calyx synapse. *Journal of Neuroscience*, 24(26):5955–5965.
- Lampe, P. D., TenBroek, E. M., Burt, J. M., Kurata, W. E., Johnson, R. G., and Lau, A. F. (2000). Phosphorylation of connexin43 on serine368 by protein kinase c regulates gap junctional communication. *Journal of Cell Biology*, 149(7):1503–1512.
- Landisman, C. E. and Connors, B. W. (2005). Long-term modulation of electrical synapses in the mammalian thalamus. *Science*, 310(5755):1809–1813.
- Landisman, C. E., Long, M. A., Beierlein, M., Deans, M. R., Paul, D. L., and Connors, B. W. (2002). Electrical synapses in the thalamic reticular nucleus. *J Neurosci*, 22(3):1002–1009.
- Lane, B. J., Samarth, P., Ransdell, J. L., Nair, S. S., and Schulz, D. J. (2016). Synergistic plasticity of intrinsic conductance and electrical coupling restores synchrony in an intact motor network. *eLife*, 5:e16879.

- Lang, E. J., Sugihara, I., and Llinas, R. (1996). Gabaergic modulation of complex spike activity by the cerebellar nucleoolivary pathway in rat. *Journal of Neurophysiology*, 76(1):255–275. PMID: 8836223.
- Latorre, R. and Brauchi, S. (2006). Large conductance  $\text{Ca}^{2+}$ -activated  $\text{K}^{+}$  (BK) channel: Activation by  $\text{Ca}^{2+}$  and voltage. *Biological Research*, 39:385 – 401.
- Lauf, U., Giepmans, B. N. G., Lopez, P., Braconnot, S., Chen, S.-C., and Falk, M. M. (2002). Dynamic trafficking and delivery of connexons to the plasma membrane and accretion to gap junctions in living cells. *Proceedings of the National Academy of Sciences*, 99(16):10446–10451.
- Lazarov, N. E. (2002). Comparative analysis of the chemical neuroanatomy of the mammalian trigeminal ganglion and mesencephalic trigeminal nucleus. *Progress in Neurobiology*, 66(1):19 – 59.
- Lazarov, N. E. (2007). Neurobiology of orofacial proprioception. *Brain Research Reviews*, 56(2):362–383.
- Lazarov, N. E. and Gratzl, M. (2006). Selective expression of histamine receptors in rat mesencephalic trigeminal neurons. *Neuroscience Letters*, 404(1–2):67 – 71.
- Lefler, Y., Amsalem, O., Vrieler, N., Segev, I., and Yarom, Y. (2020). Using subthreshold events to characterize the functional architecture of the electrically coupled inferior olive network. *eLife*, 9:e43560.
- Lefler, Y., Yarom, Y., and Uusisaari, M. Y. (2014). Cerebellar inhibitory input to the inferior olive decreases electrical coupling and blocks subthreshold oscillations. *Neuron*, 81.
- Leithe, E. and Rivedal, E. (2004). Ubiquitination and down-regulation of gap junction protein connexin-43 in response to 12-o-tetradecanoylphorbol 13-acetate treatment. *Journal of Biological Chemistry*, 279(48):50089–50096.
- Leznik, E. and Llinás, R. (2005). Role of gap junctions in synchronized neuronal oscillations in the inferior olive. *J. Neurophysiol.*, 94.
- Li, H., Zhang, Z., Blackburn, M. R., Wang, S. W., Ribelayga, C. P., and O’Brien, J. (2013). Adenosine and dopamine receptors coregulate photoreceptor coupling via gap junction phosphorylation in mouse retina. *Journal of Neuroscience*, 33(7):3135–3150.

- Li, P. H., Verweij, J., Long, J. H., and Schnapf, J. L. (2012a). Gap-junctional coupling of mammalian rod photoreceptors and its effect on visual detection. *Journal of Neuroscience*, 32(10):3552–3562.
- Li, X., Kamasawa, N., Ciolofan, C., Olson, C. O., Lu, S., Davidson, K. G. V., Yasumura, T., Shigemoto, R., Rash, J. E., and Nagy, J. I. (2008). Connexin45-containing neuronal gap junctions in rodent retina also contain connexin36 in both apposing hemiplaques, forming bihomotypic gap junctions, with scaffolding contributed by zonula occludens-1. *Journal of Neuroscience*, 28(39):9769–9789.
- Li, X., Lu, S., and Nagy, J. I. (2009). Direct association of connexin36 with zonula occludens-2 and zonula occludens-3. *Neurochemistry International*, 54(5):393 – 402.
- Li, X., Lynn, B. D., and Nagy, J. I. (2012b). The effector and scaffolding proteins af6 and muppl1 interact with connexin36 and localize at gap junctions that form electrical synapses in rodent brain. *European Journal of Neuroscience*, 35(2):166–181.
- Li, X., Olson, C., Lu, S., Kamasawa, N., Yasumura, T., Rash, J. E., and Nagy, J. I. (2004). Neuronal connexin36 association with zonula occludens-1 protein (zo-1) in mouse brain and interaction with the first pdz domain of zo-1. *European Journal of Neuroscience*, 19(8):2132–2146.
- Lichtenstein, A., Minogue, P. J., Beyer, E. C., and Berthoud, V. M. (2011). Autophagy: a pathway that contributes to connexin degradation. *Journal of Cell Science*, 124(6):910–920.
- Lin, J. and Faber, D. (1988). Synaptic transmission mediated by single club endings on the goldfish mauthner cell. i. characteristics of electrotonic and chemical postsynaptic potentials. *Journal of Neuroscience*, 8(4):1302–1312.
- Lin, Y.-C., Huang, J., Zhang, Q., Hollander, J. M., Frisbee, J. C., Martin, K. H., Nestor, C., Goodman, R., and Yu, H.-G. (2010). Inactivation of l-type calcium channel modulated by hcn2 channel. *American Journal of Physiology-Cell Physiology*, 298(5):C1029–C1037. PMID: 20164379.
- Lisman, J., Yasuda, R., and Raghavachari, S. (2012). Mechanisms of camkii action in long-term potentiation. *Nature Reviews Neuroscience*, 13(3):169–182.
- Liu, P., Chen, B., Mailler, R., and Wang, Z.-W. (2017). Antidromic-rectifying gap junctions amplify chemical transmission at functionally mixed electrical-chemical synapses. *Nature Communications*, 8(1):14818.

- Liu, Y.-C. and Hale, M. E. (2017). Local spinal cord circuits and bilateral mauthner cell activity function together to drive alternative startle behaviors. *Current Biology*, 27(5):697–704.
- Llinas, R., Baker, R., and Sotelo, C. (1974). Electrotonic coupling between neurons in cat inferior olive. *Journal of Neurophysiology*, 37(3):560–571. PMID: 4827022.
- Llinas, R., Sugimori, M., and Silver, R. (1992). Microdomains of high calcium concentration in a presynaptic terminal. *Science*, 256(5057):677–679.
- Llinás, R. (2014). The olivo-cerebellar system: a key to understanding the functional significance of intrinsic oscillatory brain properties. *Frontiers in Neural Circuits*, 7:96.
- Llinás, R. and Yarom, Y. (1986). Oscillatory properties of guinea-pig inferior olivary neurones and their pharmacological modulation: an in vitro study. *The Journal of Physiology*, 376(1):163–182.
- Long, M. A., Deans, M. R., Paul, D. L., and Connors, B. W. (2002). Rhythmicity without synchrony in the electrically uncoupled inferior olive. *Journal of Neuroscience*, 22(24):10898–10905.
- Luo, P., Wong, R., and Dessem, D. (1995). Projection of jaw-muscle spindle afferents to the caudal brainstem in rats demonstrated using intracellular biotinamide. *Journal of Comparative Neurology*, 358(1):63–78.
- Lynn, B. D., Li, X., and Nagy, J. I. (2012). Under construction: Building the macromolecular superstructure and signaling components of an electrical synapse. *The Journal of Membrane Biology*, 245(5):303–317.
- Lüscher, C. and Malenka, R. C. (2012). Nmda receptor-dependent long-term potentiation and long-term depression (ltp/ltd). *Cold Spring Harbor Perspectives in Biology*, 4(6).
- Mackie, K., Lai, Y., Westenbroek, R., and Mitchell, R. (1995). Cannabinoids activate an inwardly rectifying potassium conductance and inhibit q-type calcium currents in att20 cells transfected with rat brain cannabinoid receptor. *Journal of Neuroscience*, 15(10):6552–6561.
- Maher, B. J., McGinley, M. J., and Westbrook, G. L. (2009). Experience-dependent maturation of the glomerular microcircuit. *Proceedings of the National Academy of Sciences*, 106(39):16865–16870.

- Mann-Metzer, P. and Yarom, Y. (1999). Electrotonic coupling interacts with intrinsic properties to generate synchronized activity in cerebellar networks of inhibitory interneurons. *Journal of Neuroscience*, 19(9):3298–3306.
- Marder, E., Abbott, L. F., Turrigiano, G. G., Liu, Z., and Golowasch, J. (1996). Memory from the dynamics of intrinsic membrane currents. *Proceedings of the National Academy of Sciences*, 93(24):13481–13486.
- Marder, E. and Goaillard, J.-M. (2006). Variability, compensation and homeostasis in neuron and network function. *Nature Reviews Neuroscience*, 7(7):563–574.
- Marinelli, S., Pacioni, S., Cannich, A., Marsicano, G., and Bacci, A. (2009). Self-modulation of neocortical pyramidal neurons by endocannabinoids. *Nature Neuroscience*, 12(12):1488–1490.
- Maroso, M., Szabo, G., Kim, H., Alexander, A., Bui, A., Lee, S.-H., Lutz, B., and Soltesz, I. (2016). Cannabinoid control of learning and memory through hcn channels. *Neuron*, 89(5):1059–1073.
- Martin, E. A., Lasseigne, A. M., and Miller, A. C. (2020). Understanding the molecular and cell biological mechanisms of electrical synapse formation. *Frontiers in Neuroanatomy*, 14:12.
- Martin, P. E. M., Blundell, G., Ahmad, S., Errington, R. J., and Evans, W. H. (2001). Multiple pathways in the trafficking and assembly of connexin 26, 32 and 43 into gap junction intercellular communication channels. *Journal of Cell Science*, 114(21):3845–3855.
- Mathy, A., Clark, B. A., and Häusser, M. (2014). Synaptically induced long-term modulation of electrical coupling in the inferior olive. *Neuron*, 81(6):1290–1296.
- Matthews, G. and Fuchs, P. (2010). The diverse roles of ribbon synapses in sensory neurotransmission. *Nature Reviews Neuroscience*, 11(12):812–822.
- Medan, V. and Preuss, T. (2014). The mauthner-cell circuit of fish as a model system for startle plasticity. *Journal of Physiology-Paris*, 108(2):129 – 140. Neuroethology: A Tribute to Hector Maldonado.
- Meier, C. and Dermietzel, R. (2006). *Electrical Synapses – Gap Junctions in the Brain*, pages 99–128. Springer Berlin Heidelberg, Berlin, Heidelberg.

- Mentis, G. Z., Díaz, E., Moran, L. B., and Navarrete, R. (2002). Increased incidence of gap junctional coupling between spinal motoneurons following transient blockade of nmda receptors in neonatal rats. *The Journal of Physiology*, 544(3):757–764.
- Meyer, A. H., Katona, I., Blatow, M., Rozov, A., and Monyer, H. (2002). In vivo labeling of parvalbumin-positive interneurons and analysis of electrical coupling in identified neurons. *Journal of Neuroscience*, 22(16):7055–7064.
- Michels, G., Brandt, M. C., Zagidullin, N., Khan, I. F., Larbig, R., van Aaken, S., Wippermann, J., and Hoppe, U. C. (2008). Direct evidence for calcium conductance of hyperpolarization-activated cyclic nucleotide-gated channels and human native If at physiological calcium concentrations. *Cardiovascular Research*, 78(3):466–475.
- Miller, A. C. and Pereda, A. E. (2017). The electrical synapse: Molecular complexities at the gap and beyond. *Developmental Neurobiology*, 77(5):562–574.
- Mitropoulou, G. and Bruzzone, R. (2003). Modulation of perch connexin35 hemi-channels by cyclic amp requires a protein kinase a phosphorylation site. *Journal of Neuroscience Research*, 72(2):147–157.
- Morquette, P., Lavoie, R., Fhima, M.-D., Lamoureux, X., Verdier, D., and Kolta, A. (2012). Generation of the masticatory central pattern and its modulation by sensory feedback. *Progress in neurobiology*, 96(3):340–55.
- Murphy, M. G. and O’Leary, J. L. (1971). Neurological Deficit in Cats With Lesions of the Olivocerebellar System. *Archives of Neurology*, 24(2):145–157.
- Musil, L. S. and Goodenough, D. A. (1993). Multisubunit assembly of an integral plasma membrane channel protein, gap junction connexin43, occurs after exit from the er. *Cell*, 74(6):1065–1077.
- Nagy, J. and Lynn, B. (2018). Structural and intermolecular associations between connexin36 and protein components of the adherens junction–neuronal gap junction complex. *Neuroscience*, 384:241 – 261.
- Nagy, J. I. and Rash, J. E. (2000). Connexins and gap junctions of astrocytes and oligodendrocytes in the cns. *Brain Research Reviews*, 32(1):29 – 44.
- Nargeot, R., Le Bon-Jego, M., and Simmers, J. (2009). Cellular and network mechanisms of operant learning-induced compulsive behavior in aplysia. *Current Biology*, 19(12):975–984.



- Navarrete, M., Díez, A., and Araque, A. (2014). Astrocytes in endocannabinoid signalling. *Philosophical Transactions of the Royal Society B: Biological Sciences*, 369(1654):20130599.
- Neil, S. M., Lakey, T., and Tomlinson, S. (1985). Calmodulin regulation of adenylate cyclase activity. *Cell Calcium*, 6(3):213–226.
- Nickel, B., Boller, M., Schneider, K., Shakespeare, T., Gay, V., and Murray, S. A. (2013). Visualizing the effect of dynamin inhibition on annular gap vesicle formation and fission. *Journal of Cell Science*, 126(12):2607–2616.
- Niessen, H., Harz, H., Bedner, P., Kramer, K., and Willecke, K. (2000). Selective permeability of different connexin channels to the second messenger inositol 1,4,5-trisphosphate. *Journal of Cell Science*, 113(8):1365–1372.
- Nitsche, J. M., Chang, H.-C., Weber, P. A., and Nicholson, B. J. (2004). A transient diffusion model yields unitary gap junctional permeabilities from images of cell-to-cell fluorescent dye transfer between xenopus oocytes. *Biophysical Journal*, 86(4):2058–2077.
- Notomi, T. and Shigemoto, R. (2004). Immunohistochemical localization of ih channel subunits, hcn1–4, in the rat brain. *Journal of Comparative Neurology*, 471(3):241–276.
- O’Brien, J., al Ubaidi, M. R., and Ripps, H. (1996). Connexin 35: a gap-junctional protein expressed preferentially in the skate retina. *Molecular biology of the cell*, 7(2):233–243.
- O’Brien, J., Bruzzone, R., White, T., Al-Ubaidi, M., and Ripps, H. (1998). Cloning and expression of two related connexins from the perch retina define a distinct subgroup of the connexin family. *The Journal of Neuroscience*, 18(19):7625—7637.
- Oh, S., Rubin, J. B., Bennett, M. V., Verselis, V. K., and Bargiello, T. A. (1999). Molecular Determinants of Electrical Rectification of Single Channel Conductance in Gap Junctions Formed by Connexins 26 and 32. *Journal of General Physiology*, 114(3):339–364.
- Ohara, H., Tachibana, Y., Fujio, T., Takeda-Ikeda, R., Sato, F., Oka, A., Kato, T., Ikenoue, E., Yamashiro, T., and Yoshida, A. (2016). Direct projection from the lateral habenula to the trigeminal mesencephalic nucleus in rats. *Brain Research*, 1630:183–197.
- Oshima, A., Tani, K., and Fujiyoshi, Y. (2016). Atomic structure of the innexin-6 gap junction channel determined by cryo-em. *Nature Communications*, 7(1):13681.

- Ostojic, S., Brunel, N., and Hakim, V. (2009). Synchronization properties of networks of electrically coupled neurons in the presence of noise and heterogeneities. *J Comput Neurosci*, 26(3):369–92.
- Otsuka, T. and Kawaguchi, Y. (2013). Common excitatory synaptic inputs to electrically connected cortical fast-spiking cell networks. *Journal of Neurophysiology*, 110(4):795–806. PMID: 23678022.
- Ouyang, X., Winbow, V. M., Patel, L. S., Burr, G. S., Mitchell, C. K., and O’Brien, J. (2005). Protein kinase a mediates regulation of gap junctions containing connexin35 through a complex pathway. *Molecular Brain Research*, 135(1):1 – 11.
- O’Brien, J. (2019). Design principles of electrical synaptic plasticity. *Neuroscience Letters*, 695:4 – 11. Connexins and Pannexins in the Healthy and Diseased Nervous System.
- O’Leary, T. and Marder, E. (2016). Temperature-robust neural function from activity-dependent ion channel regulation. *Current Biology*, 26(21):2935–2941.
- O’Leary, T., Williams, A., Franci, A., and Marder, E. (2014). Cell types, network homeostasis, and pathological compensation from a biologically plausible ion channel expression model. *Neuron*, 82(4):809–821.
- Palacios-Prado, N. and Bukauskas, F. F. (2012). Modulation of metabolic communication through gap junction channels by transjunctional voltage; synergistic and antagonistic effects of gating and ionophoresis. *Biochimica et Biophysica Acta (BBA) - Biomembranes*, 1818(8):1884 – 1894. The Communicating junctions, composition, structure and characteristics Part 1.
- Palacios-Prado, N., Chapuis, S., Panjkovich, A., Fregeac, J., Nagy, J. I., and Bukauskas, F. F. (2014a). Molecular determinants of magnesium-dependent synaptic plasticity at electrical synapses formed by connexin36. *Nature Communications*, 5(1):4667.
- Palacios-Prado, N., Hoge, G., Marandykina, A., Rimkute, L., Chapuis, S., Paulauskas, N., Skeberdis, V. A., O’Brien, J., Pereda, A. E., Bennett, M. V. L., and Bukauskas, F. F. (2013). Intracellular magnesium-dependent modulation of gap junction channels formed by neuronal connexin36. *Journal of Neuroscience*, 33(11):4741–4753.
- Palacios-Prado, N., Huetteroth, W., and Pereda, A. E. (2014b). Hemichannel composition and electrical synaptic transmission: molecular diversity and its implications for electrical rectification. *Frontiers in Cellular Neuroscience*, 8:324.

- Pan, F., Paul, D. L., Bloomfield, S. A., and Völgyi, B. (2010). Connexin36 is required for gap junctional coupling of most ganglion cell subtypes in the mouse retina. *Journal of Comparative Neurology*, 518(6):911–927.
- Park, W.-M., Wang, Y., Park, S., Denisova, J. V., Fontes, J. D., and Belousov, A. B. (2011). Interplay of chemical neurotransmitters regulates developmental increase in electrical synapses. *Journal of Neuroscience*, 31(16):5909–5920.
- Patel, L. S., Mitchell, C. K., Dubinsky, W. P., and O’Brien, J. (2006). Regulation of gap junction coupling through the neuronal connexin cx35 by nitric oxide and cgmp. *Cell Communication & Adhesion*, 13(1-2):41–54. PMID: 16613779.
- Patel, M. K., Khakh, B. S., and Henderson, G. (2001). Properties of native p2x receptors in rat trigeminal mesencephalic nucleus neurones: lack of correlation with known, heterologously expressed p2x receptors. *Neuropharmacology*, 40(1):96–105.
- Payton, B. W., Bennett, M. V. L., and Pappas, G. D. (1969). Temperature-dependence of resistance at an electrotonic synapse. *Science*, 165(3893):594–597.
- Pedroarena, C. M., Pose, I. E., Yamuy, J., Chase, M. H., and Morales, F. R. (1999). Oscillatory membrane potential activity in the soma of a primary afferent neuron. *J Neurophysiol*, 82(3):1465–1476.
- Peracchia, C. (2020a). Calmodulin-cork model of gap junction channel gating—one molecule, two mechanisms. *International Journal of Molecular Sciences*, 21(14).
- Peracchia, C. (2020b). Calmodulin-mediated regulation of gap junction channels. *International Journal of Molecular Sciences*, 21(2):485.
- Pereda, A., Bell, T., and Faber, D. (1995). Retrograde synaptic communication via gap junctions coupling auditory afferents to the mauthner cell. *Journal of Neuroscience*, 15(9):5943–5955.
- Pereda, A., Nairn, A., Wolszon, L., and Faber, D. (1994). Postsynaptic modulation of synaptic efficacy at mixed synapses on the mauthner cell. *Journal of Neuroscience*, 14(6):3704–3712.
- Pereda, A., O’Brien, J., Nagy, J. I., Bukauskas, F., Davidson, K. G. V., Kamasawa, N., Yasumura, T., and Rash, J. E. (2003). Connexin35 mediates electrical transmission at mixed synapses on mauthner cells. *Journal of Neuroscience*, 23(20):7489–7503.
- Pereda, A. E., Bell, T. D., Chang, B. H., Czernik, A. J., Nairn, A. C., Soderling, T. R., and Faber, D. S. (1998). Ca<sup>2+</sup>/calmodulin-dependent kinase ii mediates simultaneous

- enhancement of gap-junctional conductance and glutamatergic transmission. *Proceedings of the National Academy of Sciences*, 95(22):13272–13277.
- Phelan, P., Goulding, L. A., Tam, J. L., Allen, M. J., Dawber, R. J., Davies, J. A., and Bacon, J. P. (2008). Molecular mechanism of rectification at identified electrical synapses in the drosophila giant fiber system. *Current Biology*, 18(24):1955–1960.
- Piehl, M., Lehmann, C., Gumpert, A., Denizot, J.-P., Segretain, D., and Falk, M. M. (2007). Internalization of large double-membrane intercellular vesicles by a clathrin-dependent endocytic process. *Molecular Biology of the Cell*, 18(2):337–347.
- Piette, C., Cui, Y., Gervasi, N., and Venance, L. (2020). Lights on endocannabinoid-mediated synaptic potentiation. *Frontiers in Molecular Neuroscience*, 13:132.
- Piggott, B. J., Liu, J., Feng, Z., Wescott, S. A., and Xu, X. S. (2011). The neural circuits and synaptic mechanisms underlying motor initiation in *C. elegans*. *Cell*, 147(4):922–933.
- Pirri, J. K. and Alkema, M. J. (2012). The neuroethology of *c. elegans* escape. *Current Opinion in Neurobiology*, 22(2):187 – 193. Neuroethology.
- Placantonakis, D. G., Bukovsky, A. A., Zeng, X.-H., Kiem, H.-P., and Welsh, J. P. (2004). Fundamental role of inferior olive connexin 36 in muscle coherence during tremor. *Proceedings of the National Academy of Sciences*, 101(18):7164–7169.
- Pose, I., Sampogna, S., Chase, M. H., and Morales, F. R. (2003). Mesencephalic trigeminal neurons are innervated by nitric oxide synthase-containing fibers and respond to nitric oxide. *Brain Research*, 960(1–2):81 – 89.
- Pouille, F., McTavish, T. S., Hunter, L. E., Restrepo, D., and Schoppa, N. E. (2017). Intraglomerular gap junctions enhance interglomerular synchrony in a sparsely connected olfactory bulb network. *The Journal of Physiology*, 595(17):5965–5986.
- Prinz, A. A., Bucher, D., and Marder, E. (2004). Similar network activity from disparate circuit parameters. *Nat Neurosci*, (7):1345–1352.
- Puil, E., Gimbarzevsky, B., and Miura, R. M. (1986). Quantification of membrane properties of trigeminal root ganglion neurons in guinea pigs. *Journal of Neurophysiology*, 55(5):995–1016. PMID: 3711977.
- Rash, J., Curti, S., Vanderpool, K., Kamasawa, N., Nannapaneni, S., Palacios-Prado, N., Flores, C., Yasumura, T., O’Brien, J., Lynn, B., Bukauskas, F. F., Nagy, J., and Pereda,

- A. (2013). Molecular and functional asymmetry at a vertebrate electrical synapse. *Neuron*, 79(5):957 – 969.
- Rash, J. E., Staines, W. A., Yasumura, T., Patel, D., Furman, C. S., Stelmack, G. L., and Nagy, J. I. (2000). Immunogold evidence that neuronal gap junctions in adult rat brain and spinal cord contain connexin-36 but not connexin-32 or connexin-43. *Proceedings of the National Academy of Sciences*, 97(13):7573–7578.
- Rash, J. E., Yasumura, T., Davidson, K. G. V., Furman, C. S., Dudek, F. E., and Nagy, J. I. (2001). Identification of cells expressing cx43, cx30, cx26, cx32 and cx36 in gap junctions of rat brain and spinal cord. *Cell Communication & Adhesion*, 8(4-6):315–320. PMID: 12064610.
- Rhett, J. M. and Gourdie, R. G. (2012). The perinexus: A new feature of cx43 gap junction organization. *Heart Rhythm*, 9(4):619–623.
- Rhett, J. M., Jourdan, J., and Gourdie, R. G. (2011). Connexin 43 connexon to gap junction transition is regulated by zonula occludens-1. *Molecular Biology of the Cell*, 22(9):1516–1528. PMID: 21411628.
- Ribelayga, C., Cao, Y., and Mangel, S. C. (2008). The circadian clock in the retina controls rod-cone coupling. *Neuron*, 59(5):790 – 801.
- Rimkute, L., Kraujalis, T., Snipas, M., Palacios-Prado, N., Jotautis, V., Skeberdis, V. A., and Bukauskas, F. F. (2018). Modulation of connexin-36 gap junction channels by intracellular ph and magnesium ions. *Frontiers in Physiology*, 9:362.
- Rituper, B., Guček, A., Jorgačevski, J., Flašker, A., Kreft, M., and Zorec, R. (2013). High-resolution membrane capacitance measurements for the study of exocytosis and endocytosis. *Nature Protocols*, 8(6):1169–1183.
- Robertson, S. J., Burnashev, N., and Edwards, F. A. (1999). Ca<sup>2+</sup> permeability and kinetics of glutamate receptors in rat medial habenula neurones: implications for purinergic transmission in this nucleus. *The Journal of Physiology*, 518(2):539–549.
- Robinson, R. B. and Siegelbaum, S. A. (2003). Hyperpolarization-activated cation currents: From molecules to physiological function. *Annual Review of Physiology*, 65(1):453–480. PMID: 12471170.
- Santin, J. M. and Schulz, D. J. (2019). Membrane voltage is a direct feedback signal that influences correlated ion channel expression in neurons. *Current Biology*, 29(10):1683–1688.e2.

- Santos-Miranda, A., Chen, H., Chen, R. C., Odoko-Ishimoto, M., Aoyama, H., and Bai, D. (2020). The amino terminal domain plays an important role in transjunctional voltage-dependent gating kinetics of cx45 gap junctions. *Journal of Molecular and Cellular Cardiology*, 143:71 – 84.
- Santos-Miranda, A., Noureldin, M., and Bai, D. (2019). Effects of temperature on transjunctional voltage-dependent gating kinetics in cx45 and cx40 gap junction channels. *Journal of Molecular and Cellular Cardiology*, 127:185–193.
- Schneggenburger, R. (1996). Simultaneous measurement of  $Ca^{2+}$  influx and reversal potentials in recombinant n-methyl-d-aspartate receptor channels. *Biophysical Journal*, 70(5):2165–2174.
- Schneggenburger, R., Zhou, Z., Konnerth, A., and Neher, E. (1993). Fractional contribution of calcium to the cation current through glutamate receptor channels. *Neuron*, 11(1):133–143.
- Schubert, T., Degen, J., Willecke, K., Hormuzdi, S. G., Monyer, H., and Weiler, R. (2005a). Connexin36 mediates gap junctional coupling of alpha-ganglion cells in mouse retina. *Journal of Comparative Neurology*, 485(3):191–201.
- Schubert, T., Maxeiner, S., Krüger, O., Willecke, K., and Weiler, R. (2005b). Connexin45 mediates gap junctional coupling of bistratified ganglion cells in the mouse retina. *Journal of Comparative Neurology*, 490(1):29–39.
- Schulz, D. J., Goaillard, J.-M., and Marder, E. (2006). Variable channel expression in identified single and electrically coupled neurons in different animals. *Nature Neuroscience*, 9(3):356–362.
- Schweighofer, N., Lang, E., and Kawato, M. (2013). Role of the olivo-cerebellar complex in motor learning and control. *Frontiers in Neural Circuits*, 7:94.
- Segretain, D. and Falk, M. M. (2004). Regulation of connexin biosynthesis, assembly, gap junction formation, and removal. *Biochimica et Biophysica Acta (BBA) - Biomembranes*, 1662(1):3 – 21. The Connexins.
- Serre-Beinier, V., Bosco, D., Zulianello, L., Charollais, A., Caille, D., Charpantier, E., Gauthier, B. R., Diaferia, G. R., Giepmans, B. N., Lupi, R., Marchetti, P., Deng, S., Buhler, L., Berney, T., Cirulli, V., and Meda, P. (2008). Cx36 makes channels coupling human pancreatic  $\beta$ -cells, and correlates with insulin expression. *Human Molecular Genetics*, 18(3):428–439.

- Sevetson, J., Fittro, S., Heckman, E., and Haas, J. S. (2017). A calcium-dependent pathway underlies activity-dependent plasticity of electrical synapses in the thalamic reticular nucleus. *The Journal of Physiology*, 595(13):4417–4430.
- Sevetson, J. and Haas, J. S. (2015). Asymmetry and modulation of spike timing in electrically coupled neurons. *Journal of Neurophysiology*, 113(6):1743–1751. PMID: 25540226.
- Shen, B., Zhou, K., Yang, S., Xu, T., and Wang, Y. (2008). The kv4.2 mediates excitatory activity-dependent regulation of neuronal excitability in rat cortical neurons. *Journal of Neurochemistry*, 105(3):773–783.
- Shigenaga, Y., Mitsuhiro, Y., Yoshida, A., Cao, C. Q., and Tsuru, H. (1988a). Morphology of single mesencephalic trigeminal neurons innervating masseter muscle of the cat. *Brain research*, 445(2):392–9.
- Shigenaga, Y., Yoshida, A., Mitsuhiro, Y., Doe, K., and Suemune, S. (1988b). Morphology of single mesencephalic trigeminal neurons innervating periodontal ligament of the cat. *Brain research*, 448(2):331–8.
- Shui, Y., Liu, P., Zhan, H., Chen, B., and Wang, Z.-W. (2020). Molecular basis of junctional current rectification at an electrical synapse. *Science Advances*, 6(27).
- Sieling, F., Bédécarrats, A., Simmers, J., Prinz, A. A., and Nargeot, R. (2014). Differential roles of nonsynaptic and synaptic plasticity in operant reward learning-induced compulsive behavior. *Current Biology*, 24(9):941–950.
- Sigworth, F. J. (1980). The variance of sodium current fluctuations at the node of ranvier. *The Journal of Physiology*, 307(1):97–129.
- Siu, R. C. F., Smirnova, E., Brown, C. A., Zoidl, C., Spray, D. C., Donaldson, L. W., and Zoidl, G. (2016). Structural and functional consequences of connexin 36 (cx36) interaction with calmodulin. *Frontiers in Molecular Neuroscience*, 9:120.
- Skeberdis, V. A., Rimkute, L., Skeberdyte, A., Paulauskas, N., and Bukauskas, F. F. (2011). ph-dependent modulation of connexin-based gap junctional uncouplers. *The Journal of Physiology*, 589(14):3495–3506.
- Skerrett, I. M. and Williams, J. B. (2017). A structural and functional comparison of gap junction channels composed of connexins and innexins. *Developmental Neurobiology*, 77(5):522–547.



- Sotelo, C., Llinas, R., and Baker, R. (1974). Structural study of inferior olivary nucleus of the cat: morphological correlates of electrotonic coupling. *Journal of Neurophysiology*, 37(3):541–559. PMID: 4827021.
- Srinivas, M., Rozental, R., Kojima, T., Dermietzel, R., Mehler, M., Condorelli, D. F., Kessler, J. A., and Spray, D. C. (1999). Functional properties of channels formed by the neuronal gap junction protein connexin36. *Journal of Neuroscience*, 19(22):9848–9855.
- Stefan Thurner, Rudolf Hanel, P. K. (2018). *Introduction to the Theory of Complex Systems*. Oxford University Press, USA, hardcover edition.
- Steinert, J. R., Robinson, S. W., Tong, H., Haustein, M. D., Kopp-Scheinpflug, C., and Forsythe, I. D. (2011). Nitric oxide is an activity-dependent regulator of target neuron intrinsic excitability. *Neuron*, 71(2):291–305.
- Stella, N. (2010). Cannabinoid and cannabinoid-like receptors in microglia, astrocytes, and astrocytomas. *Glia*, 58(9):1017–1030.
- Suchyna, T. M., Nitsche, J. M., Chilton, M., Harris, A. L., Veenstra, R. D., and Nicholson, B. J. (1999). Different ionic selectivities for connexins 26 and 32 produce rectifying gap junction channels. *Biophysical Journal*, 77(6):2968–2987.
- Szabó, G. G., Lenkey, N., Holderith, N., Andrási, T., Nusser, Z., and Hájos, N. (2014). Presynaptic calcium channel inhibition underlies cb1 cannabinoid receptor-mediated suppression of gaba release. *Journal of Neuroscience*, 34(23):7958–7963.
- Söhl, G., Degen, J., Teubner, B., and Willecke, K. (1998). The murine gap junction gene connexin36 is highly expressed in mouse retina and regulated during brain development. *FEBS Letters*, 428(1):27 – 31.
- Söhl, G., Güldenagel, M., Traub, O., and Willecke, K. (2000). Connexin expression in the retina. *Brain Research Reviews*, 32(1):138 – 145.
- Söhl, G. and Willecke, K. (2004). Gap junctions and the connexin protein family. *Cardiovascular Research*, 62(2):228–232.
- Takahashi, T., Shirasu, M., Shirasu, M., ya Kubo, K., Onozuka, M., Sato, S., Itoh, K., and Nakamura, H. (2010). The locus coeruleus projects to the mesencephalic trigeminal nucleus in rats. *Neuroscience Research*, 68(2):103–106.

- Tanaka, S. and Chandler, S. H. (2006). Serotonergic modulation of persistent sodium currents and membrane excitability via cyclic amp-protein kinase a cascade in mesencephalic v neurons. *Journal of Neuroscience Research*, 83(7):1362–1372.
- Tanaka, S., Tomita, I., Seki, S., Yamada, S., Kogo, M., and Furusawa, K. (2019). Serotonergic modulation of slow inward rectification in mesencephalic trigeminal neurons. *Brain Research*, 1718:126–136.
- Tanaka, S., Wu, N., Hsaio, C.-F., Turman, J., and Chandler, S. H. (2003). Development of inward rectification and control of membrane excitability in mesencephalic V neurons. *J Neurophysiol*, 89(3):1288–98.
- Tanimura, A., Yamazaki, M., Hashimotodani, Y., Uchigashima, M., Kawata, S., Abe, M., Kita, Y., Hashimoto, K., Shimizu, T., Watanabe, M., Sakimura, K., and Kano, M. (2010). The endocannabinoid 2-arachidonoylglycerol produced by diacylglycerol lipase; mediates retrograde suppression of synaptic transmission. *Neuron*, 65(3):320–327.
- Temporal, S., Lett, K., and Schulz, D. (2014). Activity-dependent feedback regulates correlated ion channel mrna levels in single identified motor neurons. *Current Biology*, 24(16):1899–1904.
- Tetenborg, S., Wang, H. Y., Nemitz, L., Depping, A., Espejo, A. B., Aseervatham, J., Bedford, M. T., Janssen-Bienhold, U., O’Brien, J., and Dedek, K. (2020). Phosphorylation of connexin36 near the c-terminus switches binding affinities for pdz-domain and 14–3–3 proteins in vitro. *Scientific Reports*, 10(1):18378.
- Teubner, B., Degen, J., Söhl, G., Güldenagel, M., Bukauskas, F. F., Trexler, E. B., Verselis, V. K., De Zeeuw, C. I., Lee, C. G., Kozak, C. A., Petrasch-Parwez, E., Dermietzel, R., and Willecke, K. (2000). Functional expression of the murine connexin 36 gene coding for a neuron-specific gap junctional protein. *The Journal of Membrane Biology*, 176(3):249–262.
- Thévenin, A. F., Kowal, T. J., Fong, J. T., Kells, R. M., Fisher, C. G., and Falk, M. M. (2013). Proteins and mechanisms regulating gap-junction assembly, internalization, and degradation. *Physiology*, 28(2):93–116. PMID: 23455769.
- Thévenin, A. F., Margraf, R. A., Fisher, C. G., Kells-Andrews, R. M., and Falk, M. M. (2017). Phosphorylation regulates connexin43/zo-1 binding and release, an important step in gap junction turnover. *Molecular Biology of the Cell*, 28(25):3595–3608. PMID: 29021339.

- Totland, M. Z., Rasmussen, N. L., Knudsen, L. M., and Leithe, E. (2020). Regulation of gap junction intercellular communication by connexin ubiquitination: physiological and pathophysiological implications. *Cellular and Molecular Life Sciences*, 77(4):573–591.
- Trenholm, S. and Awatramani, G. (2019). *Myriad roles for gap junctions in retinal circuits*. University of Utah Health Sciences Center, Salt Lake City (UT).
- Trenholm, S., Johnson, K., Li, X., Smith, R. G., and Awatramani, G. B. (2011). Parallel mechanisms encode direction in the retina. *Neuron*, 71(4):683–694.
- Trenholm, S., McLaughlin, A. J., Schwab, D. J., and Awatramani, G. B. (2013a). Dynamic tuning of electrical and chemical synaptic transmission in a network of motion coding retinal neurons. *Journal of Neuroscience*, 33(37):14927–14938.
- Trenholm, S., Schwab, D. J., Balasubramanian, V., and Awatramani, G. B. (2013b). Lag normalization in an electrically coupled neural network. *Nature Neuroscience*, 16(2):154–156.
- Trigo, F. F. (2019). Antidromic analog signaling. *Frontiers in Cellular Neuroscience*, 13:354.
- Turecek, J., Han, V. Z., Cuzon Carlson, V. C., Grant, K. A., and Welsh, J. P. (2016). Electrical coupling and synchronized subthreshold oscillations in the inferior olive of the rhesus macaque. *Journal of Neuroscience*, 36(24):6497–6502.
- Turecek, J., Yuen, G., Han, V., Zeng, X.-H., Bayer, K., and Welsh, J. (2014). Nmda receptor activation strengthens weak electrical coupling in mammalian brain. *Neuron*, 81(6):1375 – 1388.
- Turman Jr., J. E., Ajdari, J., and Chandler, S. H. (1999). Nmda receptor nr1 and nr2a/b subunit expression in trigeminal neurons during early postnatal development. *Journal of Comparative Neurology*, 409(2):237–249.
- Turrigiano, G., Abbott, L. F., and Marder, E. (1994). Activity-dependent changes in the intrinsic properties of cultured neurons. *Science*, 264.
- Twitchell, W., Brown, S., and Mackie, K. (1997). Cannabinoids inhibit n- and p/q-type calcium channels in cultured rat hippocampal neurons. *Journal of Neurophysiology*, 78(1):43–50. PMID: 9242259.
- Urschel, S., Höher, T., Schubert, T., Alev, C., Söhl, G., Wörsdörfer, P., Asahara, T., Dermietzel, R., Weiler, R., and Willecke, K. (2006). Protein kinase a-mediated phosphory-

- lation of connexin36 in mouse retina results in decreased gap junctional communication between aii amacrine cells. *Journal of Biological Chemistry*, 281(44):33163–33171.
- van Welie, I. and du Lac, S. (2011). Bidirectional control of bk channel open probability by camkii and pkc in medial vestibular nucleus neurons. *Journal of Neurophysiology*, 105(4):1651–1659. PMID: 21307321.
- Vandecasteele, M., Glowinski, J., and Venance, L. (2005). Electrical synapses between dopaminergic neurons of the substantia nigra pars compacta. *J Neurosci*, 25(2):291–298.
- Vanderpuye, O. A., Bell, C. L., and Murray, S. A. (2016). Redistribution of connexin 43 during cell division. *Cell Biology International*, 40(4):387–396.
- van Welie, I., Roth, A., Ho, S. S., Komai, S., and Häusser, M. (2016). Conditional spike transmission mediated by electrical coupling ensures millisecond precision-correlated activity among interneurons in vivo. *Neuron*, 90(4):810 – 823.
- Varga, A. W., Yuan, L.-L., Anderson, A. E., Schrader, L. A., Wu, G.-Y., Gatchel, J. R., Johnston, D., and Sweatt, J. D. (2004). Calcium–calmodulin-dependent kinase ii modulates kv4.2 channel expression and upregulates neuronal a-type potassium currents. *Journal of Neuroscience*, 24(14):3643–3654.
- Verdier, D., Lund, J. P., and Kolta, A. (2004). Synaptic inputs to trigeminal primary afferent neurons cause firing and modulate intrinsic oscillatory activity. *J Neurophysiol*, 92(4):2444–55.
- Verselis, V. K., Ginter, C. S., and Bargiello, T. A. (1994). Opposite voltage gating polarities of two closely related onnexins. *Nature*, 368(6469):348–351.
- Veruki, M. L. and Hartveit, E. (2002). Aii (rod) amacrine cells form a network of electrically coupled interneurons in the mammalian retina. *Neuron*, 33(6):935–946.
- Vervaeke, K., Lorincz, A., Gleeson, P., Farinella, M., Nusser, Z., and Silver, R. A. (2010). Rapid desynchronization of an electrically coupled interneuron network with sparse excitatory synaptic input. *Neuron*, 67(3):435–51.
- Vozzi, C., Dupont, E., Coppen, S. R., Yeh, H.-I., and Severs, N. J. (1999). Chamber-related differences in connexin expression in the human heart. *Journal of Molecular and Cellular Cardiology*, 31(5):991 – 1003.
- Wang, H. Y., Lin, Y.-P., Mitchell, C. K., Ram, S., and O’Brien, J. (2015). Two-color fluorescent analysis of connexin 36 turnover: relationship to functional plasticity. *Journal of Cell Science*, 128(21):3888–3897.

- Wang, H.-Z. and Veenstra, R. D. (1997). Monovalent Ion Selectivity Sequences of the Rat Connexin43 Gap Junction Channel . *Journal of General Physiology*, 109(4):491–507.
- Wang, L.-Y. and Augustine, G. J. (2015). Presynaptic nanodomains: a tale of two synapses. *Frontiers in Cellular Neuroscience*, 8:455.
- Wang, Z., long Xu, N., ping Wu, C., Duan, S., and ming Poo, M. (2003). Bidirectional changes in spatial dendritic integration accompanying long-term synaptic modifications. *Neuron*, 37(3):463–472.
- Warn-Cramer, B. J., Lampe, P. D., Kurata, W. E., Kanemitsu, M. Y., Loo, L. W. M., Eckhart, W., and Lau, A. F. (1996). Characterization of the mitogen-activated protein kinase phosphorylation sites on the connexin-43 gap junction protein. *Journal of Biological Chemistry*, 271(7):3779–3786.
- Watanabe, A. (1958). The interaction of electrical activity among neurons of lobster cardiac ganglion. *The Japanese Journal of Physiology*, 8:305–318.
- Weber, P. A., Chang, H.-C., Spaeth, K. E., Nitsche, J. M., and Nicholson, B. J. (2004). The permeability of gap junction channels to probes of different size is dependent on connexin composition and permeant-pore affinities. *Biophysical Journal*, 87(2):958–973.
- Welsh, J. and Turecek, J. (2017). Chapter 12 - implications of electrical synapse plasticity in the inferior olive. In Jing, J., editor, *Network Functions and Plasticity*, pages 265 – 299. Academic Press.
- Welzel, G. and Schuster, S. (2019). A direct comparison of different measures for the strength of electrical synapses. *Frontiers in Cellular Neuroscience*, 13:43.
- Weng, S., Sun, W., and He, S. (2005). Identification of on–off direction-selective ganglion cells in the mouse retina. *The Journal of Physiology*, 562(3):915–923.
- Westberg, K. G., Kolta, A., Clavelou, P., Sandström, G., and Lund, J. P. (2000). Evidence for functional compartmentalization of trigeminal muscle spindle afferents during fictive mastication in the rabbit. *European Journal of Neuroscience*, 12(4):1145–1154.
- Whyte-Fagundes, P. and Zoidl, G. (2018). Mechanisms of pannexin1 channel gating and regulation. *Biochimica et Biophysica Acta (BBA) - Biomembranes*, 1860(1):65–71. Gap Junction Proteins.
- Willecke, K., Eiberger, J., Degen, J., Eckardt, D., Romualdi, A., Güldenagel, M., Deutsch, U., and Söhl, G. (2002). Structural and functional diversity of connexin genes in the mouse and human genome. *Biological Chemistry*, 383(5):725 – 737.

- Wilson, R. I. and Nicoll, R. A. (2001). Endogenous cannabinoids mediate retrograde signalling at hippocampal synapses. *Nature*, 410(6828):588–592.
- Wilson, R. I. and Nicoll, R. A. (2002). Endocannabinoid signaling in the brain. *Science*, 296(5568):678–682.
- Won, J., Lee, P. R., and Oh, S. B. (2019). Alpha 2 adrenoceptor agonist guanabenz directly inhibits hyperpolarization-activated, cyclic nucleotide-modulated (hcn) channels in mesencephalic trigeminal nucleus neurons. *European Journal of Pharmacology*, 854:320–327.
- Xin, L., Gong, X.-Q., and Bai, D. (2010). The role of amino terminus of mouse cx50 in determining transjunctional voltage-dependent gating and unitary conductance. *Biophysical Journal*, 99(7):2077 – 2086.
- Yamamoto, T., Matsuo, R., Kiyomitsu, Y., and Kitamura, R. (1989). Sensory and motor responses of trigeminal and reticular neurons during ingestive behavior in rats. *Experimental Brain Research*, 76(2):386–400.
- Yang, X.-D., Korn, H., and Faber, D. S. (1990). Long-term potentiation of electrotonic coupling at mixed synapses. *Nature*, 348(6301):542–545.
- Yang, Y.-M., Wang, W., Fedchyshyn, M. J., Zhou, Z., Ding, J., and Wang, L.-Y. (2014). Enhancing the fidelity of neurotransmission by activity-dependent facilitation of presynaptic potassium currents. *Nature Communications*, 5(1):4564.
- Yarom, Y. and Cohen, D. (2002). The olivocerebellar system as a generator of temporal patterns. *Annals of the New York Academy of Sciences*, 978(1):122–134.
- Yoshida, S. and Oka, H. (1998). Membrane properties of dissociated trigeminal mesencephalic neurons of the adult rat. *Neuroscience Research*, 30(3):227–234.
- Yu, X., Chen, X.-W., Zhou, P., Yao, L., Liu, T., Zhang, B., Li, Y., Zheng, H., Zheng, L.-H., Zhang, C. X., Bruce, I., Ge, J.-B., Wang, S.-Q., Hu, Z.-A., Yu, H.-G., and Zhou, Z. (2007). Calcium influx through if channels in rat ventricular myocytes. *American Journal of Physiology-Cell Physiology*, 292(3):C1147–C1155. PMID: 17065201.
- Yu, X., Duan, K.-L., Shang, C.-F., Yu, H.-G., and Zhou, Z. (2004). Calcium influx through hyperpolarization-activated cation channels (ih channels) contributes to activity-evoked neuronal secretion. *Proceedings of the National Academy of Sciences*, 101(4):1051–1056.
- Zhang, B., Zhang, X.-Y., Luo, P.-F., Huang, W., Zhu, F.-P., Liu, T., Du, Y.-R., Wu, Q.-H., Lü, J., Xiu, Y., Liu, L.-N., Huang, H.-P., Guo, S., Zheng, H., Zhang, C. X.,

- and Zhou, Z. (2012). Action potential-triggered somatic exocytosis in mesencephalic trigeminal nucleus neurons in rat brain slices. *J Physiol*, 590(4):753–762.
- Zhang, C. (2011). Expression of connexin 57 in the olfactory epithelium and olfactory bulb. *Neuroscience Research*, 71(3):226 – 234.
- Zhang, C., Finger, T. E., and Restrepo, D. (2000). Mature olfactory receptor neurons express connexin 43. *Journal of Comparative Neurology*, 426(1):1–12.
- Zhang, W. and Linden, D. J. (2003). The other side of the engram: experience-driven changes in neuronal intrinsic excitability. *Nature Reviews Neuroscience*, 4(11):885–900.
- Zhang, Y. and Huang, H. (2017). Sk channels regulate resting properties and signaling reliability of a developing fast-spiking neuron. *Journal of Neuroscience*, 37(44):10738–10747.
- Zhang, Y., Xie, H., Lei, G., Li, F., Pan, J., Liu, C., Liu, Z., Liu, L., and Cao, X. (2014). Regulatory effects of anandamide on intracellular  $Ca^{2+}$  concentration increase in trigeminal ganglion neurons. *Neural Regeneration Research*, 9(8):878–887.
- Zhong, N., Beaumont, V., and Zucker, R. S. (2004). Calcium influx through hcn channels does not contribute to camp-enhanced transmission. *Journal of Neurophysiology*, 92(1):644–647. PMID: 15014107.
- Zou, S. and Kumar, U. (2018). Cannabinoid receptors and the endocannabinoid system: Signaling and function in the central nervous system. *International Journal of Molecular Sciences*, 19(3).
- Zsiros, V. and Maccaferri, G. (2005). Electrical coupling between interneurons with different excitable properties in the stratum lacunosum-moleculare of the juvenile ca1 rat hippocampus. *Journal of Neuroscience*, 25(38):8686–8695.
- Zsiros, V. and Maccaferri, G. (2008). Noradrenergic modulation of electrical coupling in gabaergic networks of the hippocampus. *J. Neurosci.*, 28.